

PASSENGER CARS IN HEAD-ON CRASHES WITH HEAVY GOODS VEHICLES: FOR WHAT SEVERITY SHOULD FUTURE CAR RESTRAINT SYSTEMS BE DESIGNED?

Krystoffer Mroz, Martin Östling, Nils Lubbe

Autoliv Research
Sweden

Paper Number 23-0060

ABSTRACT

Twelve passenger car-to-heavy goods vehicle (HGV) head-on crash configurations were simulated to identify which of these crashes lead to the highest crash severity for the car and are feasible, i.e., with non-compromised compartment integrity, in order to support the development of occupant restraints in high-severity crashes. These configurations comprised two impact velocities (car 39 km/h, HGV 36 km/h and car 56 km/h, HGV 53 km/h), two car overlaps (50 and 80 %) and three impact angles (0, 30 and -30 deg). Generic finite element models of a 1.7-ton car and a 7.9-ton HGV were used to investigate the crash pulse severity and car compartment structural integrity in all crash configurations; the results were compared to that of a current standard full-frontal rigid barrier 56 km/h crash. Car crash pulse severity was evaluated at the left sill using peak acceleration, delta-V, cross-zero time, and occupant load criteria, while car compartment integrity was evaluated by measuring intrusions at the toe pan, instrument panel, A-pillar, and steering wheel.

All lower-severity (39/36 km/h) crashes were found to be well represented by the full-frontal rigid barrier 56 km/h crash test. For the higher-severity (56/53 km/h) crashes, three out of six crashes (both -30 deg crashes and the 50% overlap 0 deg crash) were found as currently too severe in terms of compromised compartment integrity to be used in the development of new restraint systems. Two high-severity crashes were identified which can be targeted for new restraint systems development: The 56/53 km/h 80 % overlap 0 deg impact angle crash was determined to be the most severe in terms of peak accelerations (91 g) and OLC (63 g), and with a high delta-V (97 km/h). The 56/53 km/h 50 % 30 deg crash was found to be the most severe in terms of delta-V (105 km/h) and pulse duration in time. Both these crashes were much more severe than the full-frontal 56 km/h crash. The 56/53 km/h 80 % 0 deg crash was similar in crash severity to a full-frontal rigid barrier 90 km/h crash: we believe this configuration may be worth considering in future legislation and rating programs, which would immediately facilitate development of improved restraint system addressing fatalities in high-severity crashes.

Keywords: High-severity crash pulse, heavy goods vehicle, passenger car compatibility

INTRODUCTION

Of all road user groups in the European Union (EU), motorized transport generates the highest number of fatal crashes. Moreover, people are more likely to die in crashes that include a car than in those that comprise other transport modes such as cyclists, powered two-wheelers, trucks, or buses. In 2019 there were 22,700 road traffic fatalities in the EU, of which about 10,100 were car occupant fatalities [1]. The highest number of car occupant fatalities (44 %) occurred in crashes with no other vehicle involved, and the second highest in collisions with another car (30 %, 3067 fatalities) [2]. However, almost as many fatalities occurred in crashes between cars and trucks, which include commercial vehicles with a gross weight of less than 3.5 tons (584 fatalities, 6 %) and heavy goods vehicles (HGV) heavier than 3.5 tons (1557 fatalities, 16 %) [2]. In car-to-truck crashes, the velocity might be moderate, but the crash severity is still high due to geometric, stiffness, and mass incompatibility between the two vehicles.

In the US, there were 36,355 motor vehicle traffic fatalities during 2019, of which 34 % (12,355) were passenger car fatalities and 28 % (10,017) light truck fatalities (light trucks include SUVs, pickup trucks, and vans with a gross weight of less than 4.54 tons) [3]. In the years 2019 and 2020, there were approximately 5000 fatalities per year (approximately 14 % of all vehicle traffic fatalities) in the US from crashes involving large trucks (gross weight

>4.54 tons), increasing by approximately 13 % in 2021 compared to 2020. [4,5]. In Sweden, there were 210 road traffic fatalities in 2021, of which 18 % were from single-car crashes, 14 % from car-to-car crashes, and 17 % from car-to-truck crashes [6].

Investigating car-to-HGV crashes further is important, since car occupants killed in collisions with HGVs account for roughly 14 to 16 % of all car occupant fatalities in both EU and US (although the classification of HGVs differs between the regions). The most common accident types in car-to-HGV crashes are head-on crashes on rural roads and rear-end crashes on highways (the HGV drives into the rear of the car in front) [7].

In the EU-project SAFE-UP, researchers investigated which crash configurations future vehicles equipped with crash avoiding ADAS would be exposed to in mixed traffic [8]. Analysis of fatal crashes in the EU community database on road accidents (CARE) revealed that there were 6431 fatalities in modern cars (registration year 2000 or later) in the EU in 2018. Single-vehicle crashes and crashes with parking vehicles were then excluded, as future autonomous (L3-L4) cars are expected to avoid essentially all such crashes; crashes involving three or more vehicles were judged too complex, so these were also excluded. Of the remaining crashes, a target population of 2085 car fatalities for protection in future crash scenarios was defined from crashes in rural areas (excluding junctions) with exactly two vehicles. The most common crash scenarios remaining were car-to-car head-on (11 to 25 % of target population) and car-to-HGV head-on crashes (5 to 12 % of the target population). The percentage intervals reflect the large number of unknown values in the crash type classification in CARE: the lower bounds indicate the share of the given crash type as a percentage of the total sample while the higher bounds indicate their share among cases with known crash types. The car-to-HGV head-on crashes were further analyzed in-depth using the German In Depth Accident Study (GIDAS), in order to define the most relevant crash configurations in sufficient detail that virtual assessments of the vehicle kinematics could be performed. The crash configurations were statistically described by distribution percentiles for the car and the HGV kinematic parameters (impact speeds, overlap, impact angles, hit point, and vehicle weights). Three quartiles (at the 25, 50, and 75 % levels) of the crash configuration parameter distributions were defined with car/HGV impact speeds of 24/27 km/h, 39/36 km/h, and 56/53 km/h respectively, Table 1.

Table 1.
Distributions of crash configuration parameters for car-to-HGV (>3.5 ton) head-on collisions (from [8])

Parameter	Q25	Q50	Q75
Overlap (%)	0 to 25	50	80
Vc-PC (km/h)	24	39	56
Vc-HGV (km/h)	27	36	53
Impact Angle (deg)	up to ± 5	± 10	>10
Weight PC/HGV (ton)	-	1.5 / ≤ 10 ton	2.5 / ≤ 18 ton

High-severity crashes are less frequent than low- and moderate-severity crashes; however, the fatality rate is higher. Crashes at low severity (approximately 40 km/h and below) have more injured occupants due to the larger exposure and especially elderly occupants are at high risk [9,10]. Crashes at moderate severities (56 to 64 km/h) are well represented in the European and US legislation and rating programs, and the car structure and occupant restraints are to a large extent designed for those crash severities. It has been shown that adaptive restraint systems can improve the protection for car occupants in low-severity crashes (i.e., for the elderly) while at the same time retaining high protection in moderate-severity crashes [11]. Extending the capability of adaptive restraints to include better protection in high-severity crashes could improve the survivability in car-to-HGV crashes, but only if the compartment remains intact and challenges in sensor development for crash severity detection can be solved.

The objective of this study was to investigate which of twelve car-to-HGV head-on crash configurations, all defined from statistical descriptions of their kinematic parameters [8], lead to the highest crash severity—without compromised compartment integrity of the passenger car. Based on this analysis it can be identified which of these crashes are challenging, but immediately feasible, targets for occupant restraints development and are therefore recommended to complement conventional assessments focusing on full frontal impacts. To serve this objective,

generic simulation models of the HGV and the passenger car were used to study compatibility, car crash pulse severity, and car structural integrity for varying impact speeds, overlaps and impact angles of the head-on crashes. The results were compared to the traditional car full-frontal rigid barrier crash at 56 km/h.

METHODS

Vehicle Models

For the passenger car, a finite element (FE) model of the NHTSA 5-star and IIHS “Good/Top Safety Pick+” rated 2014 model year Honda Accord was used in the study, Figure 1. The model was correlated in the full width US-NCAP 56 km/h frontal crash test, the NHTSA oblique 90 km/h test (for both left- and right-side frontal oblique offset) and the IIHS small (25 %) and moderate (40 %) overlap 64 km/h frontal tests [12, 13].

For the heavy goods vehicle, an FE-model of a generic European cab-over-engine truck tractor was used. This HGV model was originally developed for impacts to roadside safety barriers [14]; using an accordingly adapted modelling approach [15]. In this study the trailer was not used, which reduced the HGV weight to 7860 kg, corresponding to the Q50 crash configuration in *Table 1*. As frontal (head-on) impacts were under investigation, the model was equipped with a frontal underride protection (FUP) device, created from faro-scan measurements of a European HGV. The FUP was modeled as rigidly mounted to the longitudinal rails of the HGV model, and its vertical position was aligned with the bumper of the passenger car. Its performance was assessed according to UN/ECE Regulation No 93 [16]. Distributed loading in three points (P1=80 kN, P2=160 kN and P3=80 kN) were applied, Figure A3. The measured displacement at each loading point was less than the requirement of 400 mm, Figure A4, with the lateral end of the FUP identified as the weakest part.

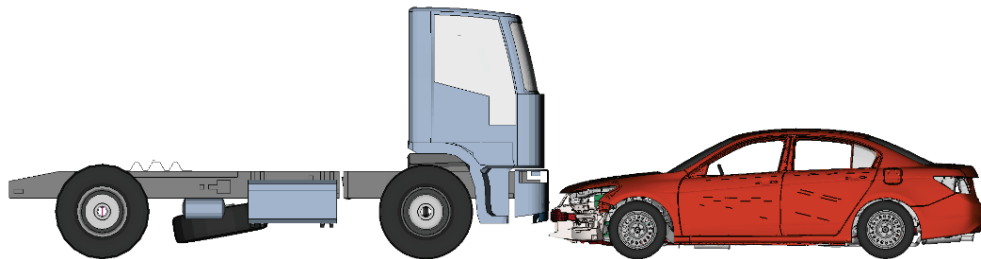


Figure 1. Heavy goods vehicle (7.9 ton) and passenger car (1.7 ton) with the FUP aligned vertically with the car bumper.

Crash Configurations

Based on the statistically defined distributions of the C2HGV head-on crash scenario (*Table 1*), twelve car-to-HGV crash configurations involving two impact velocities (car 39 km/h HGV 36 km/h and car 56 km/h HGV 53 km/h), two car overlaps (50 and 80 %, as measured on the car) and three impact angles (0, 30 and -30 deg) were selected; Figure 2. The Q25 configuration was considered too low in crash severity to fit the aim of this study. The oblique impact angles describe crashes in which either the car (30 deg) or the HGV (-30 deg) drives into the opposing lane. The results from the car-to-HGV crashes were compared to that of a car full-frontal rigid barrier (FFRB) 56 km/h crash. Additionally, full-frontal rigid barrier car crashes were simulated for use as a reference to the car-to-HGV crashes. Simulations were performed at 56 km/h (current US-NCAP), 80 km/h, and 100 km/h, common speed limits on rural roads.

Crash Severity Metrics

Car crash pulse severity was evaluated from left sill B-pillar acceleration measurements using peak acceleration, delta-V, cross-zero time, and occupant load criterion (OLC), measured in a local coordinate system with x positive forward, z upwards, and y to the left (Figure 3). Peak x-acceleration is defined as the minimum of the CFC60 filtered x-acceleration. Delta-V is the vehicle x-velocity change, calculated from the integral of CFC180 filtered x-acceleration, in the time window from impact to the time of minimum velocity. Cross-zero time is the time at

which the car starts to rebound. OLC is defined as the constant (minimum) acceleration required to decelerate an occupant from the time of 65 mm displacement relative to the vehicle (initial free-flight distance) to the time of 300 mm displacement [17]. In contrast to peak acceleration and delta-V, OLC is calculated over the whole time history.

Overlap/ Impact angle	0 deg	30 deg	-30 deg
50 %			
80 %			

Figure 2 HGV to PC crash configurations, with boundary lines around the vehicles displaying the overlap of the car relative to the HGV.

Compartment structural integrity was evaluated by means of peak intrusion measurements during the crash at locations according to IIHS [18]: the footrest, toe pan (3 points), lower instrument panel (2 points), A-pillar (door opening), and steering wheel (Figure 3). The A-pillar deformation was measured between two points on the inside of the door opening, at the vertical level of the base of the left front window at the A-pillar. Only the x-components of the intrusions were used, measured in a local coordinate system with x positive rearwards, z upwards, and y to the right. This coordinate system was rigidly attached to the left sill behind the B-pillar seat and thus followed the car in all degrees of freedom. The measured intrusions were evaluated using the rating guidelines from IIHS [19], although dynamic peak intrusions were used in this study instead of static intrusions measured post-test.

The recommended crashes for occupant restraints development were selected based on preserved compartment integrity (A-pillar deformation) and high severity of the crash pulse metrics (peak acceleration, delta-V, OLC, and cross-zero time), measured at the left sill b-pillar.

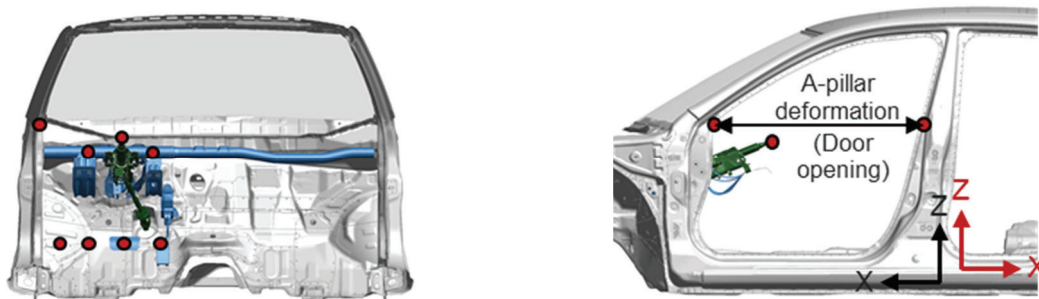


Figure 3. Car compartment intrusion measurement points together with local coordinate systems for pulse severity measurements (black) and compartment intrusions (red).

RESULTS

Crash Pulse Severity and Compartment Integrity

For the car, the 39/36 km/h crashes were similar in severity to the FFRB crash; Figure 4. The 56/53 km/h crashes were more severe, with peak accelerations of up to 91 g (excluding the very brief, likely unrealistic, peak acceleration of the 80 % 30 deg crash) and delta-Vs of 105 km/h. Of the high-speed crashes, the -30 deg crashes had less severe pulses than the 0 and 30 deg crashes but higher intrusions; Figure 5. The highest acceleration peaks and OLC were measured for the 80 % overlap crashes. The smallest cross-zero time was measured for the high-speed 80 % 0 deg crash. In the lateral direction, the highest delta-V (40 km/h) was measured for the high severity 50 % -30 deg crash, Figure A2. For the HGV, delta-Vs of 12 to 16 km/h were measured for the 39/36 km/h crashes and 19 to 21 km/h for the 56/53 km/h crashes; see Figure A1 in the Appendix. Time-history data of the x-accelerations, x- and y-velocities and z-rotations for all crashes are shown in the Appendix; Figures A5 to A8.

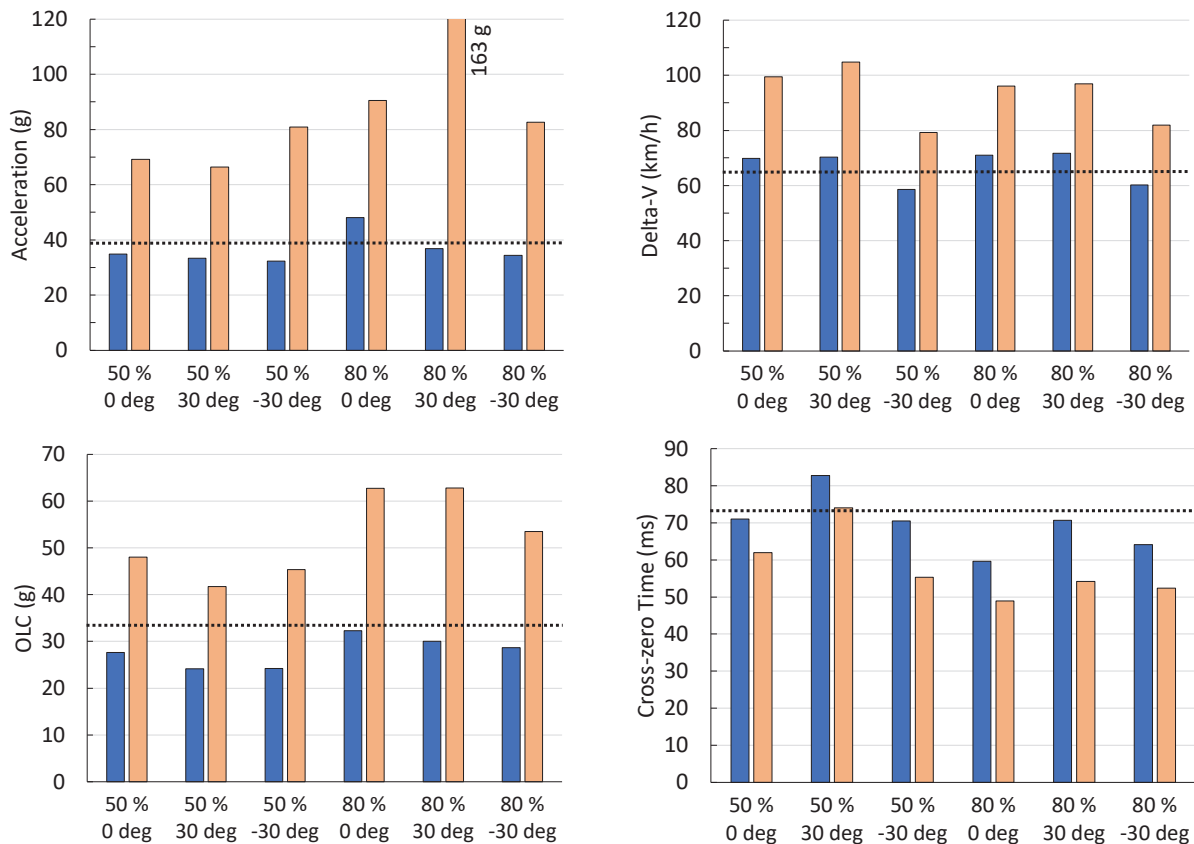


Figure 4. Sill left peak x-acceleration (upper left), delta-V (upper right), occupant load criterion OLC (lower left), and sill left cross-zero time (lower right) for the 39/36 km/h (blue) and 56/53 km/h (orange) crashes, compared to the FFRB 56 km/h crash (represented by a dotted horizontal line).

In general, compartment integrity was compromised (i.e., critically large A-pillar deformations) in the high-speed crashes when the HGV impacted locally on the left side of the car (both -30 deg crashes and the 50 % overlap 0 deg crash); Figure 5. Dynamic peak deformations up to 91 mm larger than those reported statically post-crash (at 140 ms) were measured, Figure 6. The largest footrest and toe pan intrusions, rated as marginal, were found for the high-speed 50 % and 80 % 0 deg crashes (Figure 7), 247 and 260 mm respectively. The effect of overlap on the structural compartment integrity, notably on the A-pillar deformation, is demonstrated in Figure 8, which compares the 50 and 80 % overlaps for two 56/53 km/h 0 deg crashes at the times of peak A-pillar deformations. For the 39/36 km/h crashes, all intrusion measurements were non-critical.

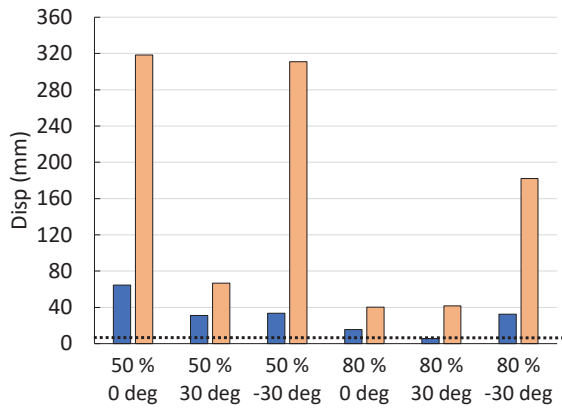


Figure 5. Peak (dynamic) A-pillar deformations for the 39/36 km/h (blue) and 56/53 km/h (orange) crashes, compared to the FFRB 56 km/h crash (represented by a dotted horizontal line).

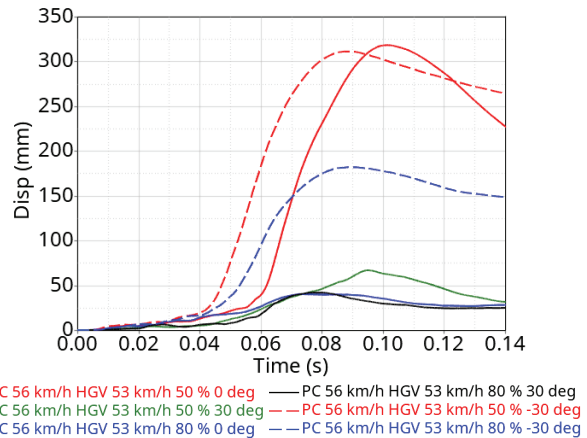


Figure 6. Time-history of the left A-pillar deformations (door opening) for the 56/53 km/h crashes.

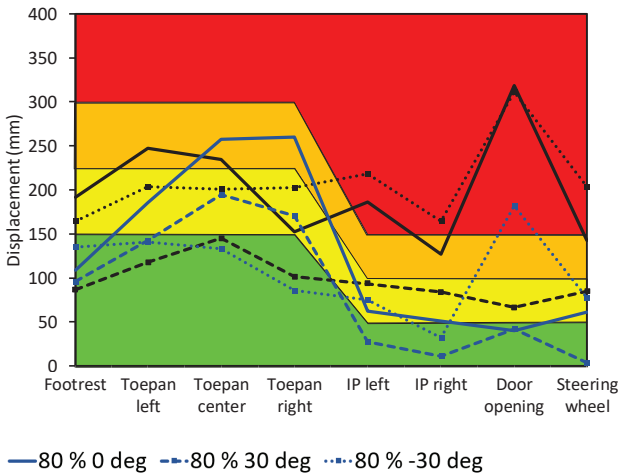
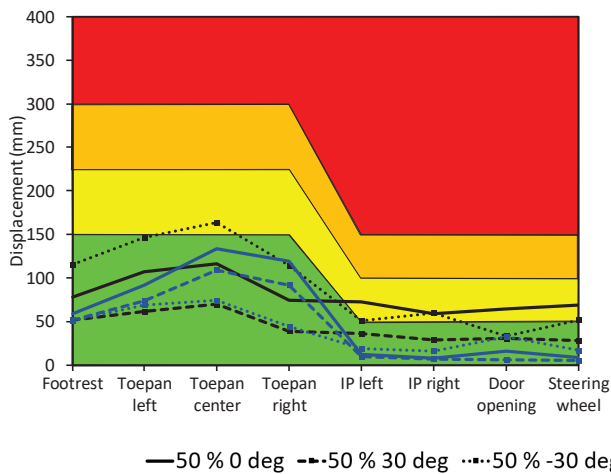


Figure 7. Passenger car peak (dynamic) compartment intrusions for the 39/36 (left) and 56/53 km/h (right) crashes. IIHS ratings: Good (green), Acceptable (yellow), Marginal (orange), and Poor (red).

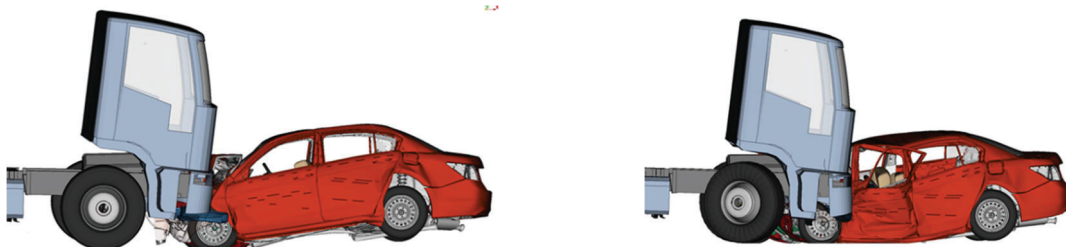


Figure 8. Car A-pillar (door opening) deformations for the 56/53 km/h 80% 0 deg crash at 90 ms (33 mm, right) and the 56/53 km/h 50% 0 deg crash at 100 ms (295 mm, left).

Crash pulses for occupant restraint development

Two crashes were selected to immediately facilitate development of occupant restraints in high-severity crashes. The selection was based on high crash severity (compared to FFRB 56 km/h crash) and non-compromised compartment integrity, i.e., with limited A-pillar deformations, Figure 5, and Figure 9:

Crash 1: the 56/53 km/h 80 % overlap in 0 deg impact angle crash with peak acceleration 91 g, delta-V 97 km/h, OLC 63 g, and cross-zero time 49 ms (highest crash severity, short duration), and

Crash 2: the 56/53 km/h 50 % overlap in 30 deg impact angle crash with peak acceleration 66 g, delta-V 105 km/h, OLC 42 g, and cross-zero time 74 ms (high crash severity, long duration).

The 56/53 km/h 80 % 0 deg was similar to the 56/53 km/h 50 % 30 deg crash in terms of delta-V and OLC, but with shorter crash duration (cross-zero time). The 56/53 km/h 50 % 30 deg crash was selected because of the long crash duration (74 ms compared to 49 ms). Although less severe than the 56/53 km/h 80 % 0 deg crash, the longer crash duration can be more challenging for the airbag systems in terms of maintaining high enough pressure to ensure avoiding strike-through (known as stand-up time). The remaining high-speed crash with non-compromised compartment integrity (the 56/53 km/h 80 % 30 deg crash) was excluded because the cross-zero time was higher than that of the 56/53 km/h 80 % 0 deg crash, additionally, the pulse measurements were judged to be unreliable due to local deformations of the structure at the sensor mounting location. In Figure 9, the selected crashes are also compared to full-frontal rigid barrier crashes at 56, 80, and 100 km/h.

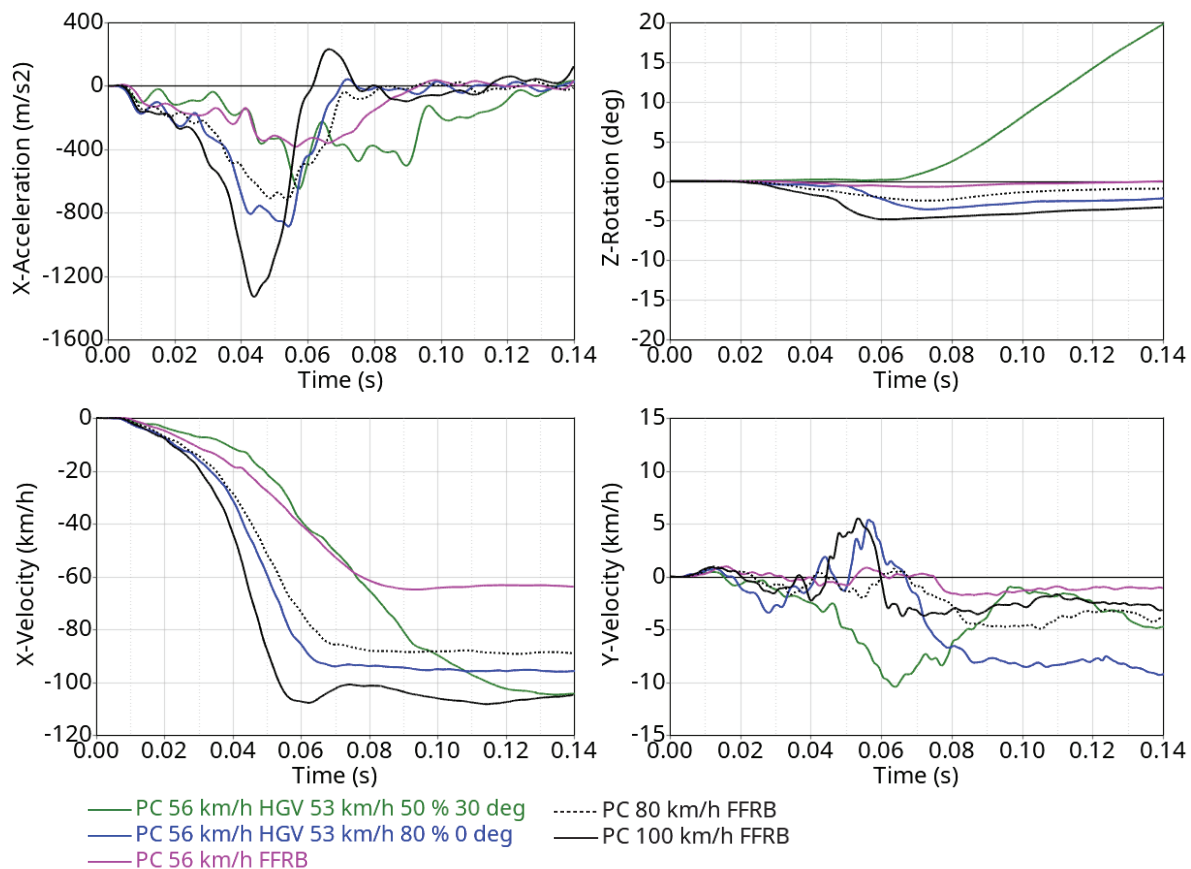


Figure 9. Passenger car kinematics (measured at sill b-pillar): X-acceleration (upper left), z-rotation (upper right), x-velocity (lower left) and y-velocity (lower right) for the two crashes that were selected feasible to use for occupant restraints development in high-severity crashes compared to full frontal crashes in 56, 80 and 100 km/h. The x-velocity was offset to start at 0 km/h to simplify comparison of delta-Vs between the crashes.

DISCUSSION

Crash compatibility between passenger cars and HGVs remains a prerequisite for safety. Only in crashes with intact structural integrity of the compartment is it meaningful to improve restraint systems to protect occupants better. Twelve car-to-HGV head-on crash configurations involving two impact velocities (car 39 km/h, HGV 36 km/h and car 56 km/h, HGV 53 km/h), two car overlaps (50 and 80 %) and three impact angles (0, 30 and -30 deg) were investigated, to identify which configurations are useful for occupant restraint development in high-severity crashes.

All 39/36 km/h crashes were found to be well represented by the full-frontal rigid barrier 56 km/h crash test in terms of the crash pulse metrics peak x-acceleration, delta-V and OLC. Slightly higher compartment intrusions were measured in the footrest and toe pan compared to the 56 km/h crash; however the results were still within the good-to-acceptable rating corridors according to the guidelines in IIHS [19]. In three out of the six 56/53 km/h crashes (both -30 deg crashes and the 50% overlap 0 deg crash), when the HGV locally impacted the left side of the car it led to the collapse of the A-pillar and concomitantly compromised compartment integrity. Thus these crashes were too severe to be used for the development of new restraint systems. Also, as most of the head-on crashes occur in frontal collision with an oncoming car in the HGV lane, in sliding, overtaking or driver inattention scenarios [7], the -30 deg crashes, which represents a crash configuration where the HGV drives into the opposing lane, are less common. Similar results in respect to compromised compartment integrity were demonstrated in a barrier test that relatively small increases in speed (from 64 to 80 and 90 km/h) can compromise the driver's survival space to the degree that the restraint systems would be ineffective in reducing the occupant's injury and fatality risk [20].

The two 56/53 km/h candidate crashes that were selected both had intact compartment and high delta-Vs. The 56/53 km/h 80 % 0 deg crash was found to be the more severe than the 56/53 km/h 50 % 30 deg crash in terms of peak accelerations and shorter duration in time, leading to higher crash severity as indicated by the OLC value (63 g vs 42 g); however, the 56/53 km/h 50 % 30 deg crash can be more challenging for the airbag systems in terms of stand-up time. Both selected crashes were much more severe than the full-frontal 56 km/h crash, with the 56/53 km/h 80 % 0 deg crash being similar in crash severity to a FFRB car crash in approximately 90 km/h (as estimated from the average of the simulated 80 and 100 km/h crashes in Figure 9). Consequently, this crash seems representative of also high-speed car-to-car crashes (as represented by a barrier crash) and can be replicated by full-scale testing in a laboratory.

The two selected 56/53 crashes were much more severe than the full-frontal 56 km/h crash in terms of toe pan intrusions, both rated marginal (247 to 260 mm) as compared to good (95 mm). This indicated a potentially increased risk of lower leg injuries in these car-to-HGV crashes and need to be considered in restraint development in addition to the high pulse severity. Such restraint development can be carried out in full-scale laboratory testing as similar toe pan intrusions (241 to 298 mm) were found in the FFRB crashes in 80 and 100 km/h.

The generic HGV in this study complies with a traditional front design, with an FUP as the main energy-absorbing structure. With the introduction of EU Directive 2015/719 [21], extra length can be added to the HGV, which can be used to improve the front of the truck cabin in terms of FUP design, geometry, and additional energy-absorbing capacity. This extended front can be used to improve the compatibility between HGVs and the car in terms of energy management, and thus reducing the forces that the car is exposed to in the crash [22]. To demonstrate the incompatibility between vehicles as well as to prepare for improved HGV front structure concepts, a frontal reference crash test between a heavy truck (28 ton) and a passenger car (1.6 ton), with each vehicle traveling at 50 km/h and a car overlap of 50 %, was recently carried out [23]. It was found that the structural interaction between the vehicles can be improved, as the FUP outside the left-side anchorage point failed in shear, leading to limited engagement of the main car crash beam as an energy-absorbing structure and a ruptured lower A-pillar structure.

In addition to structural vehicle improvements, preventive systems are another means of reducing fatalities in car-to-HGV crashes. For example, frontal collisions with the car crossing the oncoming lane can be avoided with better infrastructure, such as central separating road barriers in rural areas or reduced speed limits if separating driving lanes are not possible. Further, the increasing use of support systems in vehicles [24,25], such as lane keep assist and automatic emergency braking (AEB), can also prevent unintentional lane departure and/or reduce crash speed, to the degree that the car structure and restraint systems can fully protect the occupant. By AEB on both HGVs and passenger cars, a possible closing speed reduction of approximately 30 km/h could be reached, potentially reducing MAIS2+ injuries by 52-73 percent in head-on crashes [26].

Improved performance of current state-of-the-art restraint systems for protection in high-severity crashes has been shown necessary [27]; an improved HGV front design would facilitate the development of such restraint systems. With restraint and interior systems (such as belt load limiting, seat stiffness and knee bolster stiffness) adapted to better manage the kinetic energy of occupants involved in high-severity crashes, strike-through could be avoided [27]. Further improved head protection seems feasible using larger airbags [28], especially for a car with limited compartment intrusions and large crush distance [29]. However, although improved safety performance in severe car-to-HGV crashes can be reached [27], high injury values were still predicted for all body regions. Thus, further development of frontal restraint systems may require new injury assessment reference values, focusing on survivability as the most relevant injury in high-severity crashes. Such reference values were proposed [30], targeting a 40 % risk threshold for all body regions of the THOR-50M Anthropometric test Device [31].

Limitations

Both vehicle models were found suitable for studying passenger car structural integrity and deriving crash pulse data. However, several potential improvements to the models were identified. For the HGV model, only limited detailed analyses of the interaction with the car were possible, due to non-modelled components behind the FUP, such as the steering gear. Although the car model was proved valid in crash speeds up to 65 km/h, its predictions of material failure in structural parts (such as the A-pillar) for crash severities with delta-Vs of up to 105 km/h remain unknown. Finally, in this study a HGV weight of 7860 kg was used. For HGVs with higher weight, reduced delta-Vs of the HGVs can be expected in frontal crashes, thus increasing the impact severity to the car.

CONCLUSIONS

Twelve car-to-heavy goods vehicle head-on crash configurations were investigated in order to identify which of them can immediately facilitate occupant restraint system development in high-severity crashes:

All lower-severity (39/36 km/h) crashes were found to be well represented by the full-frontal rigid barrier 56 km/h crash test.

For the higher severity 56/53 km/h crashes, three out of six crashes (both -30 deg crashes and the 50% overlap 0 deg crash) were as currently too severe with respect to compartment structural integrity for immediate use in the development of new restraint systems. Improvement of the car compartment structure is needed before these crash configurations can be considered in restraint development.

Two high-severity crashes were identified for targeting improved occupant safety with new restraint system development. Both these crashes were much more severe than the full-frontal 56 km/h crash. The 56/53 km/h 80 % overlap 0 deg crash was found to be the most severe in terms of peak accelerations (91 g) and OLC (63 g), and, with a high delta-V (97 km/h). The 56/53 km/h 50 % overlap 30 deg crash was found to be the most severe in terms of delta-V (105 km/h) and pulse duration in time. The latter crash was similar in crash severity to a full-frontal rigid barrier 90 km/h crash.

We believe the 56/53 km/h 80 % overlap 0 deg crash configuration may be worth considering in future legislation and rating programs, which would immediately facilitate development of improved restraint systems addressing fatalities in high-severity crashes.

ACKNOWLEDGEMENTS

The work was carried out as part of the SAFE-UP project, which has received funding from the European Union's Horizon 2020 research and innovation programme under Grant Agreement No 861570. The authors would like to thank Dr. Kristina Mayberry for language editing.

REFERENCES

- [1] European Commission. 2021. Annual statistical report on road safety in the EU 2020. European Road Safety Observatory. European Commission, Directorate General for Transport, Brussels. https://road-safety.transport.ec.europa.eu/statistics-and-analysis/data-and-analysis/annual-statistical-report_en
- [2] European Commission. 2021. Mobility and Transport Road Traffic Fatalities in the EU in 2019 by Road User and (other) 'Main Vehicle' involved in the Crash. European Commission, Directorate General for Transport, Brussels. <https://transport.ec.europa.eu/system/files/2021-11/collision-matrix-2019.pdf>
- [3] Stewart, T. 2022. Overview of motor vehicle crashes in 2020. Report No. DOT HS 813 266. U.S. Department of Transportation, National Highway Traffic Safety Administration.
- [4] NHTSA National Center for Statistics and Analysis. 2021. Early estimates of motor vehicle traffic fatalities and fatality rate by sub-categories in 2020, Crash Stats Brief Statistical Summary. Report No. DOT HS 813 118. National Highway Traffic Safety Administration.
- [5] NHTSA National Center for Statistics and Analysis. 2022, May. Early estimates of motor vehicle traffic fatalities and fatality rate by sub-categories in 2021, Crash Stats Brief Statistical Summary. Report No. DOT HS 813 298). National Highway Traffic Safety Administration.
- [6] Transport Analysis. 2022. Road traffic injuries 2021, Statistik 2022:15, Date of publication: May 15, 2022. <https://www.trafa.se/en/road-traffic/road-traffic-injuries/>
- [7] Kockum, S., Örtlund, R., Ekfjorden, A., and Wells, P. 2017. Volvo Trucks Safety Report 2017. Göteborg, Volvo Trucks. <https://www.volvogroup.com/content/dam/volvo-group/markets/master/about-us/traffic-safety/Safety-report-2017.pdf>
- [8] Bálint, A., Labenski, V., Köbe, M., Vogl, C., Stoll, J., Schories, L., Amann, L., Sudhakaran, G. B., Leyva, P. H., Pallacci, T., Östling, M., Schmidt, D., Schindler, R. 2021. SAFE-UP D2.6, USE CASE DEFINITIONS AND INITIAL SAFETY-CRITICAL SCENARIOS, EU Project SAFE-UP (<https://www.safe-up.eu>). https://static1.squarespace.com/static/5efaed43294db25b18168717/t/623da6ef1762a746d2632b9e/1648207614516/SAFE-UP_D2_6_Use+case+definitions+and+initial+safety-critical+scenarios_.pdf
- [9] Forman, J. L. and McMurry, T. L. 2018. Nonlinear models of injury risk and implications in intervention targeting for thoracic injury mitigation. *Traffic Injury Prevention*, 19 (sup2) 103-S108.
- [10] Wisch, M., Lerner, M., Vukovic, E., Hynd, D., Fiorentino, A., Fornells, A. 2017. Injury Patterns of Older Car Occupants, Older Pedestrians or Cyclists in Road Traffic Crashes with Passenger Cars in Europe – Results from SENIORS. Proceedings of IRCOBI Conference, Antwerp, Belgium
- [11] Mroz, K., Pipkorn, B., Sunnevång, C., Eggers, A., Bråse, D. 2018. Evaluation of Adaptive Belt Restraint Systems for the Protection of Elderly Occupants in Frontal Impacts. Proceedings of IRCOBI Conference, Athens, Greece.
- [12] Singh, H., Ganesan, V., Davies, J., Paramasuwom, M., Gradischnig, L., Wood, P., Mogal, V. 2018a. Structural countermeasure/research program: Mass and cost increase due to oblique offset moving deformable barrier impact test. Report No. DOT HS 812 523, NHTSA, Washington, DC, USA.
- [13] Singh, H., Ganesan, V., Davies, J., Paramasuwom, M., Gradischnig, L. 2018b. Vehicle interior and restraints modeling development of full vehicle finite element model including vehicle interior and occupant restraints systems for occupant safety analysis using THOR dummies. Report No. DOT HS 812 545, NHTSA, Washington, DC, USA.
- [14] CEN. 2010, July. European Standard EN 1317-2: Road Restraint Systems Part 2: Performance Classes, Impact Test Acceptance Criteria and Test Methods for Safety Barriers Including Vehicle Parapets, European Committee for Standardization, Brussels, Belgium.

- [15] Oldani, E., Castelletti, L-M., Anghileri, M., Mongiardini, M. 2005. Impact Analysis of a 16t Truck against different Road Safety Restraint Systems. 5th European LS-DYNA Users Conference, Birmingham, Great Britain. <https://www.dynalook.com/conferences/european-conf-2005/Mongiardini.pdf>
- [16] UN/ECE. 2002. Regulation No 93 of the Economic Commission for Europe of the United Nations (UN/ECE), Uniform provisions concerning the approval of front underrun protective devices (FUPDs), vehicles with regard to the installation of an FUPD of an approved type, and vehicles with regard to their front underrun protection (FUP). [https://eur-lex.europa.eu/legal-content/EN/TXT/PDF/?uri=CELEX:42002X0201\(01\)&from=EN](https://eur-lex.europa.eu/legal-content/EN/TXT/PDF/?uri=CELEX:42002X0201(01)&from=EN)
- [17] Kübler, L., Gargallo, S. and Elsäßer, K. 2009. Frontal crash pulse assessment with application to occupant safety. ATZ worldwide, Volume 111, Issue 6, pp 12-17.
- [18] IIHS. 2021. Moderate Overlap Frontal Crashworthiness Evaluation Crash Test Protocol, Version XIX. Insurance Institute for Highway Safety, Ruckersville, Virginia, USA. https://www.iihs.org/media/f70ff6eb-d7a1-4b60-a82f-e4e8e0be7323/XPsNNA/Ratings/Protocols/current/test_protocol_moderate.pdf
- [19] IIHS. 2017. Moderate Overlap Frontal Crashworthiness Evaluation, Guidelines for Rating Structural Performance, Version III. Insurance Institute for Highway Safety, Ruckersville, Virginia, USA. <https://www.iihs.org/media/5b0cc829-1945-4dfe-9db7-1ea879f787fd/BHYYE7A/Ratings/Protocols/current/structural.pdf>
- [20] Kim, W., Kelley-Baker, T., Arbelaez, R., O'Malley, S., and Jensen, J. "Impact of Speeds on Drivers and Vehicles—Results from Crash Tests," AAA Foundation for Traffic Safety, IIHS, January 2021. <https://www.iihs.org/news/detail/new-crash-tests-show-modest-speed-increases-can-have-deadly-consequences>
- [21] European Commission. 2015. DIRECTIVE (EU) 2015/719 OF THE EUROPEAN PARLIAMENT AND OF THE COUNCIL of 29 April 2015 amending Council Directive 96/53/EC laying down for certain road vehicles circulating within the Community the maximum authorised dimensions in national and international traffic and the maximum authorised weights in international traffic. <https://eur-lex.europa.eu/legal-content/EN/TXT/PDF/?uri=CELEX:32015L0719&from=LV>
- [22] Edwards, M. J. et al. 2007. Improvement of Vehicle Crash Compatibility through the Development of Crash Test Procedures (VC-COMPAT). Final Technical Report, Transport Research Laboratory, Crowthorne, UK.
- [23] Thomson, R., Fredriksson, R., Mroz, K., Kruse, D., Törnvall, F. 2023. Frontal Crash Incompatibility of Heavy Truck in Crash Test with Passenger Car. The 27th International Technical Conference on the Enhanced Safety of Vehicles Conference (ESV), Yokohama, Japan 2023. Paper Number 23-0321.
- [24] EUROPEAN NEW CAR ASSESSMENT PROGRAMME (Euro NCAP). 2022. TEST PROTOCOL – AEB Car-to-Car systems, Implementation 2023, Version 4.1.1. <https://cdn.euroncap.com/media/70312/euro-ncap-aeb-c2c-test-protocol-v41.pdf>
- [25] EUROPEAN NEW CAR ASSESSMENT PROGRAMME (Euro NCAP). 2022. TEST PROTOCOL – Lane Support Systems, Implementation 2023, Version 4.2. <https://cdn.euroncap.com/media/70313/euro-ncap-aeb-lss-vru-test-protocol-v42.pdf>
- [26] Strandroth, J., Rizzi, M., Kullgren, A., Tingvall, C. 2012. Head-on collisions between passenger cars and heavy goods vehicles: Injury risk functions and benefits of Autonomous Emergency Braking. Proceedings of IRCOBI Conference, Dublin, Ireland.
- [27] Östling, M., Eriksson, L., Dahlgren, M., Forman, J. 2023. Frontal Head-On Car-to-Heavy Goods Vehicle Crashes and their Effect on the Restraint System. The 27th International Technical Conference on the Enhanced Safety of Vehicles Conference (ESV), Yokohama, Japan. Paper Number 23-0198.

- [28] Pipkorn, B., Mellander, H. and Håland, Y. 2005. Car Driver Protection at Frontal Impacts up to 80 km/h (50 mph). The 19th International Technical Conference on the Enhanced Safety of Vehicles (ESV) - Washington D.C. June 6-9. Paper Number 05-0102.
- [29] Pipkorn, B., Mellander, H. Olsson, J. and Håland, Y. 2006. On the Combined Effect of the Variation of Driver Restraint Configuration and Crash Pulse for High and very High Impact Velocities. Proceedings of IRCOBI Conference, Madrid, Spain.
- [30] Forman J, Östling M., Mroz K. 2023. Potential Injury Criteria for Collisions with Heavy Goods Vehicles. The 27th International Technical Conference on the Enhanced Safety of Vehicles Conference (ESV), Yokohama, Japan 2023. Paper Number 23-0334.
- [31] Humanetics Innovative Solutions. 2020. THOR-50th Percentile Male Dummy User Manual 472-9900 [Rev. F]. https://www.humaneticsgroup.com/sites/default/files/2020-11/um_thor_50m_revf.pdf

APPENDIX

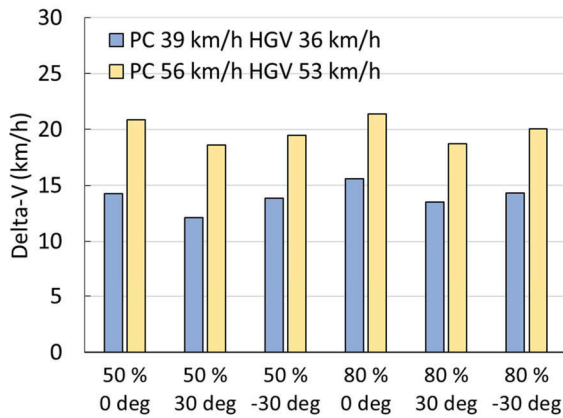


Figure A1. HGV delta-V.

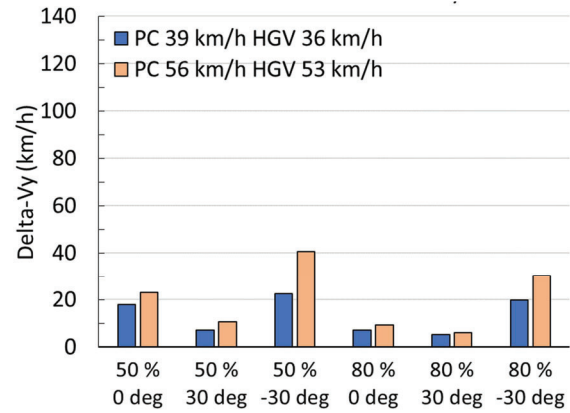


Figure A2. Car delta-V in the lateral y-direction).

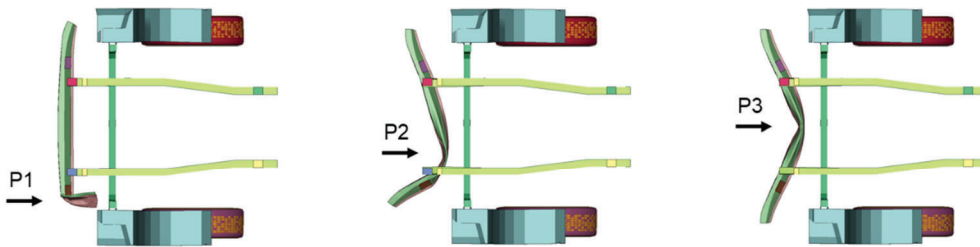


Figure A3. Assessment of FUP according to UN/ECE Regulation No 93. Loading P1 (80 kN), P2 (160 kN) and P3 (80 kN) were applied with load distribution of height 250mm and width 400mm.

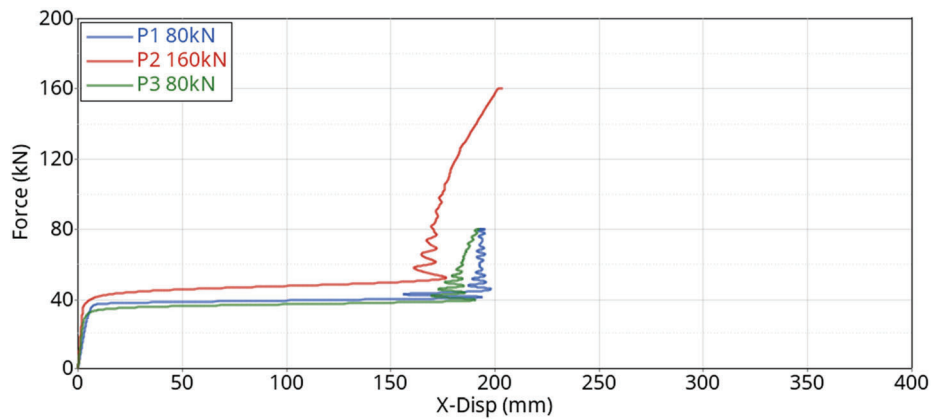


Figure A4. Force-displacement results from the FUP assessment.

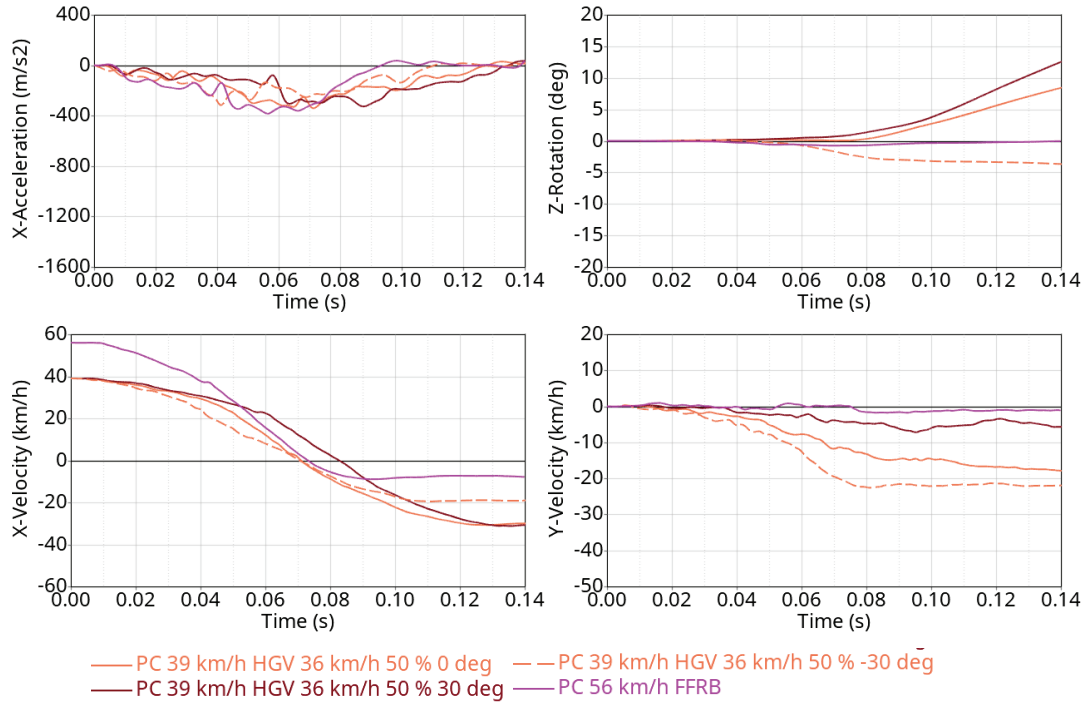


Figure A5. X-acceleration, z-rotation, x-velocity and y-velocity time-histories for the 39/36 km/h crashes with 50 % overlap.

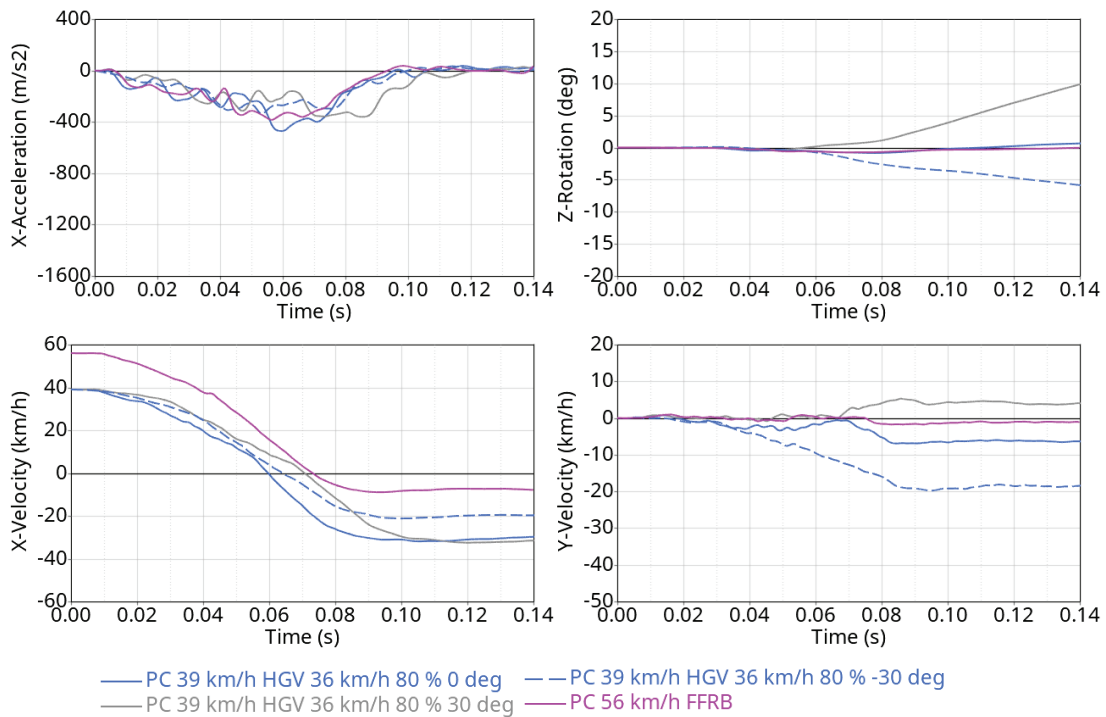


Figure A6. X-acceleration, z-rotation, x-velocity and y-velocity time-histories for the 39/36 km/h crashes with 80 % overlap.

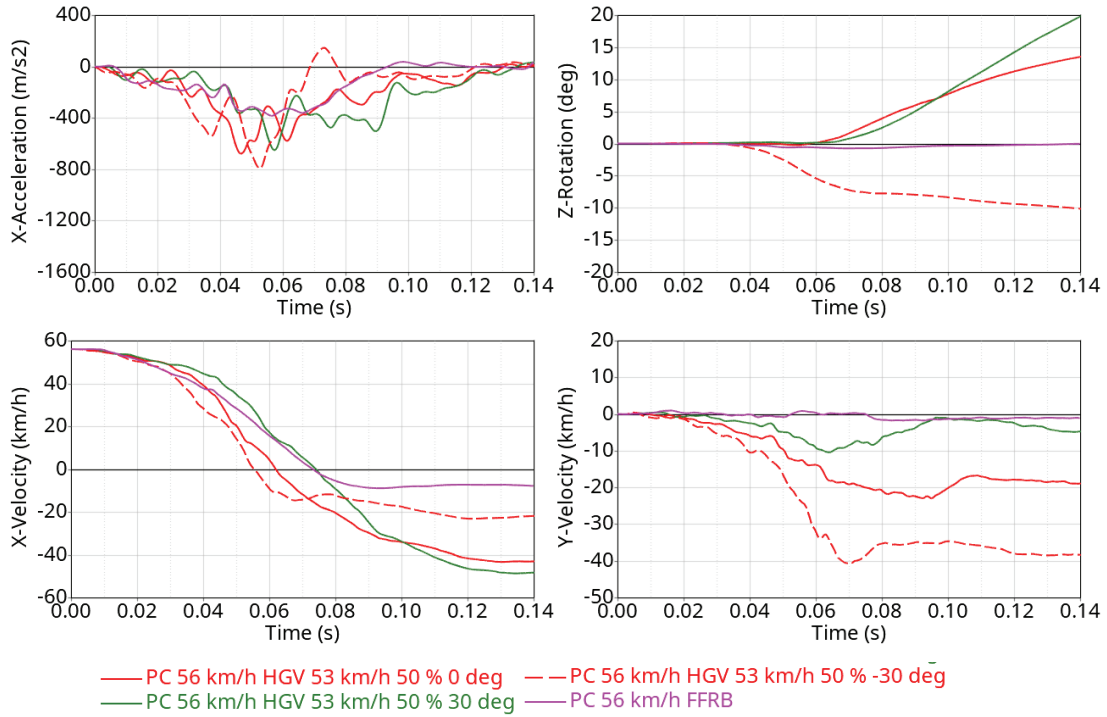


Figure A7. X-acceleration, z-rotation, x-velocity and y-velocity time-histories for the 56/53 km/h crashes with 50 % overlap.

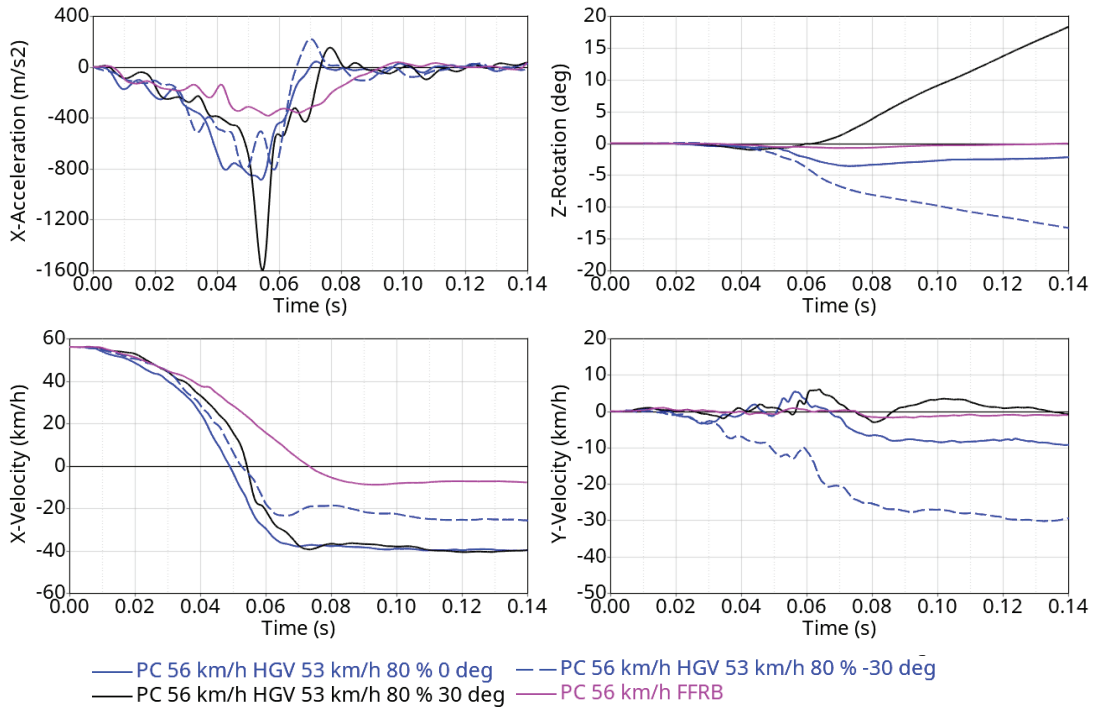


Figure A8. X-acceleration, z-rotation, x-velocity and y-velocity time-histories for the 56/53 km/h crashes with 80 % overlap.

PEER REVIEW PAPER

This paper has been peer-reviewed and published in a special edition of Traffic Injury Prevention 24(S1), by Taylor & Francis Group. The complete paper will be available on the Traffic Injury Prevention website soon. To access ESV Peer-reviewed papers click the link below
<https://www.tandfonline.com/toc/gcpi20/24/sup1?nav=toCList>

RISK FACTORS AFFECTING SEVERE THORACIC INJURIES OF OCCUPANTS BASED ON AGE GROUPS AND FRONTAL OBLIQUE COLLISIONS

Dooruh Choi
OhHyun Kim
JoonSeok Kong
Yeonil Choo
KangHyun Lee

Department of Emergency Medicine, Yonsei University, Wonju College of Medicine
Republic of Korea

Paper Number 23-0081

ABSTRACT

Frontal collision is the most common type of motor vehicle collision occurring in real-world collisions. This study aims to investigate the risk of thoracic injury depending on age and oblique direction of collision in a frontal collision.

This was a retrospective, observational study. The study used the Korean In-Depth Accident Study (KIDAS) database. We selected 1,369 adult occupant patients in frontal collisions and seated only in the first row. The severely injured occupants were defined as those who had AIS3+ injury in thoracic regions. The age of occupants was classified into three groups: <54 years, 55-64 years, and >65 years. The frontal oblique collision was classified by the PDoF. Considering the PDoF, occupants were classified into three groups: Far-frontal oblique, Near-frontal oblique, and longitudinal.

The risk of thoracic injury was significant in age, seating position, and delta-V parameters. 55-64 years occupants OR was 1.819 compared to <54 years. In addition, >65 years occupants OR were 1.950, a higher value. The frontal passenger seat had a lower risk of thoracic injury than the driver seat (OR = 0.465). An increase of 1kph delta-V made a 1.018 OR rise. The oblique direction was only significant in the occupants with fastened seatbelts. The OR of the near-frontal oblique direction was 2.964 compared to the far-frontal oblique direction. The OR of the longitudinal direction was 2.229. Occupants with unfastened seatbelts had no risk difference in the oblique parameter.

The study result showed that elderly occupants had a higher risk of severe thoracic injury. Furthermore, the oblique collisions affected to the risk of severe injury only seatbelt fastened occupants. This study showed the detailed risk of the thoracic region using the real-world collision database. The research could be used to enhance occupant safety and advance the crashworthiness of vehicle structures.

INTRODUCTION

Motor vehicle collisions are one of the global leading causes of death. In 2016, global mortality from motor vehicle collisions was 18.2 per 100,000 people, and mortality is declining every year [1,2]. The injury regions to contribute to the cause of death in collisions are various. Among the regions, the thorax is highly exposed to mortality and severe injury rates in motor vehicle collisions after the head region [3]. The thorax is a huge area in the human body that contains vital organs for life. Therefore, continuous research on the reduction of thoracic injuries is needed.

Motor vehicle collisions are classified differently according to the type of collision scenario. Classification using the collision direction of the vehicle is intuitively easy to understand. This is one of the frequently used classification methods [4]. Among the various collision direction, frontal collision is a common type of collision occurring in a real-world motor vehicle collision. The injury severity of the thoracic region is affected by frontal oblique collisions that collide with objects at an angle [5]. However, there are insufficient studies to analyze the factors of thoracic injury through statistical methods for frontal oblique collisions based on real-world collisions. Therefore, there is a need for a study analyzing the risk of thoracic injury in a frontal oblique collision using parameters from a real-world collision database.

Even in the same type of collisions, the injury severity of occupants can be different [6]. The reliability of the analysis of injury characteristics resulting from collisions can be ensured by considering the human factors of the occupants [7]. In particular, the age parameter must be considered in the analysis of occupant injuries. Globally, life expectancy is rising. This phenomenon increases the number of elderly occupants on the roadways. Elderly occupants are more vulnerable to injury. Particularly, aging is known to strongly increase the risk of severe thoracic injuries [5,8].

This study aimed to investigate the risk of thoracic injury caused by frontal oblique collision. Through this, we would like to find out which oblique scenario increases the injury risk of occupants and how to overcome oblique collisions in the future.

METHOD

Data sources

This study used data from the Korean In-Depth Accident Study (KIDAS) database. This is a real-world motor vehicle collision database that collected occupants’ injury data. The data was collected from the occupant patients who visited the emergency department of a regional trauma center in Korea. The period of data collection was 11 years, from January 2011 to February 2022. It also contains vehicle and environmental information obtained through investigation.

Study design

This is a retrospective, observational study. We selected adults and first-row seated occupant patients. The individuals who had unknown injury severity or body mass index (BMI) were excluded. In addition, the analysis excluded occupants who engaged in non-frontal collisions, non-passenger cars, and pole crashes (See Figure 1).

The occupants were classified into two groups according to thoracic injury severity. The abbreviated injury scale (AIS) was used for the classification. The severe injury group had AIS 3+ injury in the thoracic region. The non-severe groups had AIS scores between 0 to 2.

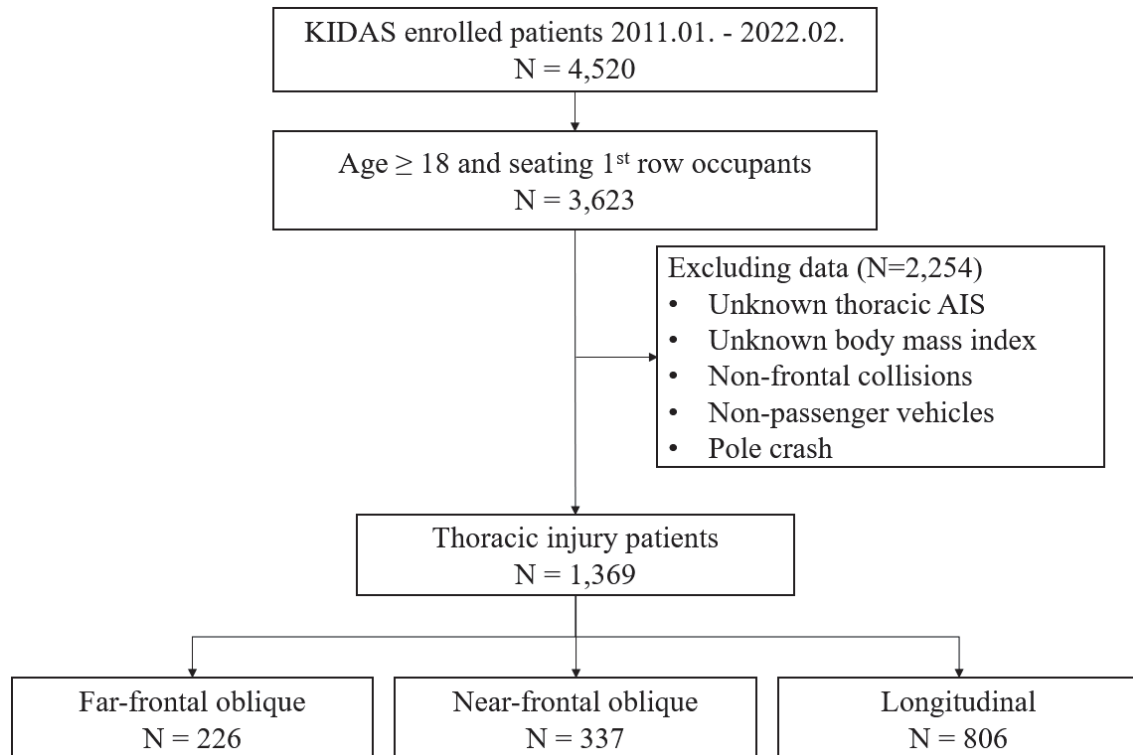


Figure 1. Flowchart of study design

The principal direction of force (PDoF) was used to classify the oblique direction in frontal collisions. All the frontal collisions had major damage to the front part of the vehicle and PDoF between 10 to 2 o'clock. The frontal collisions were classified into three groups considering seating position and PDoF. The driver with 1 and 2 o'clock PDoF and the frontal passenger with 10 and 11 o'clock were classified as far-frontal oblique collisions. The driver with 10 and 11 o'clock PDoF and the passenger with 1 and 2 o'clock PDoF were classified as near-frontal oblique collisions. The longitudinal collision had 12 o'clock PDoF (See Figure 2) [9].

The human factors used in the study were sex, age, and BMI. Age was classified into three groups to investigate the aging effect: <54 years, 55-64 years, and >65 years [10]. BMI was classified into three groups according to international standards: normal (18.5-24.9), overweight (25.0-29.9), and obese (>30.0) [11]. Underweight occupants were not considered in this study.

Vehicle type, crash object, seatbelt condition, and delta-V parameters were also used in the study for better analysis. The vehicles bigger than middle-size trucks were excluded from this study because the vehicle's curb weights and structures were highly different. Consequently, sedan, sport utility vehicle (SUV), light truck, and van types of vehicles were only used. Crash object had two sub-categories, collisions with another vehicle and fixed objects. The occupants with fastened and unfastened seatbelts were separated. Occupants with fastened seatbelts used three-point and two-point belts. Delta-V parameter was estimated using PC-Crash software. The estimation confirmed checking the trajectory error during the reconstruction stage.

Statistical methodology

Statistical analysis was performed using the IBM SPSS statistics package 25. The mean, standard deviation, and statistical significance were analyzed using Pearson's chi-square test and the independent sample t-tests. Statistical significance was set at p<.05. Risk factor analysis was performed by confirming the odds ratio and 95% confidence interval through binary logistic regression analysis. The probability of severe injury according to delta-V increase was analyzed in each oblique direction.

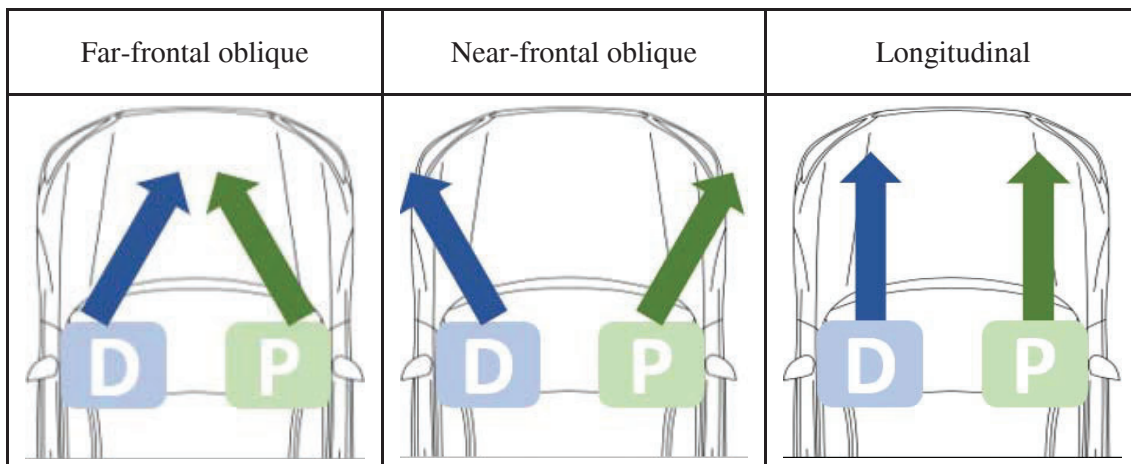


Figure 2. Oblique direction classification

RESULTS

Frequency analysis

The occupants in frontal collisions were classified into two groups according to thoracic injury severity (See Table 1). The rate of severely injured individuals was 17.4%. In the sex parameter, male occupants had a 31.8% higher frequency of thoracic injury than female occupants (p=0.004). The rate of severe injury increased in both 55-64 years and >65 years occupants (p=0.006). The occupants who belonged to the overweight or obese categories had a higher frequency of severe injury (p=0.010). The most common type of vehicle was a sedan. There was no frequency difference according to vehicle type (p=0.080). The number of driver occupants had around four times larger than the frontal passenger. The rate of severe injuries increased in the driver (p=0.004). The longitudinal direction was the most common in a frontal collision. The oblique direction had no frequency

Table 1.
General characteristics according to thoracic injury severity

Variables	Total (n=1,369)	Severe (n=238)	Non-Severe (n=1,131)	P-value
Sex, n (%)	(n= 1,369)	(n=238)	(n=1,131)	0.004
Male	902 (65.9)	176 (73.9)	726 (64.2)	
Female	467 (34.1)	62 (26.1)	405 (35.8)	
Age groups, n (%)	(n= 1,369)	(n=238)	(n=1,131)	0.006
<54 years	904 (66.0)	136 (57.1)	768 (67.9)	
55-64 years	292 (21.3)	65 (27.3)	227 (20.1)	
>65 years	173 (12.6)	37 (15.5)	136 (12.0)	
BMI*, n (%).	(n= 1,369)	(n=238)	(n=1,131)	0.010
Normal	1,026 (74.9)	160 (67.2)	866 (76.6)	
Overweight	286 (20.9)	66 (27.7)	220 (19.5)	
Obese	57 (4.2)	12 (5.0)	45 (4.0)	
Vehicle type, n (%)	(n= 1,369)	(n=238)	(n=1,131)	0.080
Sedan	783 (57.2)	130 (54.6)	653 (57.7)	
SUV**	258 (18.8)	43 (18.1)	215 (19.0)	
Light truck	238 (17.4)	54 (22.7)	184 (16.3)	
Van	90 (6.6)	11 (4.6)	79 (7.0)	
Seating position, n (%)	(n= 1,369)	(n=238)	(n=1,131)	0.004
Driver	1,077 (78.7)	204 (85.7)	873 (77.2)	
Frontal passenger	292 (21.3)	34 (14.3)	258 (22.8)	
Oblique direction, n (%)	(n= 1,369)	(n=238)	(n=1,131)	0.277
Far-frontal oblique	337 (24.6)	31 (13.0)	195 (17.2)	
Near-frontal oblique	226 (16.5)	60 (25.2)	277 (24.5)	
Longitudinal	806 (58.9)	147 (61.8)	659 (58.3)	
Crash object, n (%)	(n= 1,369)	(n=238)	(n=1,131)	0.783
Vehicle	965 (70.5)	166 (69.7)	799 (70.6)	
Fixed	404 (29.5)	72 (30.3)	332 (29.4)	
Seatbelt, n (%)	(n= 1,369)	(n=238)	(n=1,131)	0.057
Fastened	952 (71.1)	153 (65.9)	799 (72.2)	
Unfastened	387 (28.9)	79 (34.1)	308 (27.8)	
Delta-V (kph), mean±S.D.***	30.42±21.68	36.91±21.47	28.91±21.46	<0.001

*BMI; Body Mass Index, **SUV; Sport Utility Vehicle, ***S.D.; Standard Deviation

difference (p=0.227). Collisions with another vehicle accounted for about 70% of the total collision. However, the crash object parameter had no frequency difference (p=0.783). Around 71% of occupants fastened their seatbelts. Nevertheless, there was no frequency difference in injury severity (p=0.057). The delta-V had a 30.42 kph of mean value with a 21.68 kph of standard deviation. The delta-V mean value was about 6 kph higher in the severe thoracic injury group (p<0.001).

Risk analysis

Binary logistic regression analysis was performed to analyze the risk of severe thoracic injury. The analysis's parameters were the same as those used in the frequency analysis. However, vehicle type and crash object parameters were excluded because there were no significant differences. Although the oblique direction and seatbelt condition were not significant, they were included in the risk analysis because they were the main parameters of the study (See Table 2).

Female occupants had a smaller odds ratio (OR) than male occupants (OR=0.848). However, the significance of the sex parameter was over 0.05 (p=0.450). Age parameter showed that aging affected the risk of thoracic

Table 2.
A logistic regression analysis of severe thoracic injury risk

Parameter	OR**	95% CI***	P-value
Sex Male (ref)	1.000		
Female	0.848	0.553 – 1.301	0.450
Age <54 years (ref)	1.000		
55-64 years	1.819	1.192 – 2.777	0.006
>65 years	1.950	1.145 – 3.320	0.014
BMI* Normal (ref)	1.000		
Overweight	1.404	0.920 – 2.142	0.115
Obese	1.088	0.418 – 2.834	0.863
Seating position Driver (ref)	1.000		
Frontal passenger	0.465	0.271 – 0.797	0.005
Oblique direction Far-frontal (ref)	1.000		
Near-frontal	1.838	0.974 – 3.470	0.060
Longitudinal	1.879	1.053 – 3.354	0.033
Seatbelt Fastened (ref)	1.000		
Unfastened	1.394	0.961 – 2.022	0.080
Delta-V (kph)	1.018	1.010 – 1.026	<0.001

BMI; Body Mass Index, **OR; Odds Ratio, *CI; Confidence Interval*

injury. The occupants 55-64 years and >65 years had higher injury risk than <54 years adult individuals (p=0.006, p=0.014). In addition, The OR value of >65 years (OR=1.950) was higher than 55-64 years (OR=1.819). Occupants who belonged to the Overweight or obese group had higher OR than the normal group in the BMI parameter. However, there was no significance. Frontal passengers had a smaller OR than the driver (OR=0.465) with a significance under 0.05 (p=0.005). Longitudinal direction collision had a higher OR than the far-frontal direction (OR=1.879). It also had a significance under 0.05 (p=0.033). In contrast, the near-frontal direction had significance over 0.05 (p=0.060), and the OR value was 1.838 times higher than the far-frontal direction. Occupants with unfastened seatbelts had 1.394 times higher OR than occupants with fastened seatbelts. However, the significance of the seatbelt parameter was 0.080 so it was insignificant. The risk of a severe thoracic injury increased with an increased delta-V value (OR=1.018, p<0.001).

The binary logistic regression analysis showed the risk of severe thoracic injury in all frontal collisions. However, oblique direction and seatbelt parameters were insignificant. Therefore, further analysis was conformed dividing seatbelt conditions (See Table 3).

The risk of severe thoracic injury was analyzed using only occupants with fastened seatbelts. In the sex parameter, the OR of females was lower than that of males (OR=0.664). However, the significance was not confirmed (p=0.139). The OR for occupants aged 55-64 years was 1.857, the value was similar to that of the previous risk analysis. Also, the significance was under 0.05 (p=0.020). In contrast, the OR of occupants aged >65 years was 1.386, which was lower than the OR of the same parameter in the previous risk analysis. In addition, the significance was over 0.05 (p=0.354). BMI was not significant in both overweight and obese groups. The risk difference was not confirmed in the seating position parameter (p=0.176). All categories of oblique direction were identified as significant. The OR in the near-frontal direction was the highest at 2.964 (p=0.011). The OR in the longitudinal direction was 2.229 (p=0.050). The OR increased by 1.020 times as the delta-V value increased by 1 kph.

The risk of severe thoracic injury was analyzed using occupants with unfastened seatbelts. In the sex parameter, in contrast to the previous risk analysis, females had a higher OR than males (OR=1.327), but the significance was not confirmed (p=0.450). In the age parameter, the 55-64 years category was insignificant (p=0.133). However, significance was confirmed for occupants aged >65 years (p=0.011). The OR of occupants aged >65 years was 3.163, which was higher than the value of the same category in the previous risk analysis. In the BMI parameter, both the overweight and obese groups had a higher OR than the normal group. However, both sub-

Table 3
A logistic regression analysis of severe thoracic injury risk according to seatbelt parameter

Parameter	OR**	95% CI***	P-value
Seatbelt Fastened			
Sex Male (ref)	1.000		
Female	0.664	0.386 – 1.143	0.139
Age <54 years (ref)	1.000		
55-64 years	1.857	1.103 – 3.127	0.020
>65 years	1.386	0.694 – 2.767	0.354
BMI* Normal (ref)	1.000		
Overweight	1.310	0.783 – 2.192	0.304
Obese	0.293	0.037 – 2.335	0.246
Seating position Driver (ref)	1.000		
Frontal passenger	0.617	0.307 – 1.241	0.176
Oblique direction Far-frontal (ref)	1.000		
Near-frontal	2.964	1.282 – 6.852	0.011
Longitudinal	2.229	1.000 – 4.970	0.050
Delta-V (kph)	1.020	1.010 – 1.030	<0.001
Seatbelt Unfastened			
Sex Male (ref)	1.000		
Female	1.327	0.636 – 2.768	0.450
Age <54 years (ref)	1.000		
55-64 years	1.794	0.838 – 3.843	0.133
65 years over	3.163	1.296 – 7.718	0.011
BMI* Normal (ref)	1.000		
Overweight	1.540	0.716 – 3.310	0.269
Obese	2.789	0.824 – 9.445	0.099
Seating position Driver (ref)	1.000		
Frontal passenger	0.278	0.112 – 0.688	0.006
Oblique direction Far-frontal (ref)	1.000		
Near-frontal	0.623	0.202 – 1.919	0.409
Longitudinal	1.498	0.628 – 3.571	0.362
Delta-V (kph)	1.014	1.011 – 1.028	0.034

*BMI; Body Mass Index, **OR; Odds Ratio, ***CI; Confidence Interval

parameters were not statistically significant. The OR of the frontal passenger was 0.278, indicating a lower risk of thoracic injury than the driver (p=0.006). The oblique direction had no statistical significance in all sub-parameters. In contrast to the previous risk analysis, the OR of the near-frontal direction decreased. The OR increased by 1.014 times as the delta-V value increased by 1 kph (p=0.034).

Each oblique direction was independently classified, and the age-related probability of severe thoracic injuries was analyzed based on the increase in delta-V.

The probability of severe thoracic injury was confirmed for occupants with fastened seatbelts (See Figure 3). As delta-V increased, the probability of severe injury increased rapidly in the following order: near-frontal, longitudinal, and far-frontal. Occupants with <54 years of age had the lowest probability of severe thoracic injury in all oblique directions. The same analysis was conducted for occupants with unfastened seatbelts (See Figure 4). In this analysis, the probability of severe injury was increased in the following order: longitudinal, far-frontal, and near-frontal. In all oblique directions, the probability of thoracic injury for occupants was higher in the order of >65 years, 55-64 years, and <54 years.

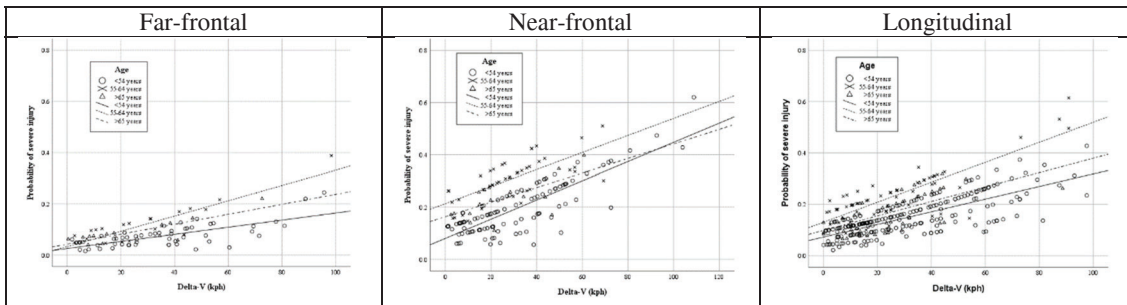


Figure 3. Probability of age-related thoracic injury for occupants with fastened seatbelts

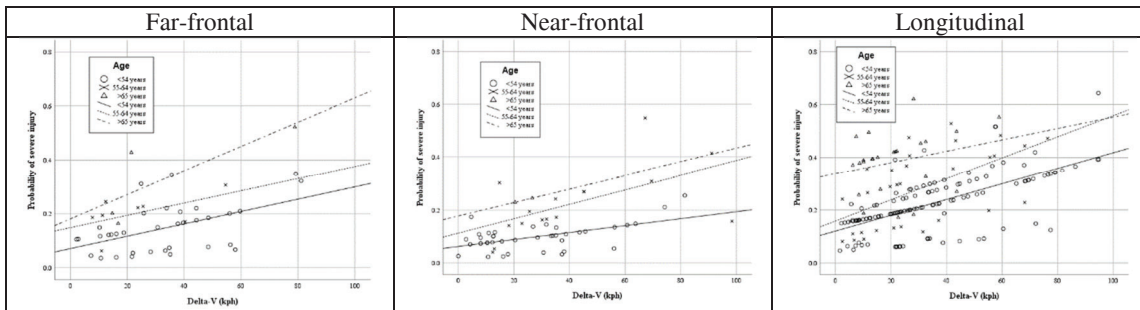


Figure 4. Probability of age-related thoracic injury for occupants with unfastened seatbelts

DISCUSSION

This study confirmed statistical differences in the risk of severe thoracic injuries in frontal oblique collisions according to age and oblique direction. Injury severity was classified in AIS3. Examples of thoracic injuries corresponding to an AIS score of 3 include multiple rib fractures, vascular injury, lung injury, and hemothorax. These AIS3+ injuries are regarded as severe because they may result in death or insufficient recovery [12]. In particular, the thorax is a structurally important region of the human body that contains various portions, including major organs, blood vessels, and skeletons [13].

As a result of frequency analysis according to the severity of the thoracic injury, the parameters that confirmed the significance were sex, age, BMI, seating position, and delta-V. Vehicle types and crash object parameters were not significant and were excluded from further risk analysis. Vehicle types were classified based on the shape of the vehicle, but additional factors such as the vehicle's curb weight were not considered. In the future, it is necessary to conduct research by classifying vehicles in more detail [14]. The crash object parameter was limited to the case of a collision with another vehicle or a fixed object. However, the pole-type object was excluded from this study. It is an important parameter, but most of the occupants engaged in pole injuries belong to the longitudinal direction. Also, in the case of a vehicle-to-vehicle collision, the difference in curb weight and shape between the two vehicles was not considered. These limitations need to be overcome by subdividing vehicle-to-vehicle collisions using globally reliable classification criteria.

Age was classified into three groups. The standard for seniors is 55 years old and the standard for the elderly is 65 years old, which is globally used [10,15]. In this study, it was confirmed that older occupants were more vulnerable to thoracic injuries. However, there were some unclear results due to the lack of elderly occupants' data. Previous research has shown a similar result that age has a significant impact on the injury severity of the thorax [16,17].

The oblique direction was classified into three groups considering PDoF and seating position. In the frequency analysis, the oblique direction had not shown an injury severity difference in the thoracic region. However, the risk difference was confirmed for each oblique direction. the occupant's seatbelt conditions made these risk

differences among the oblique directions. In the analysis using occupants with fastened seatbelts, the injury risk of near-frontal direction was found to be the greatest. The near-frontal direction of the three-point seatbelt was found to have the lowest occupant protection efficacy in previous research [9,18]. Additionally, the near-frontal direction was found to have the greatest increase in the risk of severe injury with an increase in delta-V. Significance according to the oblique direction was not confirmed using the occupant with unfastened seatbelts condition. According to this analysis, the longitudinal direction showed the highest increase in the risk of severe injury due to an increase in delta-V. The risk of thoracic injury was confirmed to be increased in the far-frontal direction than in the near-frontal direction. Previous research suggests that the risk of severe thoracic injury increased when occupants did not fasten their seatbelts in a frontal oblique collision [19]. However, the delta-V was not considered in that study. Furthermore, the result is limited to the near-frontal oblique direction and the driver position. Because of the shortage of studies on the far-frontal oblique direction, an in-depth study on the oblique direction according to individuals without seatbelts must be done in the next studies [17].

The frequency of male occupants was higher in the severe group. However, there was no significance in the risk of severe thoracic injury according to sex parameter. Previous studies have shown that male occupants have a higher risk of severe injury than female occupants [20]. However, the sample size of the study is about 100 times different from that of this study. Occupants of overweight and obese groups were found to have a higher risk of severe thoracic injuries than normal groups. However, no significant difference was observed among sub-parameters of BMI for the risk of severe injury. Previous research has shown that individuals that belonged to overweight or obese BMI are more vulnerable to thoracic injuries than normal BMI groups [21].

CONCLUSIONS

In this study, the aging effect of occupants affects to the risk of severe thoracic injury. The oblique direction also affected the risk of severe injury. However, the significance of risk due to oblique direction was limited only to occupants with fastened seatbelts. The risk of severe injury to occupants with unfastened seatbelts was the highest in the longitudinal direction. However, the research on unfastened seatbelt condition had not sufficient. This study showed the detailed risk of the thoracic region using the real-world collision database. The research could be used to enhance occupant safety and advance the crashworthiness of vehicle structures.

ACKNOWLEDGEMENT

This research was supported by the Korea Agency for Infrastructure Technology Advancement (KAIA) grant funded by the Ministry of Land, Infrastructure, and Transport (Grant 21AMDP-C162419-01), and a National Research Foundation of Korea (NRF) grant funded by the Korean government (MSIT) (no.2021R1A2C2094669).

REFERENCES

- [1] World Health Organization. 2018. "Global status report on road safety 2018: Summary." (No. WHO/NMH/NVI/18.20). World Health Organization.
- [2] CDC. 2020. "WISQARS (Web-based Injury Statistics Query and Reporting System)" Injury Center, CDC.
- [3] Ruan, J., El-Jawahri, R., Chai, L., Barbat, S., & Prasad, P. 2003. "Prediction and analysis of human thoracic impact responses and injuries in cadaver impacts using a full human body finite element model." SAE Technical Paper.
- [4] Ulfarsson, G. F., Kim, S., & Lentz, E. T. 2006. "Factors affecting common vehicle-to-vehicle collision types: Road safety priorities in an aging society." *Transportation research record*, 1980(1), 70-78.
- [5] Suarez-del Fuego, R., Junge, M., Lopez-Valdes, F., Gabler, H. C., Woerner, L., & Hiermaier, S. 2021. "Cluster analysis of seriously injured occupants in motor vehicle crashes." *Accident Analysis & Prevention*, 151, 105787.
- [6] Chen, F., Song, M., & Ma, X. 2019. "Investigation on the injury severity of drivers in rear-end collisions between cars using a random parameters bivariate ordered probit model." *International journal of environmental research and public health*, 16(14), 2632.

- [7] Lee, J., & Gim, T.-H. T. 2022. "Analysing the injury severity characteristics of urban elderly drivers' traffic accidents through the generalised ordered logit model: A case of Seoul, South Korea." *Journal of Transportation Safety & Security*, 14(7), 1139-1164.
- [8] Stitzel, J. D., Kilgo, P. D., Weaver, A. A., Martin, R. S., Loftis, K. L., & Meredith, J. W. 2010. "Age thresholds for increased mortality of predominant crash induced thoracic injuries." Paper presented at the Annals of Advances in Automotive Medicine/Annual Scientific Conference.
- [9] Östling, M., Saito, H., Vishwanatha, A., Ding, C., Pipkorn, B., & Sunnevång, C. 2017. "Potential benefit of a 3+ 2 criss cross seat belt system in frontal and oblique crashes." Paper presented at the Proceedings of IRCOBI conference.
- [10] Huber, S., Biberthaler, P., Delhey, P., Trentzsch, H., Winter, H., van Griensven, M., Lefering, R., Huber-Wagner, S., & Trauma Register, D. G. U. 2014. "Predictors of poor outcomes after significant chest trauma in multiply injured patients: a retrospective analysis from the German Trauma Registry (Trauma Register DGU(R))." *Scand J Trauma Resusc Emerg Med*, 22, 52.
- [11] Weir, C. B., & Jan, A. 2021. "BMI Classification Percentile And Cut Off Points StatPearls." Treasure Island (FL).
- [12] Carter, P. M., Flannagan, C. A., Reed, M. P., Cunningham, R. M., & Rupp, J. D. 2014. "Comparing the effects of age, BMI and gender on severe injury (AIS 3+) in motor-vehicle crashes." *Accident Analysis & Prevention*, 72, 146-160.
- [13] LoCicero III, J., & Mattox, K. L. 1989. "Epidemiology of chest trauma." *Surgical Clinics of North America*, 69(1), 15-19.
- [14] Wang, X., & Kockelman, K. M. 2005. "Use of heteroscedastic ordered logit model to study severity of occupant injury: distinguishing effects of vehicle weight and type." *Transportation research record*, 1908(1), 195-204.
- [15] Moon, S., Ranchet, M., Akinwuntan, A. E., Tant, M., Carr, D. B., Raji, M. A., & Devos, H. 2018. "The impact of advanced age on driving safety in adults with medical conditions." *Gerontology*, 64(3), 291-299.
- [16] Zhang, P., Parenteau, C., Wang, L., Holcombe, S., Kohoyda-Inglis, C., Sullivan, J., & Wang, S. 2013. "Prediction of thoracic injury severity in frontal impacts by selected anatomical morphomic variables through model-averaged logistic regression approach." *Accident Analysis & Prevention*, 60, 172-180.
- [17] Iraeus, J., Lindquist, M., Wistrand, S., Sibgård, E., & Pipkorn, B. 2013. "Evaluation of chest injury mechanisms in nearside oblique frontal impacts." *Annals of advances in automotive medicine*, 57, 183.
- [18] Wu, J., Xiao, S., Hou, J., Liu, Z., & Shi, X. 2022. "Research on characteristics of occupant's chest responses in oblique impact." *Proceedings of the Institution of Mechanical Engineers, Part D: Journal of Automobile Engineering*, 236(6), 1275-1284.
- [19] Li, P., Ma, C., Dong, Y., Li, H., & Zhang, J. 2016. "AIS 3+ Thoracic Injuries Among Drivers in Real-World Motor Vehicle Frontal Crashes: The Effect of Impact Direction, Impact Location and Status of Seat Belt." Paper presented at the 2016 Eighth International Conference on Measuring Technology and Mechatronics Automation (ICMTMA).
- [20] Ryb, G. E., Dischinger, P. C., McGwin, G., & Griffin, R. L. 2011. "Crash-related mortality and model year: are newer vehicles safer?" Paper presented at the Annals of Advances in Automotive Medicine/Annual Scientific Conference.
- [21] Turkovich, M., Hu, J. W., van Roosmalen, L., & Brienza, D. 2013. "Computer simulations of obesity effects on occupant injury in frontal impacts." *International Journal of Crashworthiness*, 18(5), 502-515.

A PHYSICS-BASED FAST-RUNNING SURROGATE MODEL FOR CRASH PULSE PREDICTION

Peter Wimmer, Oliver Zehbe
Virtual Vehicle Research GmbH
Austria

Lars Schories
ZF Friedrichshafen AG
Germany

Paper Number 23-0083

ABSTRACT

Recent developments in safety performance assessment of safety technologies by virtual simulation show a trend towards scenario-based approaches, especially for pre-crash technologies and driving automation systems. The models used for such types of simulations are rather fast, so many simulations can be performed in reasonable time. However, if the application of scenario-based approaches is extended to in-crash occupant protection technologies, finite element (FE) crash models come into play for e.g., determining the crash pulse. These models are very time-consuming and not suited for performing large-scale studies. The research objective therefore was to develop a model that delivers sufficiently accurate estimations of the crash-pulse in a frontal impact depending on crash configuration parameters while being fast enough to be used in large-scale safety performance assessment studies.

We built a multi-body-system (MBS) model consisting of the main frontal crash relevant structural elements (crash boxes, longitudinal member, cross member, engine, firewall) as well as the rest of the vehicle (passenger cabin and luggage trunk), which is modelled as one rigid body. Nonlinear force elements are used to model the elastic and plastic deformations. We optimized the parameters of the force elements by using results of 96 FE simulations of a high-fidelity full vehicle model impacting a rigid barrier. In those 96 simulations, we varied the impact speed, impact angle and lateral offset.

The physics-based surrogate model provides translational and rotational accelerations, speeds, and positions over time. The results show a good correlation to the results of the high-fidelity model: the mean absolute occupant load criterion (OLC) error for all 96 crash configurations is 0.88 g. The physics-based surrogate model needs less than one second for one run of 200 milliseconds on 1 CPU while the high-fidelity FE model needs more than 15 hours on 16 CPUs for the same task.

The model can be used to predict crash-pulses in the range of crash configuration parameters it was optimized for. It can be extended to other crash configurations. Its parameters can be adapted to represent other vehicles by adapting physical parameters like mass, lengths etc. due to the physics-based approach. This is a major advantage compared to non-physics-based black-box surrogate modelling techniques used for the same purpose, where the internal parameters do not represent any physical property. Moreover, the physics-based surrogate model can also be used to simulate a crash between two vehicles (even with different properties) by using another model instance instead of a rigid barrier as opponent. The model delivers an estimation of the crash-pulse, so its main purpose is to be used in large-scale studies, not to exactly reproduce one singular case. So far it can only be used in frontal crashes, but it could be extended for rear-end crashes as well by adding the respective structures at the rear end.

The model developed can predict crash-parameter-dependent crash-pulses and can be an essential part in accelerating large-scale safety performance assessment studies of occupant protection systems in frontal crashes.

RESEARCH QUESTION / OBJECTIVE

Two major trends currently emerge in vehicle safety system development. The first trend is related to the types of safety systems. While in-crash related safety measures (often called passive safety systems) are already quite long in the market and also systems operating in the pre-crash phase (often called active safety systems) are state of the art, the fusion of both types of systems into integrated safety is rather new.

The second trend is related to the virtual, simulation-based performance assessment of safety systems. Here scenario-based virtual testing methods are more and more used. These methods try to cover a wider range of possible scenarios that a certain safety system might encounter in real-world application. The first trend leads to the requirement of combining pre- and in-crash simulation. This in combination with the large number of simulation runs required for scenario-based testing leads to the need for fast in-crash models in order to be able to perform studies in reasonable time.

When looking at occupant protection, one essential element in assessing the performance of an integrated safety system is the determination of the resulting crash pulse in dependence of the involved vehicles and the crash configuration. A crash pulse prediction model suitable for scenario-based safety performance assessment therefore must fulfil the following requirements:

- The model should run fast. This is the basic requirement for a model to be included in large-scale studies. High-fidelity finite element (FE) models of the vehicle structure, a classical approach for determining crash pulses don't fulfil this requirement, as they typically take several hours to complete one crash simulation.
- The model should provide crash pulses at least in vehicle longitudinal direction but preferably also in lateral direction as well as around the yaw axis.
- The model should be applicable for a given range of crash configurations defined by impact speed, lateral offset and impact angle.
- The model should represent a two-vehicle crash, ideally with the possibility of using a configuration with two different vehicles.

The research objective therefore can be summarized as follows: development of a model that delivers sufficiently accurate estimations of the crash-pulse in a frontal impact depending on crash configuration parameters while being fast enough to be used in large-scale safety performance assessment studies.

METHOD

Several approaches were published for similar applications. [1] not only presents one concrete solution but also a summary of surrogate modelling approaches. Two main branches for surrogate modelling can be distinguished:

- Mathematical / black-box surrogate models which do not have a physics-based relation between in- and outputs. Various methods exist, see [1], (e.g. OSCCAR). These models are very flexible in terms of application, but they rely heavily on data for model training. As the relation between in- and outputs is usually not connected to physical parameters of the system that should be replaced, it is not possible to adapt such models to even slight differences in physical properties, like vehicle mass etc. The only possibility to enable consideration of such parameters is extending the reference data respectively.
- Physical /simplified surrogate models which model the mechanical behaviour of the vehicle during crash, but in a simplified way compared to high-fidelity FE models. Many approaches exist according to [1], most of them use FE or multi-body-system (MBS) methods but with simplifications in one or the other way.

We decided to use an MBS approach for the surrogate model as it is fast and has parameters that directly represent mechanical properties of the substituted vehicle(s). Moreover, we are mostly interested in the crash pulse, not the detailed deformation of the structure itself. The rest of this section is divided in three parts. The first part is about how we set-up the model. The second part is about generating reference data to which the new model can be fitted and compared to. The third part describes the fitting process.

Set-up of MBS model

Multi-body-systems consist of rigid bodies, joints that connect these bodies and force elements that apply forces between two bodies or between one body and the ground (the fixed reference for the model). Another way of interaction between bodies is contact between bodies. The resulting normal contact force usually depends on the intrusion and intrusion velocity, the tangential force on the defined friction coefficient.

We used the software PyBullet [2] to set up the model. PyBullet is a physics engine primarily developed to be used for robotics simulation and machine learning. It provides amongst other features forward dynamics simulation and collision detection and handling. It runs on Windows and Linux. We chose this software because it provides all required features, is fast, and multiple model instances can be used in parallel which increases performance even more. It is available under the zlib license.

The model consists of several bodies, joints, and force elements. The root body (grey box in the right part of **Figure 1**) represents the rear part of the vehicle, i.e., everything behind the firewall. Only one body is used for this part as no deformation is expected to happen here in a frontal impact. The longitudinal members (green boxes in **Figure 1**) are mounted to this root body using a combination of revolute joint (rotation axis z global) and prismatic joint (along the longitudinal axis). Parallel to the prismatic joint we added a force element which models the deformation behaviour of the longitudinal member. The lateral bending behaviour is covered by the revolute joint. The crash boxes (blue boxes in **Figure 1**) are connected via a prismatic joint allowing translation along the longitudinal axis (x-global direction in undeformed state). Again, we added a force element parallel to the prismatic joint which models the deformation behaviour of the crash box. The cross member (black box in **Figure 1**) is divided into two parts so that the cross member can also be deformed during impact. The two cross member parts are connected to the respective crash boxes via a revolute joint (rotation axis z global). Connecting the two cross members via a joint would result in a loop structure, which is not allowed in PyBullet. To create a loop structure, constraints must be used instead of joints. So, we used a prismatic constraint to connect the two cross member parts. The engine is connected to the root body using a planar joint that allows movement in the global x-y plane and with two constraints (point-to-point) to both longitudinal members. A schematic of the model can be found in **Figure 2**.

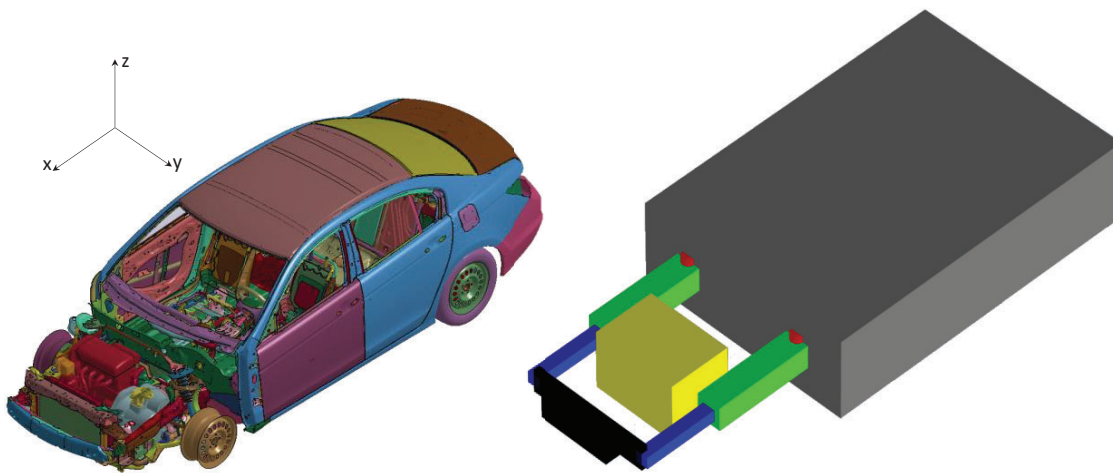


Figure 1. Left: The FE model to be replaced (some parts in front are removed to make the relevant structural elements visible). Right: The surrogate MBS model.

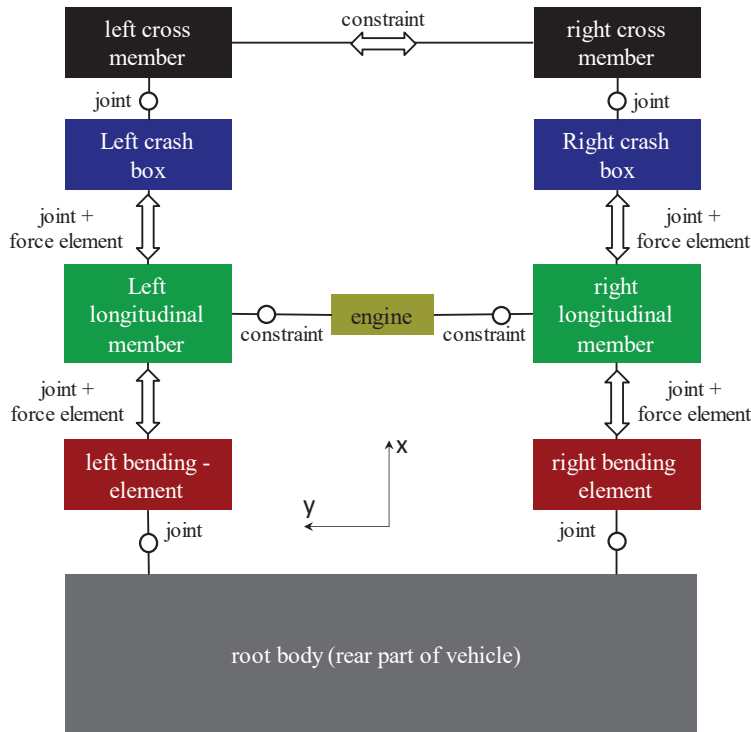


Figure 2. Schematic of the MBS model.

The force elements parallel to the prismatic joints use a characteristic as shown in **Figure 3**: The force raises linearly until a force level is reached where the collapsing of the structure begins (Point $s_{\text{collapsing begin}} / F_{\text{collapsing begin}}$ in **Figure 3**). This phase is followed by a phase where the longitudinal members and crash boxes continue to collapse until the point is reached, where no more significant plastic deformation is possible (Point $s_{\text{collapsing end}} / F_{\text{collapsing end}}$ in **Figure 3**). From this point on the structure is assumed to not deform any more. The unloading is done using a linear characteristic.

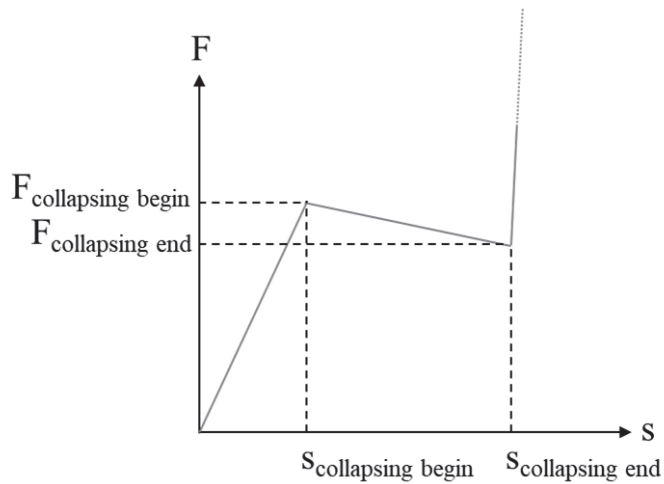


Figure 3. The displacement-force characteristics of the force elements.

The opponent in the crash simulation for the steps described in the following is a rigid barrier (modelled as one rigid body), but it is also possible to use two MBS-models colliding with each other in an oncoming crash configuration.

Generation of reference data

Now that the model is set up, model parameter values need to be defined. Some of them can be determined directly based on the information about the substituted vehicle model, like masses, positions, and dimensions of crash-relevant structures. Others, especially parameters defining the force elements cannot be derived directly but must be obtained differently. We used a model parameter optimization approach to fit those parameters so that the surrogate model output gets as close as possible to the output of the substituted vehicle model. To do so, we need reference data (as set of input data and related output data) to fit the surrogate model to.

The reference data is generated by performing simulations with the FE model for defined parameter sets. We chose three parameters that define the crash configuration: impact speed, lateral offset between vehicle and rigid barrier and impact angle. The speed values used are: 25, 35, 45, and 56 km/h. The lateral offset ranges from -1050 to +1050 mm in 350 mm increments. The impact angle ranges from 0 to 30° in 10° steps. We did a full factorial experiment design resulting in 4 speeds x 7 lateral offsets x 4 angles = 112 parameter combinations.

We used the freely available and validated Honda Accord (model year 2014) FE model [3] and added the rigid barrier as crash opponent. The simulations were performed using LS-Dyna, version 9.2.

The outputs of the simulations are the resulting accelerations, velocities, and displacements in x-, y-, and z-direction over time in the vehicle's centre of gravity. These will be used as reference data for the parameter optimization process described next.

Model parameter optimization

As mentioned above, some of the parameters cannot be derived directly from the original model but must be determined otherwise. We used optimization to find an optimal set of parameters that makes the surrogate model results fit to the FE model results as closely as possible.

As the number of parameters is large and it is not known whether there is only one optimal solution, we used in the first step a global optimisation method, more specifically a differential evolution algorithm implemented in the python package *inspyred*, version 1.0 [4]. In a follow-up step, we used a local optimisation method (Nelder-Mead algorithm implemented in the python package *scipy*, version 1.7.3, [5]) to find the final, optimal set of parameters. The quality criterion for the optimization process is based on the mean absolute error (MAE):

$$MAE = \frac{\sum_{i=1}^n |y_{pred,i} - y_{true,i}|}{n} \quad (1)$$

with y_{pred} as the value predicted by the surrogate model, y_{true} as the FE model result and n as the total number of values. The value to be minimized is a sum of five MAE values (for the rest of the paper referred to as "total error"): the MAE of the acceleration over time in x- and y-direction, the MAE of the velocity over time in x- and y-direction and the MAE of the instant in time where the velocity in x-direction reaches zero. We weighted both velocity MAEs with a factor of ten as we see this as the most important element in the optimization process. Moreover, each function call of the optimization process uses simulations of 96 of the 112 possible parameter combinations to cover the whole range of crash configurations the surrogate model should be used for. The reasons for using only 96 of 112 possible combinations are:

- The combination of an impact angle of 30° and a lateral offset of 1050 mm results in a crash configuration where the rigid barrier misses the crash box and the longitudinal member. This case cannot be covered by the MBS model. This reduces then number of combinations by 4 to 108.
- As the MBS model is symmetric about the x-axis, variations of lateral offset with same absolute value but different sign and an impact angle of zero degrees result in similar results. For those cases, the average of both results of the FE model are used. This further reduces the number of combinations by 12 to 96.

The optimization process resulted in a set of parameters which provides the results shown in the next section.

RESULTS

This section is divided into three parts. First, the results of the optimization process are presented, focussing on the model quality criteria used during the process itself. The second part focuses on the output of the models in terms of occupant load criterion (OLC), the third and final part is about calculation time.

Optimization process results

Figure 4 shows the cumulative density of the total error, MAE for longitudinal acceleration and longitudinal velocity. More than 50% of all parameter combinations result in a MAE for longitudinal acceleration of lower than 1 g and in a MAE for longitudinal velocity of lower than 2 m/s. More than 75 % of all parameter combinations result in a MAE for longitudinal acceleration of lower than 2 g and in a MAE for longitudinal velocity of lower than 3 m/s.

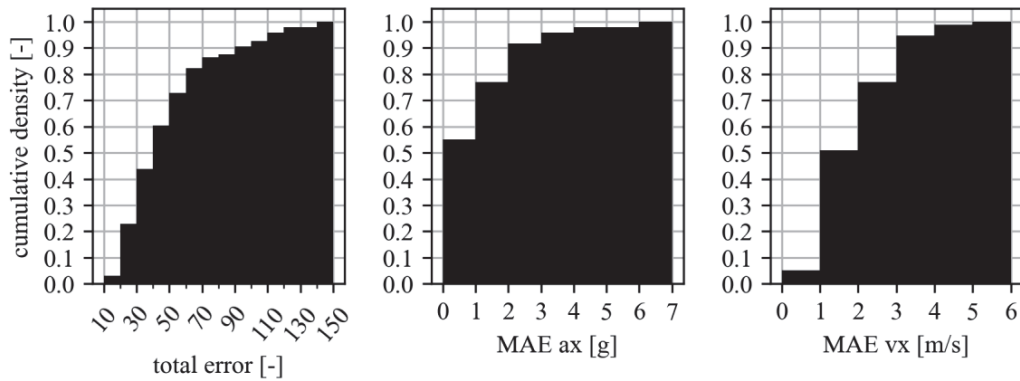


Figure 4. Cumulative density of total error (left), MAE for longitudinal acceleration (middle), and MAE for longitudinal velocity (right).

It is also of interest how much the results vary depending on the parameters describing the crash configuration.

Figure 5 therefore shows the mean values of the total error in dependence of speed, lateral offset and angle. It can be seen that the the total error increases with increasing speed and stays on the same level for angle variations. The variation of offset shows an outlier towards higher total error at 1050 mm.

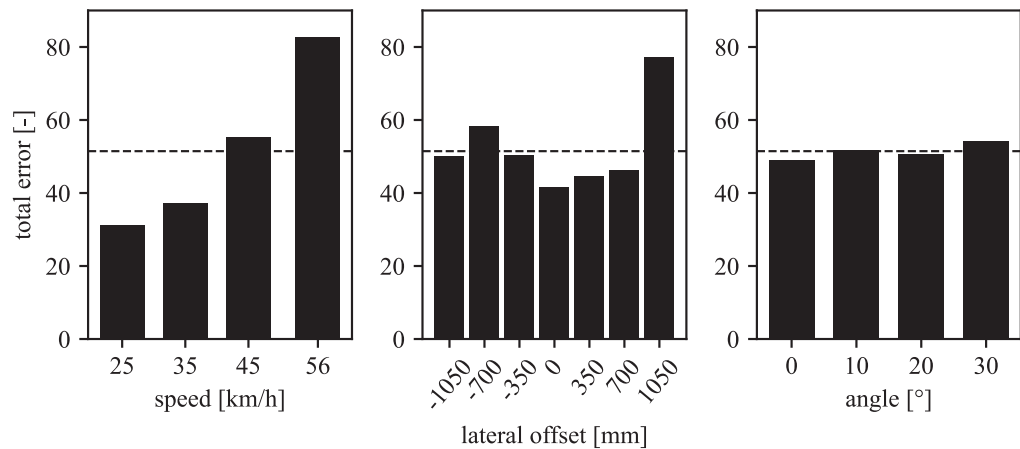


Figure 5. Mean values of total error in dependence of speed (left), lateral offset (middle) and angle (right). The horizontal dashed line indicates the mean total error of all runs.

Figure 6 shows the simulation set-ups for this lateral offset. These are configurations where the vehicle might stick to the rigid barrier and bounce back or slide laterally off the rounded corner of the rigid barrier and continue moving forward. Depending on what happens, the resulting accelerations, velocities etc. will differ significantly. Different behaviour of FE and MBS model in some of these situations is one reason for the large errors in these cases. Another reason is that even if both models behave the same, the sliding off happens in a different way in both models, also resulting in larger differences than in other configurations where this effect does not occur.

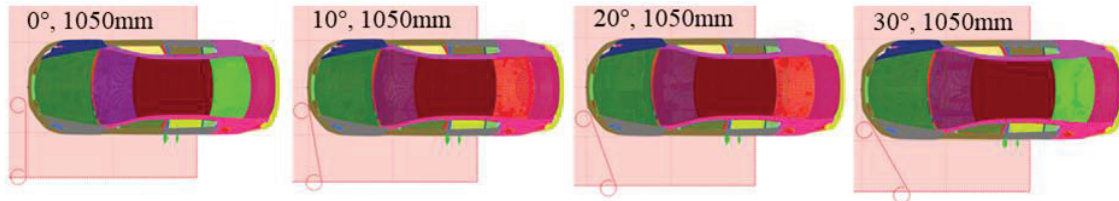


Figure 6. Simulation set-ups for lateral offset of 1050 mm and varying angle (0°, 10°, 20°, and 40°).

Figure 7 shows the time histories for longitudinal acceleration, velocity, and displacement as well as longitudinal acceleration over displacement for the parameter combinations resulting in lowest and highest total error. At the left side (best result) a very good correlation especially in terms of velocity and in the instant in time where the velocity in x-direction reaches zero can be seen. At the right side (worst result), the longitudinal velocity and displacements start to deviate at about 0.75 s. The reason for that is the same as mentioned above (sliding off the rounded corner) and shown in **Figure 8**: If the animations of both simulations for that parameter combination are laid on top of each other, it can be seen that the MBS model slides laterally off the rounded

corner of the rigid barrier resulting and continues moving forward while the FE model sticks to the wall and bounces back instead of sliding off.

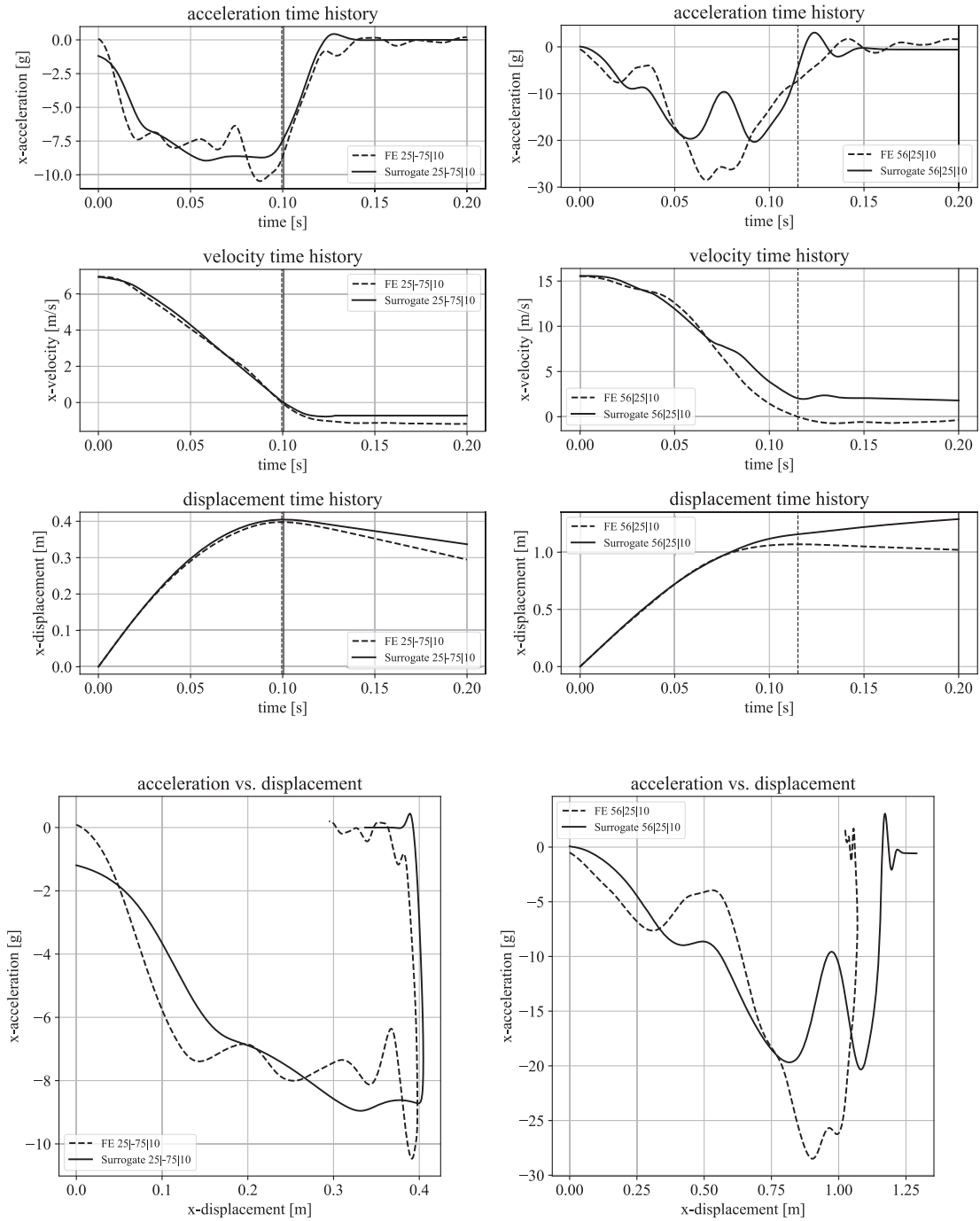


Figure 7. Results for the crash configurations resulting in lowest (left) and highest (right) total error.

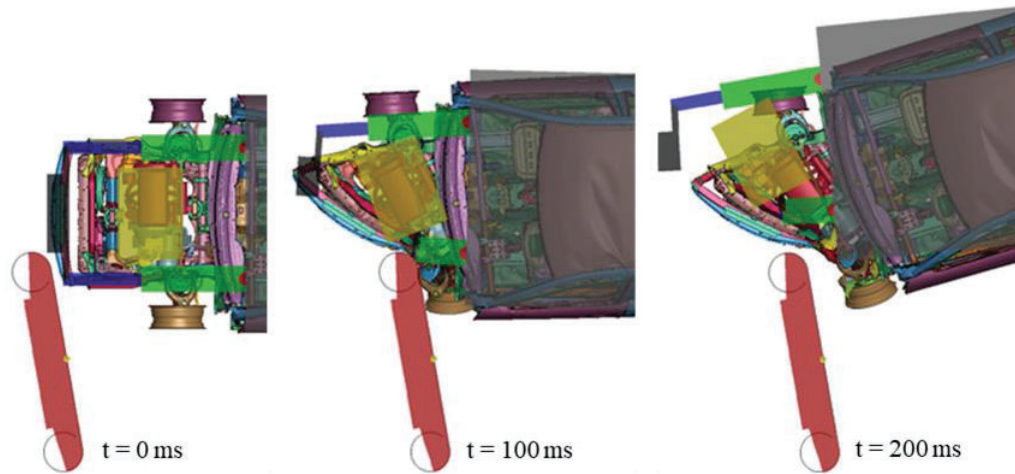


Figure 8. Overlay (top view) of simulation visualization at 0 milliseconds (left) 100 milliseconds (middle) and 200 milliseconds (right) for the parameter combination resulting in the worst model quality value.

Occupant load criterion-based analysis

The metrics used in the optimization process are suitable for assessing the similarity of the mechanical behaviour of FE and MBS model. However, they are less suitable to predict the model quality in terms of similarity in resulting occupant injury severity. We therefore did a second comparison of FE and MBS model using the occupant load criterion (OLC) [6] as it shows a good correlation to the crash pulse severity [7].

The OLC error (defined as difference between OLC calculated from MBS model output and OLC calculated from FE model output) ranges from -5.45 g to 2.38 g. As we are rather interested in the absolute deviation of the two values, we use the absolute value of the OLC error further on. The mean value of the absolute OLC error is 0.88 g, the 25th percentile value is 0.29g, the 50th percentile value is 0.62 g, and the 75th percentile value is 1.13g. **Figure 9** shows the cumulative density of the absolute OLC error.

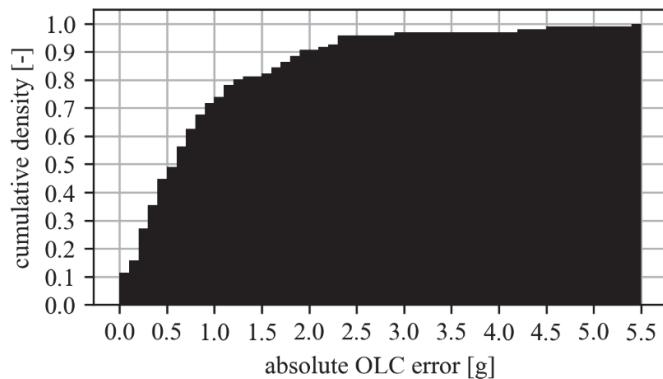


Figure 9. Cumulative density of the absolute OLC error.

As before, also the dependence of the absolute OLC errors on the parameters describing the crash configuration are analyzed, see **Figure 10**. Again, the largest spread is found at the speed variation while the variation in angle results in the smallest spread.

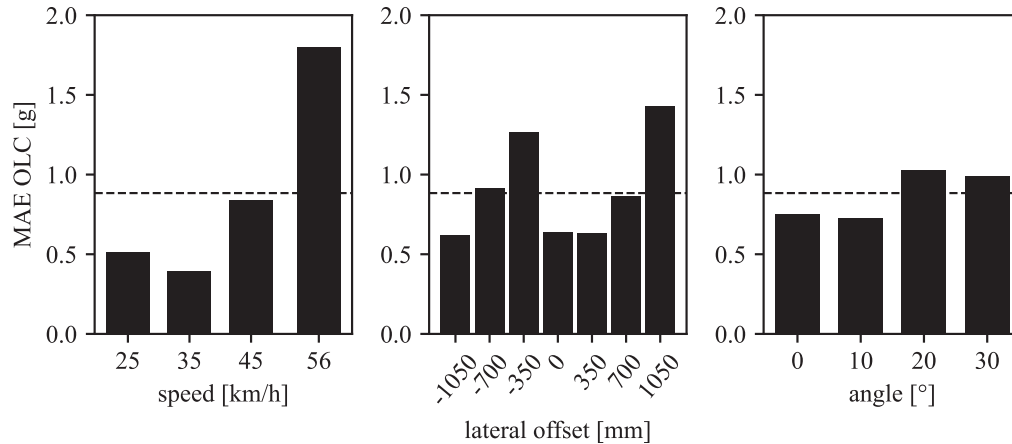


Figure 10. Mean values of absolute OLC errors in dependence of speed (left), lateral offset (middle) and angle (right). The horizontal dashed line indicates the mean of the absolute OLC errors of all runs.

OLC results for all parameter combinations can be found in the appendix in **Table 1**, **Table 2**, **Table 3**, and **Table 4**.

Calculation time

The FE model simulation takes on average 15 hours on 16 CPUs for one run of 200 milliseconds of simulated time. In comparison, the surrogate model takes on average 0.4 seconds on one CPU for one run of 200 milliseconds of simulated time.

Application in car-to-car crash

Instead of using a rigid barrier as opponent, the MBS model can also be set-up with two instances of the vehicle model thus representing a car-to-car crash. To check, whether this set-up also works, we set up a frontal collision case with two vehicles approaching each other with 56 km/h, 0 mm lateral offset and an angle of 0°. This setup should provide the same results compared to the rigid barrier case with 56 km/h. **Figure 11** shows the two set-ups. **Figure 12** shows the vehicle's centre of gravity time histories for longitudinal acceleration, velocity, and displacement as well as longitudinal acceleration over displacement for FE model and both MBS model set-ups.

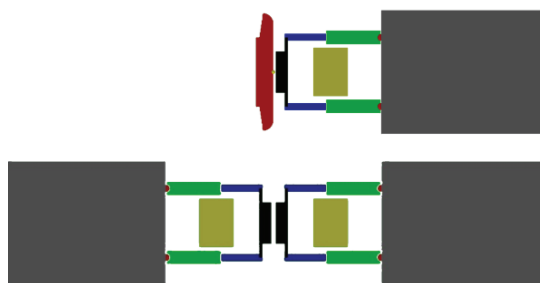


Figure 11. MBS model set-up for a lateral offset of 0 mm and angle 0° using as opponent a rigid barrier (top) or a second instance of the vehicle model (bottom).

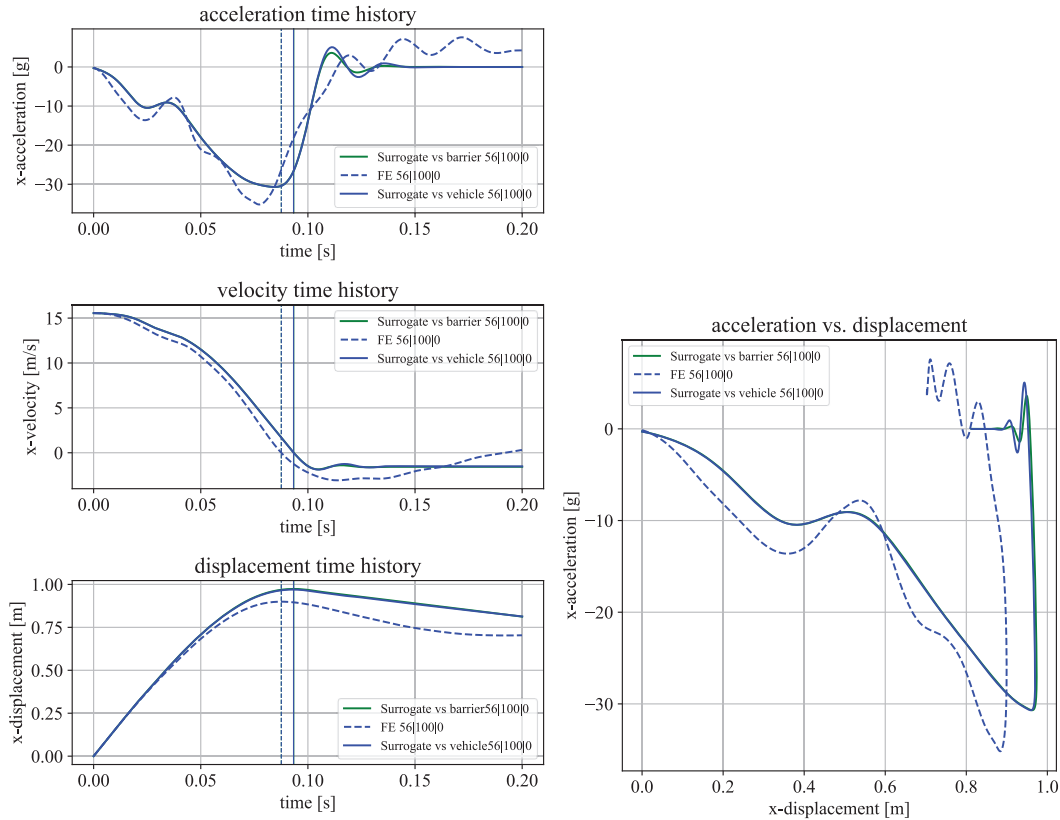


Figure 12. Comparison of results for FE-model, MBS model using as opponent a rigid barrier or a second instance of the vehicle model.

DISCUSSION AND LIMITATIONS

The surrogate model can be used to predict crash-pulses in the range of crash configuration parameters it was optimized for. The results, especially in terms of OLC error, show that most of the surrogate model's outputs are close to the ones of the FE model. With higher impact speeds, the total error and the MAE of the OLC increases. This can be expected, as higher impact speeds mean higher levels of all output quantities and the comparisons are made on absolute values, not relative ones. The model quality is less sensitive to variations in angle. When looking at specific crash configurations, larger deviations can be seen. One such group of configurations with larger deviations are the ones where the vehicle could slide off the rounded corner of the rigid barrier. However, these cases are less relevant for the practical application, as this sliding off will not happen in a similar way in car-to-car crash configurations. A possibility would be to explicitly exclude such configurations from the surrogate model's validity range, i.e., not use it for such configurations. Moreover, the surrogate model was developed to be used in large-scale studies and produce a large number of crash pulses which in total are representative and not to exactly reproduce one singular case.

The surrogate model is fast enough for such large-scale studies, even when used as single instance. As multiple instances can run in parallel, the performance in terms of simulation time can be increased even more.

The chosen, physics-based approach has two major advantages compared to non-physics-based black-box surrogate modelling techniques used for the same purpose:

- The surrogate model can be extended to be applicable for other crash configurations. So far it can only be used in frontal crashes, but by adding the respective structures at the rear end it can also be used for rear-end crashes

- The surrogate model can represent other vehicles by adapting physical parameters like mass, lengths etc. while this is not possible for a black-box model as its internal parameters do not represent any physical property.

Moreover, the physics-based surrogate model can also be used to simulate a crash between two vehicles (even with different properties) by using another vehicle model instance instead of the rigid barrier as opponent. The resulting curves for the case to check this possibility are almost identical, slight differences appear only in the rebound phase (see **Figure 12**).

CONCLUSIONS

The surrogate model developed extends the possibilities of scenario-based large-scale safety performance assessment studies to also consider the influences of the mechanical in-crash vehicle behaviour on occupants. With a simulation time of 0.4 seconds for 200 milliseconds simulated time, the surrogate model is fast enough for such types of studies. The model provides crash pulses in longitudinal and lateral direction. It is suitable to be used in the most relevant frontal crash configurations in terms of impact speed, angle and lateral offset. Although the surrogate model was set-up using a rigid barrier as crash opponent, it is also suitable for car-to-car frontal crashes by using two instances of the vehicle model. The two vehicles could even have differing physical properties like mass, lengths etc. Future work might include extending the range of application for frontal crash configurations or even going further by extending the surrogate model so that it can be used in totally different crash configurations like side or rear-end impact. The application of this modelling approach can be an essential part in accelerating large-scale safety performance assessment studies of occupant protection systems in frontal crashes.

ACKNOWLEDGEMENT

The publication was written at Virtual Vehicle Research GmbH in Graz, Austria. The authors would like to acknowledge the financial support within the COMET K2 Competence Centers for Excellent Technologies from the Austrian Federal Ministry for Climate Action (BMK), the Austrian Federal Ministry for Digital and Economic Affairs (BMDW), the Province of Styria (Dept. 12) and the Styrian Business Promotion Agency (SFG). The Austrian Research Promotion Agency (FFG) has been authorised for the programme management. They would furthermore like to express their thanks to their supporting industrial and scientific project partners, namely ZF Friedrichshafen AG.

REFERENCES

- [1] Duddeck, F., & Wehrle, E. 2015a. "Recent Advances on Surrogate Modeling for Robustness Assessment of Structures with respect to Crashworthiness Requirements". *10th European LS-DYNA Conference*.
- [2] Coumans, E., & Bai, Y. n.d.-b. *PyBullet, a Python module for physics simulation for games, robotics and machine learning*. <http://pybullet.org>
- [3] Singh, H., Kan, C.-D., Marzougui, D., Morgan, R., & Quong, S. 2016c. "Update to Future Midsize Lightweight Vehicle Findings in Response to Manufacturer Review and IIHS Small-Overlap Testing". In *Report No. DOT HS 812 237, National Highway Traffic Safety Administration (Issue February)*.
- [4] Tonda, A. 2020d. "Inspyred: Bio-inspired algorithms in Python". *Genetic Programming and Evolvable Machines*, 21, 269–272. <https://doi.org/10.1007/s10710-019-09367-z>
- [5] Virtanen, P., Gommers, R., Oliphant, T. E., Haberland, M., Reddy, T., Cournapeau, D., Burovski, E., Peterson, P., Weckesser, W., Bright, J., van der Walt, S. J., Brett, M., Wilson, J., Millman, K. J., Mayorov, N., Nelson, A. R. J., Jones, E., Kern, R., Larson, E., ... SciPy 1.0 Contributors. 2020e. "{SciPy} 1.0: Fundamental Algorithms for Scientific Computing in Python". *Nature Methods*, 17, 261–272. <https://doi.org/10.1038/s41592-019-0686-2>
- [6] Kübler, L., Gargallo, S., & Elsäßer, K. 2009f. "Frontal crash pulse assessment with application to occupant safety". *ATZ Worldwide*, 111(6), 12–17. <https://doi.org/10.1007/BF03225076>
- [7] Park, C.-K., & Kan, C.-D. (Steve). 2015g. "Objective Evaluation Method of Vehicle Crash Pulse Severity in

APPENDICES

Table 1.

OLC results for 25 km/h

Velocity [km/h]	Lateral offset [mm]	Angle [°]	OLC _{FE}	OLC _{MBS}	OLC error
25	-350	10	8.42	8.39	-0.03
25	-350	20	8.25	7.72	-0.53
25	-350	30	5.89	6.39	0.5
25	-700	10	8.45	8.5	0.05
25	-700	20	8.46	8.23	-0.23
25	-700	30	7.87	7.16	-0.71
25	-1050	10	6.67	7.14	0.47
25	-1050	20	7.82	8.48	0.66
25	-1050	30	8.01	8.36	0.35
25	1050	0	6.92	5.9	-1.02
25	1050	10	7.67	6.96	-0.71
25	1050	20	2.37	4.75	2.38
25	700	0	8.15	8.39	0.24
25	700	10	7.82	8.07	0.25
25	700	20	7.29	6.79	-0.5
25	700	30	5.72	6.21	0.49
25	350	0	9.27	8.4	-0.87
25	350	10	8.37	8.4	0.03
25	350	20	7.96	7.72	-0.24
25	350	30	6.2	6.21	0.01
25	0	0	9.37	8.38	-0.99
25	0	10	8.39	8.4	0.01
25	0	20	8.08	7.72	-0.36
25	0	30	5.82	6.39	0.57

Table 2.

OLC results for 35 km/h

Velocity [km/h]	Lateral offset [mm]	Angle [°]	OLC _{FE}	OLC _{MBS}	OLC error
35	-350	10	11.83	11.73	-0.1
35	-350	20	11.44	11.17	-0.27
35	-350	30	9.8	9.59	-0.21
35	-700	10	12.07	11.76	-0.31
35	-700	20	11.73	11.65	-0.08
35	-700	30	11.44	10.27	-1.17
35	-1050	10	11.05	11.11	0.06
35	-1050	20	12.18	11.76	-0.42
35	-1050	30	12.14	11.77	-0.37
35	1050	0	11.3	10.47	-0.83
35	1050	10	10.92	10.12	-0.8

35	1050	20	5.4	6.59	1.19
35	700	0	11.92	11.72	-0.2
35	700	10	11.64	11.35	-0.29
35	700	20	10.67	10.25	-0.42
35	700	30	8.82	8.16	-0.66
35	350	0	11.89	11.72	-0.17
35	350	10	11.94	11.73	-0.21
35	350	20	11.15	11.17	0.02
35	350	30	9.66	9	-0.66
35	0	0	12.12	11.72	-0.4
35	0	10	12.14	11.73	-0.41
35	0	20	11.28	11.17	-0.11
35	0	30	9.62	9.59	-0.03

Table 3.

OLC results for 45 km/h

Velocity [km/h]	Lateral offset [mm]	Angle [°]	OLC _{FE}	OLC _{MBS}	OLC error
45	-350	10	16.67	17.33	0.66
45	-350	20	17.56	16.45	-1.11
45	-350	30	16.34	14.54	-1.8
45	-700	10	19.3	17.71	-1.59
45	-700	20	16.64	17.39	0.75
45	-700	30	15.94	14.57	-1.37
45	-1050	10	16.95	17.23	0.28
45	-1050	20	18.6	17.8	-0.8
45	-1050	30	17.17	17.88	0.71
45	1050	0	15.7	15.7	0
45	1050	10	15.27	13.61	-1.66
45	1050	20	8.82	9.99	1.17
45	700	0	17.38	17.78	0.4
45	700	10	16.02	16.98	0.96
45	700	20	16.19	15.51	-0.68
45	700	30	12.34	11.08	-1.26
45	350	0	16.89	17.8	0.91
45	350	10	16.29	17.33	1.04
45	350	20	16.83	16.44	-0.39
45	350	30	14.52	14.04	-0.48
45	0	0	17.07	17.81	0.74
45	0	10	17.03	17.33	0.3
45	0	20	17.07	16.46	-0.61
45	0	30	14.94	14.57	-0.37

Table 4.

OLC results for 56 km/h

Velocity [km/h]	Lateral offset [mm]	Angle [°]	OLC _{FE}	OLC _{MBS}	OLC error
56	-350	10	24.27	24.02	-0.25
56	-350	20	26.21	21.97	-4.24
56	-350	30	25.9	20.45	-5.45
56	-700	10	26.69	25.03	-1.66

56	-700	20	25.12	23.31	-1.81
56	-700	30	21.71	20.47	-1.24
56	-1050	10	22.72	21.92	-0.8
56	-1050	20	27.06	25.15	-1.91
56	-1050	30	25.95	25.33	-0.62
56	1050	0	22.18	19.81	-2.37
56	1050	10	22.47	17.94	-4.53
56	1050	20	12.65	13.1	0.45
56	700	0	27.44	25.16	-2.28
56	700	10	23.76	23.45	-0.31
56	700	20	23.01	20.07	-2.94
56	700	30	15.9	13.95	-1.95
56	350	0	24.78	25.21	0.43
56	350	10	24.81	23.99	-0.82
56	350	20	24.03	21.93	-2.1
56	350	30	20.59	18.87	-1.72
56	0	0	25.4	25.21	-0.19
56	0	10	25.74	23.96	-1.78
56	0	20	24.35	21.96	-2.39
56	0	30	21.39	20.42	-0.97

HEAVY TRUCK FRONTAL IMPACTS AND FIRES

Brian Herbst
Lauren Bell
Christopher Clarke
Safety Analysis and Forensic Engineering (SAFE)
USA

Jack Bish
SAFE Laboratories
USA

Paper Number 23-0165

ABSTRACT

Industry and government studies have noted the dangers of heavy truck frontal and underrun crashes, suggesting various measures to improve safety in these types of accidents including strengthening front suspension components and adding protective structures. In 1986, The USDOT found post-crash fires were involved in 16% of heavy truck fatalities compared to only 4% for cars. The report identified several mechanisms of fuel tank rupture including frontal impacts resulting in front axle contact with fuel tanks. The hazards of exposed side saddle fuel tanks have been known for decades, yet heavy trucks still use this vulnerable outboard location for fuel tanks.

In 1994, the United Nations ECE published a standard for heavy truck front underrun protective structures (FUPS); however, the United States still has no requirements regarding front underrun protection of heavy trucks. A FUPS prevents underrun and engages the energy absorbing structures of smaller impacting vehicles, provides protection of the trucks steering components, and helps prevent the truck's front axle from being displaced into the fuel tank which can cause rupture and fire.

Three real-world crashes are presented wherein heavy trucks experienced a frontal impact, resulting in fire and serious injury. In each of these cases, testing was conducted on a production truck front structural assembly and compared to a similar FUPS equipped assembly. The effectiveness of FUPS in mitigating damage in these frontal crashes was assessed.

INTRODUCTION

Fuel tanks in heavy trucks have traditionally been placed outside the frame rails in a side-saddle arrangement. This fuel tank arrangement was abandoned decades ago in passenger cars, light trucks, and vans due to the vulnerability of the fuel tanks. The photo below shows the side saddle fuel tank location that Consolidated Freightways, the precursor to Freightliner, was using at least as early as the 1940s (see Figure 1).



Figure 1. Consolidated Freightways Truck (Precursor to Freightliner) Fuel Tank Placement

In 1983, the University of Michigan studied fires and fatalities in heavy truck accidents.[1] This study found the rate of fire-associated fatalities in diesel fueled road tractors was 15 times as high as the corresponding fatality rate among passenger car occupants. The study noted “Yet some improvement might result from strengthened front axle mountings, from moving the fuel tanks in from the absolute edge of the vehicle side boundary, etc.”

The United States Department of Transportation (DOT) published Truck Occupant Protection in 1986.[2] This study found that post-crash fires were involved in 16% of heavy truck fatalities compared to only 4% for passenger cars. The report identified several mechanisms that could rupture the fuel tank including the following:

- Frontal impact with low object: Front axles, battery boxes, etc. contacting tanks
- Side impact, vehicle into truck: Direct impact into tank
- Rollover: Scraping along ground, contact with object, fuel cap leakage
- Collision with fixed objects: Mounting guardrails/barriers, direct contact

In 1986, the DOT also published the Heavy Truck Safety Study.[3] This study identified post-crash non cargo related fires as a vehicle related safety issue. This study notes the American Trucking Association (ATA) recommended exploring the concept of cab fireworthiness and developing a cab capable of protecting an occupant in a fire for a specific period of time. This study also suggested that truck front end structures could be designed for energy absorption and deflection in order to manage full frontal and offset frontal impacts.

In 1994, the United Nations ECE published a standard for the design of a front underrun protective device, also known as a FUPD. The FUPD is required to resist loads of 80 kN and 160 kN at different locations (see Figure 2). In addition, the displacement during the test is limited to 400 mm. A FUPD resists underride and engages the energy absorbing structures of passenger cars and LTVs, providing a significant improvement protection to the occupants of these vehicles. By 2003, European trucks were required to comply with ECE R93.

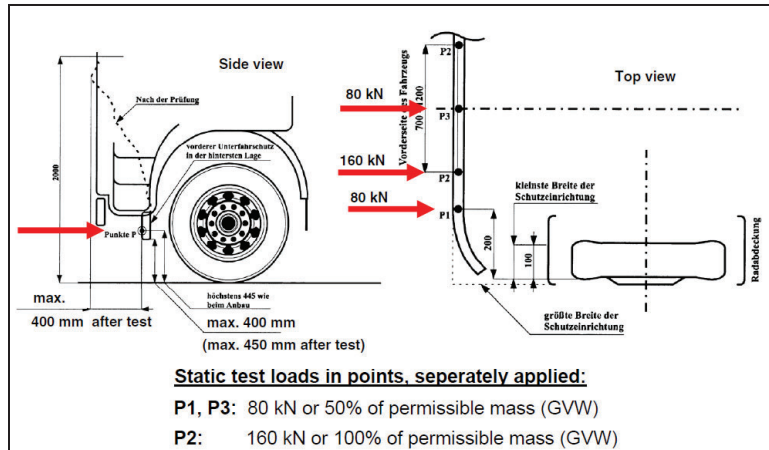


Figure 2. ECE R93 Test

In a study commissioned by the Australian government, Lambert and Rechnitzer of Monash University noted that head on crashes are more severe than other crash modes, and the performance of FUPS devices must be at a significantly higher standard of at least double that of a rear underride barrier. They recommended strength levels at the load points specified in ECE93 as follows. [4]

- P1: 400kN (~90,000 lbs)
- P2: 300kN (~67,000 lbs)
- P3: 200kN (~45,000 lbs)

Despite these findings, Australia adopted the requirements of ECE R93 in 2009 as Australian Design Rule 84/002.

CASE STUDIES

Three real-world crashes are presented wherein a heavy truck experienced a frontal impact, resulting in fire and serious injury. In each of these cases, sled testing was conducted on a production truck front structural assembly and compared to a similar FUPS equipped assembly. The effectiveness of FUPS in mitigating damage in these frontal crashes was assessed.

Case Study 1

A tractor/trailer was travelling east in the number two lane when it side swiped a parked tow truck on the side of the road, resulting in a flash fire. A separate fire source and origin analysis determined that diesel fuel vapor was released from the right fuel tank of the truck and the ignition of these vapors resulted in a flash fire or a "fireball." The fireball engulfed the driver of the tractor/trailer, resulting in burn injuries (See Figure 3).



Figure 3. Scene Photographs

A production heavy truck frame including bumper assembly and front axle was subjected to a sled impact on the right side of the front bumper to evaluate the structure's resistance to impact forces. The assembly was rigidly supported by an impact barrier at the rear of the frame and to the floor at several locations along the assembly at approximately

zero degrees of yaw, pitch and roll, so that the striking sled's vertical face would initially contact the vehicle's right front side of the bumper outboard of the interior frame supports (see Figure 4).



Figure 4. Production Sled Test

The sled impacted the front of the heavy truck frame assembly at 27.4 mph and decelerated at a peak rate of approximately 11.3 g's displacing 76.0 inches towards the rear of the frame. Prior to impact, the kinetic energy of the sled was approximately 132,000 ft-lb. Utilizing the sled mounted accelerometers filtered at 10 Hz, the peak load was calculated to be approximately 52,600 lb. at a displacement of 66.3 inches.

The test progressed as planned with the striking sled's vertical face impacting the right front side of the bumper assembly. The first contact was to the external plastic fascia of the bumper. The impact tore the fascia and bent the corner support inward towards the frame. The sled continued to move forward striking the right front tire. The leaf spring/axle clamping fixture broke free of positioning pin allowing the axle to move rearwards. As this motion continued, an axle U-bolt failed on both the passenger and driver side of the vehicle. The tire continued to move rearward striking the Diesel Particulate Filter (DPF) and the attached steps. The steps were driven into the Selective Catalytic Reduction (SCR) assembly, which was driven rearward (see Figure 5).

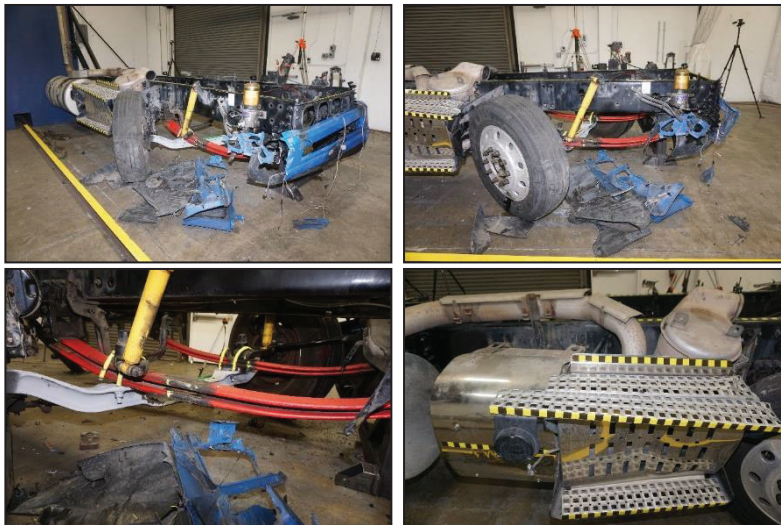


Figure 5. Production Sled Post-Test Photographs

Additionally, a FUPS system was constructed and attached to a production heavy truck frame, front axle and bumper assembly and was subjected to a similar sled test impact. The main FUPS beam was composed of ASTM A500 six inches by six inches square tube with a thickness of 0.25 inches with a four inches by four inches square tube with a thickness of 0.120 inches welded on top, aligned along the front. The four by four was attached with the production attachment points to the bumper center bumper beam location and the production bumper assembly was placed over the completed FUPS (see Figure 6).

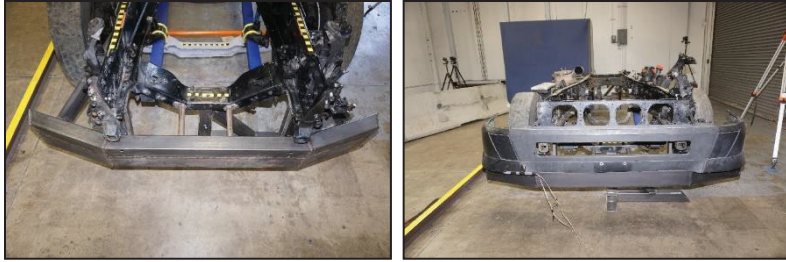


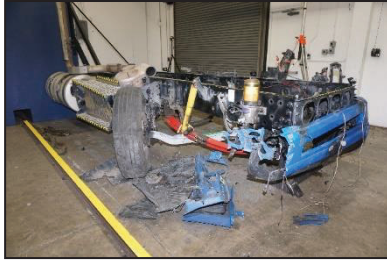
Figure 6. FUPS Sled Test

The sled impacted the front of the heavy truck frame assembly at 27.1 mph and decelerated at a peak rate of approximately 16.9 g's displacing approximately 47.0 inches towards the rear of the frame before rotating to rest. Prior to impact, the kinetic energy of the sled was approximately 130,000 ft-lb. The striking sled's vertical face impacting the right front side of the bumper assembly. The first contact was to the external plastic fascia of the bumper. The impact tore the fascia and began loading the FUPS. The sled continued to move forward bending the FUPS attachments to the frame. The sled continued to move rearward striking the right front tire driving it rearward. The leaf spring/axle clamping fixture broke free of its positioning pin allowing the axle to move rearwards. The tire continued to move rearward contacting the DPF and the attached steps (see Figure 7).



Figure 7. FUPS Sled Post-Test Photographs

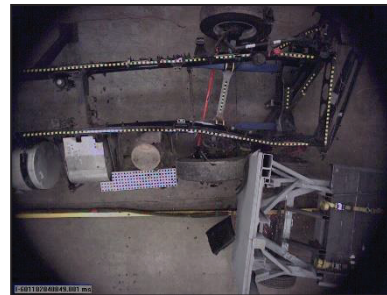
SAFE's sled testing of a heavy truck production design showed the susceptibility of the front axle under foreseeable crash conditions. SAFE's sled testing shows that a FUPS significantly reduces penetration and results in reduced depth of damage into the truck's structure. A comparison between the production and FUPS tests indicated a displacement reduction for the FUPS test by approximately 40%. Additionally, a FUPS increases the initial stiffness and energy absorption characteristics of the front structure. This increased initial stiffness allows for earlier and faster separation of the sled and reduced probability of interaction with the fuel tank (see Figure 8 and Figure 9).



Production Sled Test

FUPS Sled Test

Figure 8. Post-Test Photographs



Production Sled Test

FUPS Sled Test

Figure 9. Point of Maximum Penetration

Case Study 2

A heavy truck impacted a bear in the roadway with the left front bumper of the tractor. The impact caused the tractor trailer to be directed towards the southerly edge of the roadway ultimately leading to the vehicle interaction with the roadside culverts, catching fire, and tipping over. A separate fire source and origin analysis found that the first fuel ignited was diesel fuel vapors released from the passenger side's fuel tank (see Figure 10).



Figure 10. Scene Photographs

A production frame, front axle and bumper assembly were subjected to an impact on the left front bumper in order to evaluate the structure's resistance to impact forces. The frame assembly was rigidly supported by an impact barrier at the rear of the frame assembly and positioned such that a 255 lb impactor designed to approximate the subject bear would initially contact the left front side of the bumper outboard of the frame rails (see Figure 11).



Figure 11. Production Sled Test

The impactor struck the bumper at 58.0 mph. Prior to impact, the kinetic energy of the impactor was approximately 29,000 ft-lb. The test progressed as planned with the rubber face of the impactor striking the left front side of the bumper. The impact bent the metallic bumper and supporting rods inwards towards the frame and steering box. The impactor began to rotate and then struck the left front wheel assembly. The rotation of the impactor continued as its forward motion stopped. The wheel assembly rotated outward, and the impactor moved away from the chassis in a lateral direction before striking the surrounding test containment barriers and coming to rest. The left front tire continued to rotate outward until the impactor disengaged from it. At that point, the rotation of the tire reversed and the leading edge of the tire moved towards the frame. This causes the steering wheel to forcefully spin and would impact the ability to steer or control the truck (see Figure 12).



Figure 12. Production Sled Post-Test Photographs

A FUPS system was constructed and attached to a production frame, front axle and bumper assembly, and was subjected to a similar sled test impact. The main FUPS beam was composed of ASTM A500 six inch by six inch square tube with a thickness of 0.25 inches (see Figure 13).



Figure 13. FUPS Sled Test

The impactor struck the bumper at 59.6 mph. Prior to impact, the kinetic energy of the impactor was approximately 30,000 ft-lb. The rubber face of the impactor struck the left front side of the FUPS. The impact caused the impactor to go into a counterclockwise rotation (as seen from above). At approximately 90 degrees of rotation, the impactor came into very light contact with the front tire. The impactor continued to rotate, moving away from the chassis before striking the surrounding test containment barriers and coming to rest (see Figure 14).



Figure 14. FUPS Sled Post-Test Photographs

This sled testing shows that the production design allows for significant engagement and rotation of the steer wheel during a collision with a foreseeable roadway object, like an animal, which would affect the driver’s ability to control the directionality of the truck. The testing also showed that a FUPS virtually eliminates wheel assembly engagement, preserving steering control (see Figure 15).



Production Sled Test

FUPS Sled Test

Figure 15. Post-Test Photographs

Case Study 3

An SUV crossed the roadway centerline and impacted a heavy truck (both travelling at approximately 50-55 mph) in an offset orientation and outside of the heavy truck frame rail, causing major damage to the left front of both vehicles. The impact compromised the truck’s side saddle fuel tank, leading to a large fire (see Figure 16).



Figure 16. Scene and Vehicle Photographs

In order to investigate if a FUPS could protect the heavy truck steering and fuel tank from significant damage, a full scale crash test was conducted with a FUPS equipped chassis. The main FUPS beam was composed of an ASTM A500 rectangular tube six inches by eight inches with a thickness of 0.25 inches. The truck chassis was rigidly mounted at the rear in a level orientation parallel to the direction of travel of the impacting SUV. The front of the FUPS equipped chassis was supported by the front axle assembly and was ballasted with approximately 7,000 lbs of concrete blocks in order to represent a typical front axle load. The SUV struck the driver's side of the FUPS equipped chassis with 35% overlap (on the SUV) and a 0° PDoF at 55 mph (see Figure 17).

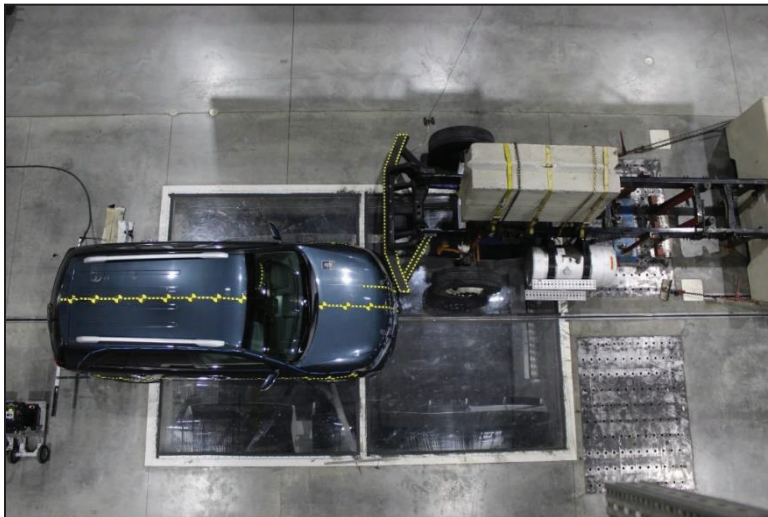


Figure 17. FUPS Full Scale Crash Test

The SUV impacted the FUPS, distorted it, overloaded many of the bolted attachments, and contacted the left steer tire. Ultimately the SUV was deflected away from the truck and ran into the test containment barriers. The steer tire rebounded and the axle remained attached to the truck suspension, although the entire side had been shifted rearward. The front suspension and front axle assembly remained intact, and the rearward displacement of the front wheel assembly was limited such that the front tire did not make contact with the fuel tank during the test. In addition, all steering linkages remained intact, and the steering mechanism was observed to be functional after the test, indicating steering control would have been maintained after the impact. Full scale testing showed that a properly constructed FUPS was able to effectively deflect a mid-sized SUV at 55 mph, while protecting the front axle and fuel tank (see Figure 18).

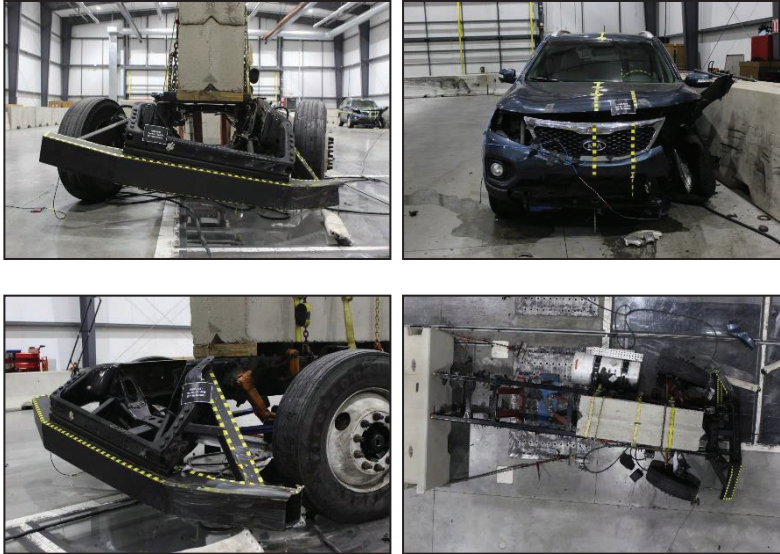


Figure 18. Post-Test Photographs

CONCLUSIONS

Common heavy truck construction in the United States lacks structural components outboard of the frame rails and below the frame rails. This lack of structure creates a major crash compatibility mismatch that puts occupants of smaller impacting vehicles at risk from intrusion and can make it difficult for deployable restraints to respond appropriately. In addition, heavy trucks are vulnerable to damage to their steering components, displacement of their axles, and rupture of their fuel tanks. The resulting risk of loss of control and fire, places the occupants of the heavy truck and other road users at risk in the event of secondary impacts and fires. Sled impact testing was an effective methodology for evaluating the frontal impact mode and demonstrated front axle, steering component, and fuel tank damage consistent with that seen in real world accidents. The testing has also shown that front underrun protective structures are effective in mitigating the damage caused in these frontal impact crashes, improving safety for heavy truck occupants and other road users alike.

REFERENCES

- [1] O'Day, James. "Fires and Fatalities in Tractor-Semitrailer Accidents," UMTRI Research Review, Vol. 14, No. 2, Sept.-Oct. 1983
- [2] "Truck Occupant Protection," DOT HS 807 081, NHTSA Technical Report, December 1986
- [3] "Heavy Truck Safety Study," DOT HS 807 109, Final Report, Clarke, et al.
- [4] Review of Truck Safety: Stage 1: Frontal, Side and Rear Underrun Protection, Lambert and Rechnitzer, 2002

FRONTAL HEAD-ON CAR-TO-HEAVY GOODS VEHICLE CRASHES EFFECT ON THE RESTRAINT SYSTEM

Martin Östling

Autoliv Research
Sweden

Linda Eriksson, Mikael Dahlgren

Autoliv
Sweden

Jason Forman

University of Virginia Center for Applied Biomechanics
U.S.A.

Paper Number 23-0198

ABSTRACT

For car occupants in Europe, a car-to-HGV (heavy goods vehicle) crash is the third most frequent fatal crash type after single and car-to-car crashes. Within car-to-HGV fatal crashes, frontal head-on crashes are most common. These crashes can result in larger structural deformation of the car or higher velocity changes and accelerations than single or car-to-car crashes typically do.

Structural compatibility and energy absorbing structures are prerequisites for good crashworthiness, so also for severe head on car-to-HGV crashes. If the car compartment can be kept intact there is a potential to improve the current state-of-the-art frontal restraint systems to provide the occupant with good protection also in high-severity car-to-HGV crashes.

The goal of this study was to identify potential limitations in a state-of-the-art frontal restraint system in high-severity car-to-HGV head-on crashes with an intact compartment and propose improvements to the restraint system to reduce and balance the risk of injury for all body regions.

Finite element simulations were performed using a frontal sled interior model with a geometry representing a mid-size sedan. The frontal sled model was equipped with the semi-rigid seat, a generic seat consisting of spring-loaded seat and submarining pans, developed to represent the characteristics of a front seat, and a seat integrated belt system consisting of a shoulder belt retractor with a 4 kN load limiter and a 2 kN pretensioner, and a 2 kN lap belt pretensioner. Further, the model was equipped with a driver airbag, a steering wheel, a collapsible steering column, a knee bolster, and a foot support. The model was validated by means of mechanical sled tests using generic 40 and 56 km/h full frontal rigid barrier crash pulses and THOR-50M v1.9. After validation the performance of the restraint system was evaluated with the THOR-50M by implementing crash pulses from two car-to-HGV head-on crashes.

For both car-to-HGV crash pulses there were severe strikethroughs of the restraint system. Improved seat stiffness, increased shoulder belt load limiter force, and increased knee bolster energy absorption prevented the strikethroughs and reduced the injury criteria values. However, the injury criteria values were still higher than current NCAP performance limits for most of the body regions. To guide the development of adaptive occupant protection tailored for high severity crashes, injury criteria targets are required. Such targets should be balanced between feasibility and still challenging enough to prompt improvements relative to the current state of risks.

Occupant protection in different crash severities is of high priority. The occupant protection system should be designed to be adaptive to the crash, i.e. more compliant in low-severity crashes and stiffer in high-severity crashes. Current occupant restraint systems are most likely capable of the proposed improvements with existing technologies. However, they are currently not designed with the level of adaptivity that this study indicates may be beneficial. More research is needed to develop injury criteria target values for survival in high severity crashes, as well as sensors that distinguish between low-, mid- and high-severity crashes with the purpose to adapt the restraint system thereafter.

INTRODUCTION

In 2019, about 22,700 road traffic related fatalities occurred in the European Union (EU) and more than 1.2 million people were injured [1]. Car occupants represent approximately 44% (10,090) of the fatalities in the EU [2]. Car drivers represent 71% of fatally injured car occupants, where of 82% were males and 18% were females [2]. Moreover, car occupant fatalities in car-to-HGV crashes have a larger proportion of occupants in the age group of 25 to 64 year-olds (65%) [3] compared to all car fatalities (58%) [4].

Although heavy good vehicles (HGVs) were only involved in 4.5% of all crashes, HGVs were involved in approximately 14% of all road fatalities in the EU in 2019 [3-4]. A car-to-HGV crash was the third most frequent fatal crash mode for car occupants in the EU (1557 fatalities), after single car crashes (4400 fatalities), and car-to-car crashes (3067 fatalities) [5]. The consequence of a car-to-HGV crash is often serious for the car occupants due to the incompatibility in mass and vehicle structure stiffness and geometry [6-11]. Most of the fatal crashes involving HGVs occurred on rural roads (53%), followed by highways (24%) and urban roads 23% [4]. The largest proportion of these crashes occurred on road stretches (82%) and only few occurred at intersections (9%) or other places [4]. The most frequent fatal car-to-HGV crash in the EU is a head-on crash on a rural road stretch [12-13].

Car crash pulses are a prerequisite when investigating the risk of injury for car occupants using finite element (FE) simulations. The German In-Depth Accident Study (GIDAS) data was analysed to describe car-to-HGV head-on crashes at a level of detail that enable setting up vehicle-to-vehicle FE simulation to generate crash pulses for the car [13]. Car-to-HGV crash configuration distributions were statistically described using relevant kinematic parameters from GIDAS (collision velocities of car and HGV, relative velocities, impact angles, hit points, vehicle weights). Using this data set as starting point, car crash pulses from car-to-HGV head on crashes were created by FE simulations of a 1.7-ton car and a 7.9-ton HGV including a frontal underride protection device (FUPD) [14]. 12 different crash configurations were simulated by varying the impact velocities of the two vehicles (car velocity 39 km/h and HGV velocity 36 km/h, and car velocity 56 km/h and HGV velocity 53 km/h), the impact overlaps (50% and 80%) and the impact angle (0°, 30° and -30°). Peak acceleration and delta velocity from the left sill, the compartment structural integrity, and pulse duration were analysed to identify relevant car crash pulses to be used for car occupant protection simulations. Structural integrity was evaluated because it remains a prerequisite for the occupant restraint system to be effective; if there is major A-pillar collapse the occupant protection system will be of less importance for the crash outcome. Two crash configurations out of the 12 were recommended for car occupant protection simulations:

1. 56/53 (Car/HGV) km/h, 50% overlap in 30° angle. This crash configuration was selected because it had a relatively long duration when compared to a standard 56 km/h full front rigid barrier test. Such crash pulse characteristics are challenging for a state-of-the-art restraint system in terms of for example the stand-up time for the driver airbag. This crash pulse is referred to as the *long duration crash pulse*. This pulse has a peak acceleration of 66g and a delta velocity of 105 km/h.
2. 56/53 (Car/HGV) km/h, 80% overlap in 0° angle. This crash configuration was selected because it had a relatively high acceleration level when compared to a standard 56 km/h full front rigid barrier test. Such crash pulse characteristics are challenging for a state-of-the-art restraint system in terms of for example strikethrough of the driver airbag because the high acceleration will lead to a higher change in velocity to the interior. This crash pulse is referred to as the *high acceleration crash pulse*. This pulse has a peak acceleration of 91g and a delta velocity of 97 km/h.

Occupant protection in high-severity collisions is not a new concept. In an investigation of 80 km/h full frontal rigid barrier (FFRB) crashes, it was concluded that “with proper design of an adaptive restraint system efficient occupant protection can be achieved at both high and very high impact velocities” [15].

The aim of this study was to identify potential occupant protection limitations in a state-of-the-art frontal restraint system in high-severity car-to-HGV head-on crashes with an intact compartment, defined by [14], and propose potential improvements to the restraint system to reduce and balance the risk of injury to equal level for all body regions [16].

METHODS

The methodology chapter is divided into four sub-sections describing the different steps in the investigation. First, we describe the frontal sled FE model incorporating a state-of-the-art frontal driver restraint system. Second, we describe the validation of the frontal sled model by means of mechanical sled tests using generic crash pulses representing full frontal rigid barrier (FFRB) tests in 40 km/h and 56 km/h. Third, we describe the implementation of two car-to-HGV head-on crash pulses from [14] and its effect to the system model and identify limitations in the state-of-the-art frontal restraint system in terms of occupant protection. Fourth, we describe potential improvements of the state-of-the-art frontal driver restraint system with the aim to reduce the risk of injury in car-to-HGV head-on crashes referencing target injury criteria values for high severity crashes identified in a parallel investigation [16].

Description of the frontal sled FE model

A frontal sled FE model including a state-of-the-art driver restraint system was developed using LS-Dyna, R9.3.1 r140922, LSTC. The frontal sled model includes: generic floor geometry and foot support; semi-rigid seat [17]; seat-back to support the occupant; generic knee bolster (Ethafaom 220 mounted to a rigid plate); seat integrated belt geometry (belt-in-seat) with a rigid attached belt guide in the seatback, a shoulder belt retractor with a 2 kN pretensioner and a 4 kN load limiter, a wire buckle, a crash-locking tongue, and a 2 kN lap belt pretensioner; generic stroking steering column at a force limit of 5.5 kN and a stroke of 85 mm; and a steering wheel with a generic driver airbag module including a cushion with coated fabric, vent holes and an inflator.

The driver was represented by the THOR-50M (Test device for Human Occupant Restraint 50th percentile adult male dummy) based on the occupant characteristics in terms of sex and age observed in the field data investigations of fatal car-to-HGV crashes [2-4]. The THOR-50M v1.9 Euro NCAP version from Humanetics Inc was positioned with the H-point 4 mm behind and 29 mm up from the seat reference points (*Figure 1*).

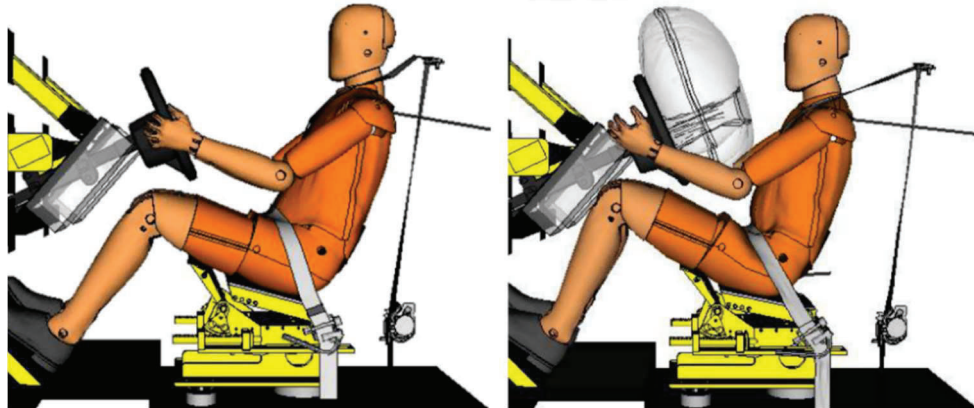


Figure 1. THOR-50M in the frontal sled FE model with a seat integrated belt system at two different time steps. Left: Figure plotted at 0 ms. Right: Figure plotted at 40 ms with the generic 56 km/h FFRB crash pulse applied. Note: for visibility reason the seat back is removed in these to figures.

Validation of the frontal sled FE model

The frontal sled model was validated by means of mechanical sled tests, see *Figure 2*. For the validation, repeated tests were conducted using two different generic crash pulses representing a 40 km/h and a 56 km/h FFRB crash [18], in total four sled tests. The model correlated well with the tests; validation results are described in the appendix.

Simulation of 56 km/h FFRB and car-to-HGV head-on crash pulses

The two car-to-HGV crash pulses recommended in [14] were implemented in the validated frontal sled model, *Figure 3*. To simplify the simulation only the x-component of the car crash pulses from [14] were used. Simulations with the state-of-the-art restraint system with the THOR-50M as driver were then conducted. The THOR-50M response in the two high-severity car-to-HGV crash pulses were compared to the generic 56 km/h FFRB crash pulse and used to identify potential limitations in the state-of-the-art restraint system.

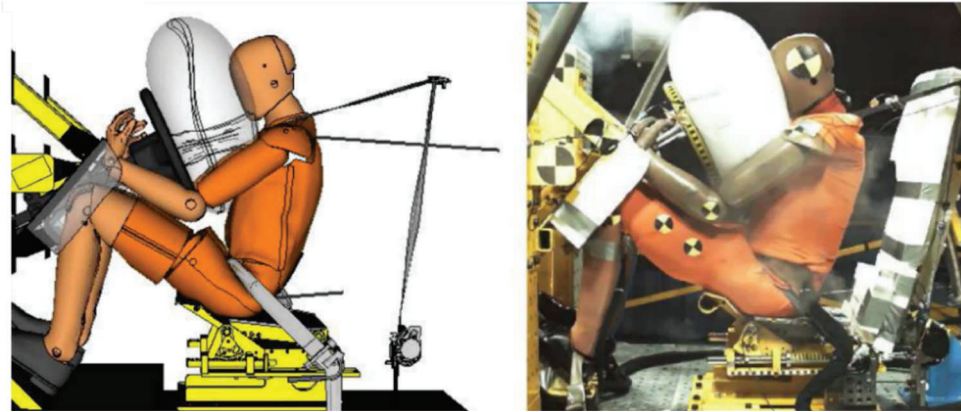


Figure 2. Virtual and physical version of the frontal sled with the seat integrated belt in the 56 km/h FFRB crash pulse. Left: Frontal sled FE model plotted at 60 ms. Right: Sled test plotted at 60 ms.

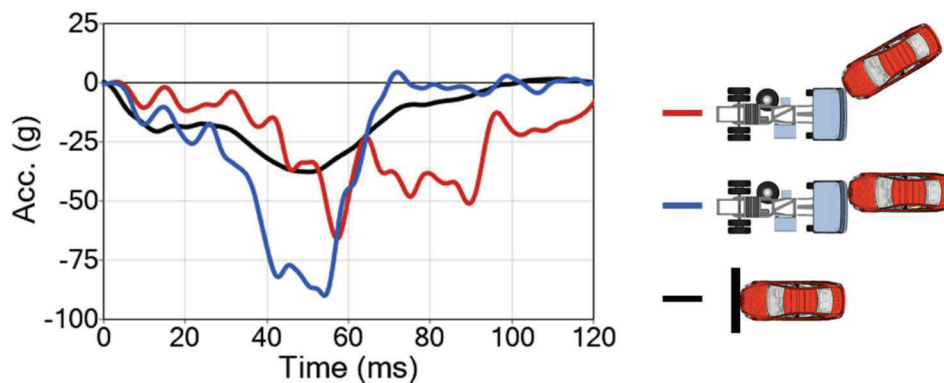


Figure 3. Crash pulses used in the simulation study. Generic 56 km/h FFRB crash pulse in black [18]. High acceleration crash pulse, peak acceleration of 91g and a delta velocity of 97 km/h in blue [14]. Long duration crash pulse, peak acceleration of 66g and a delta velocity of 105 km/h in red [14].

Target criteria and improvements of state-of-the-art restraint system

Target criteria addressing both occupant kinematics and risk of injury were identified. For occupant kinematics three criteria were identified:

1. No head-to-steering wheel strikethrough, i.e., avoid hard contact between the head and the steering wheel.
2. No knee-to-knee bolster strikethrough, i.e., avoid hard contact between knee and underlying structure.
3. No pelvis-to-seat pan strikethrough, i.e., avoid hard contact between pelvis and underlying structure.

Target injury criteria values for THOR-50M associated with a 40% risk of injury for all body regions [19] were identified and proposed in a parallel investigation [16] and are presented in *Table 1*.

Guided by these target criteria, improvements were made to the state-of-the-art restraint system with the purpose to improve the occupant protection of THOR-50M when exposed for the car-to-HGV crash pulses. The target with the improvements was to keep the design of the state-of-the-art restraint system, e.g., not adding any unconventional restraint components such as an extra belt [20], but to add a second functionality level to balance the higher energy from the car-to-HGV crash pulse. Adding such functionality to the occupant restraint system based on the crash severity level makes the occupant restraint system adaptable. This can be exemplified by implementing a higher load limiting force in the shoulder belt. However, improvements might be best fulfilled by adding an already state-of-the-art component, e.g., a knee airbag and/or a seat pan mounted airbag, also called pelvis restraint cushion [21-22].

Table 1.
THOR-50M target injury criteria values proposed for high severity car crashes, balanced for equal risk of injury for all body regions [16].

Criteria	Unit	Risk	Value
HIC15 (AIS3+)		40%	1430
BrIC (AIS3+)		40%	0.89
Nij (AIS3+)	mm	40%	1.04
Chest deflection (3+ fracture 40 years)	mm	40%	46.5
Chest deflection (6+ fracture 40 years)	mm	40%	56.5
Acetabulum resultant force (AIS2+), 15° Femur flexion	N	40%	3180
Acetabulum resultant force (AIS2+), 0° Femur flexion	N	40%	3910
Femur compression force (AIS2+)	N	40%	9800
Upper Tibia axial force (AIS2+)	kN	40%	6.5
Lower Tibia axial force (AIS2+)	kN	40%	7.15
Tibia bending moment (AIS2+)	Nm	40%	290
Revised Tibia index (AIS2+)		40%	1.13

Several simulation iterations were performed to identify how the state-of-the-art restraint system could be improved to fulfil the set targets. Avoiding strikethrough of the head, knees and pelvis were considered as the top initial priorities for tuning the restraint system, and the resulting THOR-50M injury criteria values from that initial tuning were then compared to the values of *Table 1* to identify potential areas for further refinement.

RESULTS

Simulation results from 56 km/h FFRB crash pulse with the state-of-the-art restraint system

The state-of-the-art restraint system performed well in the generic 56 km/h FFRB crash pulse, seen in a controlled kinematic of the THOR-50M, e.g. >50 mm remaining distance between the head and the steering wheel, and predicted overall low risk of injury, except for the chest and the acetabulum *Table 2*. However, if the risk function for 0-degree femur flexion [19] is applied as proposed by [16] the risk of acetabulum fracture is reduced from 71% to 37%. Corresponding seatbelt characteristic, driver airbag pressure, and steering column force and stroke are presented in *Figure 4* and *Figure 5*. The driver airbag pressure reached almost 50 kPa, the lap belt forces reached approximately 8 kN and the steering column reached its end position at approximately 90 ms with a force of approximately 8 kN.

Simulation results from car-to-HGV crash pulses with the state-of-the-art restraint system

Both car-to-HGV head-on crash pulses were challenging for the state-of-the-art restraint system, reaching its limit in terms of controlled kinematics (head-to-steering wheel strikethrough). The *high acceleration crash pulse* was the worst crash pulse among the two car-to-HGV crash pulses as it resulted in an earlier strikethrough of the driver airbag (head-to-steering wheel strikethrough), high pelvis acceleration (pelvis-to-seat pan strikethrough), and high femur compression forces (knee-to-knee bolster strikethrough), see *Figure 6* and *Figure 7*.

A visualisation of the initial THOR-50M position, at maximum pelvis forward displacement (knee-to-knee bolster strikethrough and pelvis-to-seat pan strikethrough), and at maximum chest forward displacement (head-to-steering wheel contact) for the simulation with the *high acceleration crash pulse* is presented in *Figure 8*.

Again, corresponding seatbelt characteristics, driver airbag pressure, and steering column force and stroke for the state-of-the-art restraint system are presented in *Figure 4* and *Figure 5*. For the *high acceleration crash pulse*, the driver airbag pressure reached above 80 kPa, the lap belt forces reached above 12 kN and the steering column reached its end position at approximately 70 ms at a force of above 20 kN.

In terms of injury criteria values the *high acceleration crash pulse* was the more challenging crash pulse, seen in risk of injury between 38% and 100% compared to 1% to 94% for the long duration crash pulse, *Table 2*. Therefore, the improvements of the state-of-the-art restraint system were explored with focus on the *high acceleration crash pulse* and then checked with the *long duration crash pulse*.

Table 2.

Injury criteria values and the risk of injury calculated according to the proposed risk functions in [16] from simulations of the state-of-the-art restraint system with the generic 56 km/h FFRB crash pulse and the two car-to-HGV head-on crash pulses.

Crash pulse	Unit	56 km/h FFRB		Car-to-HGV long duration crash pulse		Car-to-HGV high acceleration crash pulse	
		Value	Risk	Value	Risk	Value	Risk
HIC15 (AIS3+)		365	2%	536	6%	2162	62%
BrIC (AIS3+)		0.55	1%	0.58	2%	1.15	74%
Nij (AIS3+)		0.32	1%	0.50	4%	1.42	84%
Chest deflection (3+ fracture 40 years)	mm	40.4	29%	45.7	39%	56.8	61%
Chest deflection (6+ fractures 40 years)	mm	40.4	17%	45.7	24%	56.8	41%
Acetabulum resultant force (AIS2+), 15°	N	3851	71%	4848	94%	20813	100%
Acetabulum resultant force (AIS2+), 0°	N	3851	37%	4848	75%	20813	100%
Femur compression (AIS2+)	N	2683	0%	4887	1%	34697	100%
Upper Tibia axial force (AIS2+)	kN	1.6	1%	2.6	3%	11.0	96%
Lower Tibia axial force (AIS2+)	kN	1.8	5%	2.9	8%	6.9	38%
Tibia bending moment (AIS2+)	Nm	103.9	2%	186.3	11%	1144.6	100%
Revised Tibia index (AIS2+)		0.53	5%	0.92	24%	5.68	100%

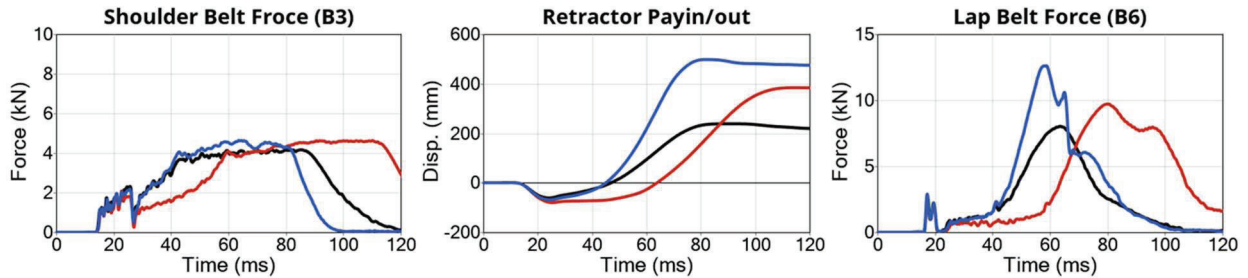


Figure 4. Left: Upper shoulder belt force. Middle: Retractor belt pay-out. Right: Outer lap belt force. 56 km/h FFRB crash pulse in black, high acceleration crash pulse in blue and long duration crash pulse in red.

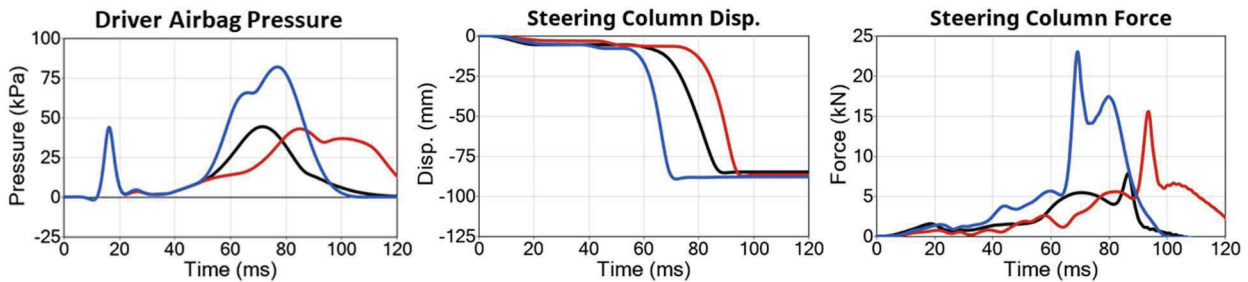


Figure 5. Left: Driver airbag pressure. Middle: Steering column displacement. Right: Steering column force. 56 km/h FFRB crash pulse in black, high acceleration crash pulse in blue and long duration crash pulse in red.

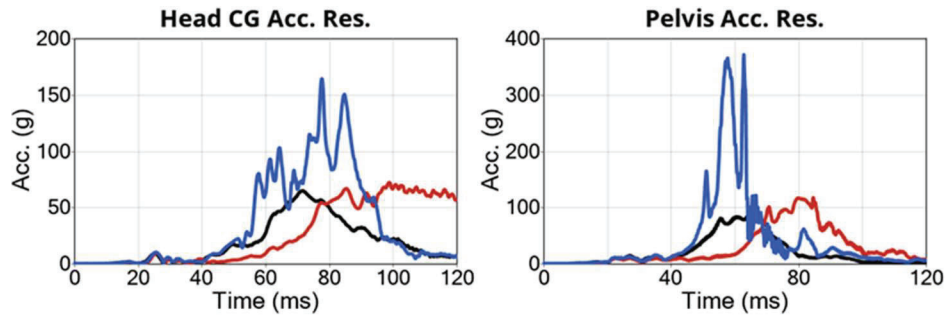


Figure 6. Left: Head resultant acceleration. Right: Pelvis resultant accelerations. 56 km/h FFRB crash pulse in black, high acceleration crash pulse in blue and long duration crash pulse in red.

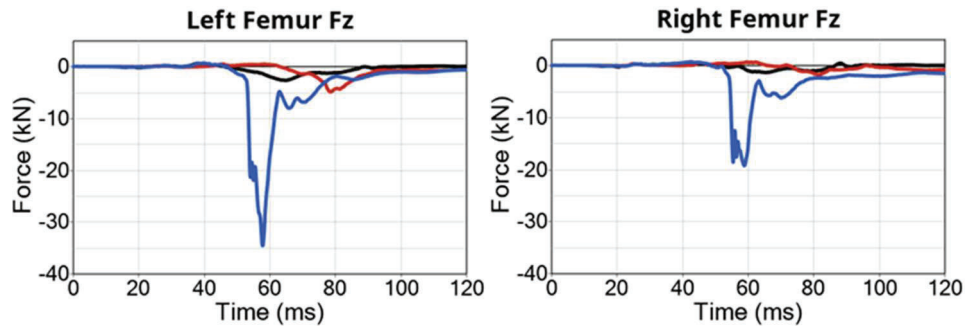


Figure 7. Left: Left femur compression force. Right: Right femur compression forces. 56 km/h FFRB crash pulse in black, high acceleration crash pulse in blue and long duration crash pulse in red.

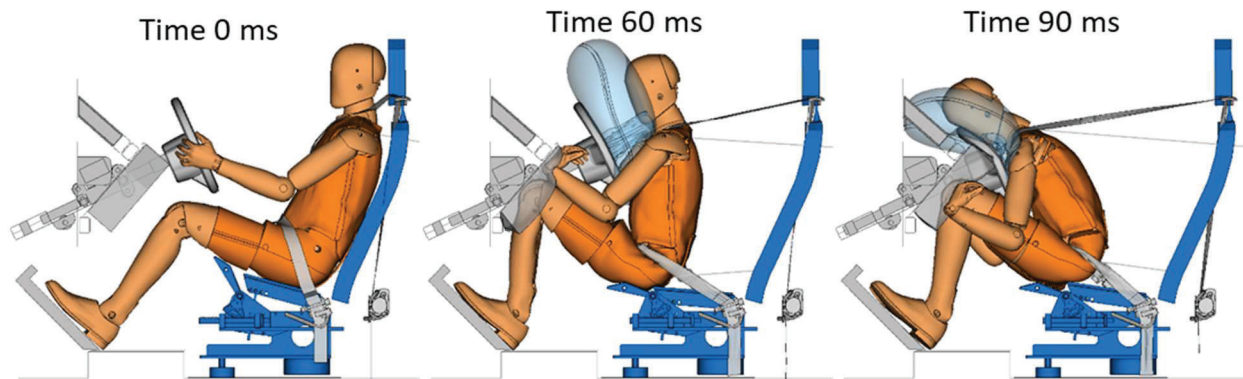


Figure 8. THOR-50M in the high acceleration crash pulse. Left: Initial position. Middle: Position at maximum pelvis displacement (knee-to-knee bolster strikethrough and pelvis-to-seat pan strikethrough). Right: Position at maximum chest forward displacement (head-to-steering wheel strikethrough).

Simulation results from car-to-HGV crash pulses with the improved restraint system

With the target to avoid strikethrough of any body part, an improved restraint system was designed in several simulation iterations.

The strikethrough of the pelvis-to-seat pan was addressed by stiffening the seat pan springs until the pelvis strikethrough was avoided.

The strikethrough of the knee-to-knee bolster was addressed by splitting the knee bolster into left and right parts, placing these close to the knees to take load early, and adding load limiters to avoid hard contact to the rigid plate, see

Figure 9. The knee bolster load limiter stroke was 80 mm on the left side and 65 mm on the right side in the *high acceleration crash pulse*.

The strikethrough of the head-to-steering wheel was avoided by increasing the shoulder belt force, from 4 kN to 8 kN, in combination with adding additional 25 mm steering column stroke.

A visualisation of the effect of the improved restraint system to THOR-50M kinematic in the *high acceleration crash pulse* is presented in Figure 10. Similar to Figure 8, the three figures are at initial position, maximum pelvis displacement, and maximum chest forward displacement. Head-to-steering wheel strikethrough was avoided with a remaining distance of 27 mm and 52 mm for the *high acceleration crash pulse* and the *long duration crash pulses*, respectively. Seatbelt characteristic, driver airbag pressure, steering column characteristic, and strikethrough related measurements (head resultant acceleration, pelvis resultant acceleration and femur forces) of the improved restraint system compared to the state-of-the-art restraint system for the *high acceleration crash pulse* are presented in Figure 11 to Figure 14.

For the improved restraint system, the driver airbag pressure was reduced from above 80 kPa to below 60 kPa (Figure 12) and the lap belt force was reduced from approximately 12.5 kN to approximately 8 kN (Figure 11).

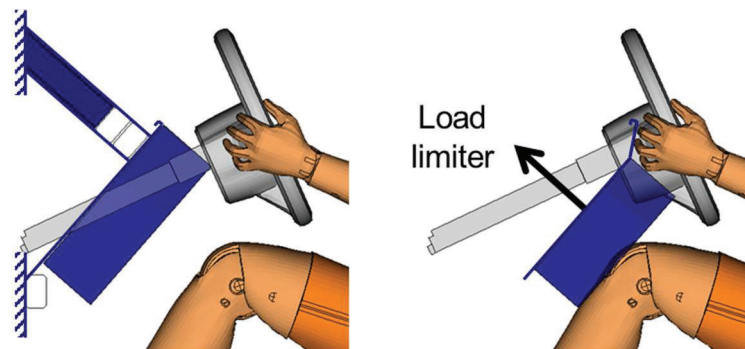


Figure 9. Left: Knee bolster position in the state-of-the-art restraint system. Right: Knee bolster moved close to the knees in combination with adding load limiters.

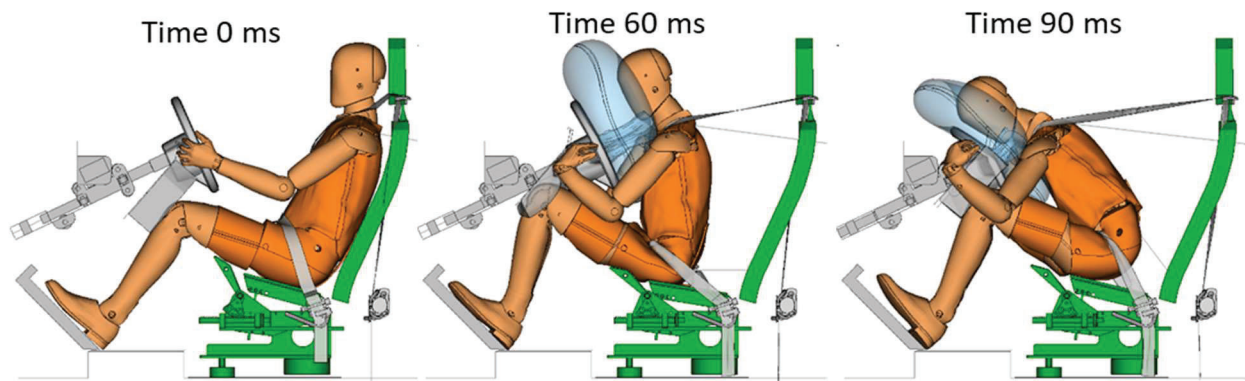


Figure 10. THOR-50M in the high acceleration crash pulse. Left: Initial position. Middle: Position at maximum pelvis displacement. Right: Position at maximum chest forward displacement with remaining 27 mm to head-to-steering wheel strikethrough.

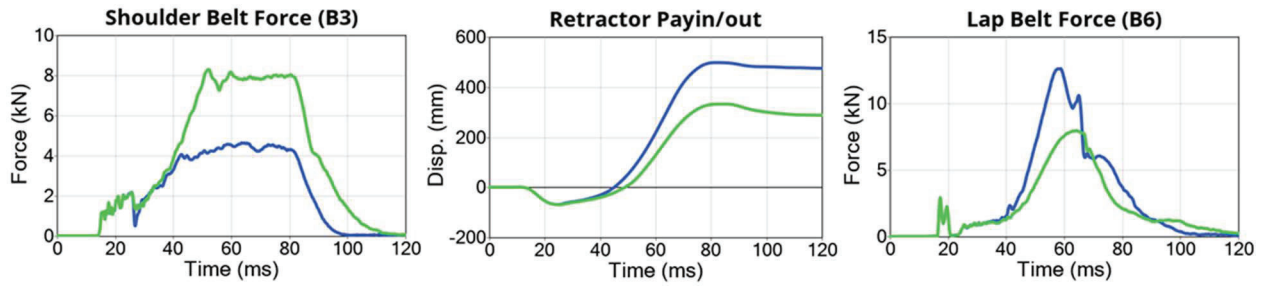


Figure 11. Left: Upper shoulder belt force. Middle: Retractor belt pay-out. Right: Outer lap belt force. High acceleration crash pulse, state-of-the-art restraint system in blue and improved restraint system in green.

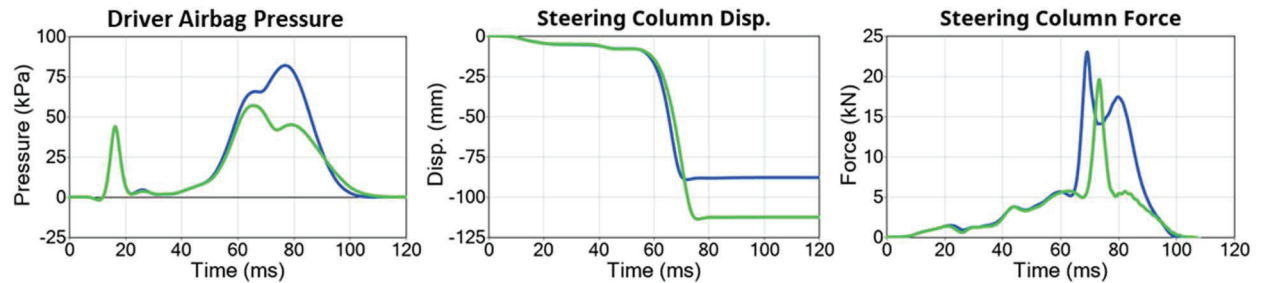


Figure 12. Left: Driver airbag pressure. Middle: Steering column displacement. Right: Steering column force. High acceleration crash pulse, state-of-the-art restraint system in blue and improved restraint system in green.

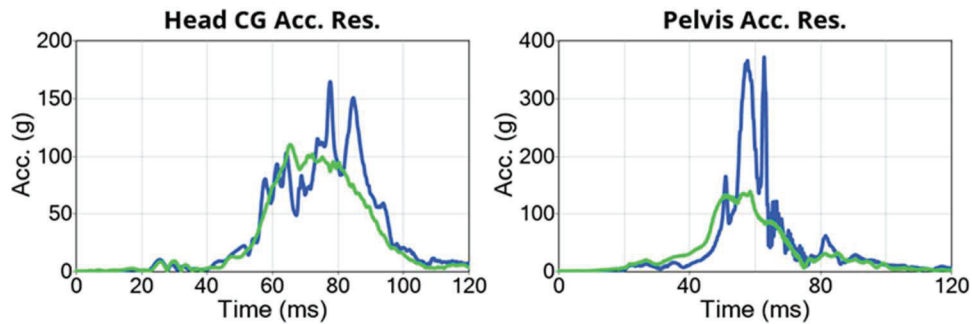


Figure 13. Left: Head resultant acceleration. Right: Pelvis resultant accelerations. High acceleration crash pulse, state-of-the-art restraint system in blue and improved restraint system in green.

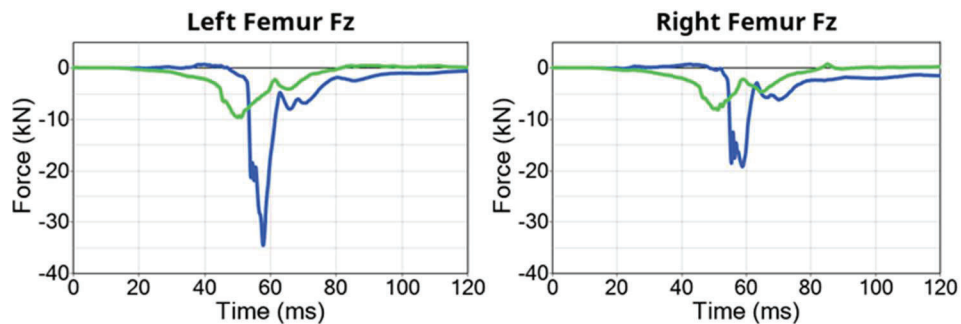


Figure 14. Left: Left femur compression force. Right: Right femur compression forces. High acceleration crash pulse, state-of-the-art restraint system in blue and improved restraint system in green.

The improved restraint system met the top initial priorities i.e., avoiding strikethrough for all body regions. The resulting injury criteria values are found in *Table 3*. Overall, the injury criteria values were reduced with the improved system, though some measures remained above the target 40% risk level.

Table 3.
Injury criteria values and the risk of injury calculated according to the proposed risk functions in [16] from simulations of the improved restraint system with the two car-to-HGV head-on crash pulses.

Crash pulse	Unit	Car-to-HGV long duration crash pulse		Car-to-HGV high acceleration crash pulse	
		Value	Risk	Value	Risk
HIC15 (AIS3+)		742	13%	1382	38%
BrIC (AIS3+)		0.63	5%	0.85	33%
Nij (AIS3+)		0.55	5%	0.98	33%
Chest deflection (3+ fracture 40 years)	mm	43.6	35%	56.4	60%
Chest deflection (6+ fractures 40 years)	mm	43.6	21%	56.4	40%
Acetabulum resultant force (AIS2+), 15°	N	3891	73%	5667	99%
Acetabulum resultant force (AIS2+), 0°	N	3891	39%	5667	91%
Femur compression (AIS2+)	N	7124	10%	9742	39%
Upper Tibia axial force (AIS2+)	kN	2.5	2%	3.3	5%
Lower Tibia axial force (AIS2+)	kN	2.7	8%	3.4	10%
Tibia bending moment (AIS2+)	Nm	168.2	8%	234.1	22%
Revised Tibia Index (AIS2+)		0.90	22%	1.23	49%

DISCUSSION

Occupant protection for different crash severities is of high priority. Occupant protection systems should be designed to be adaptative to the crash, i.e., more compliant in low-severity crashes and stiffer in high-severity crashes. Most car crashes occur at a relative low delta velocity [23-24]. While the per-crash risk is relatively low, the high exposure to low-severity crashes leads to most injuries occurring in crashes of relatively low delta velocity [16, 24]. However, this does not contradict that most fatal car crashes occur at relative high crash severity, such as car-to-HGV crashes or car-to-car crashes with high delta velocity. Using FE simulations, we investigated the effect from high severity head-on car-to-HGV crash pulses to the occupant protection with a state-of-the-art restraint system. We identified three critical limitations: head-to-steering wheel strikethrough, knee-to-knee bolster strikethrough and pelvis-to-seat pan strikethrough, all resulting in high risk of injury when evaluated with THOR-50M.

With a more efficient knee bolster that engages the femur early in the crash and is load limited at approximately 10 kN (40% risk of an AIS2+ injury [16]), the kinetic energy of the occupant was effectively managed, and knee-to-knee bolster strikethrough was avoided. This resulted in a high predicted risk of acetabulum fracture, but as stated in [16] the injury risk function for acetabulum as described in [19] might overestimate the risk of acetabulum fractures as such injuries seems to be less frequent than femur fractures in the field [16]. The knee bolster with foam and a load limiting function used in this study can potentially be replicated by a knee airbag by adapting the geometry and pressure to similar shape and stiffness levels.

The seat pan stiffness of the semi-rigid seat was increased to avoid pelvis-to-seat strikethrough. The increased stiffness was implemented because the semi-rigid seat reached its limit in terms of seat pan displacement after approximately 40 mm deflection. The semi-rigid seat was designed to replicate the stiffness of a production seat, but not evaluated in high severity crashes [25]. A stiffer seat than current production seats can potentially be achieved by implementing an inflatable seat pan airbag, also called pelvis restraint cushion [21-22].

The shoulder belt load limiter level was increased from 4 kN to 8 kN. In combination with a somewhat longer steering column stroke, the head-to-steering wheel strikethrough was avoided. In terms of accelerations, forces, and moments the simulation outcomes seem useful, but it seems unlikely that an 8 kN shoulder belt force in combination with the

high acceleration crash pulse would result in less than 20 mm increase of the chest deflection for a human, (40.4 mm chest deflection for the state-of-the-art restraint system in 56 km/h FFRB crash pulse and 56.4 mm chest deflection for the improved restraint system in *high acceleration crash pulse*). Therefore, caution should be taken when interpreting the risk of rib fractures (3+ and 6+) predicted in this study.

By implementing the proposed improvements to the state-of-the-art restraint system, it appears feasible to avoid strikethrough of any body part and thereby increase the occupant protection in high severity collisions. However, despite the improvements explored here, higher injury criteria values than normally seen in NCAP testing were still observed for all body regions. In a parallel study a 40% risk of injury for all body region was proposed for high-severity collision evaluations [16]. Targeting equal risk for all body regions make it possible to rebalance the occupant restraint system compared to current NCAP performance limits, where the risk differs per body region. In addition to the improvements identified here, further reduction of the risk of head injury could potentially be achieved by introducing a dual depth driver airbag [15].

Occupant protection systems are most likely capable of these improvements with existing technologies, although they are currently not designed with the level of adaptivity that this study indicates may be beneficial. Moreover, to activate such adaptive restraint systems correctly would require a sensor system that can identify the crash severity level accurately, either during the first milliseconds of the crash or, ideally, just prior to the crash (e.g., using data streams on the closing velocity combined with sensing classification of the impending collision partner). This could potentially be done by incorporating already present pre-crash sensor data from camera, LIDAR, and RADAR sensors. Today, these are mainly used to avoid crashes and to activate pre-crash functions such as electrical pretensioners of the seat belts [26].

The improved frontal restraint system was shown to be effective in reducing risk of injury in a head-on car-to-HGV crashes with the THOR-50M. However, for the restraint system to work as intended an intact vehicle structure is required. Improvements to the vehicle fleet to increase the compatibility in this type of crashes are fundamental. Incompatibility in terms of geometry and stiffness between cars and HGV often result in that the car underrun the HGV structure [6-11]. The EU project *Improvement of Vehicle Crash Compatibility through the Development of Crash Test Procedures* (VC-COMPAT) [9] identified head-on car-to-HGV crashes as the worst car-to-HGV collision type in terms of the car underrunning the HGV structure. To reduce the risk of the car underrunning the HGV structure, frontal underrun protection devices (FUPD) are obligatory in the EU since August 10, 2003 [27]. However, it is indicated that the structural interaction between cars and HGVs in some cases remain poor, despite the presence of a FUPD [10-11]. To further improve the compatibility in head-on crashes between cars and HGVs, and thereby reduce the risk of injury, it was proposed to fit an energy-absorbing structure to the FUPD [6, 9-10]. Such devices would not only reduce the risk of underrun but also reduce the high acceleration of the car, making head-on car-to-HGV more survivable [6, 9-10]. In crash tests with 75 km/h relative velocity and 75% overlap, it was concluded that equipping the HGV with an energy-absorbing front structure with a force level of 200 kN and 360 mm deformation zone, 30% of the fatal crashes could be avoided, compared to 20% with a 100% rigid FUPD [6]. It appeared that an energy absorbing FUPD may change the severity of a 75 km/h 75% overlap frontal car-to-HGV crash into the severity of a 56 km/h crash [6]. The weights and dimensions directive for HGV, EC 2015/719 was revised to allow additional length of HGVs if the extra length incorporates an energy absorption structure [28] which open up for improved compatibility and energy absorption.

Limitations

This investigation includes several limitations. The frontal sled model was validated to existing sled tests in 40 km/h and 56 km/h FFRB. To expand its usage to a high severity crash pulse reaching 80g is to use the model outside its validation range. In addition to this, all simulations were conducted with a sled-type set-up meaning that no compartment intrusions were included, instead the compartment was rigid. This means, that the risk of strikethroughs might have been underpredicted although the risk of injuries due to strikethroughs was overpredicted. Therefore, focus should be on kinematic criteria rather than on THOR injury criteria values. Strikethrough of a restraint system indicates that the system has reached its limits.

Further work

While first-order gains may be made by adapting restraint systems to crash severity, further refinement will likely require adapting also to occupant characteristics such as stature, mass, and body shape, seat position, and seating posture. Only then will the occupant protection system be truly adaptive. Therefore, we encourage the use of human body models that could be morphed to represent the diversity of the human population and be seated in any seat

position. However, further refinements of human body models are necessary to accurately represent kinematics and to predict injuries in different seating postures as well as in high severity crashes.

CONCLUSIONS

Several limitations in the state-of-the-art restraint system were identified both in terms of occupant kinematic criteria (strikerthroughs) and high risk of injury for several body regions. Potential improves was proposed to the knee bolster, seat, seat belt and steering column; all these judged feasible with existing technologies. The improved restraint system met the top initial priorities i.e., avoiding strikerthrough for all body regions. Overall, the injury criteria values were reduced with the improved system though some injury criteria values remained above the target 40% risk level.

ACKNOWLEDGEMENTS

The authors want to thank Per-Erik Johansson, Mikael Videby, Sonny Muhoray and Mikael Lindberg all at Autoliv Safety Center in Sweden for executing the sled tests and for their patience when changes were made at the last minute. We would also like to thank Linus Larsson, Nicklas Brunnegård and Stefan Knutsson all at Autoliv Sweden for expertise support in designing the prototype used in the sled tests.

The work was partly carried out as part of the EU project SAFE-UP which has received funding from the European Union's Horizon 2020 research and innovation programme under Grant Agreement 861570.

REFERENCES

- [1] European Commission. 2021. Road safety thematic report – Fatigue. European Road Safety Observatory. Brussels, European Commission, Directorate General for Transport. https://road-safety.transport.ec.europa.eu/statistics-and-analysis/statistics-and-analysis-archive/annual-accident-report-archive_en. Accessed 24.10.2022.
- [2] European Commission. 2021. Facts and Figures Car occupants. European Road Safety Observatory. Brussels, European Commission, Directorate General for Transport. <https://road-safety.transport.ec.europa.eu/system/files/2021-12/F%26F%20Car%20occupants%2020210707.pdf>. Accessed 24.10.2022.
- [3] Schindler R, Jänsch M, Bálint A, Johannsen H. 2022. Exploring European Heavy Goods Vehicle Crashes Using a Three-Level Analysis of Crash Data. *Int J Environ Res Public Health*. 2022 Jan 7;19(2):663. doi: 10.3390/ijerph19020663. PMID: 35055484; PMCID: PMC8775486.
- [4] European Commission. 2020. European Road Safety Observatory Facts and Figures Buses / coaches / heavy goods vehicles - 2020. Brussels, European Commission, Directorate General for Transport. https://road-safety.transport.ec.europa.eu/system/files/2021-07/facts_figures_buses_and_hgv_final_20210323.pdf. Accessed 24.10.2022.
- [5] European Commission, Mobility and Transport. 2021. Road traffic Fatalities in the EU in 2019. https://road-safety.transport.ec.europa.eu/system/files/2021-11/DG%20MOVE%20ROAD%20SAFETY_INFOGRAPHICS_twitter.pdf. Accessed 24.10.2022.
- [6] de Coo PJA., Blaauw GJ, Huijbers, JJW. 1997. EEVC working group 14 activities in energy-absorbing front underrun protection. SAE heavy vehicle underride protection TOPTEC, 15-16 April 1997, Palm Springs, CA, USA.
- [7] Adalian C, Russo J-L, Cesari D, Desfontaines H. 1998. Improvement of car-to-truck compatibility in head-on collisions. The 16th International Technical Conference on the Enhanced Safety of Vehicles (ESV) Proceedings - Windsor, Ontario, Canada, May 31- June 4, 1998. Paper Number 98-S4-O-12.
- [8] Forsman, L. 2002. Compatibility in truck to car frontal impacts. 7th International Symposium on Heavy Vehicle Weights & Dimensions Delft, The Netherlands, Europe, June 2002.

- [9] Edwards, M. J. et al. 2007. Improvement of Vehicle Crash Compatibility through the Development of Crash Test Procedures. VC-COMPAT Final Technical Report, Transport Research Laboratory, Crowthorne, UK.
- [10] Knight I. 2016. Energy Absorbing Front Underrun Protection for Trucks: Developing a test Procedure. DOI: 10.13140/RG.2.2.32120.75529. Project: Safer Aerodynamic Trucks Apollo Vehicle Safety. https://www.researchgate.net/profile/Iain-Knight/publication/325719308_Energy_Absorbing_Front_Underrun_Protection_for_Trucks_Developing_a_test_Procedure/links/5b1fe45c0f7e9b0e373eccbb/Energy-Absorbing-Front-Underrun-Protection-for-Trucks-Developing-a-test-Procedure.pdf Assessed 07.12.2022.
- [11] Thomson R, Fredriksson R, Mroz K, Kruse D, Törnvall F. 2023. Frontal Crash Incompatibility of Heavy Truck in Crash Test with Passenger Car. The 27th International Technical Conference on the Enhanced Safety of Vehicles Conference (ESV), Yokohama, Japan 2023. Paper Number 23-0321.
- [12] Kockum S. et al. 2017. Volvo Trucks Safety Report 2017. <https://www.volvogroup.com/content/dam/volvogroup/markets/master/about-us/traffic-safety/Safety-report-2017.pdf>. Accessed 24.10.2022.
- [13] Balint A, Labenski V, Schories L, Leyva PH, Östling M, Schmidt D, Schindler R, et al. 2021. Use Case Definitions and Initial Safety-critical Scenarios. Deliverable 2.6, EU Project SAFE-UP, Grand Agreement No. 861570, 2021. https://static1.squarespace.com/static/5efaed43294db25b18168717/t/627e752a8d7775630d2ea94a/1652454782434/SAFE-UP_D2_6_Use%2Bcase%2Bdefinitions%2Band%2Binitial%2Bsafety-critical%2Bscenarios_.pdf. Accessed 24.10.2022.
- [14] Mroz K, Östling M, Lubbe N. 2023. Passenger cars in head-on crashes with heavy goods vehicles: for what severity should future car restraint systems be designed? The 27th International Technical Conference on the Enhanced Safety of Vehicles Conference (ESV), Yokohama, Japan 2023. Paper Number 23-0060.
- [15] Pipkorn B, Mellander H, Håland Y. 2005. Car driver protection at frontal impacts up to 80 km/h (50 mph). The 19th International Technical Conference on the Enhanced Safety of Vehicles Conference (ESV), Washington D.C; 2005. Paper Number 05-0102.
- [16] Forman J, Östling M, Mroz K, Lubbe N. 2023. Potential Injury Criteria for Collisions with Heavy Goods Vehicles. The 27th International Technical Conference on the Enhanced Safety of Vehicles Conference (ESV), Yokohama, Japan 2023. Paper Number 23-0334.
- [17] Mroz K, Östling M, Richardson R, Kerrigan J, Forman J, Gepner B, Lubbe N, Pipkorn B. 2020. Effect of Seat and Seat Belt characteristics on the Lumbar Spine and Pelvis Loading of the SAFER Human Body Model in reclined Postures. Proceedings of the IRCOBI Conference, 2020, Munich, Germany.
- [18] Höschele P, Smit S, Tomasch E, Östling M, Mroz K, Klug C. 2021. Generic Crash Pulses Representing Future Accident Scenarios of Highly Automated Vehicles. SAE Int. J. Trans. Safety 10(2):2022, doi:10.4271/09-10-02-0010.
- [19] Craig M, Parent D, Lee E, Rudd R, Takhounts E, and Hasija V. 2020. Injury Criteria for the THOR 50th Male ATD. Available at: <https://lindseyresearch.com/wp-content/uploads/2021/10/NHTSA-2020-0032-0005-Injury-Criteria-for-the-THOR-50th-Male-ATD.pdf> Accessed 24.10.2022.
- [20] Östling M, Saito H, Vishwanatha A, Ding C, Pipkorn B, Sunnevång C. 2017. Potential Benefit of a 3+2 Criss Cross Seat Belt System in Frontal and Oblique Crashes. Proceedings of IRCOBI conference, 2017, Antwerp, Belgium.
- [21] Baudrit P, Potier P, Petit P, Trosseille X, Vallancien G. 2005. Cadaver and dummy investigation of injury risk with anti-sliding system in case of static deployment. The 19th International Technical Conference on the Enhanced Safety of Vehicles Conference (ESV), Washington DC, 2005. Paper Number 05-0084.

- [22] Shaw G, et al. 2018. Pelvic restraint cushion sled test evaluation of pelvic forward motion, *Traffic Injury Prevention*, 19:3, 250-255, DOI: 10.1080/15389588.2017.1326106.
- [23] Hu J, Flannagan C, Bao S, McCoy RW, Siasoco KM, Barbat S. 2015. Integration of Active and Passive Safety Technologies - A Method to Study and Estimate Field Capability. *Stapp Car Crash Journal; Ann Arbor* Vol. 59, (Nov 2015): 269-296.
- [24] Forman J, McMurry T. 2018. Nonlinear models of injury risk and implications in intervention targeting for thoracic injury mitigation, *Traffic Injury Prevention*, 19:sup2, S103-S108, DOI:10.1080/15389588.2018.1528356.
- [25] Uriot J, Potier P, Baudrit P, Trosseille X, Petit P, Richard O, Compigne S, Masuda M, Douard R. 2015. Reference PMHS Sled Tests to Assess Submarining. *Stapp Car Crash Journal*. Vol 59, 2015.
- [26] Fujita K, Fujinami H, Moriizumi K, Enomoto T, Kachu R, Kato H. 2003. Development of pre-crash safety system. The 18th International Technical Conference on the Enhanced Safety of Vehicles (ESV), Nagoya, Japan, May 19-22, 2003. Paper Number 544.
- [27] DIRECTIVE 2000/40/EC OF THE EUROPEAN PARLIAMENT AND OF THE COUNCIL. <https://eur-lex.europa.eu/LexUriServ/LexUriServ.do?uri=OJ:L:2000:203:0009:0028:EN:PDF> Accessed 07.12.2022.
- [28] DIRECTIVE (EU) 2015/719 OF THE EUROPEAN PARLIAMENT AND OF THE COUNCIL of 29 April 2015. <https://eur-lex.europa.eu/legal-content/EN/TXT/PDF/?uri=CELEX:32015L0719&from=LV> Accessed 07.12.2022.

APPENDIX A: VALIDATION OF THE FRONTAL SLED FE MODEL

Frontal sled FE model

The frontal sled FE model used in this study includes generic open versions of Autoliv's detailed global belt component models. The generic open retractor model does not contain details such as different retractor locking behaviour for different retractor types or influence of the initial amount of webbing inside the retractor on the load limiter force. Further, the generic open CLT model lock on predefined time, and the generic open webbing model is a mix of different webbings. Nevertheless, the generic open belt component models have been useful in collaborations when encrypted models have not been accepted.

As described in the Method, the frontal sled model is a generic driver belt-in-seat environment aimed for frontal crashes. This model was initially built up in two versions, belt-in-seat and B-pillar mounted D-loop installations, using Autoliv's detailed global belt component models for the retractor (version 4.1.1), the PLP (version 1.1.3), the crash-locking tongue (version 002), and the webbing with bending beams (version 1.1.6). The frontal sled model was validated to five repeated sled test setups with the THOR-50M. Later, Autoliv's detailed global belt component models were replaced by the generic open versions.

After the open belt component models replaced Autoliv's detailed global belt component models in the frontal sled model, no tuning was done to any part of the model. However, during the validation of the frontal sled model using Autoliv's detailed global belt models, minor tuning of the original models of the knee bolster, the driver airbag, the steering wheel, and the steering column were done to more accurately represent their physical counterparts and to increase run stability. No tuning was done to the Humanetics THOR-50M v1.9 Euro-NCAP version model, to the semi-rigid seat model [1], or to Autoliv's detailed global belt component models since all these already were thoroughly validated. The friction coefficient in the belt guide at the seat-back top was calculated using the belt load cell measurements from the physical sled tests. THOR-50M-to-seat friction coefficients were obtained from earlier studies [1], and THOR-50M friction coefficients for contacts to the driver airbag and the belt webbing were those generally used by Autoliv. All FE sub models were positioned to match the 3D-scans of the physical sled tests. All validation simulations were conducted in LS-Dyna, r9.3.1 R140922, LSTC.

In this appendix, the validation with the belt-in-seat frontal sled model using the open belt component models will be presented.

Conducted physical sled tests

Five repeated test set-ups were performed to validate the frontal sled models with Autoliv's detailed global belt component models, both for the belt-in-seat and for the B-pillar mounted D-loop installations. Here, for the validation of the belt-in-seat frontal sled model using the open belt component models, two of these five set-ups are relevant. The difference between these two is the crash pulse: generic FFRB crash pulses of 40 and 56 km/h, respectively, which has previously been used in several simulation investigations [2-4], *Figure A1*. The tests were performed in a hydraulic-type sled catapult manufactured by Mannesmann Rexroth with maximum acceleration of 50 g.

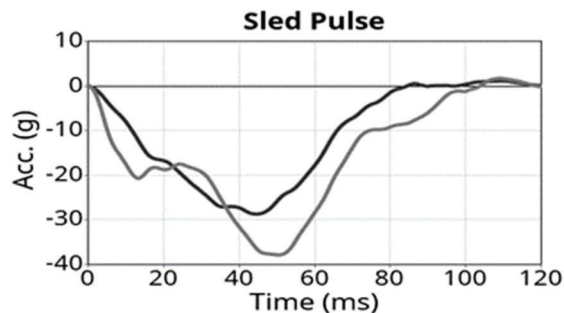


Figure A1. Crash pulses used in the sled tests. Black curve is the 40 km/h FFRB generic crash pulse and grey curve is the 56 km/h FFRB generic crash pulse.

The sled set-up represented a state-of-the-art driver restraint system of a mid-sized European car. The set-up includes generic floor geometry and foot support, semi-rigid seat [1], a seat-back to support the occupant, a generic knee bolster

(Ethafoam 220 mounted to a rigid plate), a belt system (belt-in-seat geometry with the belt guide attached to the rigid seat-back, shoulder belt retractor with a 2 kN pretensioner and a 4 kN load limiter, a wire buckle, a crash-locking tongue, and a 2 kN lap belt pretensioner), a generic stroking steering column (force limit of 5.5 kN and a stroke of 85 mm), and a steering wheel with a driver airbag module (coated fabric, vent holes and an dual stage inflator). The THOR-50M was used in all tests and positioned with the H-point 4 mm behind and 29 mm up from the seat reference points

The driver airbag was triggered 10 ms after T0 (crash pulse start). The shoulder belt retractor was triggered 10 ms after T0. The lap belt pretensioner was triggered 15 ms after T0.

Six on-board high-speed cameras recorded the tests at 1000 Hz. The cameras provided images of the left and right side overview, a top and a front view, and left and right side detailed view of the pelvis, its interaction with the seat and lap belt, the lap belt pretensioner, and the buckle and crash locking tongue, *Figure A2*.



Figure A2. Overview of the six high-speed camera film views.

Accelerometer sensors were mounted to the sled to measure the acceleration in the direction of the motion, accelerometer signals were filtered with CFC 60 (*Figure A1*). The shoulder belt retractor included a webbing pay-out sensor to measure webbing pull in and pay-out. Three uniaxial webbing load cells were placed on the seat belt webbing to measure belt forces: just outside the retractor (B1), at the upper shoulder belt between the THOR-50M shoulder and the belt guide (B3), and at the lap belt outboard side between the THOR-50M right hip and the lap belt pretensioner (B6). The webbing load cells signal were filtered with CFC 600. Moreover, the slip in tongues and lap belt pretensioner pay-ins were tracked from videos (*Figure A3* and *Figure A4*). Further the airbag pressure was measure with pressure sensors. Pressure signals were filtered with CFC 180. Load cell were mounted between the steering wheel and the steering column to measure the transferred force, these load cell signals were filtered with CFC 180. Four string-potentiometers were used to measure motions. One string-potentiometer was attached to the seat pan, 210 mm from its rotation axis measured in the seat pan plane, to measure seat pan displacement. A second string-potentiometer was attached to the THOR-50M pelvis to measure the forward displacement relative to the sled. A third string-potentiometer was attached to the rear part of the spine at T1 level to measure the chest forward displacement relative to the sled. The fourth string-potentiometer was attached to the steering wheel to measure the steering column stroke. String-potentiometers signals were filtered with CFC 60. All sensors used are listed with manufacturer and model name in *Table A1*. For all sensor signals see *Figure A3* - *Figure A6*.

Table A1
Sensor used in test set-up.

Sensor type	Manufacturer	Model
Webbing load cells	Messring	DK11-35-23
String potentiometers	Space Age	160-1615-C8U9
Webbing pay-out sensor	IES	IES-2098
String potentiometers	Space Age	160-1615-C8U9
Pressure sensors	Kulite	Kulite XTL-142B-190-7BARG
Load cells	Load Indicator	M16-30

The THOR-50M was equipped with the instrumentation specified in the Euro NCAP test protocol [5], including three axis accelerometers in the head, spine (at T1, T4, T12) and pelvis, Infra-Red Telescoping Rods for the Assessment of Chest Compression (IR-TRACCS) for the chest (4) and abdomen (2), six axis load cells (upper neck and femur (left and right), five axis load cells (thoracic spine and tibia (upper, lower, right and left), three axis load cell (forces), left and right acetabulum, two-axis load cells for the anterior superior iliac spines (left and right ASIS), and head, chest and pelvis angular rate sensors. All signals from the THOR-50M were filtered according to SAE J211. The sensors used are listed with manufacturer and model name in *Table A2*. Selected THOR-50M signals are plotted in *Figure A7* to *Figure A20*. One complete 3D scan was performed before one of the tests to facilitate accurate positioning of the THOR-50M and the FE sub models.

Table A2
THOR-50M instrumentation.

Sensor type	Manufacturer	Model
Accelerometers (head, spine and pelvis)	Endevco	7264C-2000
Angular rate head, chest and pelvis	Diversified Technical Systems, Inc	ARS PRO-18K DTS
Upper neck load cell	Humanetics	10380 JI4
Thoracic spine (T12)	Humanetics	10415 JS1I4
IR-TRACCS (Chest and abdomen)	Humanetics	9945
ASIS load cells	Humanetics	10387 JS1I4
Acetabulum right load cells	Humanetics	10670 JS1I4
Acetabulum left load cells	Humanetics	10530 JS1I4
Femur load cells	Humanetics	W50-71010S11
Tibia upper load cells	Denton	3643
Tibia lower load cells	Denton	3644

Frontal sled FE model validation results

Using the generic open belt component models resulted in good matching of the seat belt loads for both crash pulses, but the retractor payout for the 40 km/h crash pulse was a bit too long in simulation model compared to the test measurements, *Figure A3 and Figure A4*.

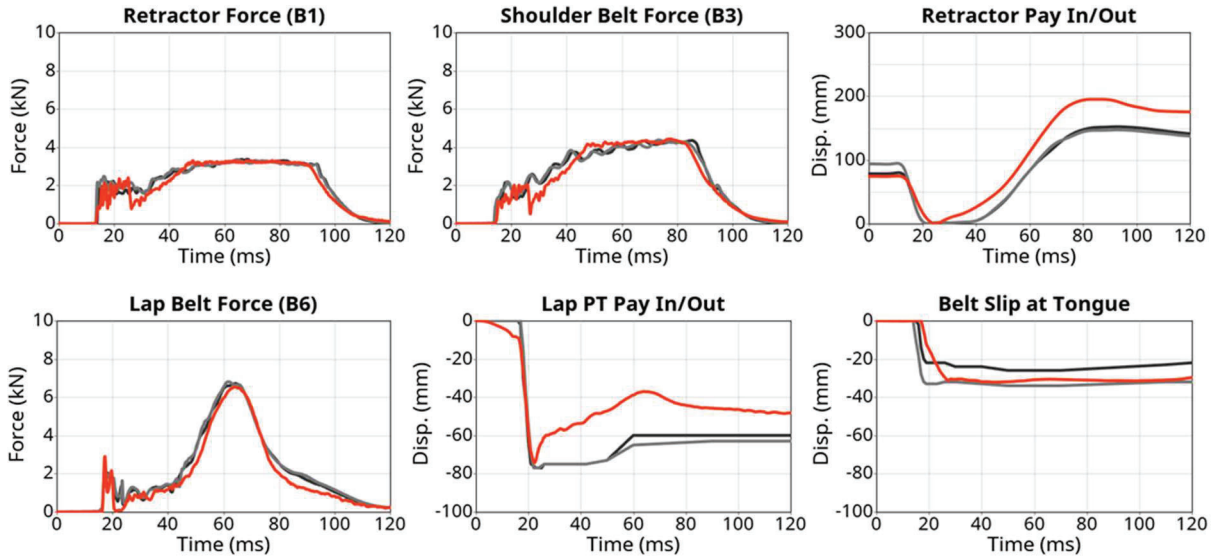


Figure A3. Belt measurements for 40 km/h crash pulse. Sled curves in grey and simulation curves in red.

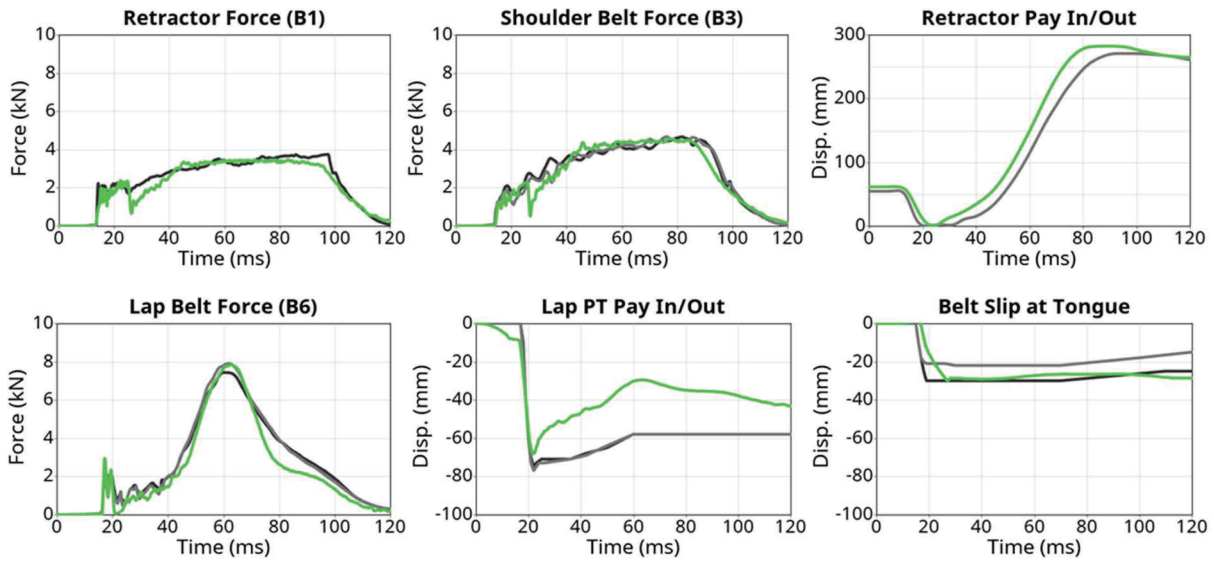


Figure A4. Belt measurements for 56 km/h crash pulse. Sled curves in grey and simulation curves in green.

Airbag pressure and steering column force and displacement matched test measurements good for both crash pulses, and so did the seat pan, T1 and pelvis string-potentiometers *Figure A5* and *Figure A6*.

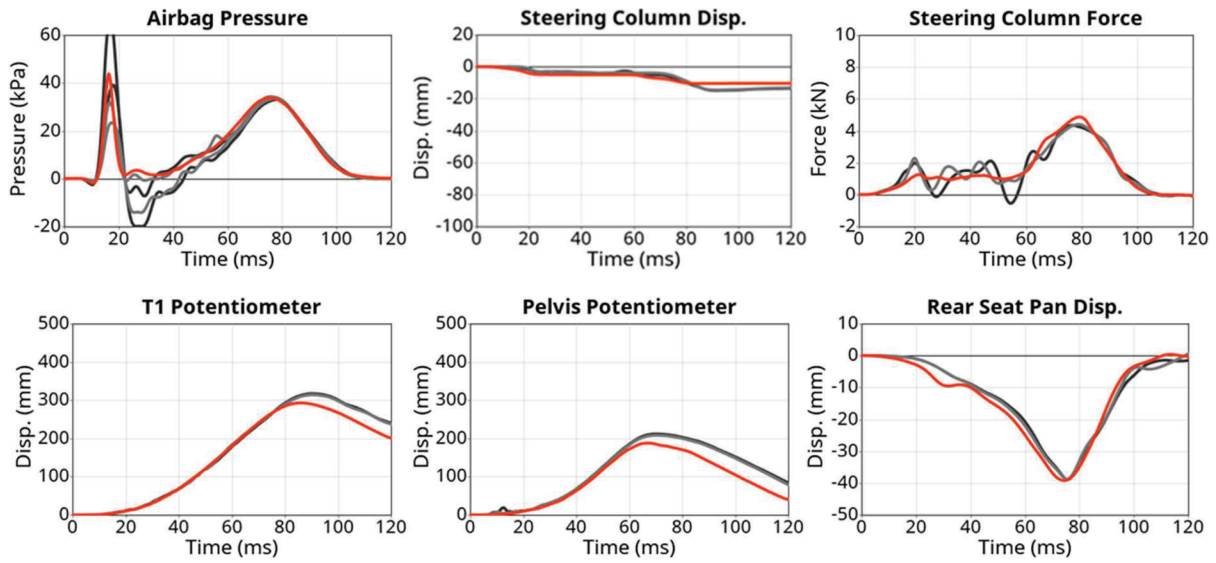


Figure A5. Measurements for 40 km/h crash pulse. Sled curves in grey and simulation curves in red.

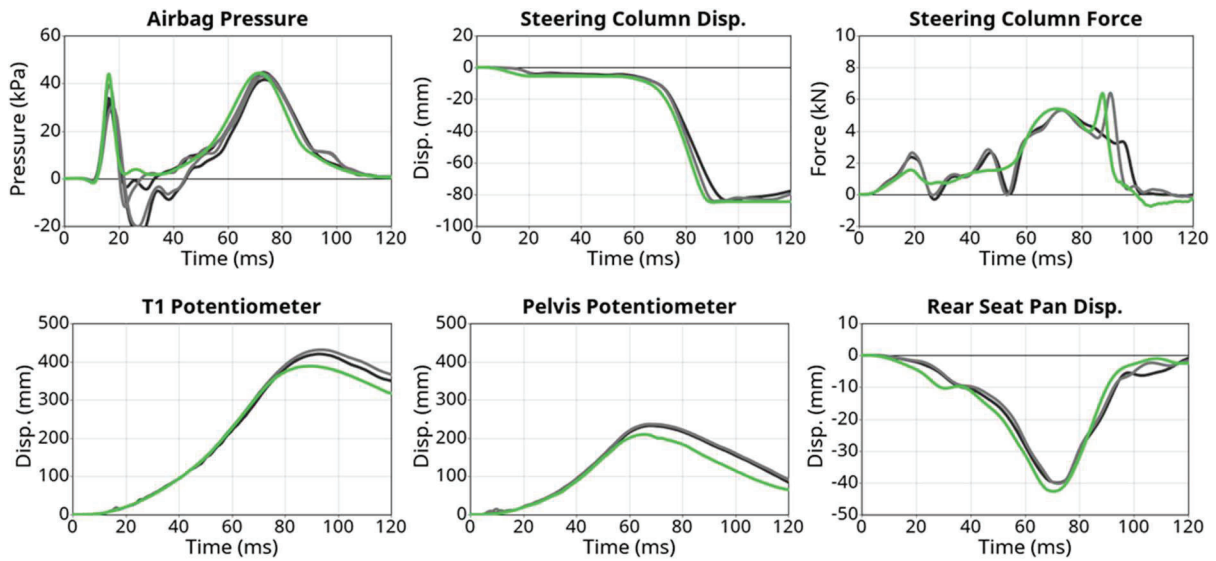


Figure A6. Measurements for 56 km/h crash pulse. Sled curves in grey and simulation curves in green.

All simulation acceleration measurements (head, T1, and pelvis) as well as head angular y-velocity, matched test measurements good for both crash pulses. The simulation pelvis angle matched the tests good for both crash pulses, although the rebound phase for the 40 km/h crash pulse was not captured correctly in simulation, *Figure A7* and *Figure A8*. These curves, together with the restraint output and the string-potentiometers, shows that the overall validation of the THOR-50M kinematics is good. Additional validation curves for THOR-50M related signal are shown in *Figure A9* to *Figure A20*.

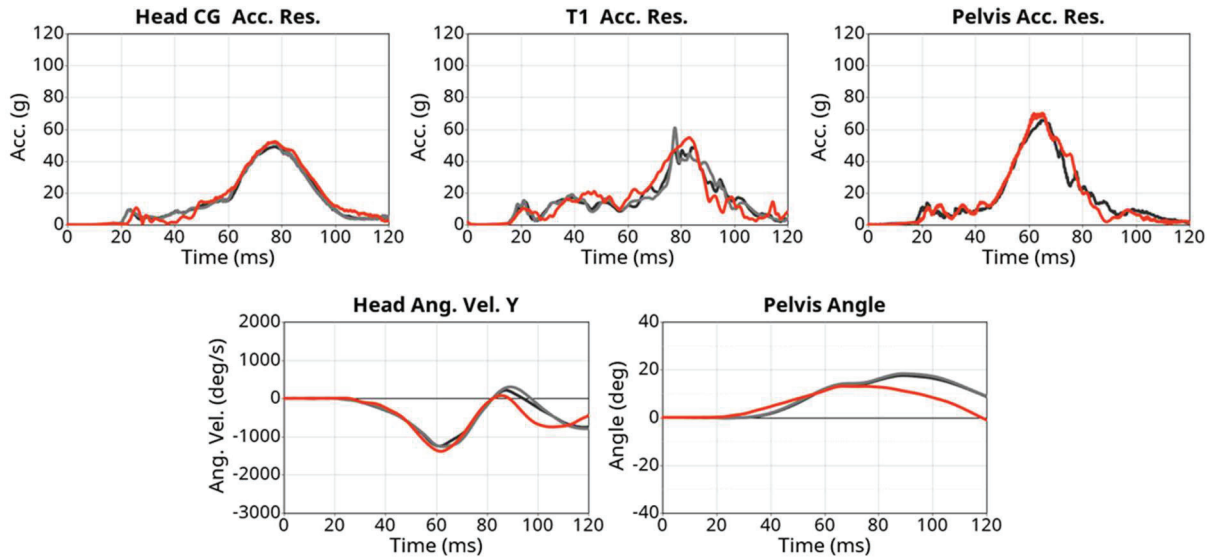


Figure A7. THOR-50M signals for 40 km/h crash pulse. Sled curves in grey and simulation curves in red.

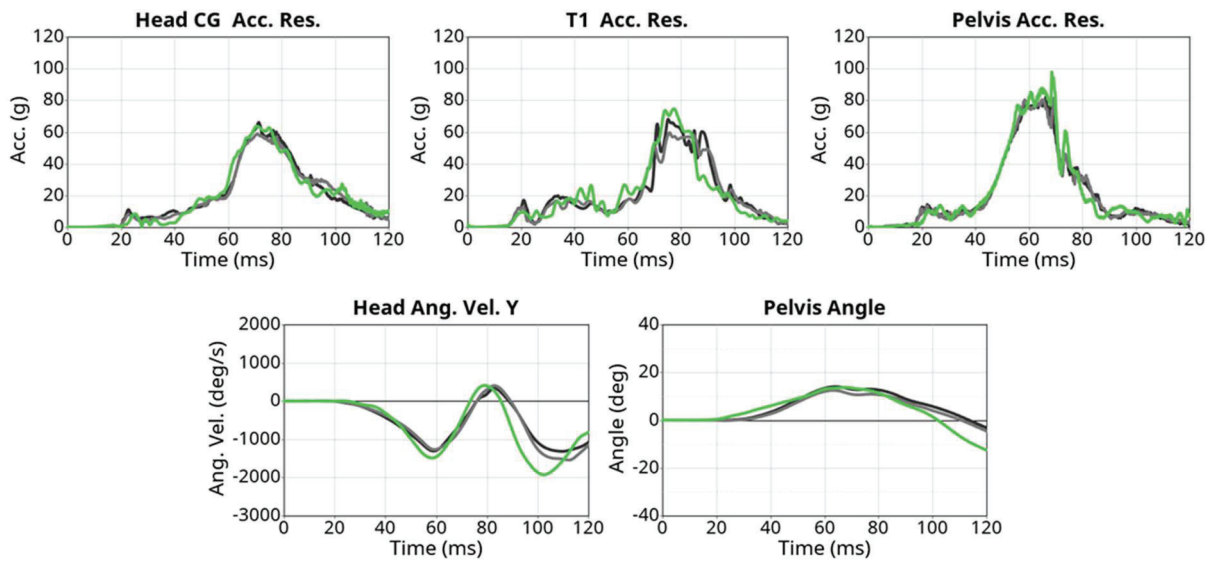


Figure A8. THOR-50M signals for 56 km/h crash pulse. Sled curves in grey and simulation curves in green.

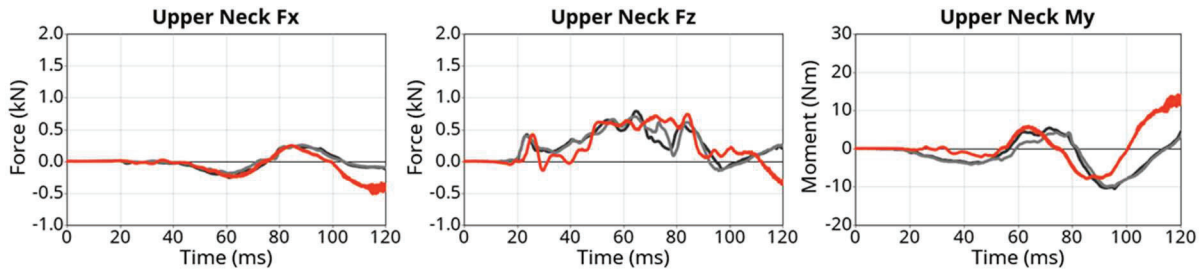


Figure A9. THOR-50M signals for 40 km/h crash pulse. Sled curves in grey and simulation curves in red.

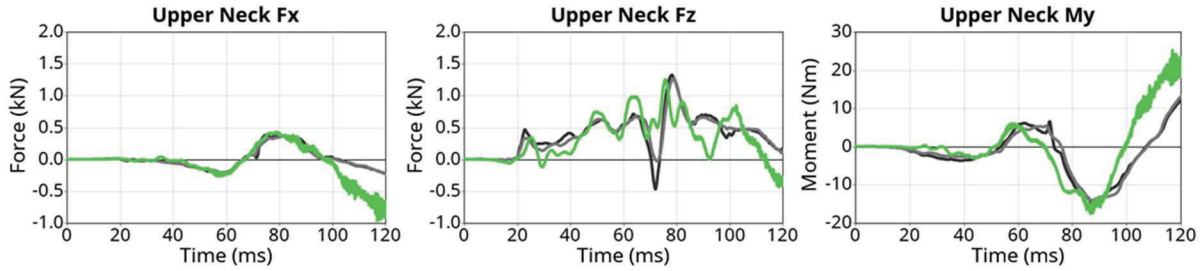


Figure A10. THOR-50M signals for 56 km/h crash pulse. Sled curves in grey and simulation curves in green.

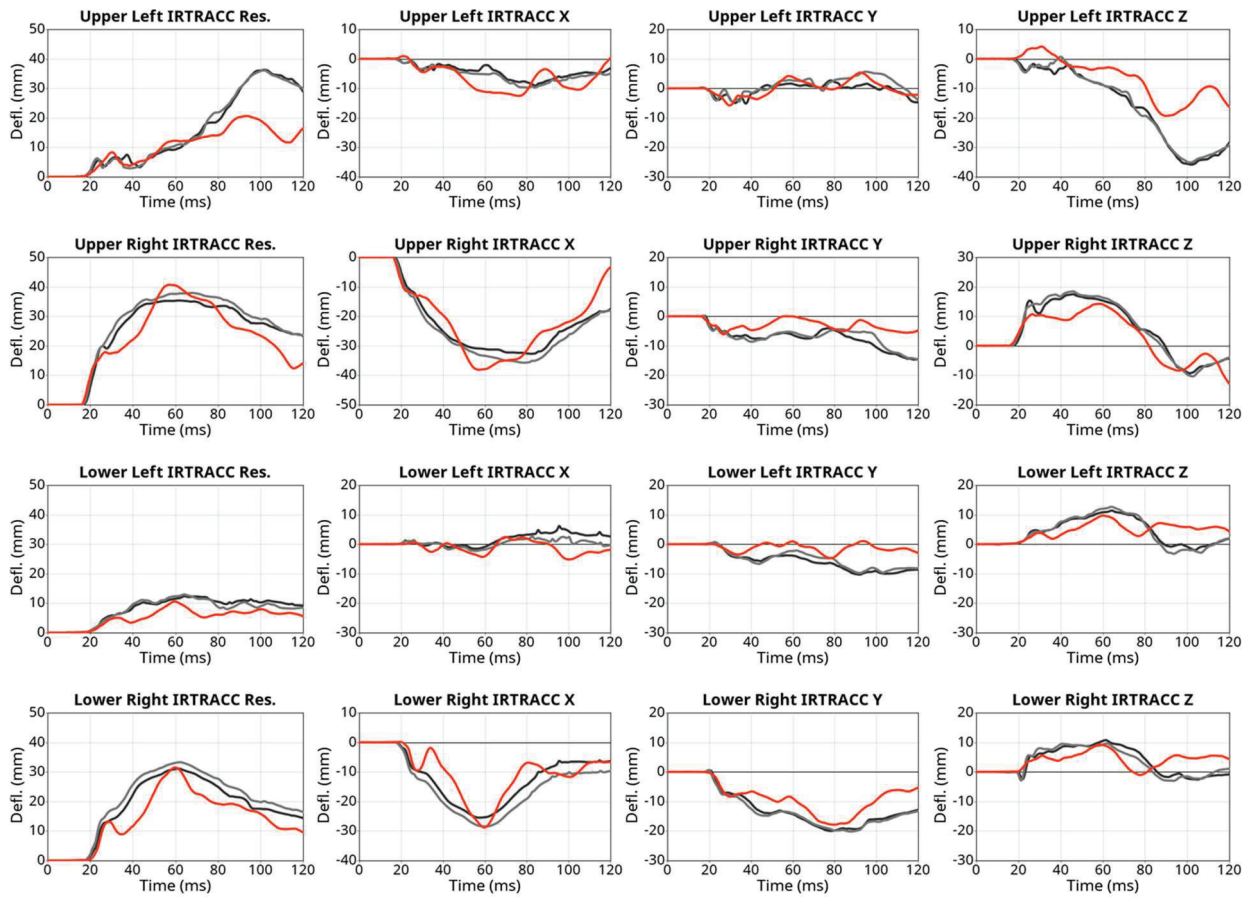


Figure A11. THOR-50M signals for 40 km/h crash pulse. Sled curves in grey and simulation curves in red.

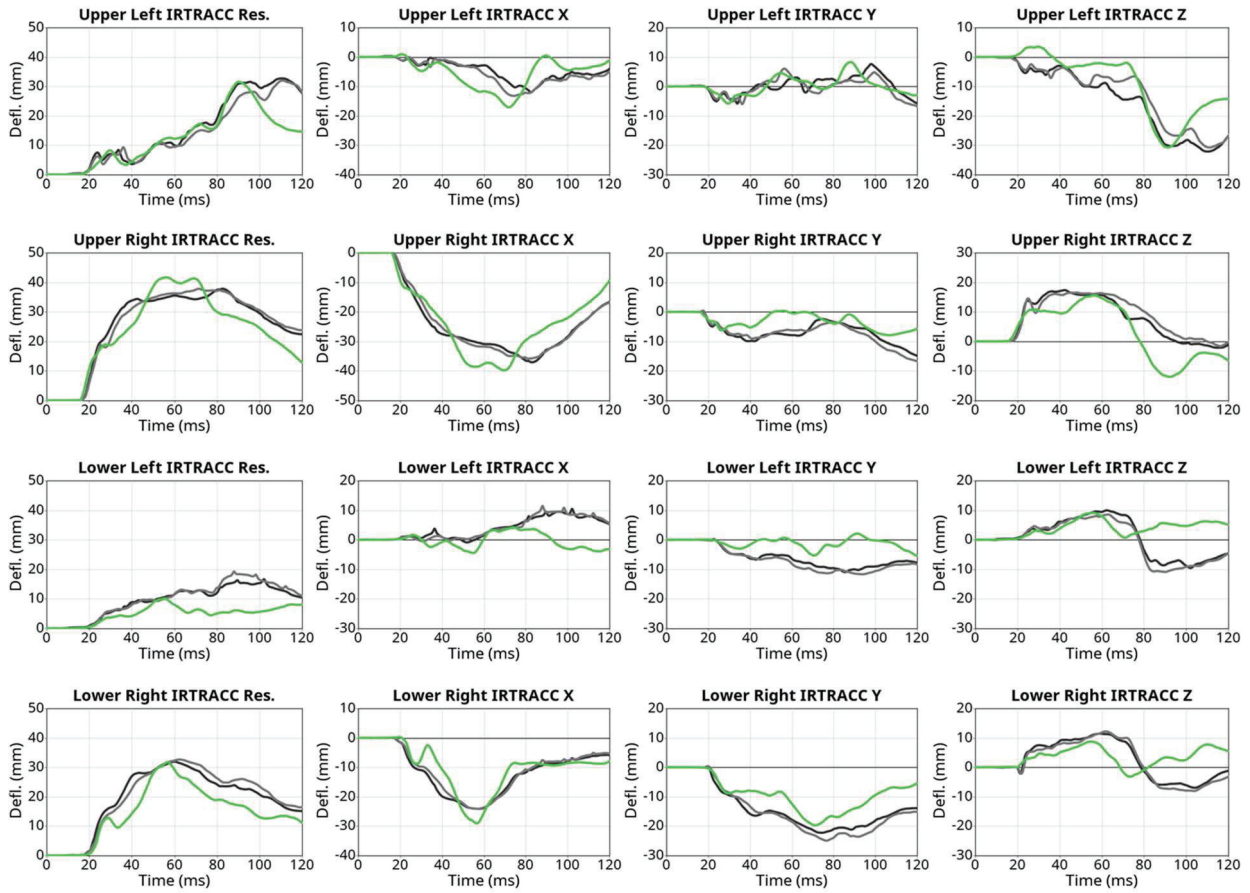


Figure A12. THOR-50M signals for 56 km/h crash pulse. Sled curves in grey and simulation curves in green.

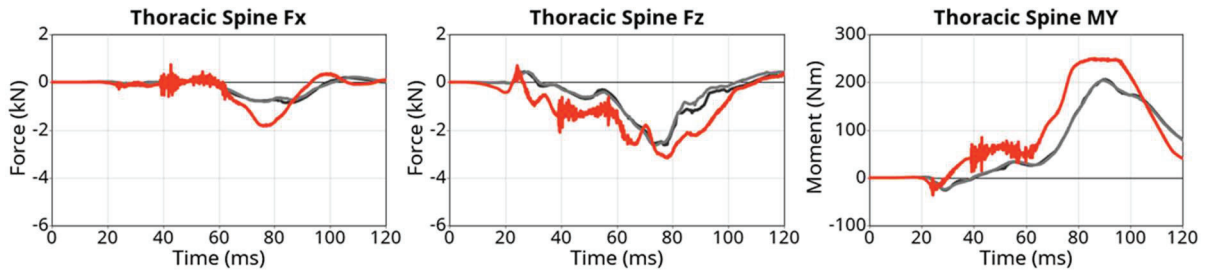


Figure A13. THOR-50M signals for 40 km/h crash pulse. Sled curves in grey and simulation curves in red.

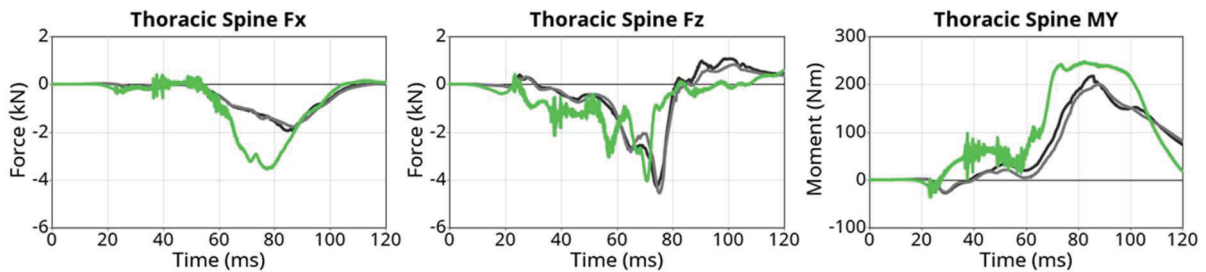


Figure A14. THOR-50M signals for 56 km/h crash pulse. Sled curves in grey and simulation curves in green.

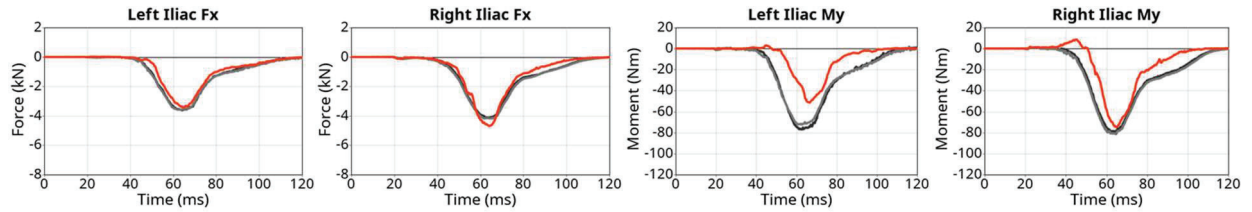


Figure A15. THOR-50M signals for 40 km/h crash pulse. Sled curves in grey and simulation curves in red.

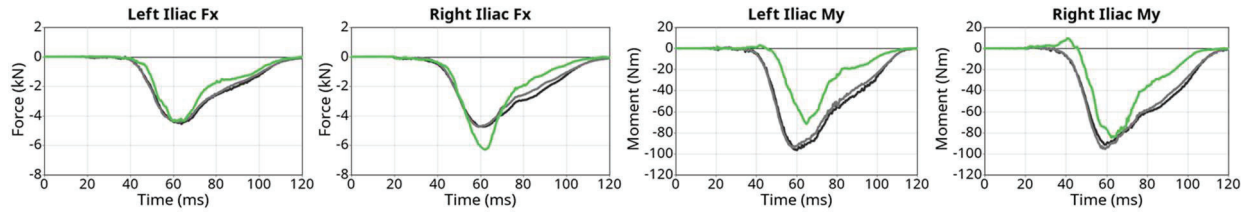


Figure A16. THOR-50M signals for 56 km/h crash pulse. Sled curves in grey and simulation curves in green.

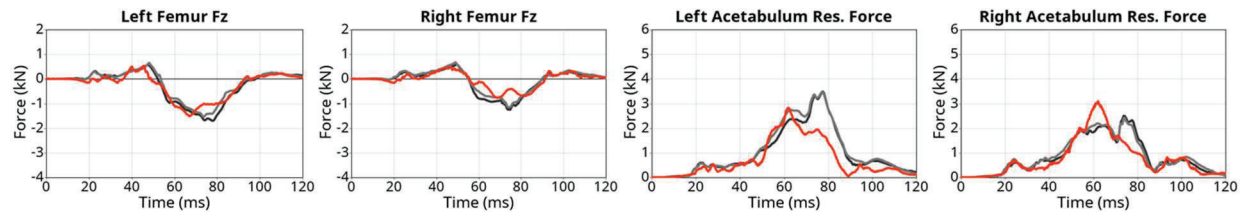


Figure A17. THOR-50M signals for 40 km/h crash pulse. Sled curves in grey and simulation curves in red.

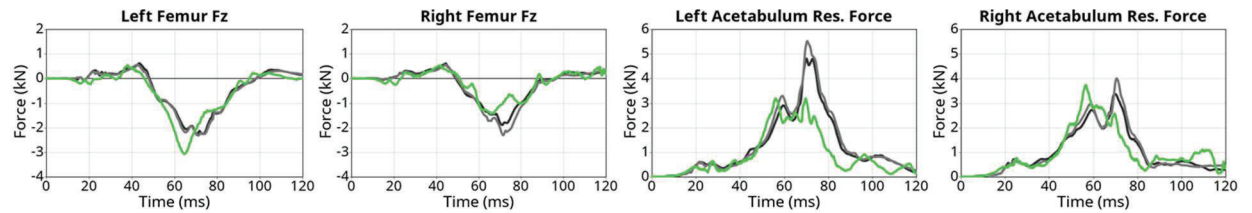


Figure A18. THOR-50M signals for 56 km/h crash pulse. Sled curves in grey and simulation curves in green.

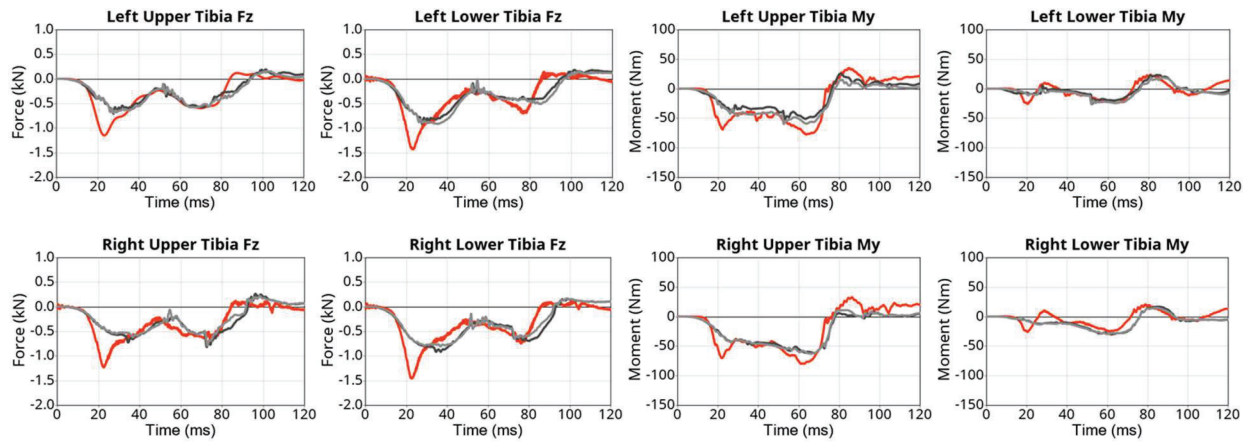


Figure A19. THOR-50M signals for 40 km/h crash pulse. Sled curves in grey and simulation curves in red.

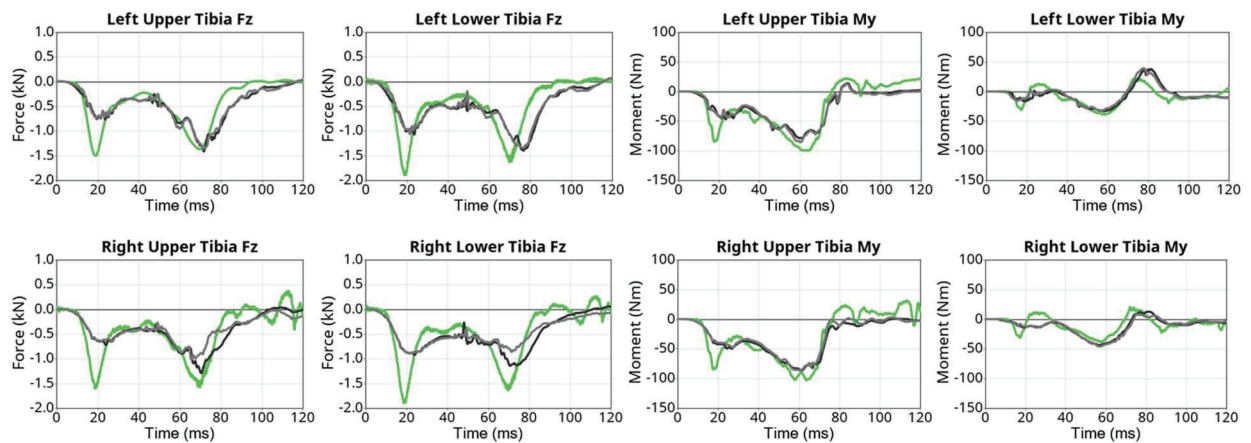


Figure A20. THOR-50M signals for 56 km/h crash pulse. Sled curves in grey and simulation curves in green.

REFERENCES

- [1] Mroz K, Östling M, Richardson R, Kerrigan J, Forman J, Gepner B, Lubbe N, Pipkorn B. 2020. Effect of Seat and Seat Belt characteristics on the Lumbar Spine and Pelvis Loading of the SAFER Human Body Model in reclined Postures. Proceedings of the IRCOBI Conference, 2020, Munich, Germany.
- [2] Schiessler M., et al. 2021. Validation and Demonstration of Advanced Passenger Protection Principles. Deliverable D2.5; OSCCAR Project; Grant Agreement No. 768947; 2021. <https://www.osccarproject.eu/media/deliverables/>. Accessed 01.12.2022.
- [3] Höschel P, Smit S, Tomasch E, Östling M, Mroz K, Klug C. 2021. Generic Crash Pulses Representing Future Accident Scenarios of Highly Automated Vehicles. SAE Int. J. Trans. Safety 10(2):2022, doi:10.4271/09-10-02-0010.
- [4] Mroz K, Östling M, Klug C, Höschel P, Lubbe N. 2021. Supplementing Future Occupant Safety Assessments with Severe Intersection Crashes Selected Using the SAFER Human Body Model. SAE Int. J. Trans. Safety 10(2):2022, doi:10.4271/09-10-02-0011.
- [5] EUROPEAN NEW CAR ASSESSMENT PROGRAMME (Euro NCAP) ASSESSMENT PROTOCOL – ADULT OCCUPANT PROTECTION Implementation 2023 Version 9.2.1 14th November 2022. <https://cdn.euroncap.com/media/75471/euro-ncap-assessment-protocol-aop-v921.pdf>. Accessed 05.12.2022.

DRIVER AIRBAG SOLUTIONS FOR NEXT GENERATION STEERING WHEELS

Marc Schledorn

Johannes Morhart

ZF Automotive Safety Germany GmbH

Germany

Paper Number 23-0221

ABSTRACT

The steering wheel as the central vehicle motion control device gives today's drivers a high level of trust in the controllability of their vehicles. Changing vehicle interiors as well as new occupant positions / postures related to highly automated driving are impacting the form and function of steering devices. Three technology trends are influencing future steering wheels: growing electronic content, changing steering wheel geometries and transformation capabilities and seamless designs.

Over the last decades the appearance of the steering wheel was determined by a round 360° steering wheel shape, a visible gap between driver airbag & steering wheel, and driver safety enabled by an airbag deployment centrally from the front surface. However, future steering wheels are becoming increasingly seamless with higher integration of HMI functionalities and new surface appearances like wood optic or glass applications. Such innovative designs require new driver airbag solutions.

This paper examines an alternative concept capable of revolutionizing the front panel of a steering wheel by incorporating a driver airbag inside of the steering wheel. The airbag cushion can deploy from the top side of the wheel through the rim and covers the front panel, thus helping to protect the driver in case of a crash.

STATE OF THE ART

Today's driver airbag modules are mechanically fixed in the center of the steering wheel, the cushion volume is released by a frontal opening through an airbag cover (thermo plastic material, TPE) towards the driver. Future interior designs, in-vehicle digitalization and a higher degree of automation [1], are providing new design possibilities for future steering wheels. The frontal opening of conventional driver airbags have limitations regarding design, functional enrichment and material selection in the opening area especially when those designs become seamless with a hard surface; e.g. polycarbonate or the integration of displays, figure 1.



Additionally new steering wheel shapes like yoke designs [2, 3] are offering alternative approaches for deployment of driver airbag cushion volumes. Byton's M-Byte concept [4] presented in 2018 was a round shaped steering wheel incorporating a central 8-inch display while the airbag inflates below the display screen. Driver airbag modules with a top mounted display are in opposition to the interior trend of slim steering wheel designs and a frontal deployment might lead to incompatibility with seamless designs.

Figure 1. ZF concept (seamless design incorporating a top deployed airbag)

TECHNICAL SOLUTION AND APPROACH

ZF has begun development of an alternative driver airbag solution where the driver airbag is not located in its traditional area. The airbag cushion can deploy from the top side of the wheel through the rim and covers the front panel, thus helping to protect the driver in case of a crash. [5, 6]

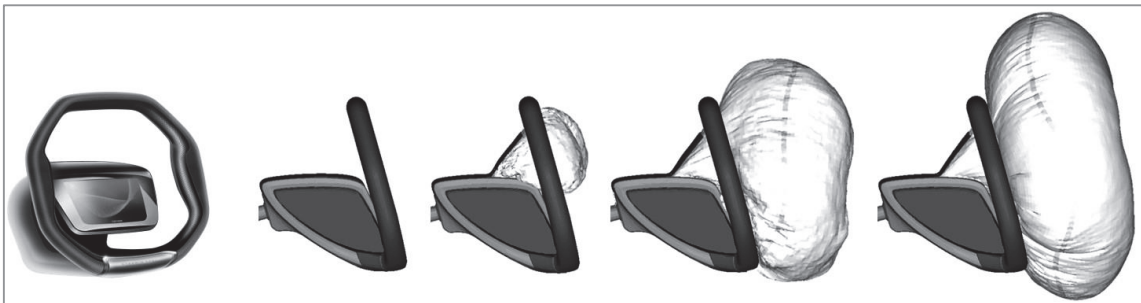


Figure 2. Safety concept for a top deployed airbag

Main challenges to deploy the airbag from the top side of such a concept are enabling stable deployment through the steering wheel rim, a rapid coverage of the rim at the 6 o'clock position and to maintain today's steering wheel and driver airbag packaging options.

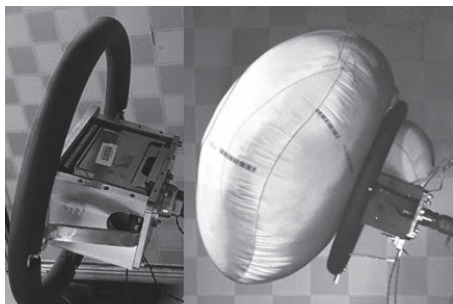


Figure 3. Test device

The aim was to investigate and validate an adaptive test device design that represents a wide range of current known steering wheel geometries. This steering wheel device is a modular design, so different sizes / positions of the rim and the dimensions of the housing can easily be adjusted, figure 3.

As a sample reference a serial driver airbag was selected as a baseline for the study using a dual stage inflator with the same propellant and a bag size of 700mm diameter. For validation the following tests have been considered: Static deployment, head impact, body block, linear impactor, out of position and sled tests.

RESULTS

To evaluate robustness static deployment test were employed at full temperature ranges from -35°C to +85°C and at low temperature the main challenges are ensuring a fast deployment through the steering wheel rim, the 6 o'clock rim coverage and the bag filling times. At high temperature the focus is on integrity requirements, a slow initial unfolding that can lead to high pressure in the first chamber and leading to potential integrity issues. At all temperatures the 6 o'clock rim coverage and the filling time are in the same range as the reference module (table 1).

Table 1.
Static deployment test results

Temperature	Top deployed Driver Airbag		Conventional Driver Airbag (Reference)	
	6:00 coverage	Filling time	6:00 coverage	Filling time
-35°C	20 ms	44 ms	16 ms	34 ms
+23°C	18 ms	32 ms	14 ms	28 ms
+85°C	17 ms	29 ms	13 ms	22 ms

Conformity of head impact and body block test according to ECE R12 [7] as a legal requirement is mandatory. For head impact the criteria of head acceleration has a 3ms limit (80g) and a max limit (120g) that must be fulfilled and for body block the upper limit is 111 daN. For both test cases two impact positions were tested at the 3 and 6 o'clock positions. Both test load cases are not critical, see figure 4 and table 2.

Table 2.
Head impact and body block

Head impact		Body block	
Impact position	a_3ms_max / a_max	Impact position	Max. force
3 o'clock spoke	25.2g / 37.1g	3 o'clock spoke	6.6kN
6 o'clock spoke	16.8g / 42.1g	6 o'clock spoke	6.9kN

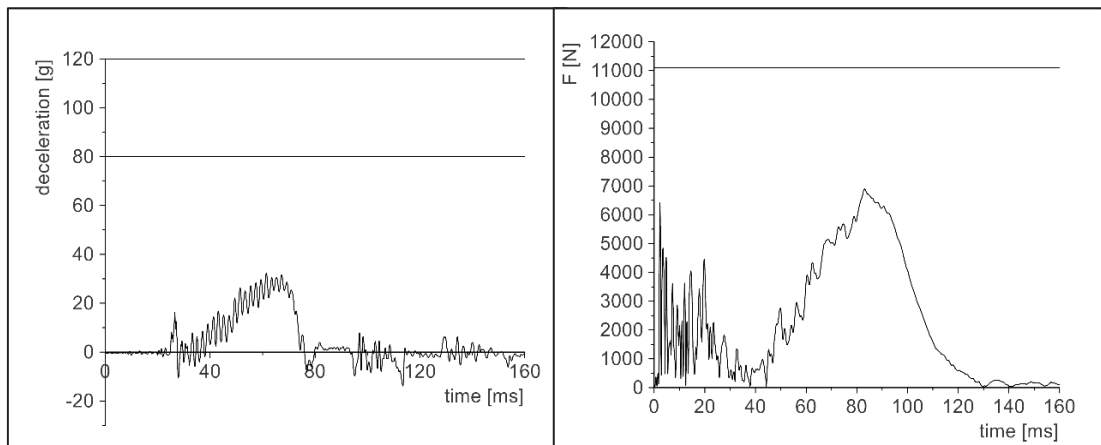


Figure 4. Head impact and body block test results

To evaluate the restraint performance of the airbag module a comparison with the reference driver airbag on a linear impactor device was used, and two setups were considered. Configuration 1 is representing a scenario of late dummy contact to the cushion with low energy and configuration 2 is representing an early contact with high energy.

**Table 3.
Linear impactor configuration**

	Configuration 1	Configuration 2
Mass	33 kg	37 kg
Velocity	5.3 m/s	7 m/s
Trigger distance	450 mm	400 mm
Kinetic energy	463 J	907 J

When comparing to the reference the performance is similar for both configurations, the deceleration peak for the top deployed airbag is slightly higher compared to the reference driver airbag, however by increasing the venting size the performance can be adjusted.

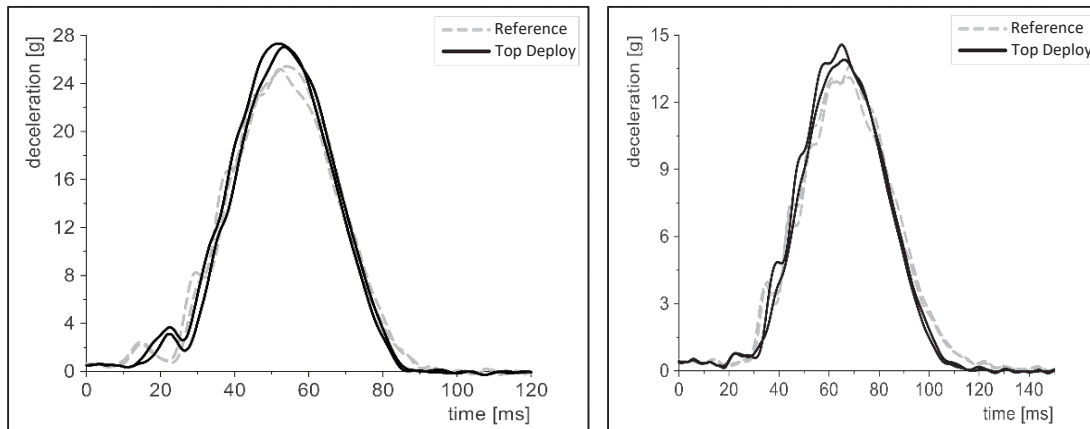


Figure 5. Linear impactor (configuration 1 and 2)

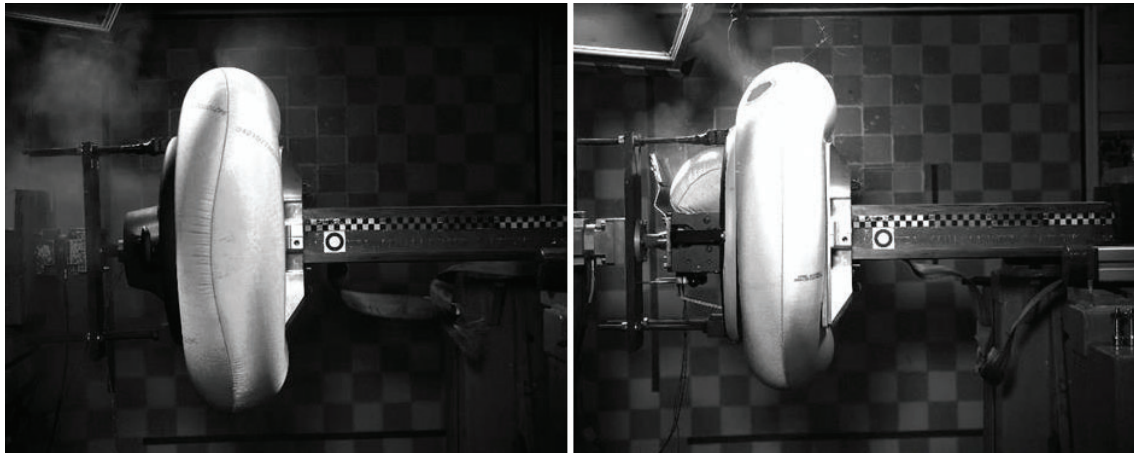


Figure 6. Linear impactor, conventional vs. top deployed airbag

The fulfillment of OoP requirements [8] are crucial for driver airbag modules. In today’s standard driver airbag systems high neck forces and torsions can be reduced by guiding a bag deployment through and behind the rim. For a top deployed airbag this effect can’t be used because the cushion remains under the chin and deploys between occupant and steering wheel in the 6 o’clock direction and pushes the occupant backwards, figure 7. An appropriate bag design is required to reduce the NIJ criteria (neck injury) due to its neck forces and momentum.

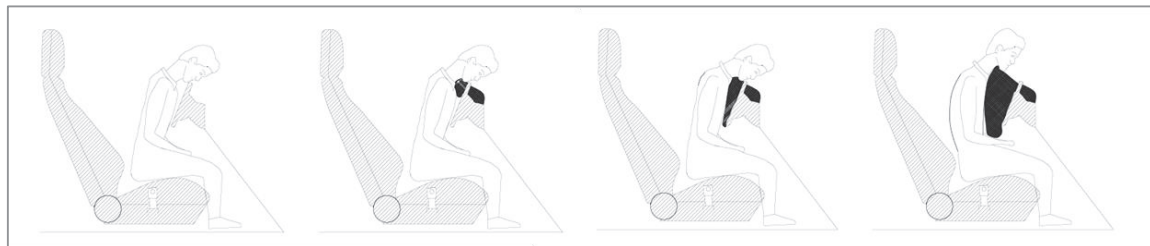


Figure 7. OoP - Chin on rim

The Out of Position results for dummy position 1 (DP1, chin on rim) and dummy position 2 (DP2, chin on module) are listed in table 4.

**Table 4.
OoP Results (Alternative test device)**

DP1 NIJ	DP1 FZ	DP2 NIJ	DP2 FZ
52.7%	52.8%	73.1%	35.2%
49.0%	37.6%	77.3%	32.6%

Preliminary tests to evaluate the restraint system performance were considered with a hybrid III 5% dummy and a second one with a THOR 50% dummy.


The Euro NCAP [9] full-frontal sled test with hybrid III 5% dummy showed a fast and straight bag positioning in the small area between lower rim section and chest, a de-folding towards the driver was not observed, figure 8.



Figure 8. Hybrid III 5% dummy

The sled test with a THOR 50% dummy was performed according to Euro NCAP MPDB setup [10]. Compared to a conventional driver airbag the top deployed airbag is showing an equal restraint performance, see table 5.

Table 5.
Euro NCAP MPBD

Sled Test Front Impact		Euro NCAP MPDB		Euro NCAP 2020	
Type of Test		Driver SP 1 (T3)		ZF	
Regulation					
Criterion					
Head & Neck	(4P)		4.000	*	
Head					
Hard contact?		no			
HIC 15		335.54			
Acceleration a_t		62.65 g			
3ms cumulative		57.64 g			
Modifiers					
BrIC (monitoring)		0.88			
UBrIC (monitoring)		0.44			
DAMAGE (monitoring)		0.57			
HAIC (monitoring)		69.47 rad/s			
CIBIC (monitoring)		0.56			
Neck					
Shear Force Fx (abs)		0.67 kN	4.000	*	
Tensile Force Fz+		0.70 kN	4.000	*	
Extension My-		-16.55 Nm	4.000	*	
Chest & Abdomen	(4P)		3.114		
Chest					
Deflection Upper Left		31.71 mm	4.000	*	
Deflection Upper Right		40.54 mm	3.114	*	
Deflection Lower Left		19.93 mm	4.000	*	
Deflection Lower Right		24.30 mm	4.000	*	
Diagonal belt upper force ¹⁾		4.10 kN	-0.000	✓	
Modifiers					
Abdomen					
DeflectionLeft		-39.62 mm	4.000	*	
DeflectionRight		-45.51 mm	4.000	*	
Knee, Femur & Pelvis	(4P)		4.000	*	
Left					
Acetabulum Force		0.60 kN	4.000	*	
Femur Compression Fz-		-0.65 kN	4.000	*	
Knee Slider Displacement		-0.20 mm	4.000	*	
Knee & Femur Modifiers					
Right					
Acetabulum Force		0.45 kN	4.000	*	
Femur Compression Fz-		-2.22 kN	4.000	*	
Knee Slider Displacement		-0.52 mm	4.000	*	
Knee & Femur Modifiers					
Ilium Fx-		378.72 N	0.000	✓	
Submarining					
Abdomen & Pelvis Modifiers					
Lower Leg & Foot	(4P)		3.733		
Left					
Compression upper Fz-		-1.33 kN	4.000	*	
Compression lower Fz-		-1.86 kN	4.000	*	
Tibia Index upper		0.32	4.000	*	
Tibia Index lower		0.24	4.000	*	
Right					
Compression upper Fz-		-1.49 kN	4.000	*	
Compression lower Fz-		-2.04 kN	3.973	*	
Tibia Index upper		0.46	3.733	*	
Tibia Index lower		0.19	4.000	*	
Modifiers					
Foot & Ankle					
Brake rearward displacement		0 mm	4.000	*	
Clutch rearward displacement		0 mm	4.000	*	
Accel. rearward displacement		0 mm	4.000	*	
Modifiers					
Total Assessment²⁾	(16P)	92.8	%	14.847	
Notes:					
1) based on polynomial cal.					
2) listed modifiers are included only					
Points					
* 4.000					
⊙ 2.670 - 3.999					
* 1.330 - 2.669					
* 0.001 - 1.329					
* 0.000					
					

CONCLUSION

Deploying a cushion volume from the top side of a driver airbag module and through the steering wheel rim is an innovative approach and enables new possibilities for future steering wheel designs. Even when the applied tests have been conducted in a specific device it can be shown that upcoming customer demands can be fulfilled, specific styling investigations and near-series toolings must be considered in order to bring higher confidence to the solution. Furthermore, a top deployed airbag must be tested with new steering wheel rim geometries e.g. Yoke shapes. Instead of deploying the airbag from the top side investigations from the bottom are notable. As future interior styling aims to provide comfort seating positions, dual contour bag solutions which have not yet been considered must be investigated.

REFERENCES

- [1] SAE, J3016, "Levels of Driving Automation," https://www.sae.org/binaries/content/assets/cm/content/blog/sae-j3016-visual-chart_5.3.21.pdf, accessed Dec. 2022.
- [2] Tesla, "Model S - Interior of the Future – Yoke Steering," <https://www.tesla.com/models>, accessed Dec. 2022.
- [3] CNET, "Lexus' New Steering Yoke Is Weird but Kinda Wonderful," <https://www.cnet.com/roadshow/news/lexus-rz-steering-yoke>, accessed Dec. 2022.
- [4] CNET, "Byton electric concept car: All the details you need to know," <https://www.cnet.com/roadshow/news/byton-electric-concept-car-all-the-details>, accessed Dec. 2022.
- [5] Safetywissen, "Bereit für autonomes Fahren: ZF entwickelt neues Lenkrad-Konzept mit fortschrittlichen HMI-Lösungen," <https://www.safetywissen.com/object/A11/N01.p377367168uptx3ve3u35614jlrds63652211614/safetywissen>, accessed Dec. 2022.
- [6] Schledorn M., Balbas A., "Alternative approaches to steering devices of the future", Airbag Conference Mannheim, 2018
- [7] ECE R12 / Regulation No. 12 Regelung Nr. 12 der Wirtschaftskommission der Vereinten Nationen für Europa (UN/ECE), "Einheitliche Bedingungen für die Genehmigung der Kraftfahrzeuge hinsichtlich des Schutzes des Fahrzeugführers vor der Lenkanlage bei einem Aufprall"
- [8] 49 CFR Part 571.208 (FMVSS 208), 49 CFR 571.208 - Standard No. 208, Occupant crash protection
- [9] European New Car Assessment Programme, (Euro NCAP), Full Width Frontal Impact Testing Protocol, 2019
- [10] European New Car Assessment Programme, (Euro NCAP), MPDB Frontal Impact Testing Protocol, 2019

INVESTIGATING SLOUCHING IN FRONTAL IMPACTS USING AN HBM IN THE REAR SEAT

Katarina Bohman

Emil Fågelberg

Lotta Jakobsson

Volvo Cars

SAFER, Vehicle and Traffic Safety Centre at Chalmers

Gothenburg, Sweden

Paper Number 23-0300

ABSTRACT

Car occupants may choose a wide range of sitting postures, including rearward rotation and forward excursion of the pelvis, through slouching. The overall objective of the study was to contribute to the understanding of restraint interaction, as a function of pelvis orientation and lumbar spine posture. Specifically, the aim was to investigate kinematics of and loading to the occupant in frontal impacts by comparing slouched and upright sitting postures using state-of-the-art restraints.

A human body model (HBM) of a mid-sized male, the SAFER HBM, was restrained in a simulation model of the rear seat of a large passenger car and exposed to a full frontal 50 km/h impact. Three different sitting postures, with constant seat backrest angle were included; a nominal upright sitting posture and two slouched sitting postures, representing moderate and extreme slouching, respectively. The position of the seat in front of the occupant was varied to the mid-track position and the most forward-track position, respectively, to allow for different knee-interaction.

When the front seat was in a mid-track position, submarining did not occur in any of the slouched postures, while partial submarining occurred for the extreme slouched posture with the front seat in the most forward-track position in the model.

During the impact, both slouched postures of the HBM resulted in less torso pitch compared to the nominal posture. The shoulder belt moved up the sternum to a higher extent in the slouched postures, leading to less balanced kinematics with the pelvis moving forward and the upper torso held back by the shoulder belt, contributing to the less torso pitch. These changes in kinematics for the slouched postures resulted in higher lumbar spine compression and lower chest loading, relative to the nominal posture.

In summary, slouched sitting postures affect occupant kinematics and loadings in a frontal impact. By exploring variations in sitting posture in terms of slouching using a HBM, knowledge can be gained in understanding the mechanisms of submarining and lumbar spine loading. These findings are relevant for sitting postures in conventional cars today, in addition to a wider range of sitting postures as a result of future seat developments.

Keywords: sitting posture, slouching, HBM, rear seat, submarining, pelvis orientation

INTRODUCTION

In most standardized vehicle crashworthiness assessment tests, anthropomorphic test devices (ATDs) are positioned in upright sitting postures; centralized in the seat and with the back against the seat backrest. Only in a few exceptions a minor slouched sitting posture is allowed, for instance for the 10-year-old ATDs in frontal impact tests (FMVSS 213, EuroNCAP). Their slouched sitting posture is achieved by adding a spacer of 20 mm behind the pelvis.

However, changing posture is part of natural sitting behavior to feel comfortable over time (Helander and Zhang, 1997), whereby a range of sitting postures is expected to occur during a drive. A driving study on adult front seat passengers showed a wide range of sitting postures, for which a slouched posture was detected 3.9% of the time (Reed et al. 2020). For rear seat occupants, driving studies on older child occupants confirmed a wide range of sitting postures including slouched sitting posture (Jakobsson et al. 2011, Osvalder et al. 2013). A naturalistic driving study with rear seat adult passengers, showed that the passengers spend about 27% of the time leaning laterally inboard or outboard. However, slouching was not annotated in the study (Reed et al. 2022). In a laboratory

setting, Park et al. (2016) conducted a sitting posture study on rear seat adult passengers, deriving a statistical model to predict adult sitting postures.

Sitting postures at impact may influence injury risks in vehicle crashes. Occupant posture was identified as a major influencing factor on front seat occupant response on injury outcome in frontal impacts (Bose et al. 2010) as well as in side impacts (Hwang et al., 2016). Izumiyama et al. (2018) quantified initial pelvis orientation through x-ray of 75 individuals, and there after morphed an HBM into several initial pelvis orientations. A more rearward tilt of the pelvis prior the impact, resulted in increased pelvis excursion and rotation, when exposed to frontal impact. Beck et al. (2014) found an increased risk of submarining in frontal impacts, when positioning rear seated ATDs in slouched sitting postures. Uriot et al. (2015) conducted postmortem human subject (PMHS) tests in standard and slouched sitting postures with the pelvis 60 mm moved forward. All three PMHS tests in this slouched posture resulted in submarining while no submarining occurred in the standard posture. Furthermore, submarining has been addressed focusing on restraint geometries (Håland et al. 1991), influence of occupant size (Gepner et al. 2018) and reclined seats (Boyle et al. 2019, Mroz et al. 2020).

There is a need to further understand the details in lap belt interaction and the balance between risk for submarining and lumbar spine loading, especially in the rear seat. Addressing a natural everyday situation of slouching, the overall objective of the study was to contribute to the understanding of restraint interaction, when influenced by pelvis orientation and lumbar spine posture. Specifically, the aim of this study was to investigate kinematics and loading to the occupant in frontal impacts by comparing slouched upright sitting postures, using an HBM in a rear seat environment.

METHODS

Finite element (FE) simulations were run using MPP LS-DYNA (LSTC, Livermore, CA) R9.3.1 with the SAFER Human Body Model (HBM) v10, investigating the effect of different degree of slouched sitting postures in a simulated frontal impact. The SAFER HBM is a 50th percentile male HBM (stature 175 cm and weight of 77 kg), originally based on the THUMS v3, but as of v10 most parts have been updated or replaced. The SAFER HBM was validated for occupant kinematics in reclined postures (Mroz et al. 2020). Since then, a new pelvis model with 50th percentile male shape based on a data set of 57 CT scans and positioned to the average male pelvic angle of 45° (Izumiyama et al. 2018) has been implemented (Pipkorn et al. 2021), together with an updated improved hexahedral soft tissue mesh which is continuous from the torso to the extremities and the updated model was once more validated for reclined kinematics and compared with other HBMs (Gepner et al. 2022). The HBM was positioned in a nominal sitting posture and two slouched sitting postures, in a model of the rear seat of a large passenger car.

User range of slouched sitting posture

In a laboratory user study, 18 test participants were seated in the outboard rear seat of a large passenger car. The participants gave their consent to participate in the study and they were informed about their unconditional right to abort the test at any time. Their buttock to knee measures ranged from 556 mm to 597 mm, corresponding to 10 percentile females up to 30 percentile males (Hanson et al. 2009). The participants were asked to enter the car and buckle up, without further information. This initial sitting posture is referred to as their self-selected posture, and measurements were taken. Thereafter, they were asked to position their pelvis in contact with the seat backrest. This position is referred to as their reference posture. Their left and right ASIS (Anterior superior iliac spine) were identified through palpation and measured with a digital arm, for both sitting postures. The longitudinal difference between the two sitting postures is referred to as the distance of slouching of the pelvis. All participants except one, experienced some extent of slouching. The average slouching was 23 mm, and the 3rd quartile of the boxplot was 36 mm (see Appendix A for details).

Based on the results from the user study, three sitting postures were selected for the simulation series. A nominal sitting posture and a moderate slouched posture of 40 mm H-point forward translation to cover the 3rd quartile of the slouched postures in the user study. In addition, a slouch of 60 mm H-point forward translation was chosen, to cover an extreme slouched posture.

Sitting postures in simulation series

Figure 1 shows the three different sitting postures; nominal, 40 mm slouch and 60 mm slouch. Following rigid body translation and rotation using Primer pre-processor (v17.1, Oasys Ltd, Solihull, UK), the HBM was positioned by simulating a system of tension cables attached to the skeleton. At the end of the positioning simulation, the system was at rest. In the slouched postures, the cables attached to the pelvic bones were modified.

Any change in position of other body regions is thus a result of the pelvis positioning. The positioning simulations were run for 300 ms on 120 CPUs.

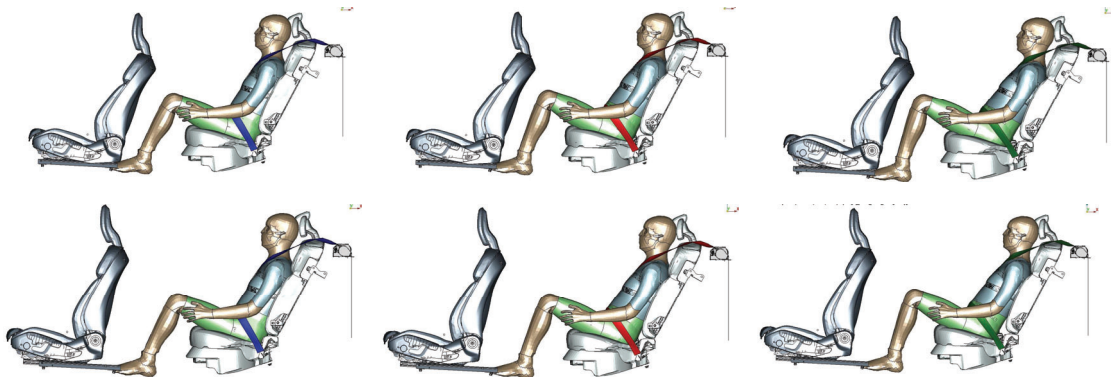


Figure 1 The SAFER HBM v10 positioned in three sitting postures in the rear seat; nominal (blue seat belt), 40 mm slouch (red seat belt) and 60 mm slouch (green seat belt). First row shows set-ups with the front seat in mid-track position, and second row with the front seat in most forward-track position.

In the resulting nominal sitting posture, the HBM was positioned with the H-point 10 mm in front of the SAE manikin position and rotated 5° rearward to match the angle of the seat back. The knees were 300 mm apart with the feet resting flat on the carpet with a knee flexion angle of approximately 90°. The resulting pelvic angle (Izumiyama et al. 2018, see Appendix B) after the positioning simulation was 52.5°.

For the 40 mm slouch posture, the resulting ASIS coordinates were 40 mm forward and 5 mm upward relative the nominal posture after the positioning simulation. The resulting pelvic angle was 56.0° and the knee to mid-track front seat distance was 96 mm. For the 60 mm slouch posture, the resulting ASIS coordinates were 60 mm forward and 10 mm upward relative the nominal posture after the positioning simulation. The resulting pelvic angle was 58.9° and the knee to mid-track front seat distance was 77 mm. See Appendix C for details on pelvis and spine posture.

Simulation series set-up

The HBM was positioned in the outboard left side of a large passenger vehicle interior FE model. The front seat fore-aft track position was varied to enable variation of leg and knee interaction. The two front seat positions used were mid-track position and the most forward-track position (Figure 1). For the HBM in the nominal posture, the distances from the knees to the back of the front seat were 127 mm and 296 mm, for the mid-track position and the most forward-track position, respectively.

A state-of-the-art load limited three-point seat belt model with a pyrotechnical shoulder belt pretensioner was used. The shoulder belt was routed using pre-processor Primer (v17.1, Oasys Ltd, Solihull, UK) without any friction, enabling the seat belt to follow the shortest path over the occupant chest from anchor to retractor outlet.

Six degree-of-freedom vehicle motions simulating a full-frontal rigid barrier impact at 50 km/h was applied to the sled model. All simulations were run for 110 ms using 120 CPUs.

Study design and analyses

The three sitting postures and the two front seat positions are combined in six configurations, see Appendix D for the simulation series matrix. Submarining was evaluated from the simulation animations and defined if the lap belt slipped completely over the ASIS. Left and right ASIS were analyzed separately to detect partial submarining. The moment at the medial-lateral axis in a cross-section through the ilium passing above the ASIS and below the ASIS, was analyzed to understand the lap belt interaction with the pelvis. The shoulder belt fit was evaluated using the measure of the vertical distance between jugular notch (top edge of sternum) and shoulder belt mid-line. Head acceleration, rib strain, lumbar spine compression, femur forces and pelvis acceleration were analyzed.

RESULTS

Kinematics and seat belt interaction

No submarining occurred in any of the six configurations. However, partial submarining, with lap belt slip-off of the ASIS on the outboard side, was detected in the 60 mm slouch posture with the front seat in most forward-track position. See Figure 2 and Appendix E for lap belt to pelvis interaction.

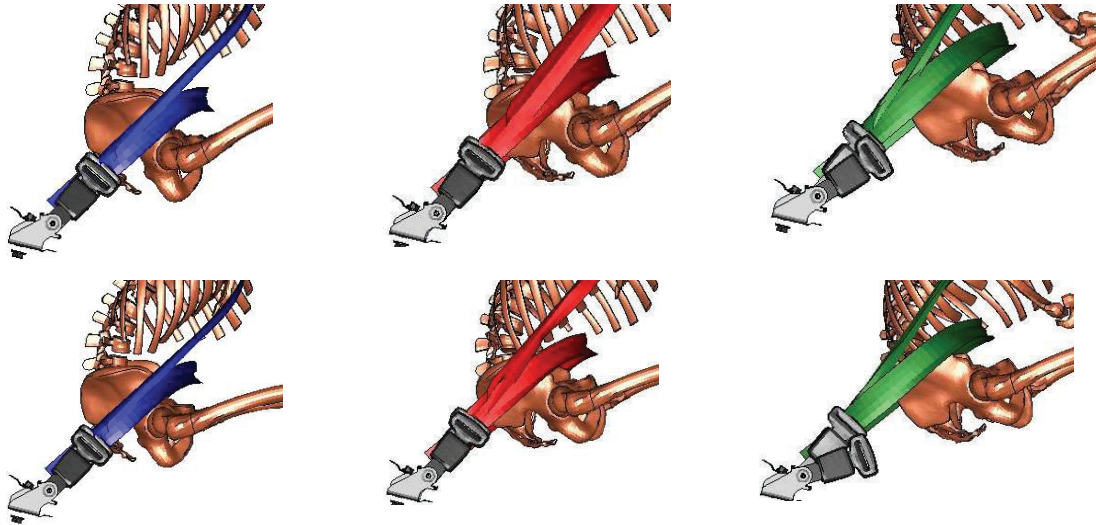


Figure 2 Close-up on inboard side view of the HBM at maximum forward excursion; nominal (blue seat belt), 40 mm slouch (red seat belt) and 60 mm slouch (green seat belt). First row shows simulations with the front seat in mid-track position, and the second row with the front seat in the most forward-track position.

Negative ASIS moment values (left and right side) in the nominal posture and 40 mm slouch, with either front seat position, indicated that the lap belt was engaging the pelvis below the center of the ASIS load cell. In the 60 mm slouch posture, positive ASIS moments suggest that the belt was partly or completely over the ASIS load cell, which indicated a potential risk of submarining (see Appendix F).

The displacement trajectories over time showed that kinematics varied with sitting posture (Figure 3). For the two slouched postures the pelvis was positioned further forward at start. The nominal posture showed a greater torso pitch with a greater head displacement compared to the other two sitting postures. The 60 mm slouch posture showed less torso pitch and shorter head displacement compared to the 40 mm slouch posture (Figure 3). The different front seat positions had limited influence on the trajectories.

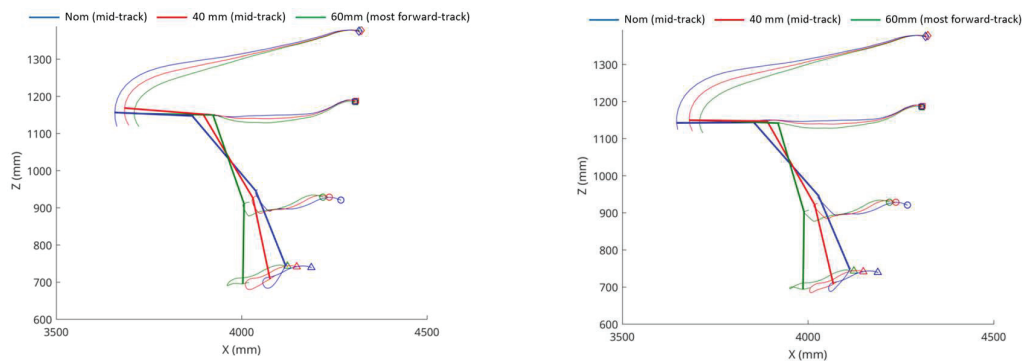


Figure 3 Visualization of trajectories and posture at peak forward displacement for head (diamond), T1 (square), T12 (circle), and pelvis (triangle) displacement, for the three different sitting postures (nominal : blue; 40 mm slouch: red; 60 mm slouch: green); when front seat in mid-track position (left) and front seat in the most forward-track position (right).

The top views of the T1 trajectory and the arms (Appendix G) showed that the nominal posture resulted in a more inboard torso rotation compared to the two slouched sitting postures, and it was not influenced by the front seat position.

With the front seat in mid-track position, the legs were restricted to stretch out to the extent possible in the configuration with front seat in most forward-track position (Appendix E).

The rearward rotation of the pelvic angle started earlier in the slouched sitting postures compared to the nominal posture (Appendix H). For the nominal and the 40 mm slouch postures, the pelvis rotation changed direction at about 80 ms, while no change of direction occurred in the 60 mm slouch posture.

The jugular notch/shoulder belt vertical distance showed that the shoulder belt has an initially higher position on sternum at time 0, and that it moved closer to the neck and up the sternum in the two slouched postures during the crash compared to the nominal posture (Appendix I and Figure 4). In both slouched postures, the spine got into a lateral s-shape during the event, being most pronounced for the 60 mm slouch posture (Figure 4).

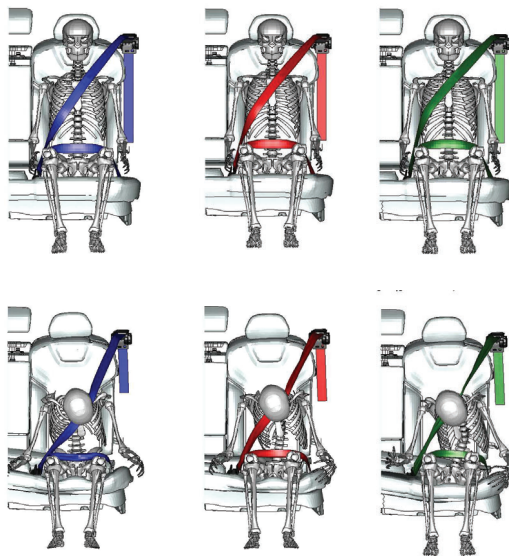


Figure 4 Shoulder belt position at start (first row) and at approximately time of maximum forward displacement (second row), for nominal (blue seat belt), 40 mm slouch (red seat belt) and 60 mm slouch (green seat belt) postures. Front seat in mid-track position.

Occupant response

The maximum responses are presented as normalized values relative to the nominal sitting posture with the front seat in mid-track position (Table 1). A small increase in head acceleration was seen in the slouched postures compared to nominal posture. A minor relative increase of neck tension was also seen.

The upper chest band deflection was 44-67% lower for the slouched postures relative the nominal posture with mid-track front seat position (Table 1). The lower chest band deflection was substantially less in the slouched postures, compared to the nominal; especially the 60 mm slouch posture with 99% lower deflection than the nominal. The rib strain pattern shows that the highest strain was obtained for upper left rib (L1), in all postures (Appendix J). Furthermore, a higher strain was seen to the left upper ribs (L2 to L4) and to the right mid ribs (R5 to R8) in the nominal posture, as compared to in the slouched postures.

Up to 38% relative difference between slouched and nominal postures is seen for lumbar spine compression forces (Table 1). Lumbar spine sagittal flexion moments follow the trend of the compression forces. Lateral bending moment in the lumbar spine changes sign from negative values (lumbar vertebrae L1, L2, L3) to positive moments (lumbar vertebrae L3, L4), for both slouched postures (Appendix K). Shoulder belt forces are at the same levels for all configurations, due to the seat belt load limiting function (Table 1). However, the shoulder belt forces started slightly earlier in the nominal posture with its more upright torso, compared to the slouched sitting postures.

When comparing the influence of the two front seat positions for the nominal sitting posture, the head and neck loadings were slightly lower, while lumbar spine forces are slightly higher in the most forward-track position

(Table 1). Overall, the simulations with most forward-track front seat showed similar trends to both kinematics and loadings as for the mid-track comparison, when comparing the nominal sitting posture with the slouched postures.

Table 1 The maximum responses of head, chest, lumbar spine, femur and seat belt, normalized relative the simulation with nominal sitting posture with front seat in mid-track position and most forward-track position.

	Mid-track position			Most forward-track position		
	Nominal	40 mm slouched	60 mm slouched	Nominal	40 mm slouched	60 mm slouched
Max head acceleration	1	1.04	1.02	0.95	1.00	0.99
Max chest acceleration (T8)	1	1.19	1.08	0.94	1.02	0.91
Upper neck force (tension)	1	1.04	1.06	0.95	1.01	1.07
Chestband (upper)	1	0.56	0.33	1.11	0.73	0.40
Chest band (lower)	1	0.25	0.01	1.01	0.28	0.01
Lumbar spine force (compression)						
L1	1	1.22	1.38	1.03	1.20	1.37
L2	1	1.20	1.34	1.04	1.21	1.33
L3	1	1.16	1.26	1.04	1.16	1.22
L4	1	1.14	1.20	1.02	1.10	1.15
L5	1	1.13	1.17	1.01	1.08	1.11
Shoulder belt force	1	0.99	0.99	1.02	1.01	1.01
Lap belt force	1	0.93	0.97	1.04	0.97	0.99

DISCUSSIONS

This study investigated the effect of slouched posture on occupant kinematics and responses in frontal impact by HBM simulations in a rear seat environment with a state-of-the-art restraint. It illustrates the importance of balanced interaction with the lap and shoulder belt in a frontal impact and shows that this interaction can be influenced by the initial pelvis rotation and its longitudinal position on the seat. Balanced interaction with the lap and shoulder belt comprises of an early and tight coupling to the pelvic bones, enabling a controlled forward torso and head movement, including a desired torso pitch (Adomeit and Heger, 1975, Adomeit, 1977, Kent and Forman, 2015). The preferred balance of lap and shoulder belt interaction was affected by the initially more rearward tilted and further forward positioned pelvis in the slouched postures, also resulting in a more rearward reclined torso and a slightly higher lap belt position on the pelvis. In comparison to the nominal posture, this unbalance influenced the restraint of the pelvis and the torso pitch during the simulated crash, having impact on the movement of the shoulder belt and the loading of the spine.

During the impact, both slouched postures exhibited less torso pitch compared to the nominal posture. The pelvis was not restrained as efficiently as in the nominal posture simulation since the lap belt had a slightly higher initial position on the ASIS. Furthermore, the shoulder belt moved up the sternum to a higher extent in the slouched postures. In the extreme slouched posture, the mid-line of the shoulder belt even moved above the sternum. This shoulder belt interaction amplified the kinematics imbalance with the pelvis moving forward and the upper torso held back by the shoulder belt, reducing the torso pitch. This type of kinematics contributed to the higher lumbar spine compression forces in the slouched postures.

As the mid and upper part of the shoulder belt moved up the sternum and closer to the neck in the slouched postures, the lower part of the shoulder belt moved upwards as well. This is seen when comparing the rib strain pattern in Figures J1 and J2 (Appendix J). Although the shoulder belt interaction in the slouched postures was undesirable, the maximum rib strain was favorable relative to the nominal posture, while the neck tension was slightly higher. In addition, the shoulder belt interaction resulted in a prominent lateral s-shape of the spine in the slouched postures, which can be seen when studying the front view of the spine (Figure 4) at maximum forward displacement. The potential consequences of this lateral s-shape of the spine are reflected in the lumbar spine lateral bending moment, where the highest moments are negative for L1 to L2 and then gradually shift to positive values for L4 and L5 (see Appendix K). This change in lumbar spine lateral bending is not seen in the nominal posture, with the shoulder belt spread over the sternum embracing larger part of the ribcage.

No submarining of the whole pelvis occurred. However, partial submarining occurred in the extreme slouched posture of 60 mm forward translation and with the most forward-track front seat position, with the outboard lap belt slipping over the ASIS. Lack of contact with the front seat allowed some upward rotation of the leg, which contributed to the lap belt sliding off the pelvis. Exploring submarining risk in frontal impacts, Beck et al. (2014) found that a slouched sitting posture, achieved with 38 mm foam behind the pelvis, had the largest effect in a parameter study varying pretensioner, anti-submarining seat pan and upper anchorage points, in addition to a slouched posture. Furthermore, Forman et al. (2022) also found a slouched sitting posture being one of two most important parameters increasing the risk of submarining, when investigating various parameters influence on protection for a booster seated child HBM exposed to a frontal impact.

The modelled vehicle is spacious, offering 127 mm knee to front seat distance in the nominal posture with the front seat in mid-track position. In the nominal posture, there was no knee to front seat contact during the crash, but the feet and the lower part of the leg interacted with the front seat. In the slouched postures, larger areas of both legs were in contact with the front seat, but there was still no loading through the knee, meaning no femur compression forces. Especially for front seat occupants in conventional passenger cars, knees often serve as load paths in frontal impacts, and have shown to be efficient in reducing the risk of submarining in reclined seating position (Rawska et al., 2019). In some vehicle seat configurations, such as living room seating or limousine configuration with generous leg space, there are limited possibilities to use the knees as a load path to control the pelvis movement. The choice of the spacious rear seat environment in the present study, would likely better reflect such environments, and the study can contribute to the understanding of load paths and means to control the kinematics for submarining and lumbar spine forces.

Limited data is available regarding slouched sitting postures in vehicles. Reed et al. (2020) identified slouched posture in 3.9% of the time, for adult front seat passengers in a driving study. Identifying slouching is difficult, especially through camera detection only. In the study by Reed et al. (2020) it is not clear how much forward pelvis movement was needed to identify it as slouched posture. Due to lack of data for adult rear seat passengers, and the need to get more precise measurements, a limited laboratory user study was used as input in the present study. Eighteen individuals participated and the degree of slouch could be established by measuring ASIS location, comparing their initial self-selected posture to an upright reference sitting posture. The selected slouched postures for the simulations were based on representative slouching (40 mm), in addition to an extreme slouched posture (60 mm), which was not found among the self-selected postures in the user study. Being a limited user study in a stationary car, it probably does not cover all real-world slouched postures. A driving study would likely contribute to a wider range of slouched postures compared to this laboratory user study. The test persons covered 10 percentile females up to 30 percentile males. Additional studies, with wider range of test persons and evaluation of time influence, is needed to further understand the range of sitting postures in terms of slouched sitting posture.

Several of the findings in this study would not have been possible without the use of an advanced HBM. With its anatomically representative design, an HBM offers the possibilities to detect occupant detailed kinematics, such as the phenomenon of lateral s-shape of the spine due to unfavorable shoulder belt interaction. This would not be possible if using a crash test dummy, due to the lack of segmented spinal design. Also, the increased stiffness in the lumbar spine in certain crash test dummies, limits the sensitivity to parameters influencing submarining (Uriot et al., 2015). Although not validated for different pelvis rotations and the rearward reclined torso, it is believed that the HBM was able to capture the essence of the study. The HBM used in this study has a lumbar spine which was validated on a subsystem level (Östh et al., 2020), and the model's kinematics has previously been validated for reclined seating positions (Mroz et al., 2020). Since then, the pelvis model has been updated with a new pelvis which is more representative of a 50th percentile male occupant (Pipkorn et al., 2021). Gepner et al. (2022) showed that the kinematic response of SAFER HBM v10 compared relatively well with respect to PMHS tests in a reclined posture, and the SAFER HBM v10 was also found to correlate equally well as the GHBM v6.0 and THUMS v6.0, but all three models showed a more compliant lumbar flexion than the PMHS.

The study focuses on kinematics. Some occupant responses are included to quantify relative differences in load transfer through the body parts. Due to lack of validated injury criteria and risk functions for all body parts, and to focus on the relative comparison, the occupant responses are presented as normalized values relative to the nominal sitting posture with the front seat in mid-track position.

Today, there is a high research interest on reclined seating positions, since it is expected that customers will demand relaxed seating as new possibilities are made possible in autonomous vehicles (Jorlöv et al., 2017). In addition, consumer information test organizations are starting to investigate virtual testing possibilities, which allows a wider range of parameters, also including sitting posture. Some of the challenges emphasized in this study, especially regarding lumbar spine loads and pelvis rotation, are also seen in reclined seating positions. There is an increased risk of submarining in reclined seating positions, and when that is addressed, lumbar spine forces increase (Mroz et al., 2020, Boyle et al., 2019). Research programs are ongoing to establish validation data for reclined seating positions. This progress will likely benefit tools to be used to evaluate slouched sitting postures

as well, since there are many similarities in these loading conditions. However, as wider range of sitting postures are addressed in the development of vehicles, validation data is needed to cover those aspects.

This study was limited to slouching of the pelvis, by modifying the position and orientation of the pelvis. A slumped posture, with more kyphosis in thoracic spine, was not included in the study. The amount of slouching was based on observations of short occupants. Seat cushion length may be a possible parameter influencing slouched posture of shorter occupants to a higher extent than taller occupants, due to reduced ability to comfortably bend their legs around the seat cushion. It is possible that taller occupants, such as 50th percentile males, would be less prone to slouch. Further studies, with a larger range of test persons is needed to further understand the extent of slouched posture.

CONCLUSION

Slouched sitting postures affect occupant kinematics and loading in a frontal impact. The slouched postures resulted in less torso pitch, contributing to higher lumbar compression forces. By exploring variations in sitting posture in terms of slouching, within a reasonable user range, knowledge can be gained in understanding mechanisms of submarining and lumbar spine loading. These learnings are relevant for sitting postures in conventional cars today, in addition to a wider range of sitting postures, such as reclined seats, likely increasing as a result of future car interior developments.

ACKNOWLEDGEMENT

The authors would like to acknowledge Jonas Östh, Volvo Cars, for his support with the HBM.

The project was partly financed by FFI (Strategic Vehicle Research and Innovation); by VINNOVA, the Swedish Transport Administration, the Swedish Energy Agency and the Swedish vehicle industry. The project partners are Chalmers University of Technology and Autoliv. The project is associated to SAFER, Vehicle and Traffic Safety Centre at Chalmers.

REFERENCES

- Adomeit D, Heger A. Motion sequence criteria and design proposals for restraint devices in order to avoid unfavorable biomechanics conditions and submarining, Proceedings of 19th Stapp Car Crash Conference, 1975:139-165.
- Adomeit D. Evaluation methods for the biomechanical quality of restraint systems during frontal impact. Proceedings of 21st Stapp Car Crash Conference, 1977: 911-932.
- Beck B, Brown J, Bilston L. Assessment of vehicle and restraint design changes for mitigating rear seat occupant injuries. *Traffic Inj Prev.* 2014;15(7):711-9.
- Bose D, Crandall JR, Untaroiu CD, Maslen EH. Influence of pre-collision occupant parameters on injury outcome in a frontal collision. *Accid Anal Prev.* 2010;42(4):1398-407.
- Boyle KJ, Reed MP, Zaseck LW, Hu J. A Human Modelling Study on Occupant Kinematics in highly reclined seats during frontal crashes. Proc. of the IRCOBI Conference, Paper no IRC-19-43, 2019, Florence, Italy.
- Forman J, Miller M, Perez-Rapela D, Gepner B, Edwards M, Jermakian J, Investigation of factors influencing submarining mitigation with child booster seats, *Traffic Inj Prev.* 2022:16:1-7.
- Gepner B D, Joodaki H, Sun Z, Jayathirtha M, Kim T, Forman J, Kerrigan J. Performance of the Obese GHBMCM models in the sled and belt pull test conditions. Proc. of the IRCOBI Conference, Paper no IRC-18-45, 2018, Athens, Greece.
- Gepner B, Perez-Rapela D, Forman J, Ostling M, Pipkorn B, Kerrigan J. Evaluation of GHBMCM, THUMS and SAFER Human Body Models in Frontal Impacts in Reclined Postures, Proc. the IRCOBI Conference, Paper No IRC-22-27, 2022, Porto, Portugal.
- Hwang E Hu J, Chen C, Klein K, Miller C, Reed M, Rupp J, Hallman J, Development, evaluation and sensitivity analysis of parametric finite element whole-body human models in side impacts, *Stapp Car Crash Journal* 2016:60:473-508.

- Hanson L, Sperling L, Gard G, Ipsenc S, Vergera C, Swedish anthropometrics for product and workplace design, *Applied Ergonomics*, 2009;40(4): 797-806.
- Helander MG, Zang L. Field studies of comfort and discomfort in sitting. *Ergonomics*, 1997;40(9): 895-915,
- Håland Y, Nilsson G. Seat belt pretensioners to avoid the risk of submarining – a study of lap belt slippage factor. Proc. of the 13th International Technical Conference of Enhanced Safety of Vehicles, 1991, Gothenburg, Sweden.
- Izumiyama T, Nishida N, Iwanaga H, Chen X, Ohgi J, Mori K, Hayashi T, Sakuramoto I, Asahi R, Sugimoto S, Ueno, M. The analysis of individual difference in human skeletal alignment in seated posture and occupant behavior using HBMs. Proc. of the IRCOBI Conference, Paper No IRC-18-84, 2018, Athens, Greece.
- Jakobsson L, Bohman K, Stockman I, Andersson M, Osvalder AL. Older children's sitting postures when riding in the rear seat. Proc. of the IRCOBI Conference, Paper No IRC-11-44, 2011, Krakow, Poland.
- Jorlöv S, Bohman K, Larsson A. Seating Positions and Activities in Highly Automated Cars – A Qualitative Study of Future Automated Driving Scenarios. Proc. of the IRCOBI Conference, Paper no IRC-17-11, 2017, Antwerp, Belgium.
- Kent R, Forman J. Restraint System Biomechanics. In: Yoganandan N, Nahum A, Melvin J. (Eds). *Accidental injury*. Springer, New York. 2015: 116-120.
- Mroz K, Östling M, Richardson R, Kerrigan J, Forman J, Gepner B, Lubbe N, Pipkorn B. Effect of seat and seat belt characteristics on the lumbar spine and pelvis loading of the SAFER human body model in reclined postures, Proc. of the IRCOBI Conference, Paper No IRC-20-58, 2020 (online).
- Osvalder AL, Hansson I, Stockman I, Carlsson A, Bohman K, Jakobsson L. Older children's sitting postures, behaviour and comfort experience during ride – A comparison between an integrated booster cushion and a high-back booster. Proc. of the IRCOBI Conference, Paper No IRC-13-105, 2013, Gothenburg, Sweden.
- Östh J, Bohman K, Jakobsson L. Evaluation of kinematics and restraint interaction when repositioning a driver from a reclined to upright position prior to frontal crash using active human body model simulations. Proc. of the IRCOBI Conference, Paper No IRC-20-50, 2020 (online).
- Park J, Ebert SM, Reed MP, Hallman J. A statistical model including age to predict passenger postures in the rear seats of automobiles, *Ergonomics*, 2016;59(6): 796–805
- Pipkorn B, Östh, J, Brynskog E, Larsson E, Rydqvist L, Iraeus J, Perez-Rapela D, Jakobsson L. Validation of the SAFER Human Body Model kinematics in far-side impacts, Proc. of the IRCOBI Conference, 2021 (online).
- Rawska K, Bronislaw G, Kulkarni S, Chastain K, Zhu J, Richardson R, Perez-Rapela D, Forman J, Kerrigan J, Submarining sensitivity across varied anthropometry in an autonomous driving system environment, *Traffic Inj Prev*. 2019;20(sup2):S123-S127.
- Reed MP, Ebert SM, Jones MLH, Hallman JJ. Prevalence of non-nominal seat positions and postures among front-seat passengers. *Traffic Inj Prev*. 2020;21:1-6.
- Reed MP, Ebert SM, Jones MLH, Hallman A naturalistic study of passenger seating position, posture, and restraint use in second-row seats. *JJ.Traffic Inj Prev*. 2022;15:1-6.
- Uriot J, Potier P, Baudrit P, Trosseille X, Richard O, Duard R. Comparison of HII, HIII and THOR dummy responses with respect to PMHS sled tests. Proc. of the IRCOBI Conference, Paper No IRC-15-55, 2015, Lyon, France.

APPENDIX A. RESULTS FROM THE LABORATORY USER STUDY

The boxplot (Figure A1) shows the slouching of the 18 test participants, by calculating the difference in x-position of the left and right ASIS in their self-selected posture and their reference posture.

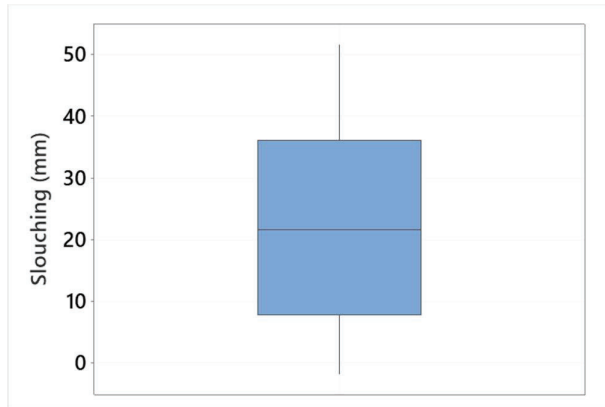


Figure A1 The boxplot shows the slouching of the 18 test participants.

APPENDIX B. THE PELVIC ANGLE (PA) MEASUREMENT

The pelvic angle (PA) was measured as the angle between pubic symphysis (mid) and ASIS in the mid-sagittal plane, similar as Izumiyama et al. (2018).

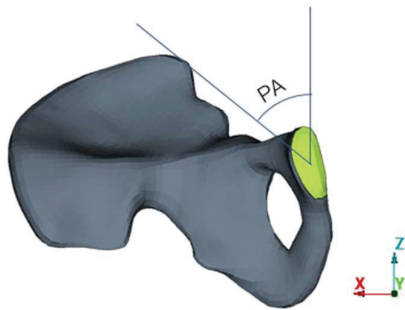


Figure B1 The pelvic angle.

APPENDIX C. PELVIS AND SPINE POSTURE

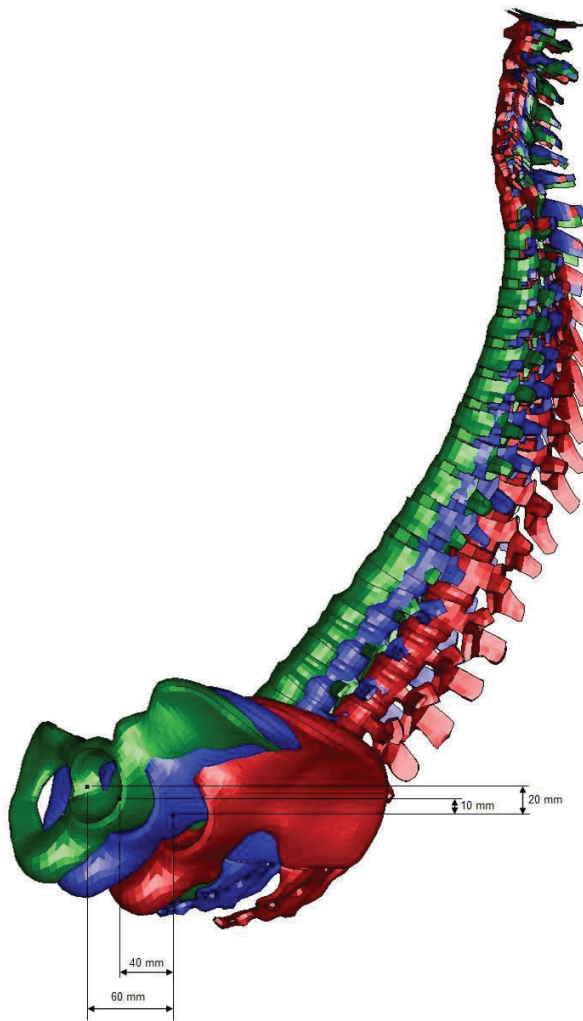


Figure C1 A side view of the three sitting postures (green-nominal, blue-40 mm slouch, red – 60 mm slouch), viewing pelvis orientation and spine curvature.

APPENDIX D. SIMULATION SERIES MATRIX

Table D1 The simulation series matrix.

Sim. No.	Sitting posture	Pelvic Angle	Front seat position
1	Nominal	52,5°	Mid-track
2	Nominal	52,5°	Most forward-track
3	40 mm slouch	56°	Mid-track
4	40 mm slouch	56°	Most forward-track
5	60 mm slouch	59°	Mid-track
6	60 mm slouch	59°	Most forward-track

APPENDIX E. SIDE VIEWS

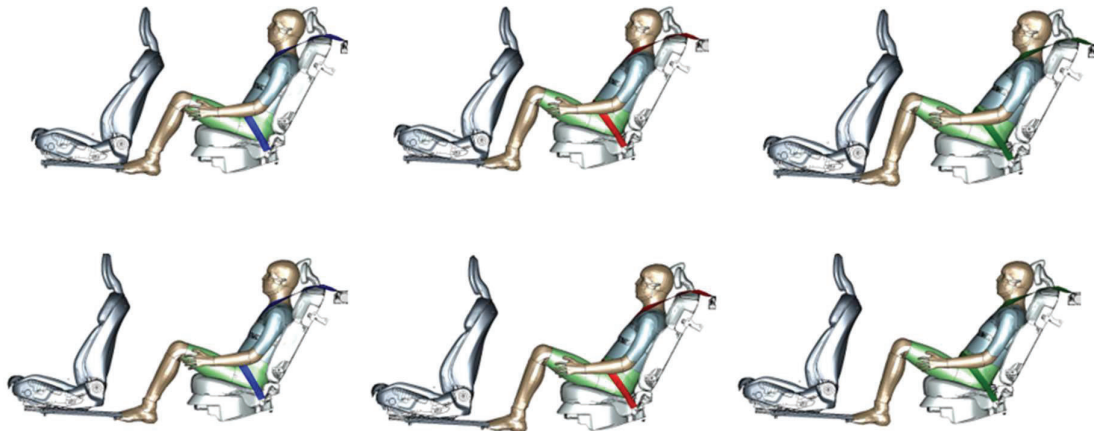


Figure E1 Outboard side view of the HBM at time 0; nominal (blue seat belt), 40 mm slouch (red seat belt) and 60 mm slouch (green seat belt). First row shows simulations with front seat in mid-track position, and second row shows front seat in most forward-track position.

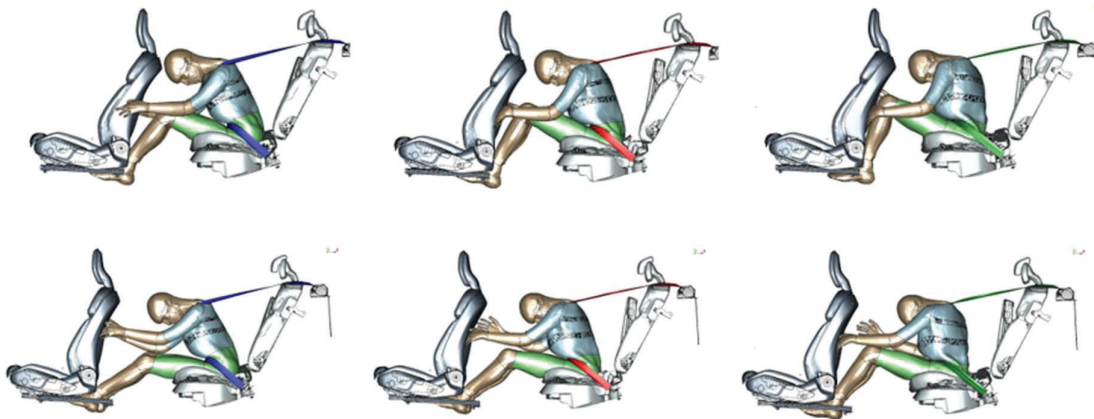


Figure E2 Outboard side view of the HBM at maximum excursion; nominal (blue seat belt), 40 mm slouch (red seat belt) and 60 mm slouch (green seat belt). First row shows simulations with front seat in mid-track position, and second row shows front seat in most forward-track position.

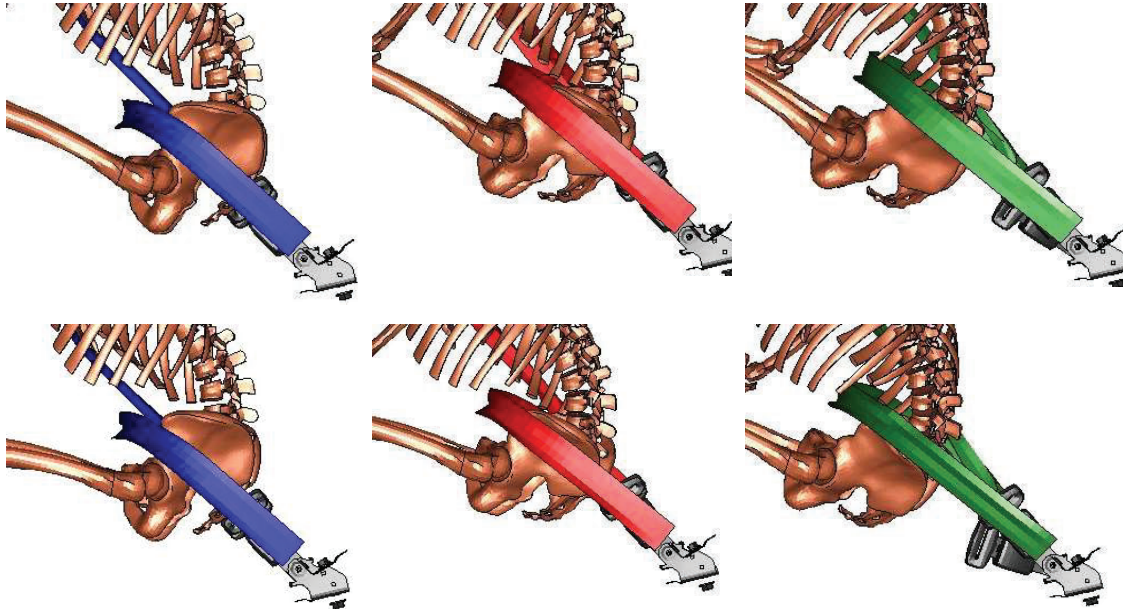
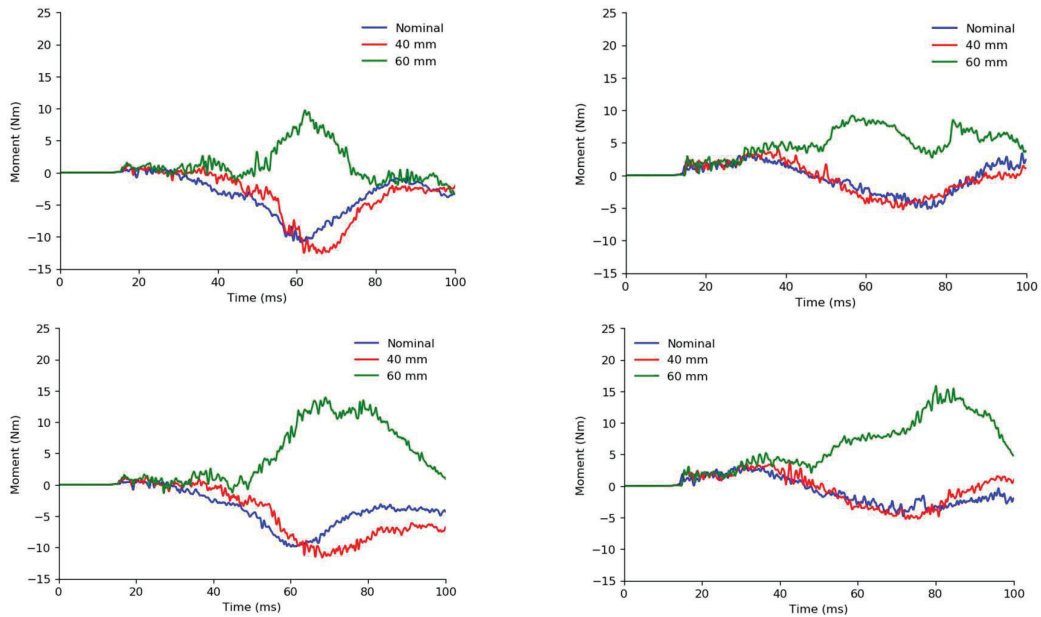


Figure E3 Close-up on outboard side view of the HBM at maximum forward excursion; nominal (blue belt), 40 mm slouch (red belt) and 60 mm slouch (green belt). First row shows simulations with front seat in mid-track position, and second row shows front seat in most forward-track position.

APPENDIX F. ASIS MOMENTS

The negative ASIS moment values indicate that the lap belt is engaging the pelvis below the center of the ASIS load cell.



Appendix F1 The moment of ASIS as function of time. First row shows left and right ASIS with front seat in mid-track position. Second row shows left and right ASIS with front seat in most forward-track position.

APPENDIX G. TOP VIEW T1 TRAJECTORIES

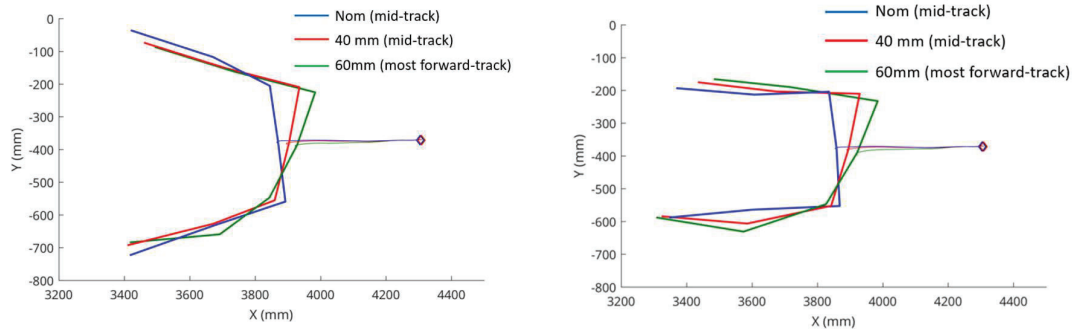


Figure G1 Top views showing the T1 trajectories and the arms connected to the T1 vertebra via nodes on the acromion processes at time of maximum excursion, for the three different sitting postures (nominal: blue; 40 mm slouch: red; 60 mm slouch: green), when front seat in mid-track position (left) and front seat in most forward-track position (right).

APPENDIX H. PELVIC ANGLE AS FUNCTION OF TIME

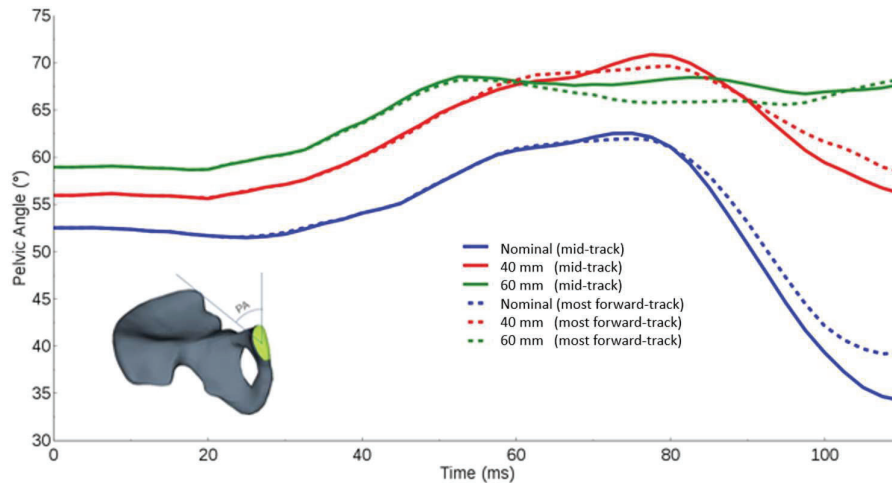


Figure H1 Pelvic angle as function of time, for the three sitting postures (Nominal, 40 mm slouch and 60mm slouch) and with the front seat in the two positions (mid-track, and most forward-track).

APPENDIX I. VERTICAL DISTANCE BETWEEN JUGULAR NOTCH AND SHOULDER BELT

Table I1 The vertical distance between the jugular notch and the shoulder belt mid-line. A negative value indicates that the mid-line of the shoulder belt is above the jugular notch.

Sitting posture	1st row	Distance at 0 ms	Distance at max forward excursion
		(mm)	(mm)
Nom	Mid-track	73	69
40 mm	Mid-track	62	18
60 mm	Mid-track	49	-14
Nom	Most forward-track	73	48
40 mm	Most forward-track	62	-3
60 mm	Most forward-track	49	-16

APPENDIX J. MAXIMUM RIB STRAIN

Figures J1 and J2 show the maximum strain for each rib. Please note that the time for maximum strain may differ between the ribs.

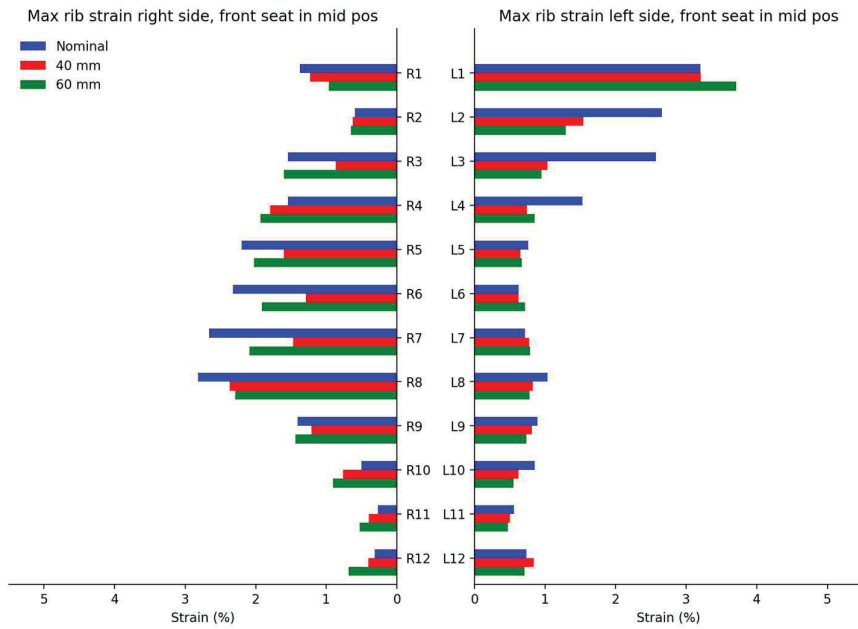


Figure J1 Rib strain (%) for each rib, on right and left side, for nominal (blue), 40 mm slouch (red) and 60 mm slouch (green) postures, with front seat in mid-track position.

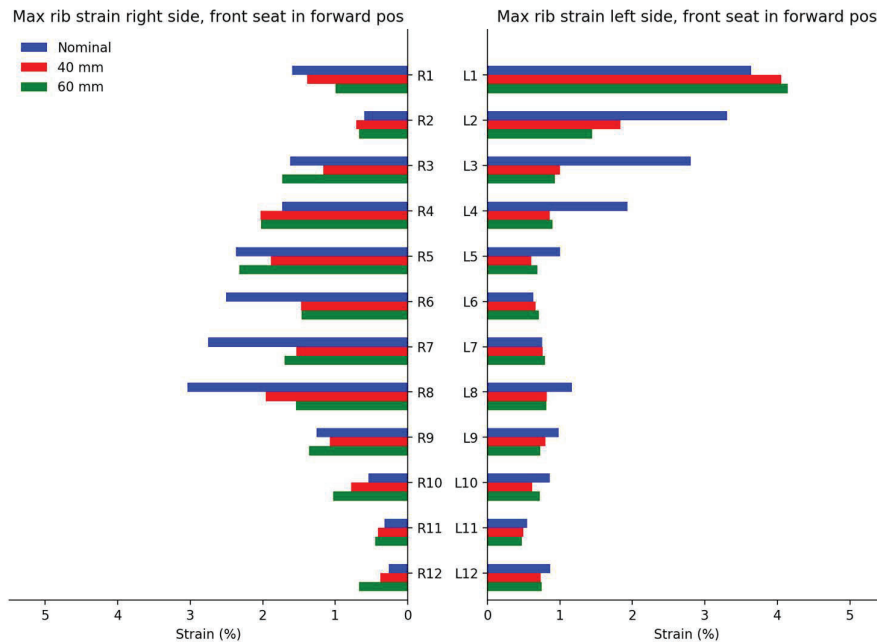


Figure J2 Rib strain (%) for each rib, on right and left side, for nominal (blue), 40 mm slouch (red) and 60 mm slouch (green) postures, with front seat in most forward-track position.

APPENDIX K. LUMBAR SPINE LATERAL BENDING MOMENT

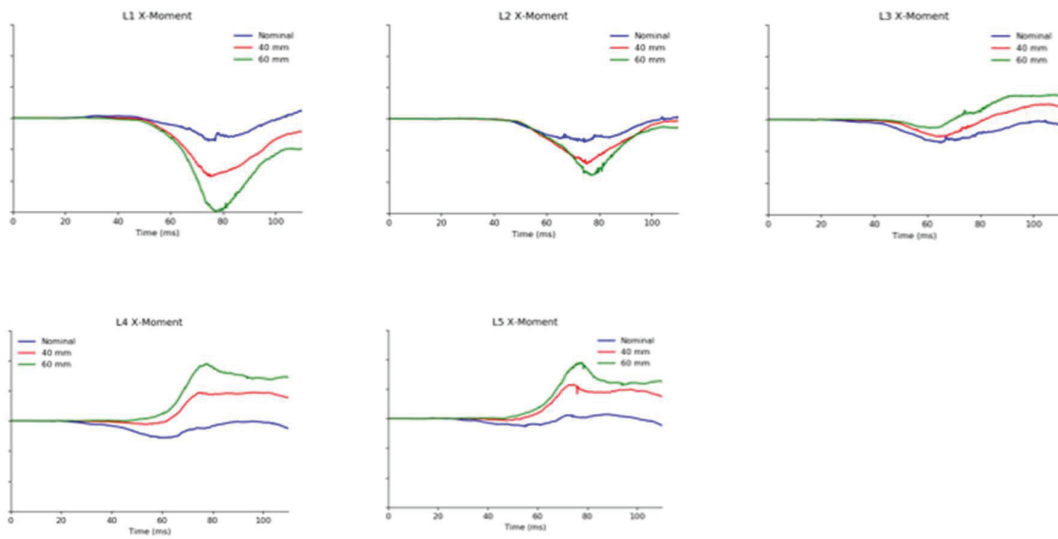


Figure K1 Lumbar spine lateral bending moment (x-moment) for L1, L2, L3, L4 and L5 vertebrae, for the simulations in nominal (blue), 40 mm slouch (red) and 60 mm slouch (green) postures, with front seat in mid position .

COMPARISON OF THE INJURY RISK PREDICTION OF THE THOR-RECLINED DUMMY AND THE THUMS HBM

Pablo Lozano, Simona Roka, Alessandro Gravina, María de Odrizola, Genís Mensa
IDIADA Automotive Technology
Spain

William Marshall
CELLBOND
England

Paper Number 23-0302

ABSTRACT

Autonomous vehicles are expected to allow car occupants to position themselves in more relaxed positions inside the vehicle. These new seating positions constitute a new challenge for crash safety analysis. Therefore, new crash test protocols, adapted to this new paradigm, may be required in the future.

In the literature, most of the virtual reclined posture analysis has been performed using Human Body Models (HBMs) which are increasingly used to assess vehicle safety and injury risk, as currently regulated ATDs (Anthropomorphic Test Devices) are neither designed nor validated for reclined seating configurations. Nevertheless, these HBM simulation studies need to be correlated against repeatable physical tests that allow future cars to be rated according to regulation and consumer testing protocols. New options for crash dummies such as the THOR-Reclined kit from CELLBOND; which allows adapting the THOR ATD for these new reclined seating postures, are being developed and may enable the performance of physical tests in reclined occupant positions. However, the question of whether its performance is comparable to that of an HBM remains unanswered.

A series of simulations were then conducted comparing the behavior of the THOR-Reclined simulation model and the THUMS v4.1 by means of kinematics and injury risk prediction. Also, a series of tests using the THOR-Reclined in IDIADA's deceleration facility have been planned and the results will be shared in future publications. Injury risk prediction was then compared between the HBM and the ATD.

The ATD and the HBM FE models were compared by means of kinematics, restraint system outputs, injury criteria, and injury risk prediction. The result of this comparison will be discussed in this paper.

Some differences were observed between the models. THUMS allowed to study injury risk criteria based on the strain of the rib cage, while the ATD is mainly designed for measuring displacements and accelerations.

The primary limitation of this work is the lack of thorough validation data of the active HBM and the ATD model in the studied position. However, this work provides further insight into the comparability of their performance and the differences found between the studied models.

Differences have been found between the two models, mainly due to their physical dissimilarities. Nevertheless, some comparisons can be made between them from a kinematic and injury criteria perspective and will be shared in this paper.

INTRODUCTION

Future traffic scenarios, in 5 to 10 years, will most likely include mixed traffic (vehicle fleets composed of both traditional vehicles and vehicles with a high level of automation) or automated ones. Based on this information, Level 3 [1] vehicles are considered in the study. Level 3 vehicles represent "conditional automation" meaning that a human driver will respond appropriately to a request if needed. This level of automation allows the driver to be seated in a more relaxed, reclined position.

A current state-of-the-art frontal restraint system, i.e., a 3-point seat belt with B-pillar mounted belt guide, driver airbag in the steering wheel and knee bolster in the instrument panel, has limited protection functionality in the new proposed seating positions in which seatback angles are further from nowadays regulations' seatback angles. In particular, a reclined occupant posture may increase the risk of submarining [2] [3] [4], which is where the lap belt translates over the anterior superior iliac spines (ASIS) to load the abdomen directly and can result in injuries to the lumbar spine and hollow organs of the lower digestive system.

To assess in detail the injuries that may result from a crash, the injury output from a HBM or ATD is needed. The injury criteria output from an ATD is generally limited to specific scenarios (one specific ATD for one specific type of crash test) and limited by the mechanical elements that form the surrogate. Therefore, some of the measurements that can be done with these ATDs, like the chest displacement, are limited to four specific measurement points in the case of the THOR dummy (Upper Left, Upper Right, Lower Left, and Lower Right) or even one single measurement point for the Hybrid III dummy. HBMs, however, can measure the strain of every point of the rib cage, measuring all the circumference of the body and estimating the probability of 2, 3, 4, or 5 rib fractures depending on the age of the occupant. They can even be used to calculate if the structural integrity of the rib cage is in danger. Nevertheless, it is important to understand the variation of the outputs of both technologies, HBMs and ATD.

In the literature, most of the virtual reclined posture analysis has been performed using Human Body Models (HBMs) which are increasingly used to assess vehicle safety and injury risk, as currently regulated ATDs (Anthropomorphic Test Devices) are neither designed nor validated for reclined seating configurations. Nevertheless, these HBM simulation studies need to be correlated against repeatable physical tests that allow future cars to be rated according to regulation and consumer testing protocols. New options for crash dummies such as the THOR-Reclined kit from CELLBOND; which allows adapting the THOR ATD for these new reclined seating postures, are being developed and may enable the performance of physical tests in reclined occupant positions. However, the question of whether its performance is comparable to that of an HBM remains unanswered. The purpose of this study was to compare the outputs of a HBM and an ATD.

METHODOLOGY

Two simulation models (one HBM -THUMS- and one ATD -THOR-Reclined-) were compared by means of kinematics, injury criteria, and injury risk prediction in a generic frontal simulation environment [5] with a semi-rigid seat¹ during a frontal crash simulation. This semi-rigid seat was proposed by Uriot et al. [6] in 2015 and consists of two plates attached to a set of strings that can be changed to adjust the stiffness of the seat. The plate in the front recreates the anti-submarining foam of a standard seat and the second plate recreates the seat pan. This allows recreating a foam seat in a repeatable way while being a simple seat to model for simulation. The simulation model used in this study is shown in Figure 1.

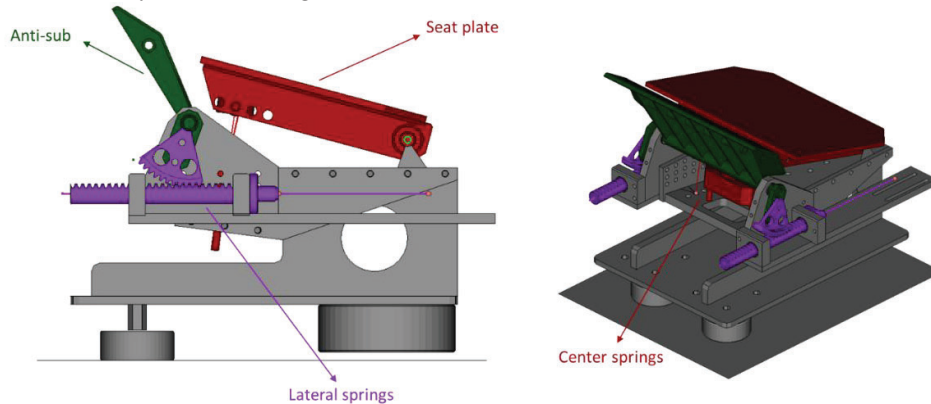


Figure 1: LAB CEESAR Semi-Rigid seat simulation model in the frontal configuration

Two impact simulations were performed using LS-DYNA MPP R9.3.1 (ANSYS/LST, Livermore, CA, USA) as solver and the Total HUMAN Model for Safety (THUMS, version 4.1) AM50 Occupant model (Toyota Motor Corporation, Japan) and the ATD-TH50R-D00.17_R00.06 model (ATD-MODELS GmbH, Weißwasser, Germany) as surrogates for the study. These two models are presented in Figure 2.

¹ The semi-rigid seat CAE model was provided by Autoliv [17] from the EU project OSCCAR [20]. This model replicates the lab CEESAR [18] semi-rigid seat which has been used in previous studies regarding frontal collisions [6] [19] [3].

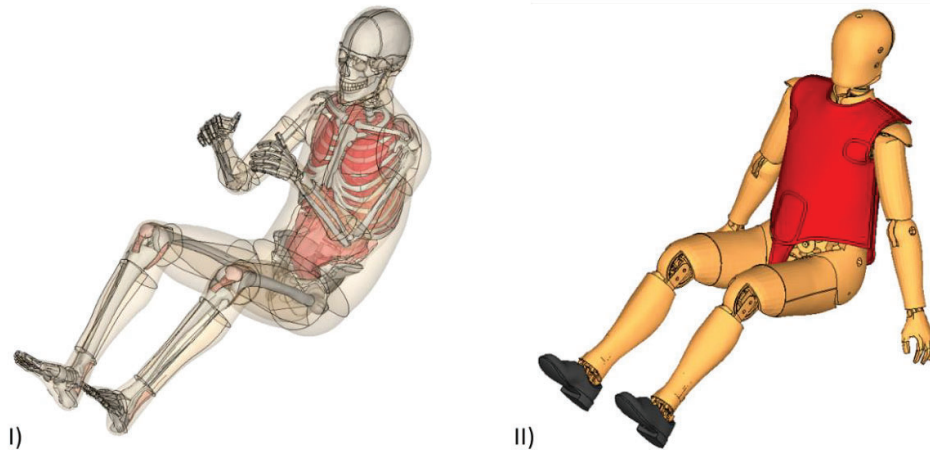


Figure 2: THUMS (Left, I) and THOR-Reclined (Right, II) simulation models in their original postures

Simulation Environment

The simulation environment used for this study is an adaptation of the generic frontal simulation environment used in the SAFE-UP project [5] (Figure 3). This environment consisted of a generic floor geometry and foot support, a semi-rigid seat, a generic seatback, a generic knee bolster, a State-Of-The-Art (SOTA) belt system installed in the seat, a simplified retractor with pre-tensioning and load limiting capabilities, a buckle with a crash locking tongue, an end bracket with pre-tensioner, a simplified belt webbing (defined using *MAT_SEATBELT card from LS-DYNA), a generic steering column (SC) with a production steering wheel, and a generic driver airbag (DAB). This generic environment model was validated by Autoliv.

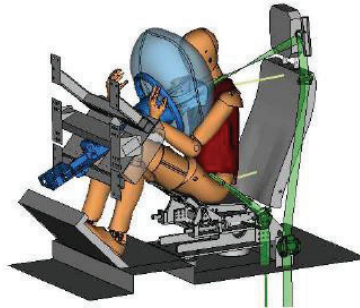


Figure 3: SAFE-UP Generic environment simulation model [5]

Some modifications were made to adapt the proposed environment to the IDIADA’s sled testing facilities and to be able to reproduce it physically. The semi-rigid seat was used in the frontal configuration proposed by Richardson in 2020 [3] using 128N/mm seat pan lateral springs, a 379N/mm seat pan center spring, and 132 N/mm anti-submarining springs.

The seatback was simplified for easier construction as a physical part. The adapted model consisted of a rigid steel plate with foam on top to protect the dummy on the rebound phase for future sled tests. This foam was modeled as Ethafoam 220 and had no specific function during the crash phase. The dynamic model of this foam was provided by Autoliv for the SAFE-UP project. The seatback was positioned at a 45-degree angle according to the SAE standard [7] [8].

Regarding the footrest, an expanded polypropylene (EPP) foam with a density of 30g/l was used to reduce tibia loads and stabilize the contacts between the surrogates and the floor. The material characterization was done internally in IDIADA.

The geometry of the knee bolster was maintained from the original model. However, the foam material was changed to an EPP of 60g/l to recreate a stiffer dashboard that can apply higher loads to the occupant’s femurs.

The belt system elements were adapted to the new seatback configuration. The D-ring was positioned close to the seatback, simulating a belt-in-seat mount. The retractor was positioned right below the D-ring to emulate a physical testing routing. The firing parameters of the belt remained the same as in the original model. The 3-point belt system consisted of a shoulder belt retractor with two load limiters (3.5 kN and 10 kN) and 2 kN pre-tensioners, a 2 kN lap belt pre-tensioners, and a crash locking tongue.

The steering column and the belt system remained unchanged from the original model. The collapsible column had a force level of 4.5kN with 100mm of maximum stroke. The updated environment model is presented in Figure 4.

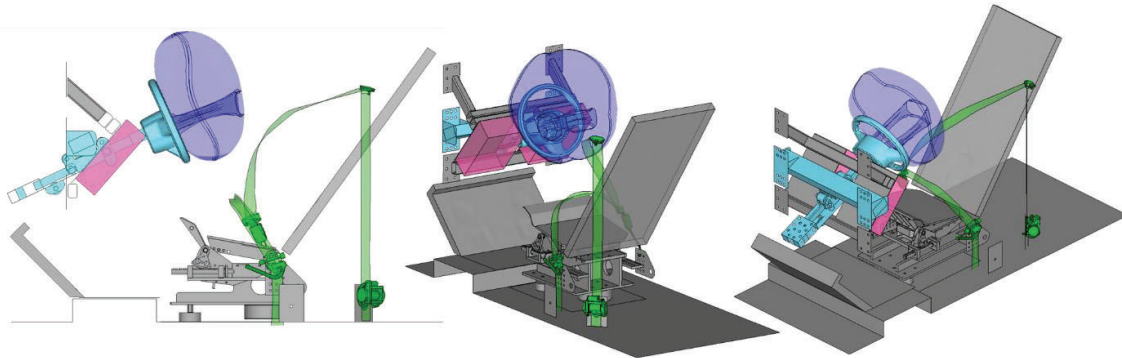


Figure 4: Adapted generic frontal model used in the study. In grey: the semi-rigid seat, seatback, foot support, and structures. In light blue: collapsible steering column and steering wheel. In dark blue: driver airbag. In pink: knee bolster. In green: seatbelt system.

Occupant Positioning and Belt Routing

The study used the THUMS model as the main finite element HBM. This model represents a 50th-percentile male with a stature of 178.6 cm and a weight of 78.5 kg and was used as the baseline model. THUMS was positioned via a (pre)simulation and the THOR-Reclined ATD was positioned based on the achieved posture of the FE HBM. The two models were positioned in a reduced environment with just the semi-rigid seat plates (which were considered rigid), the seatback, and the foot support.

First, the final posture was estimated based on the UMTRI 2018 study [9]. The anatomical landmarks (ankle joint, knee joint, acetabulum joint, L5/S1 joint, T12/L1 joint, C7/T1, Head/C1 joint, head and center of the eye) were calculated using the complete regression model including the anthropometric predictors using Python v3.10.6 (Python Software Foundation, Beaverton, USA). The values used for the posture estimation and the obtained landmarks are shown in Figure 5.

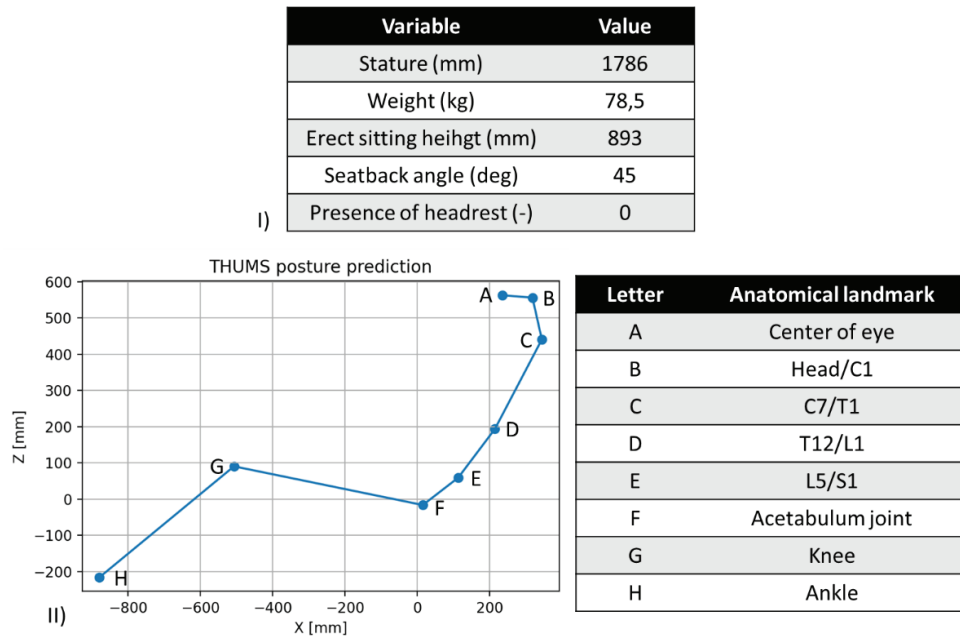


Figure 5: I) Variable values used for the posture estimation, and II) coordinates of the anatomical landmarks obtained if the seat H-point was placed in the (0,0)

To position the occupant model, a (pre)simulation was run using the marionette method [10]. The previously mentioned anatomical landmarks were used as targets to achieve the desired pre-impact posture. The knee and ankle landmarks were modified so the leg's posture fitted the simulation model used for this study. Regarding the arms, they were placed in line with the torso and the hands were placed in contact with the seat to obtain an achievable posture for the THOR-Reclined dummy model. The THUMS nodes used for this (pre)simulation are shown in the following Table.

Table 1: Node IDs used for each anatomical landmark

Anatomical Landmarks	NODE ID	Anatomical Landmarks	NODE ID
Left Ankle	82002574	C7/T1 joint	89000708
Right Ankle	81002574	Left Shoulder	86007088
Left Knee	82074216	Right Shoulder	85007088
Right Knee	81074216	Left Elbow	86006275
Left Acetabulum	83001318	Right Elbow	85006275
Right Acetabulum	83501318	Left Wrist	86003794
L5/S1 joint	89066294	Right Wrist	85003794
T12/L1 joint	89065464	Head/C1 joint	87000782

The positioning was performed based on the work presented by Alexandros Leledakis et al. [11]. A two-step (pre)simulation was used to position the model. The first stage had a duration of 450 ms. During the first phase, one-dimensional elements were used, applying a force from 0 to 500 N to position the model. Simultaneously, the geometrical constraints of the generic environment that had contact with the HBM were moved to their original position. These surfaces (the anti-submarining plate and seat plate of the semi-rigid seat, the footrest, and the seatback) were originally moved 150 mm away from their original position in X and Z directions. The second stage had a duration of 300 ms. In this phase, the one-dimensional elements force was set to 0 and the model was allowed to reach equilibrium. Gravity was activated throughout the complete simulation and a global damping of 0.15 was used. This process is illustrated in Figure 6.



Figure 6: HBM positioning (pre)simulation. The environment elements (in grey) start 150 mm away from their original position and are repositioned during the first stage of the simulation. The last 300 ms are used to reach equilibrium in the model.

The position of the nodes of the HBM, the footrest foam, and the seatback foam were retained for the impact simulation. Foam and internal HBM stresses were not retained.

The same procedure was applied to the THOR-Reclined dummy model. In this case, the reference was the achieved posture of the HBM, so the dummy was positioned as close as possible to the THUMS. Due to the differences between both models, priority was given to the similar positioning of the internal structure of the dummy and the HBM skeleton, starting from the iliac spines. The dummy was (pre)simulated using the same simulation process of the HBM as can be seen in Figure 7.

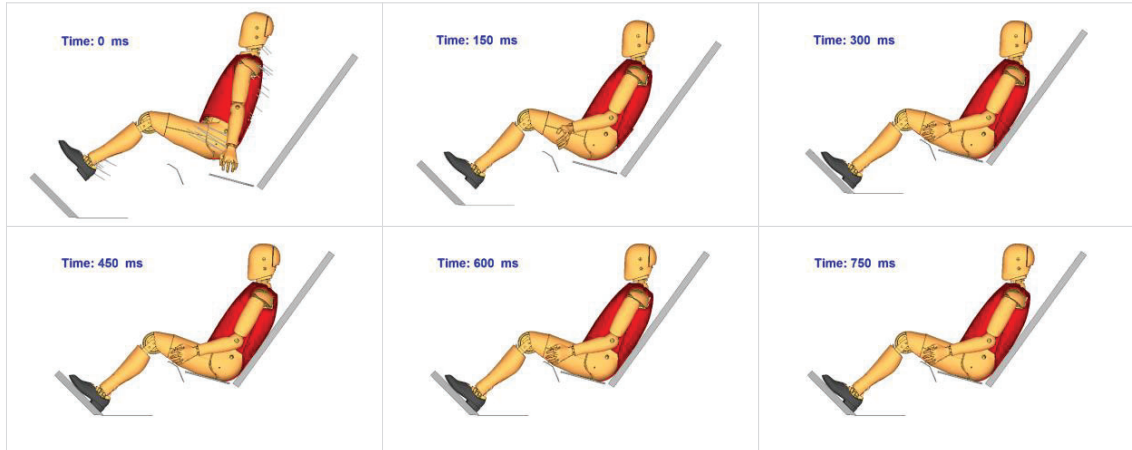


Figure 7: ATD positioning (pre)simulation. The environment elements (in grey) start 150 mm away from their original position and are repositioned during the first stage of the simulation. The last 300 ms are used to reach equilibrium in the model.

Following this method, a comparable posture of the ATD was obtained. A comparison between the posture achieved with each model is shown in Figure 8.

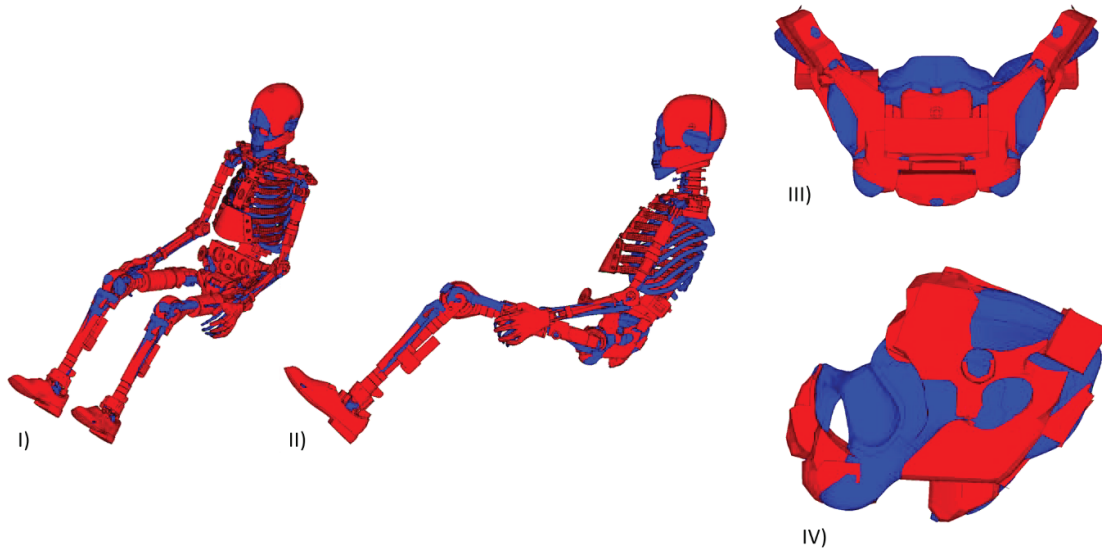


Figure 8: Comparison of the achieved postures of the HBM (blue) and the ATD (red). I) Isometric perspective. II) Lateral view. III) Frontal view of the pelvis of both models. IV) Lateral view of the pelvis of both models.

Regarding the belt routing, in both cases the shoulder belt was positioned following a straight line between the D-ring and the belt tongue, using the shortest path possible that allowed the belt to pass through the middle part of the collarbone of each model. The lap belt was positioned following a straight line between the buckle and the end bracket of the belt, placing the webbing in the lowest part of the abdomen possible for each model (Figure 9). No initial pretension was given to the belt.

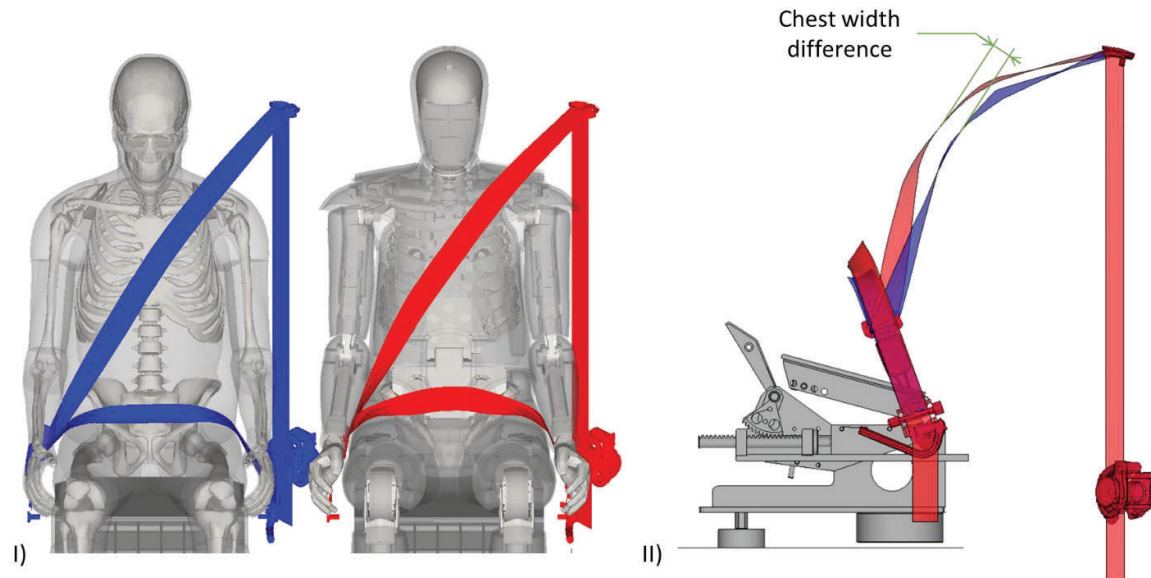


Figure 9: Belt fit comparison of both models. The THUMS belt is presented in blue and the THOR-Reclined belt is presented in red. I) Side-by-side comparison of belt fit over each surrogate. II) Lateral view of the belt and the semi-rigid seat. A gap between both belt models can be observed due to the difference in the chest width of both models.

Crash configuration

The full frontal 56km/h Car-to-Car (C2C) crash pulse from EU project OSCCAR [12] was used for this analysis. The characteristics of this pulse are presented in Figure 10. The pulse was chosen due to its high severity, as this would highlight the similarities and differences that may exist between the HBM and the ATD.

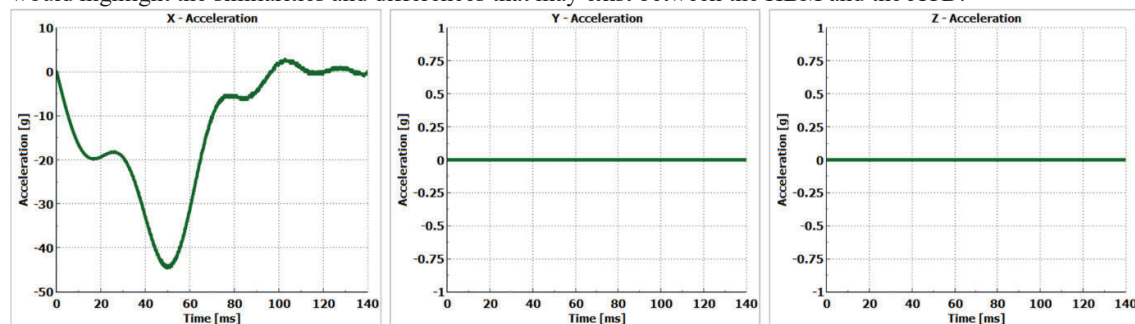


Figure 10: Full frontal 56 km/h C2C crash pulse from EU project OSCCAR

Analysis methods

Both simulation models were compared using surrogate kinematics, restraint system outputs, injury risk prediction, and visual inspection.

Regarding kinematics, the head center of gravity (CG), T1, T4, T12, and pelvis Anterior Superior Iliac Spine (ASIS) kinematics were compared between both models.

Seat belt forces, webbing pay-outs at the retractor, belt tongue slip, webbing pay-ins at the end bracket pretensioner, DAB pressures and volume changes, steering column strokes and forces, and rotations of anti-submarining and seat pan plates were chosen as the main restraint system outputs to use for the comparison.

To evaluate the injury risk, outputs were defined for the HBM following the recommendations of the OSCCAR deliverable D3.3 [13]. Regarding the ATD, the standard outputs were used for the analysis, and injury risk criteria was evaluated based on [14]. For the head, HIC and BrIC injury risks were evaluated according to [14]. DAMAGE was as well evaluated based on [15]. Regarding the neck, cross sections were defined in the cervical vertebrae of the HBM (C1-C7) to analyze axial loading through cortical and spongy bones, left and right transverse processes, spinous process, and the ligaments connected to the respective vertebrae according to [13]. The maximum values

of forces from all the vertebrae were then compared with the maximum loads measured by the load cells of the upper and lower sections of the neck of the ATD. Regarding the thorax, rib fracture risk was assessed according to [13] [16] for the HBM using cortical bone maximum principal strain. This risk of rib fracture was then compared to the peak resultant chest deflection injury criterion for the ATD [14]. The anterior superior iliac spine (ASIS) peak force was also measured in the HBM by cross sections through cortical and spongy bone to assess iliac wing fracture risk. This load was then compared to the one measured in the THOR-Reclined ASIS load cells. The leg injury was assessed by femur force measurement. A comparison between the recorded values of the ATD's load cells and the HBM cross sections was made.

Submarining and overall behavior of both models in the generic frontal environment simulation model were assessed based on visual inspection.

RESULTS

The two FE (pre)simulations and the two impact simulations were performed successfully. All the simulations were checked regarding simulation quality. In all the simulations, the percentage of added mass was below the 5% limit and the hourglass energy remained below the 10% of the internal energy maximum of each simulation. The four simulations reached normal termination.

Surrogate kinematics

Head CG, T1, T4, T12 and left pelvis ASIS trajectories were compared between both models. Some differences and similarities were found between both models, which are presented in Figure 11.

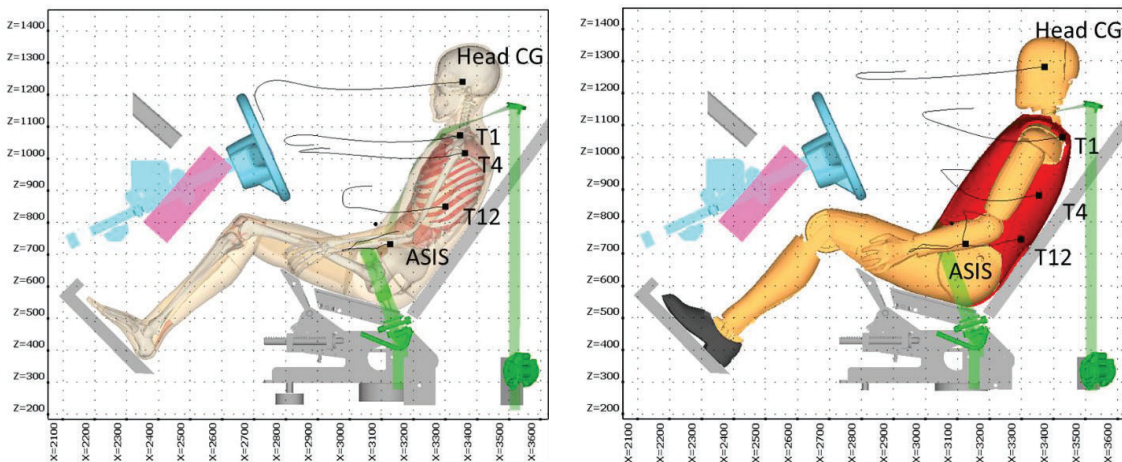


Figure 11: Kinematic comparison of THUMS (left) and THOR-Reclined (right) simulation models during the impact simulation.

Torso and head kinematics differed significantly between both models. THUMS had higher forward displacements, while the THOR-Reclined was stiffer and longitudinal displacements were smaller. Also, several differences were found regarding initial sensor positions between the ATD and the HBM. T4 and T12 dummy sensors had different positions compared to the initial position of the HBM T4 and T12. Nevertheless, the ASIS kinematics during the loading phase was very similar between both models, reaching a maximum of around 140 mm of forward displacement. Overall body movement during the first 80 ms is very similar (Figure 12) between both models as well. At 102 ms, the shoulder belt of the THUMS model wraps and slips from the shoulder of the surrogate. This does not happen to the THOR-Reclined simulation model and therefore the kinematics from that moment differ significantly.

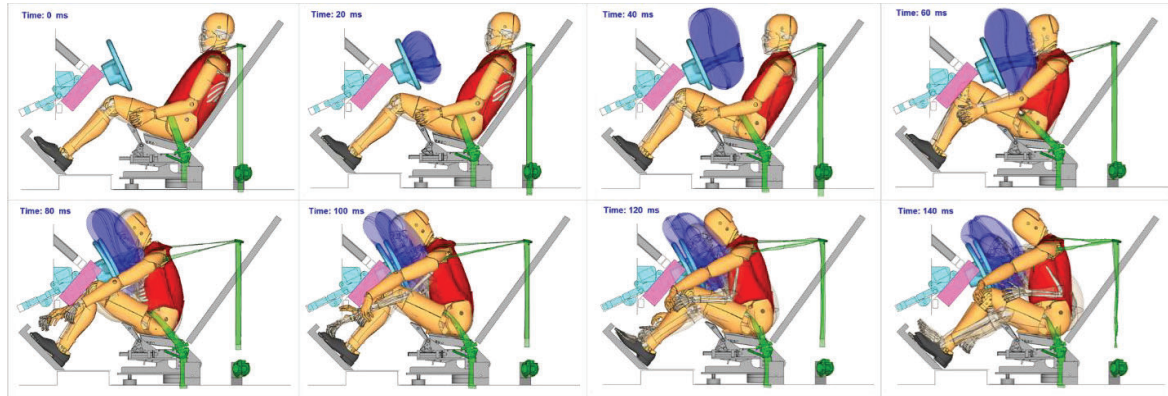
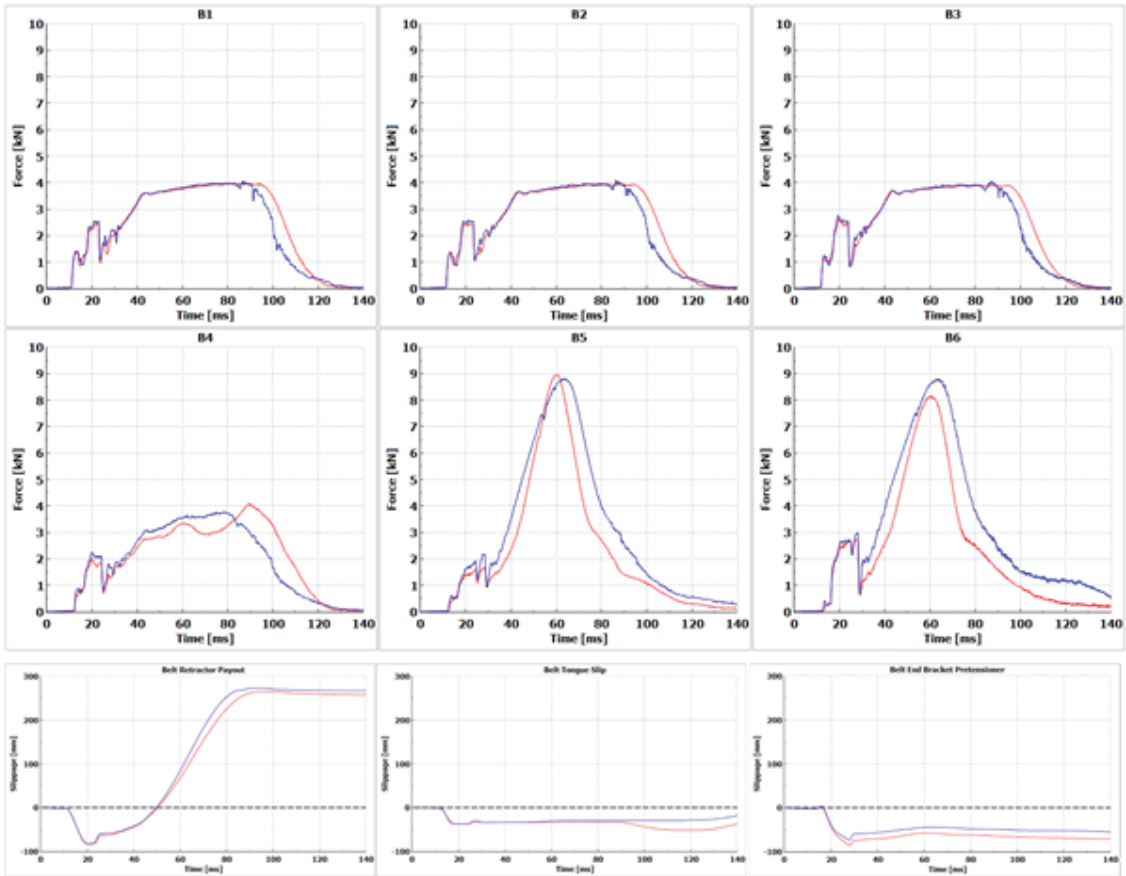


Figure 12: Visual comparison between both models during the impact simulation

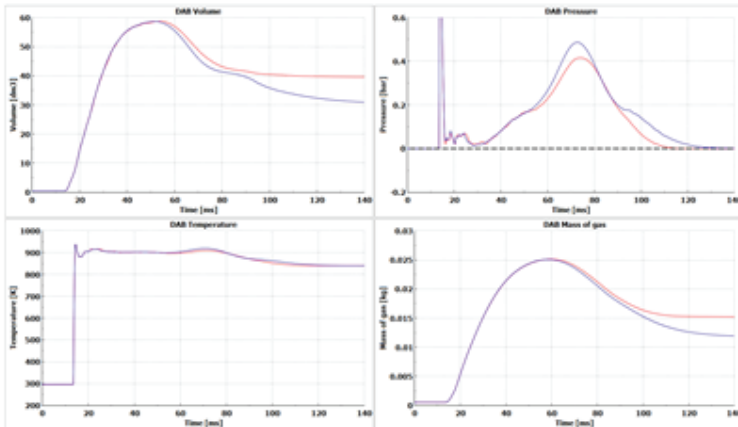
Restraint system outputs

The restraint system had a comparable performance for both surrogates. Figure 13 shows a very similar behavior of the belt regarding both forces and payouts. The shoulder belt tension of the THUMS model decays a few milliseconds earlier than the THOR-Reclined due to the slippage of the belt. Also, higher forces are measured in section B6 for the THUMS model. The seat plate rotations are very similar for both models as well. The steering column and the DAB however show different behaviors in each simulation. The maximum collapsing distance of the SC for THUMS is 100mm, while the THOR-Reclined dummy reaches a maximum of 58 mm. The DAB registered higher pressure for the THUMS simulation.

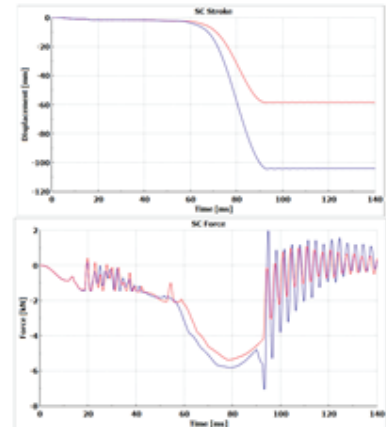
Belt



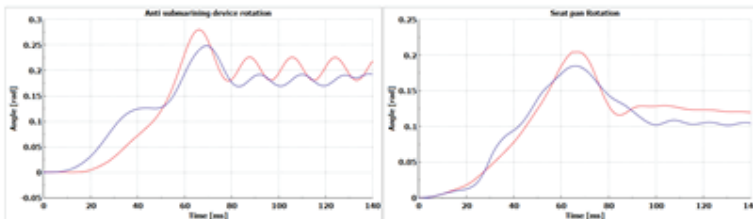
DAB



SC



Seat



— THUMS v4.1
 — THOR-Reclined

Figure 13: Restraint system comparison

Injury risk prediction

For the head, HIC 15, BrIC, and DAMAGE injury values were calculated based on each model head kinematics. The injury risk functions recommended by [14] for HIC and BrIC (based on cumulative strain damage measure) were as well applied. In general, values differed between both models. THUMS was always the model with higher injury values. The closest injury value between both models was the DAMAGE, with 0.543 for THUMS and 0.343 for the THOR-Reclined.

Regarding the neck, the THUMS model registered the maximum tension force of 2.02 kN in C3 at 85 ms. The THOR-Reclined registered a maximum tension force of 0.3 kN at 78 ms in the upper cell of the neck. Maximum tension was obtained in similar places of the neck at approximate times. The peak values obtained however differed by almost 2 kN.

Thorax compression was measured in the THOR-Reclined dummy in the upper-left, lower-left, upper-right, and lower-right IR-TRACCs, obtaining a peak resultant chest deflection of 49.13 mm in the upper-left section of the chest. This deflection translates into a 45.36% probability of AIS 3+ injury. In the case of the HBM, the maximum principal strain of the rib cortical bone was measured. Strain values were obtained at a frequency of 5000 Hz (every 0.2 ms) and elements with a strain rate higher than 0.04 ms^{-1} were eliminated from the analysis as suggested by [13]. Results are presented in Table 2. The risk of two or more rib fractures for a 65-year-old person resulted in a close value to the one predicted by the THOR-Reclined chest deflection.

Pelvis and femur forces were compared, showing similar results in the left iliac wing and the right femur (Table 2).

Table 2: Injury values obtained for each simulation model

		THUMS	THOR-Reclined
HEAD	HIC 15 [-]	1942,240	487,624
	BrIC (CSDM) [-]	1,008	0,524
	DAMAGE	0,543	0,343
	HIC P(AIS 2+)	76,36%	18,03%
	HIC P(AIS 3+)	56,40%	4,40%
	BrIC P(AIS 3+)	57,24%	0,00%
	BrIC P(AIS 4+)	44,86%	0,00%
THORAX	Peak resultant chest deflection [mm]		49,130
	Chest P(AIS 3+)		45,36%
	Risk for rib fractures 2+ (45 yr)	4,59%	
	Risk for rib fractures 2+ (65 yr)	48,28%	
PELVIS	Left iliac wing peak compression [kN]	3,810	3,524
	Right iliac wing peak compression [kN]	3,657	4,915
FEMURS	Left femur peak compression [kN]	1,083	0,212
	Right femur peak compression [kN]	0,450	0,204

LIMITATIONS

The following aspects were not included in the study and may have affected some of the results here obtained:

- Only one ATD was used for the analysis, so results do not represent all the dummy population.
- Only one FE HBM was used for the analysis. Further work needs to be done to get a general overview of the outputs generated by each HBM.
- One reclined posture was used for the study. More seating postures with different seat pan and seatback angles may be necessary to do a full comparison between the THUMS and the THOR-Reclined.

- No physical tests have been performed, in the scope of this work, to correlate the dummy FE model behavior. These will be done in the near future and the results will be published accordingly. In addition, further validation test results (found in the literature) will be used for the analysis.
- A simplified belt material card (*MAT_SEATBELT) was used for the FE simulations. A more detailed material definition like *MAT_FABRIC could help clarify the difference in shoulder kinematics, as the wrapping of the seatbelt could be avoided.
- No optimization of the restraint system was made for the studied posture. A SOTA restraint system was used with the only objective of comparing both simulation models in the same conditions.

CONCLUSIONS

A one-to-one comparison was made between the THOR-Reclined dummy and the THUMS HBM regarding kinematics, restraint system outputs, and injury criteria. Some differences have been found between both models, mainly due to their physical dissimilarities but also in the way both models are designed to output results. While the ATD is mainly designed for generating acceleration and displacement results, the HBM could not only offer acceleration and displacement outputs but stress and strain outputs as well.

Results suggest that the THOR-Reclined ATD has a stiffer behavior compared to the HBM. Low deformations were observed in the dummy compared to the HBM. One main difference was found in the shoulder behavior. The HBM generated a concave area around the shoulder that provoked the wrapping and slippage of the shoulder belt, changing the kinematics of the surrogate towards the end of the simulation. The THOR-Reclined however did not show that deformation and the shoulder belt stayed in position during the simulation, even though both models had comparable seat belt routings. Both models had similar pelvis kinematics and no submarining was observed in any simulation.

Regarding restraint systems, even though the seat behaved similarly, and the belt loads were comparable in both impact simulations, higher loads were transferred to the DAB and the SC in the HBM simulation, as higher pressures were obtained in the airbag and a larger stroke in the SC. This higher transfer of loads might have occurred due to the shoulder belt slippage, the more flexible behavior of the HBM, and the physical dissimilarities of both models.

THUMS consistently sustained higher injury values and injury risk predictions compared to the ones obtained by the THOR-Reclined. The biggest differences were found in the head. The HBM showed injury risk predictions of over 50% (regarding BrIC) while the ATD had a 0% of injury risk.

These results suggest that while nowadays cars are being rated with dummies, properly restraining a human body might be more challenging, as in the same environment the THUMS model has shown to have larger displacements and strains, worse coupling with the seat belt, and higher injury outputs compared to the THOR-Reclined.

This study offers the first direct comparison between a HBM and a dummy. Nevertheless, further work needs to be done to be able to fully compare both models regarding postures and restraint systems. Also, the addition of more models to the study could be beneficial to fully understand the similarities and differences between ATDs and HBMs to be able to properly improve and test restraint systems and their impact on real humans.

FUTURE WORK

Currently, the authors are undergoing a similar study using the MADYMO Active Human Model (AHM). This work will be compared with the results from this study to increase the number of studied models.

Physical tests will be performed shortly to correlate the dummy FE model behavior and the environment used for this study. This future work will as well be published accordingly.

ACKNOWLEDGEMENTS

The authors would like to thank the European Commission for funding the SAFE-UP project under Grant Agreement No. 861570. IDIADA has been coordinating SAFE-UP within the H2020 EU funding program. This study was performed as part of this project to study the performance of different restraint system strategies with different HBMs during a crash in reclined positions.

Furthermore, the authors would like to acknowledge CEESAR for sharing the semi-rigid seat used for the performance of the sled test series.

REFERENCES

- [1] SAE International, "Taxonomy and Definitions for Terms Related to Driving Automation Systems for On-Road Motor Vehicles J3016_202104," SAE International, 30 04 2021. [Online]. Available: https://www.sae.org/standards/content/j3016_202104/.
- [2] Leung et al., "A Comparison between Part 572 Dummy and Human Subject in the problem of Submarining," *Proceedings of the 23rd Stapp Car Crash Conference*, pp. 677-719, 1979.
- [3] Richardson R, Donlon JP, Jayathirtha M, et al., "Kinematic and Injury Response of Reclined PMHS in Frontal Impacts," *Stapp Car Crash J.*, vol. 153, p. 64:83, 2020.
- [4] R.Richardson, M. Jayathirtha, J.P. Donlon et al., "Pelvis Kinematics and Injuries of Reclined Occupants in Frontal Impacts," *IRCOBI Proceedings*, Vols. IRC-20-60, 2020.
- [5] Becker J, Östling M, Lozano P, et al., "Occupant Monitoring Based Restraint Strategies For Future Seating Configurations," *SAFE-UP Project*, vol. Deliverable D4.4, no. Grant Agreement No. 861570, 2022.
- [6] Uriot J, Potier P, Baudrit P, Trosseille X, Petit P, Richard O, Compigne S, Masuda M, Douard R., "Reference PMHS Sled Tests to Assess Submarining," *Stapp Car Crash Journal*, vol. 59, pp. 203-223, Nov 2015.
- [7] SAE International, "Devices for Use in Defining and Measuring Vehicle Seating Accommodation J826_202106," 22 06 2021. [Online]. Available: https://www.sae.org/standards/content/j826_202106/.
- [8] SAE International, "Motor Vehicle Dimensions J1100_200911," 20 11 2009. [Online]. Available: https://www.sae.org/standards/content/j1100_200911/.
- [9] Matthew P. Reed, Sheila M. Ebert, "Effects of Recline on Passenger Posture and Belt Fit," UMTRI, Michigan, 2018.
- [10] Poulard, D., Subit, D., Donlon, J-P., Kent, R. W., "Development of a computational framework to adjust the pre-impact spine posture of a whole-body model based on cadaver tests data," *Journal of Biomechanics*, vol. 48, no. 4, pp. 636-643, 2015.
- [11] A. Leledakis, J. Östh, J. Iraeus, J. Davidsson, L. Jakobsson, "The Influence of Occupant's Size, Shape and Seat Adjustment in Frontal and Side Impacts," *IRCOBI conference*, no. IRC-22-75, pp. 549-584, 2022.
- [12] Dobberstein J, Schmidt D, Östling M, et al., "Final results on detailed crash configurations from collisions expected to remain for automated vehicles," *OSCCAR Project*, vol. Deliverable D1.3, no. Grant Agreement No. 768947, 2021.
- [13] Mayer C, Iraeus J, Meyer F, et al., "Criteria and risk functions for prediction of injury risks in new sitting positions and new crash scenarios," *OSCCAR*, vol. Deliverable D3.3, no. Grant Agreement No. 768947, 2021.
- [14] Craig M, Parent D, Lee E, et al., "Injury Criteria for the THOR 50th Male ATD," *Human Injury Research Division NHTSA*, 2020.
- [15] Gabler, L.F., Crandall, J.R. & Panzer, M.B., "Development of a Second-Order System for Rapid Estimation of Maximum Brain Strain," *Ann Biomed Eng*, vol. 47, p. 1971-1981, 2019.
- [16] Forman J, Kulkarni S, Perez-Rapela D, et al., "A Method for Thoracic Injury Risk Function Development for Human Body Models," *IRCOBI Proceedings*, Vols. IRC-22-97, 2022.
- [17] Autoliv, "Home | Autoliv," [Online]. Available: <https://www.autoliv.com/>. [Accessed 12 2022].
- [18] CEESAR, "Centre Européen d'Etudes de Sécurité et d'Analyse des Risques," [Online]. Available: <https://www.ceesar.fr/>. [Accessed 12 2022].
- [19] Richardson R, Jayathirtha M, Chastain K, et al., "Thoracolumbar spine kinematics and injuries in frontal impacts with reclined occupants.," *Traffic Injury Prevention*, vol. 21(sup1), pp. S66-S71, 2020.
- [20] Compigne S, Schiessler M, Hamacher M, et al., "Validation and Demonstration of Advanced Passenger Protection Principles," *OSCCAR Project*, vol. Deliverable D2.5, no. Grant Agreement No. 768947, 2021.

UPDATE ON NHTSA'S OMDB'S HALF BARRIER ANALYSIS

James Saunders
Dan Parent
NHTSA
USA

Paper Number 23-0314

ABSTRACT

Research Question/Objective: National Highway Traffic Safety Administration (NHTSA) has developed an Oblique Offset Moving Deformable Barrier (OMDB) test procedure. The OMDB test procedure uses an energy absorbing honeycomb that covers the front face of the OMDB. Originally, this barrier had a full-width design that was representative of a typical passenger car. During the development of this test procedure, it was realized that less than half of the barrier face was being deformed. Since only half the honeycomb was being deformed it was determined this was a waste of material and added cost to perform the test. Also, it was brought to NHTSA's attention that the manufacturing of the full-width barrier face was complicated by the need for straps. Therefore, NHTSA is developing a barrier with a face whose width is about half of the original. It is referred to as the "Half Barrier." Two different versions of the Half Barrier design, V0 and V1, are investigated herein.

Methods and Data Sources: The Full, Half V0, and Half V1 barrier faces were tested using the OMDB test procedure with rigid moving barrier and production vehicles, representing different size vehicles. In each test with production vehicles, THOR-50M Anthropomorphic Test Devices (ATDs) were positioned in the driver and right front passenger seat. Differences in barrier, vehicle, and occupant response were assessed using CORA rating software. To eliminate the variability of production vehicles a set of tests using a rigid moving barrier was used as the target vehicle. Differences in barrier, vehicle, and occupant response were assessed using CORA.

Results: The impacts into the rigid moving barrier showed a "Good" CORA score for the rigid moving barrier responses, though the barrier crush and energy had different trends. In the production vehicle tests, some differences were seen in the vehicle crash pulses and intrusions when comparing different barrier faces within the same vehicle. For example, the large pickup truck showed a more severe crash pulse using the Half V1 barrier face, suggesting that V1 is stiffer than the other barrier faces

Discussion and Limitations: During this testing it was noted that the two layers of honeycomb had a slight separation. This separation was seen in the full-width barrier and both designs of the Half Barrier. It is unknown how much this separation affects the vehicle and ATD response. This study was limited by the number of observations, as only one test was conducted for each barrier face/vehicle combination, and only three production vehicles were tested. However, the range of vehicles was selected to cover a wide range of characteristics.

Conclusions and Relevance to Session Submitted: The Half V0 barrier face design has been tentatively selected as a replacement for the full-width barrier for use in NHTSA's OMDB test procedure. It shows comparable results to the full-width barrier for both the vehicle and THOR-50M performance. The Half Barrier V1 design seemed to be too stiff for larger vehicles.

INTRODUCTION

National Highway Traffic Safety Administration (NHTSA) has developed an Oblique Offset Moving Deformable Barrier (OMDB) test procedure. The OMDB test procedure uses an energy absorbing honeycomb that covers the front face of the OMDB. This barrier is referred to as "Full" (Figure 1) [1]. During the development of this test procedure, it was realized that less than half of the barrier face was being deformed. Since only half the honeycomb was being deformed, it was determined this was a waste of material and added extra cost to perform the test.

HALF-BARRIER DESIGNS

Two versions of a half-barrier are explored herein:

Half-barrier version V0: This version was designed to be a smaller and more simplistic version of the Full barrier. For the Full barrier, it was noted that the manufacturing of the barrier face is complicated by the use of strapping. Therefore, the barrier face width was reduced by about half and outer cladding was made from one piece of metal, eliminating the need to rivet and allowing the straps and the side cladding to be removed. The resulting barrier face is referred to as “Half V0” (Figure 2) [2]. To eliminate the movement of the honeycomb from deforming toward the outer edge of the OMDB a support was added (*Figure 5*) (Appendix A). It should be noted that the honeycomb is not connected to the support. The support was designed to composite for the difference in mass between the honeycombs

Half-barrier version V1: It was noted after performing tests with Half V0 that the honeycomb layers were separating for both Full and Half V0. This separation was noted by looking at pictures from previous tests. Separation included both delamination and the honeycomb sliding relative to each other. *Figure 4* shows an example of barrier separation for the Full barrier. The front honeycomb is lower compared to the back honeycomb and there is a gap between the two pieces of honeycomb. Also, it was noted that the interior edge of the Half V0 face was expanding out from the barrier, whereas at the same location for the Full barrier it stayed the same (*Figure 5*). Again, it is unknown if all tests had separation since the barrier faces were not available to investigate. While it is not known how the honeycomb separation affects the test results, the initial perception was that the separation could present reproducibility concerns. Therefore, another version of the half-barrier face was designed in an attempt to prevent the separation from occurring. This version is referred to as “Half V1.” The medial end of the cladding was fixed to the barrier and the lateral end of the barrier was capped (Figure 3).

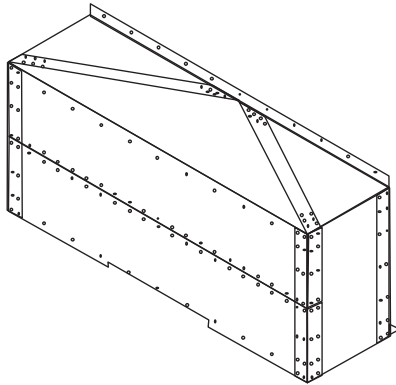


Figure 1 Original barrier face (Full)

- Width slightly > 50%
- Same materials
- Removed straps, rivets, side cladding
- One-piece outer cladding

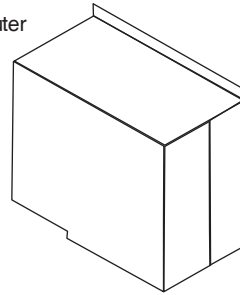


Figure 2 1st version reduced face design (Half V0)

- Medial end of cladding fixed to barrier
- Lateral end of barrier capped

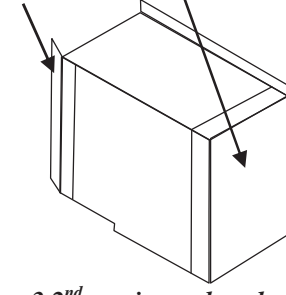


Figure 3 2nd version reduced face design (Half V1)

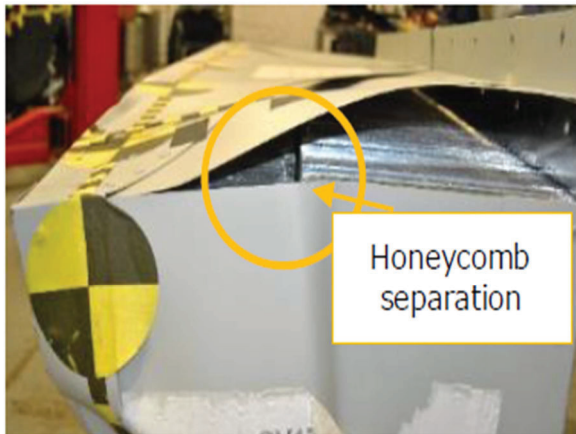


Figure 4 Example of Full honeycomb separation

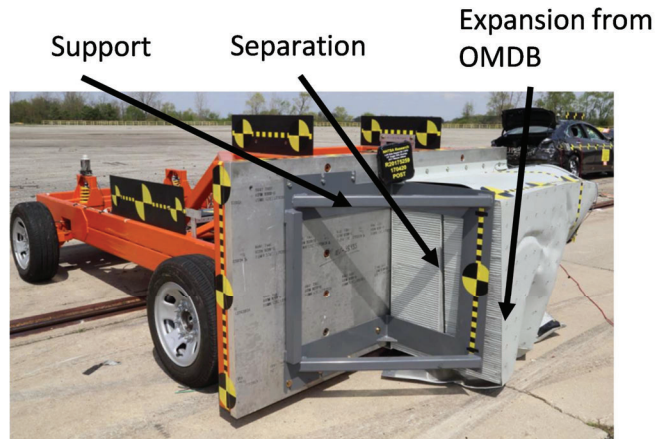


Figure 5 Picture showing extra support added for half barrier design and honeycomb separation

Saunders [3] demonstrated that the OMDB, vehicle, and Test Device for Human Occupant Restraint 50th percentile male (THOR-50M) responses in the OMDB test procedure were repeatable and reproducible. For the half barrier to be used, it needs to be demonstrated that the results from the half barrier test are equivalent to those from the full barrier test. This report follows the same methodology as Saunders [3].

METHODOLOGY

Test Setup

Figure 6 shows the general test setup for the OMDB crash test. The OMDB impacts the target vehicle at a test speed of 90 km/h at a 15-degree offset and at 35 percent overlap of the target vehicles' overall width (excluding mirrors and door handles). The outer edge of the OMDB is aligned with the overlap mark on the target vehicle.

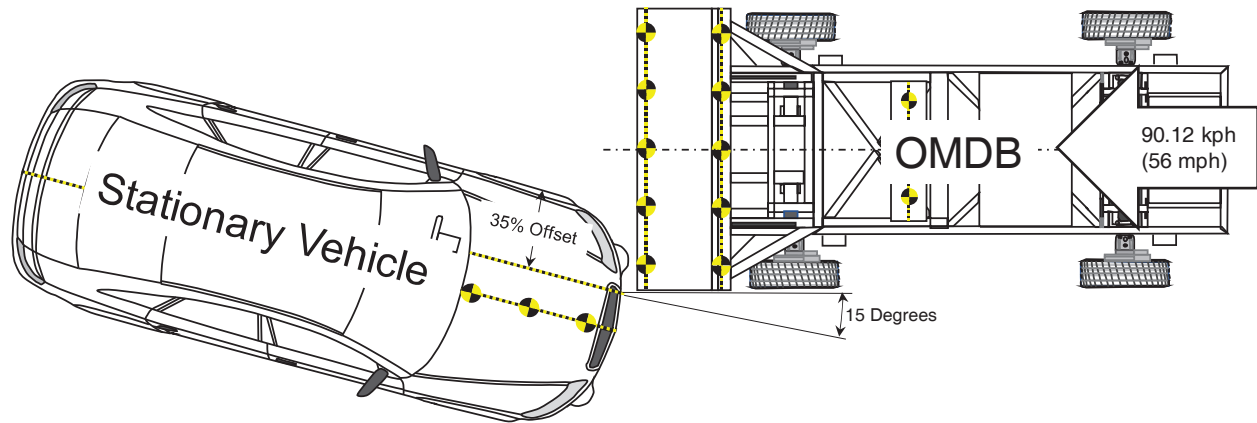


Figure 6 OMDB test setup

Vehicle Selection

The production vehicles selected for this testing were intended to cover a range of vehicle sizes. Table 1 shows the naming convention used for this analysis and the NHTSA test numbers for each test [4]. To determine if the Half V1 version prevented honeycomb separation only the Small and Large PU tests were performed. If Half V1 prevented honeycomb separation than additional vehicles would be tested.

Table 1
Vehicle naming convention and relative NHTSA test numbers

Vehicle Type	NHTSA Test Number		
	Half V0	Half V1	Full
Small	10134	10824	10133
Mid-size	10072	NA	10154
Large PU	10119	10825	10099

Honeycomb Crush

To measure the crush of the honeycomb, the barrier face was divided by ten evenly spaced horizontal lines relative to the vertical axis of the OMDB (R1 through R10) (Figure 7). Post-test the crush was measured along these horizontal lines, i.e., holding at the same z-height as pre-test. The lab measured enough points along each horizontal line to represent the deformation. It should be noted that the plots of barrier crush throughout the paper only show the same portion of the Full barrier that overlaps the half barrier. Also, R3, R6, and R9 crush measurements are used to get a representation of the crush throughout the barrier.

This barrier crush was used to calculate the energy absorbed by the honeycomb. To calculate the energy, the honeycomb was assumed to be the same constant stiffness as the first layer of honeycomb. While there are two layers of honeycomb with different stiffnesses, this assumption was made because the crush into the second layer was seen to be less than 50 mm. The Equation 1 shows the equation used to calculate the energy absorbed by the honeycomb during the test.

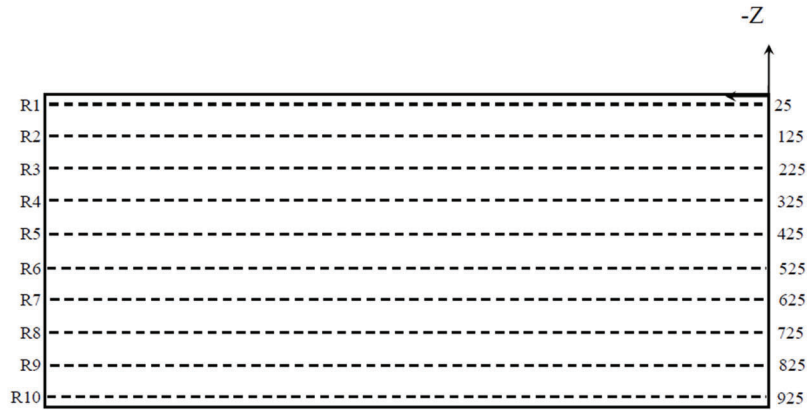


Figure 7 Barrier crush measurements

$$energy (kJ) = \frac{V}{k * 1000 * 1000 * 1000 * 1000} \quad (1)$$

V = crushed honeycomb volume (mm^3)

k = crush strength of first layer of honeycomb (689475.729 psi)

Vehicle Interior Intrusions

For all tests, pre- and post-test measurements were collected from the interior of the test vehicles following the OMDB procedure [5]. Figure 6 shows the location of each of these points.

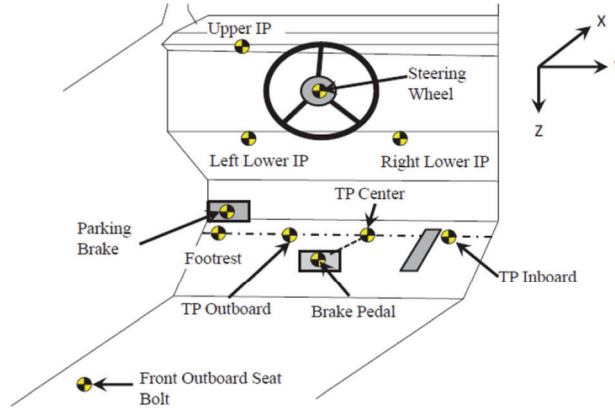


Figure 6 Driver side interior pre- and post-test points

Objective Evaluation

CORrelation and Analysis (CORA) [6] provides a methodology to objectively compare the time histories of the measurements and quantify how two or more signals compare on a scale of 0 to 1, where a higher total CORA score represents a higher correlation between each test or measurement, and a score of 1 indicates that the signals are identical. CORA software uses two methods to evaluate the correlation of two or more signals: corridor and cross-correlation. The corridor method compares the deviation between curves, while the cross-correlation method compares curve characteristics such as shape, phase shift, and size.

For this analysis the CORA examples provided when downloading the CORA [5] were used. The only modification to these files was the reference to the time-history data and the time range for evaluation. As specified in the manual,

all data was sampled at 0.1 ms. CORA scores were calculated by assuming that the Full barrier test for each production vehicle was the experimental baseline, and the Half V0 and Half V1 tests (when available) were compared to this baseline. For this study, as in Saunders [3] **Error! Reference source not found.**, the time range used for calculation of CORA score was from 0 to 100 ms for the vehicle and OMDB time-histories, and from 0 to 200 ms for the occupant time-histories. The grading system presented in Saunders [3], which is divided into three categories based on CORA scores as shown in Table 2, was used in this study as well. Vehicle and OMDB time-histories used in the CORA analysis were selected to be able to compare vehicle and OMDB kinematics, accelerations, and velocities. Occupant response time-histories selected for CORA analysis were those used as input in the calculation of injury criteria for the THOR-50M ATD [3].

Table 2
CORA scores ranges

Grade	Calculated Score
Good	$R > 0.80$
Fair	$0.58 < R \leq 0.80$
Poor	$R \leq 0.58$

RESULTS

A total of 8 OMDB tests were conducted, with the closing speeds, impact angle, and vertical and lateral offset all within the specifications of the OMDB Laboratory Test Procedure (Table 3) [5]. Table 3 also shows the mass of Vehicle were similar between tests. There was a 82 kg difference in the mass of the OMDB. This is because not all tests were performed at the same test facility. Each facility had different equipment attached to the OMDB to pull it down the track. The moment of inertia and exact CG of the OMDB were not measured for any of these tests.

Table 3
Input parameters of the OMDB into production vehicles

Vehicle Description	Barrier	Closing Speed (kph)	OMDB Mass (kg)	Vehicle Mass (kg)	Angle (degrees)	Vertical Offset (mm)	Lateral Offset (mm)
Small	Full	90.79	2531.9	1574	15	-13	0
Small	Half V0	90.72	2518.5	1573	15	-3	2
Small	Half V1	89.62	2471	1572	14.5	8	48
Mid-size	Full	90.04	2450.2	1708.6	15	-14	-5
Mid-size	Half V0	90.33	2437	1717.8	15	-20	17
Large PU	Full	89.5	2462.3	2246.5	15.1	-12	-8
Large PU	Half V0	89.87	2451.2	2258	14.9	-16	10
Large PU	Half V1	90.12	2471	2272	15.2	-5	2

The remainder of the results section is presented in four subsections. The first describes the response of the OMDB itself, including both the kinematics of the moving barrier and the crush of the deformable honeycomb barrier faces. The second describes the response of the target vehicles, including kinematics, crush, and intrusion. The last two sections describe the response of the two occupants in each vehicle, the driver and the right front passenger.

OMDB Response

The magnitude of energy absorbed by the different honeycomb faces did not show any consistent trends across production vehicle sizes (Figure 8). The energy absorbed by the Half V0 for the Small and the Mid-size production vehicle decreased by 2.9 and 8.5 percent when compared to the Full barrier face, while the energy absorbed by the honeycomb for the Large PU increased by 13.8 percent. However, for the Half V1 barrier face, the energy absorbed

in the Small production vehicle increased by 12.2 percent compared to the Full barrier face, whereas the energy absorbed in the Large PU test decreased by 31.8 percent.

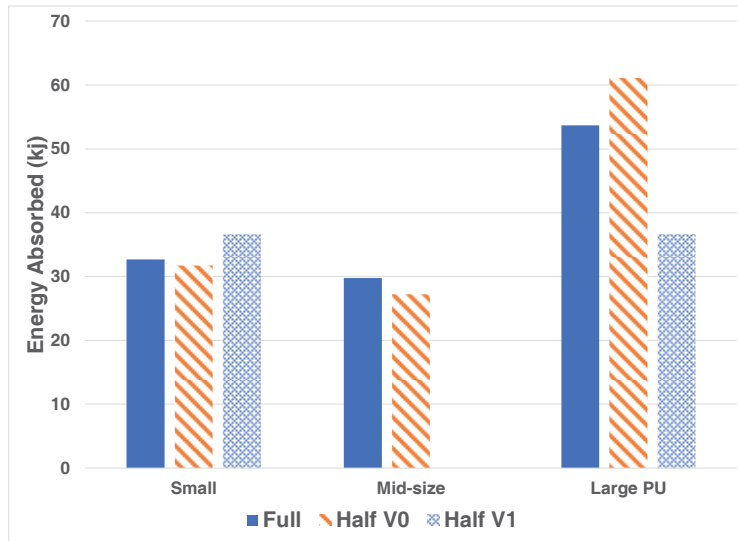


Figure 8 Energy absorbed by the honeycomb when the OMDB impacts production vehicles

Figure 9 through Figure 11 show the physical honeycomb crush for the Small production vehicle tests for comparison. Figure 12 through Figure 14 show the measured crush for R3, R6, and R9 for the Small production vehicle tests for comparison. Since the crush of the left half (-1200 to 0 mm), when looking from in front of the OMDB, of the Full honeycomb barrier face is negligible, only the common portions of the barrier faces (0 to +1200 mm) are shown. It is seen that the Half V0 expands away from the OMDB for all three rows and then is similar, except for R9. R9 followed the Full crush just after crush stopped expanding and then did not rise as high as the Full. The crush for R3 and R9 for Half V1 was shifted to the left at the beginning of crush and then had similar shape. R6 for Half V1 was similar, except for around 750 mm, it had more crush than both the Full and Half V0.



Figure 9 Picture of Full honeycomb crush for the OMDB impacting Small production vehicle



Figure 10 Picture of Half V0 honeycomb crush for the OMDB impacting Small production vehicle *



Figure 11 Picture of Half V1 honeycomb crush for the OMDB impacting Small production vehicle

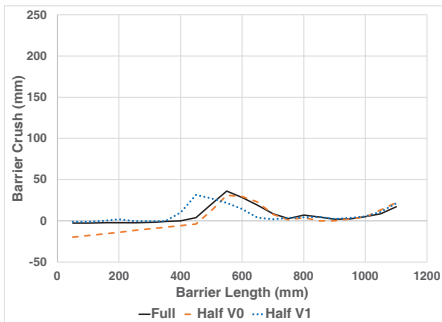


Figure 12 R3 honeycomb crush when impacting Small production vehicle

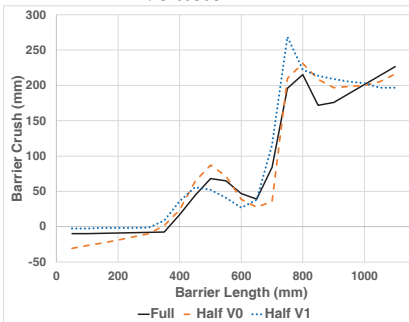


Figure 13 R6 honeycomb crush when impacting Small production vehicle

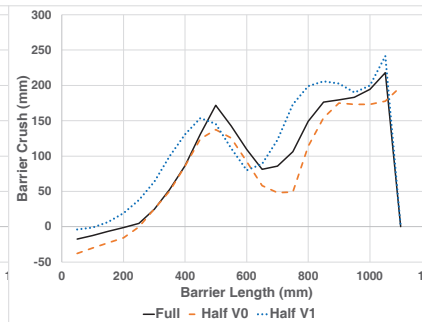


Figure 14 R9 honeycomb crush when impacting Small production vehicle

* Oblique picture not available

Figure 15 and Figure 16 show the physical honeycomb crush for the Mid-size production vehicle tests for comparison. Figure 17 through Figure 19 show the measured crush for R3, R6, and R9 for the Mid-size production vehicle tests for comparison. It is seen that the Half V0 expands away from the OMDB for all three rows and then is similar, except for the middle of the honeycomb. Each row does not crush as much as the Full.

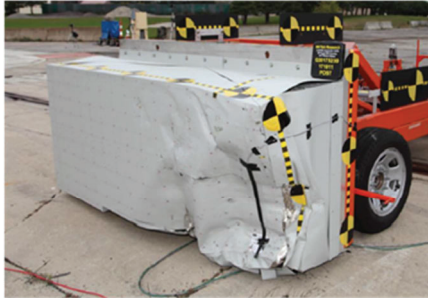


Figure 15 Picture of Full honeycomb crush for the OMDB impacting Mid-size production vehicle



Figure 16 Picture of Half V0 honeycomb crush for the OMDB impacting Mid-size production vehicle

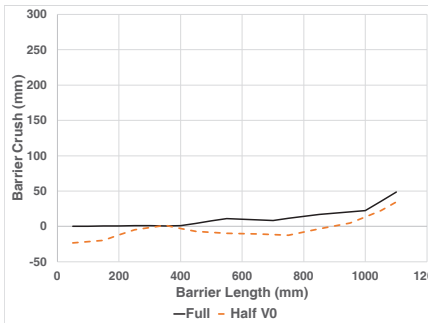


Figure 17 R3 honeycomb crush when impacting Mid-size production vehicle

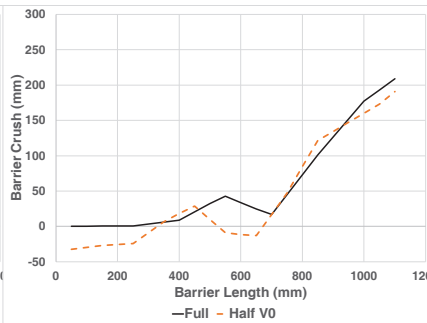


Figure 18 R6 honeycomb crush when impacting Mid-size production vehicle

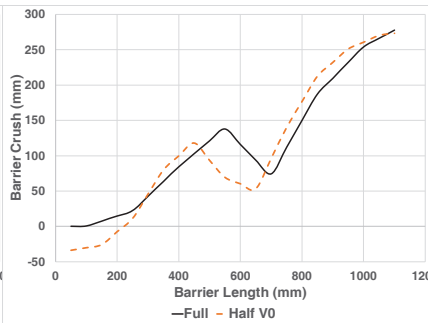


Figure 19 R9 honeycomb crush when impacting Mid-size production vehicle

Figure 20 through Figure 22 show the physical honeycomb crush for the Large PU tests for comparison. Figure 23 through Figure 25 show the measured crush for R3, R6, and R9 for the Large PU tests for comparison. It is seen that the Half V0 expands away from the OMDB for all three rows for the left side of the honeycomb. R3 crush was similar and R6 was similar up to 500 mm. R3 crush was less for the Half V1. Also, R6 was less up to 700 mm and then was greater for a short distance. R9 showed more crush than Full.



Figure 20 Picture of Full honeycomb crush for the OMDB impacting Large PU production vehicle



Figure 21 Picture of Half V0 honeycomb crush for the OMDB impacting Large PU production vehicle



Figure 22 Picture of Half V1 honeycomb crush for the OMDB impacting Large PU production vehicle

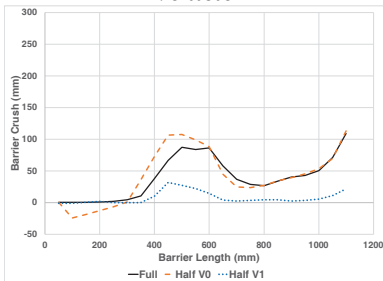


Figure 23 R3 honeycomb crush when impacting Large PU production vehicle

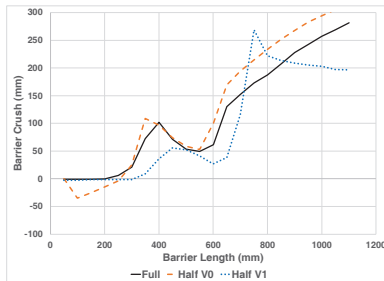


Figure 24 R6 honeycomb crush when impacting Large PU production vehicle

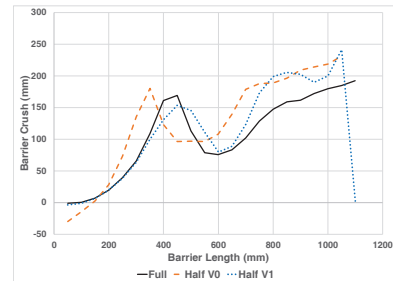


Figure 25 R9 honeycomb crush when impacting Large PU production vehicle

Table 4 shows the naming convention used throughout the paper for the time-histories of the OMDB measurements. Table 5 shows the CORA scores for the OMDB responses, which range from 0.884 to 1.000. Table 5 also shows that the average CORA score was greater than 0.95 for all vehicle sizes.

Table 4
Naming convention for OMDB time-histories

Name	Description
OMDBCgaccRes	OMDB CG resultant acceleration (x,y)
OMDBCgvelRes	OMDB CG resultant velocity (x,y)
OMDBCgav	OMDB CG angular velocity (z)
OMDBCgang	OMDB CG rotation (z)
OMDBRearAcc	OMDB Rear resultant acceleration (x,y)
OMDBRearVel	OMDB Rear resultant velocity (x,y)

Table 5
CORA scores for OMDB response when the OMDB impacts production vehicles

	Small		Mid-size		Large PU	
	V0	V1 ¹	V0	V1 ²	V0	V1
OMDBCGaccRes	0.993	0.942	0.968	NA	0.940	0.971
OMDBCGvelRes	0.998	0.976	0.998	NA	0.990	0.997
OMDBCGav	0.878	0.913	0.884	NA	0.931	0.956
OMDBCGang	0.960	0.989	0.941	NA	0.980	0.996
OMDBRearAcc	0.980	ND	0.987	NA	0.935	0.917
OMDBRearVel	0.997	ND	0.995	NA	0.993	0.986
Average	0.968	0.955	0.962	NA	0.962	0.971

ND – No data collected

NA – Not applicable, test was not performed for this vehicle

Vehicle Response

Figure 26 through Figure 28 show the bumper crush for each production vehicle when impacted by different honeycomb faces. The bumper crush for the Small production vehicle had similar shape for all honeycomb faces. The largest differences can be seen at the outer edge of the vehicle, where Half V0 had slightly more crush and Half V1 had slightly less crush than the Full barrier face. For the Mid-size vehicle, crush was similar for both barriers tested (Figure 27). For the Large PU, the bumper crush for the Half V0 is similar to the Full (Figure 28), except for minor differences at the outer edge of the vehicle. The Half V1, however, showed deviation from the Full barrier face at the outer edge of the vehicle, where crush was roughly 150 mm lower, and between 400 mm and 1200 mm of its profile, where there was more crush than both the Full and Half V0 barrier faces.

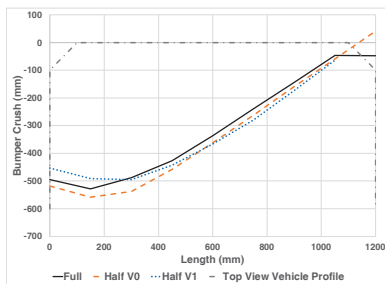


Figure 26 Bumper beam crush when the OMDB impacts Small production vehicle

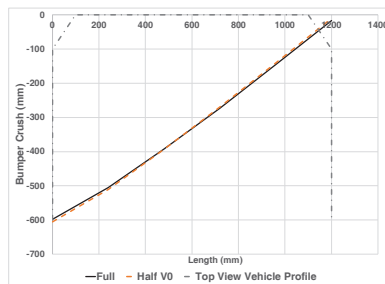


Figure 27 Bumper beam crush when the OMDB impacts Mid-size production vehicle

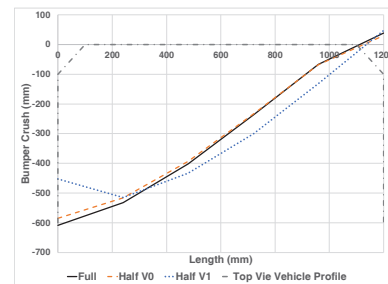


Figure 28 Bumper beam crush when the OMDB impacts Large-PU production vehicle

Figure 29 through Figure 31 show the interior intrusion for all production vehicles. The interior intrusions for the Small production vehicle were similar between the Half V0 and Full barrier tests (Figure 29), with the largest differences occurring in the TP Inboard and Brake Pedal measurement locations where the Half V0 intrusion was roughly 20 mm larger. Comparing the Half V1 and Full tests, the Half V1 resulted in about 80 mm more intrusion at the TP Footrest location, more intrusion at the Steering Wheel and Right Lower IP locations, and less intrusion at the Upper IP and Left Lower IP locations. The Mid-size production vehicle showed similar results when comparing Full versus Half V0 tests, except for the Brake Pedal location, where the Half V0 intrusion was 35 mm larger, and the Steering Wheel location, where Half V0 test showed 20 mm greater motion in the opposite direction. For the Large PU, the Half V0 test showed less intrusion than the Full barrier test in the Upper IP, Left Lower IP, and Brake Pedal locations. The Half V1 test showed more pronounced intrusion differences compared to Full and Half V0 tests (Figure 31), including 80 mm more intrusion at the TP Center location, 80-90 mm more intrusion at the TP Inboard

location, 40 mm more intrusion at the Right Lower IP location, and 20-40 mm less intrusion at the Brake Pedal location.

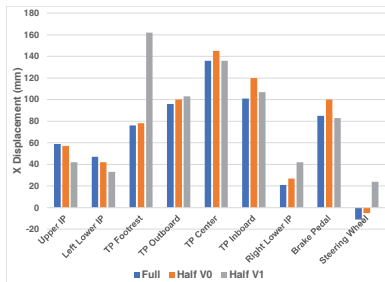


Figure 29 Interior points intrusions when the OMDB impacts Small production vehicle

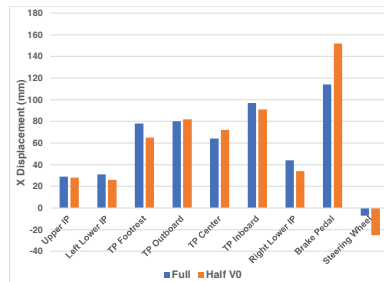


Figure 30 Interior points intrusions when the OMDB impacts Mid-size production vehicle

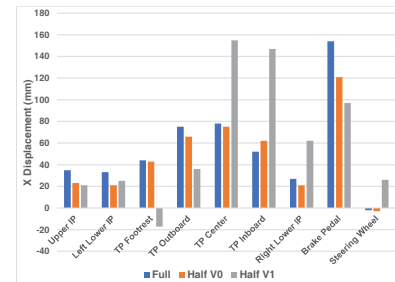


Figure 31 Interior points intrusions when the OMDB impacts Large-PU production vehicle

Table 6 shows the naming convention for the vehicle measurement time-histories. Table 7 shows that most of the CORA scores for the three production vehicles were rated “Good”. The VehLRaccRes for both V0 and V1 were rated “Fair” for the Large PU. The VehLRvelRes were rated “Good”. The scores for the VehCGav of all production vehicles were rated “Fair”, except for Large PU Half V0 which was “Good”. When integrating the angular velocity to get the rotation (VehCGang), it is seen that the CORA scores are rated “Good” for all the vehicles, except the Large PU.

Table 6

Naming convention for vehicle time-histories when a production vehicle is used as the target vehicle

Name	Description
VehLRaccRes	Test vehicle left rear sill resultant acceleration (x,y)
VehLRvelRes	Test vehicle left rear sill resultant velocity (x,y)
VehRRaccRes	Test vehicle right rear sill resultant acceleration (x,y)
VehRRvelRes	Test vehicle right rear sill resultant velocity (x,y)
VehCGaccRes	Test vehicle CG acceleration (x,y)
VehCGvelRes	Test vehicle CG resultant velocity (x,y)
VehCGav	Test vehicle CG angular velocity (z)
VehCGang	Test vehicle CG rotation (z)

Table 7
CORA scores for production vehicles response when the OMDB impacts production vehicles

	Small		Mid-size		Large PU	
	V0	V1	V0 ¹	V1 ²	V0	V1
VehLRaccRes	0.968	0.920	0.908	NA	0.798	0.702
VehLRvelRes	0.999	0.998	0.971	NA	0.988	0.993
VehRRaccRes	0.972	0.912	0.898	NA	0.860	0.915
VehRRvelRes	0.995	0.989	0.900	NA	0.991	0.996
VehCGaccRes	0.984	0.831	QD	NA	0.826	0.818
VehCGvelRes	1.000	0.978	QD	NA	0.978	0.969
VehCGav	0.636	0.734	0.719	NA	0.845	0.745
VehCGang	0.810	0.923	0.924	NA	0.991	0.681
Average	0.921	0.911	0.887	NA	0.910	0.852

QD – Questable data

NA – Not applicable, test was not performed for this vehicle

Figure 32 and Figure 33 show the left rear sill resultant acceleration of the Large PU when impacted by Half V0 and Half V1, respectively. Compared to the Full barrier test, the acceleration in the Half V0 test had a similar shape but a lower overall peak acceleration. The Half V1 test did not exhibit the rise in acceleration between 40 and 50 ms seen in the Full and Half V0 tests.

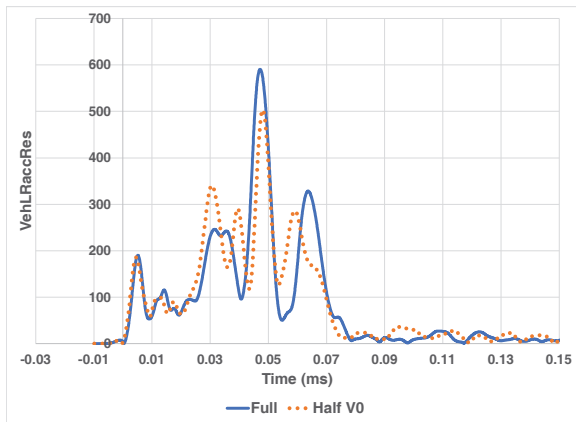


Figure 32 Left rear sill resultant acceleration for Large PU when impacted by Half V0 compared to Full

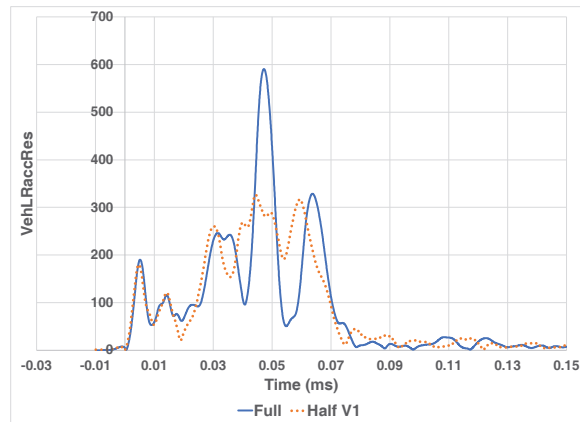


Figure 33 Left rear sill resultant acceleration for Large PU when impacted by Half V1 compared to Full

Figure 34 shows the integration of the angular velocity compared to film analysis for the Large PU Half V1. It is seen from film analysis that from 90 ms to 150 ms the rotations are similar, while the calculated angle keeps on diverging. Figure 35 zooms in on the film analysis between Full and Half V1. This is the time the two curves separate and then come back together. During this time the average difference was 0.31 degrees. It is interesting that this occurs about the same time as the difference in acceleration occurs (Figure 33).

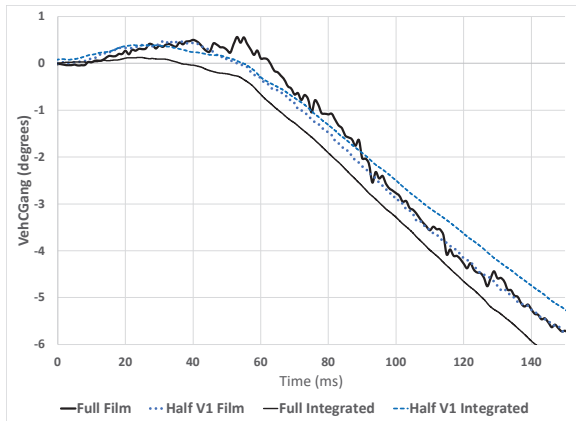


Figure 34 VehCGang from integrating VehCGav and film analysis for Large PU Half V1 compared to Full

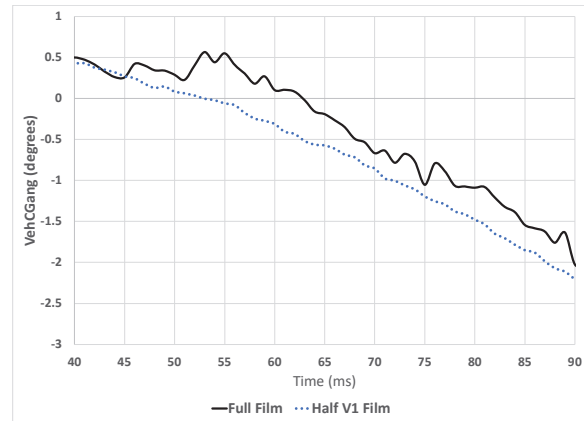


Figure 35 Zoom in on VehCGang from integrating VehCGav and film analysis for Large PU Half V1 compared to Full

Occupant Response: Driver

Within each production vehicle, driver kinematics were similar across all barrier designs. The minor differences that did occur are described in this section as they related to differences in occupant response time-histories. Table 8 shows the naming convention for the THOR-50M time-histories. Table 9 shows the CORA scores for the belted THOR-50M driver. For the Half V0 tests, the average CORA scores for the driver in the Small, Mid-size, and Large PU vehicles were 0.866, 0.760, and 0.723, respectively. For the Half V1 tests, the average CORA scores for the driver in the Small and Large PU were 0.789 and 0.658, respectively.

For the Small vehicle, the Half V0 test showed relatively comparable results for the driver measurements, with all CORA scores in the “Good” or “Acceptable” range and the lowest CORA score being 0.720. In the Half V1 test, on the other hand, there were more “Acceptable” results and one “Poor” result. The “Poor” result occurred in the upper left tibia axial force measurement (TibiaLUFz), where the shape, phase, and magnitude of the Half V1 time-history appear qualitatively similar to the Half V0 and Full designs (Figure 36). However, quantitatively, the CORA component scores were below 0.58 for the corridor and shape components, resulting in an overall score of 0.572. For comparison, the upper right tibia axial force measurement (TibiaRUFz) in the Half V1 test showed a CORA score of 0.729, but was visually distinct from tests of the Half V0 and Full barrier designs (Figure 37).

Table 8
Naming convention for THOR-50M time-histories

Name	Description
HeadACRes	Head CG resultant acceleration
HeadAVx	Head CG angular velocity (x)
HeadAVy	Head CG angular velocity (y)
HeadAVz	Head CG angular velocity (z)
NeckFz	Upper neck force (z)
NeckMy	Upper neck moment (y)
ChestLL	Resultant left lower chest displacement
ChestRL	Resultant right lower chest displacement
ChestLU	Resultant left upper chest displacement
ChestRU	Resultant right upper chest displacement
AcetabRIRes	Resultant right acetabular force
AcetabLERes	Resultant left acetabular force
FemurLE	Left femur force (z)
FemurRI	Right femur force (z)
TibiaRUFz	Right upper tibia force (z)
TibiaRUMomRes	Right upper tibia moment resultant (x,y)
TibiaRLFz	Right lower tibia force (z)
TibiaRLMomRes	Right lower tibia moment resultant (x,y)
TibiaLUFz	Left upper tibia force (z)
TibiaLUMomRes	Left upper tibia moment resultant (x,y)
TibiaLLFz	Left lower tibia force (z)
TibiaLLMomRes	Left lower tibia moment resultant (x,y)

Table 9
CORA scores for belted driver THOR-50M response when the OMDB impacts production vehicles

	Small		Mid-size		Large PU	
	V0 ¹	V1	V0	V1 ²	V0	V1
HeadACRes	0.928	0.961	0.936	NA	0.888	0.826
HeadAVx	0.772	0.921	0.904	NA	0.652	0.629
HeadAVy	0.904	0.847	0.920	NA	0.714	0.787
HeadAVz	0.827	0.884	QD	NA	0.508	0.501
NeckFz	0.873	0.903	0.873	NA	0.851	0.331
NeckMy	0.799	0.661	0.657	NA	0.718	0.672
ChestLL	QD	QD	0.509	NA	0.750	0.637
ChestRL	0.926	0.948	0.535	NA	0.681	0.927
ChestLU	QD	QD	0.621	NA	0.826	0.586
ChestRU	0.936	0.919	0.621	NA	QD	QD
AcetabRIRes	0.928	0.741	0.907	NA	0.799	0.619
AcetabLERes	0.808	0.743	0.855	NA	0.908	0.622
FemurLE	0.813	0.763	0.470	NA	0.772	0.736
FemurRI	0.969	0.783	0.883	NA	0.627	0.601
TibiaRUFz	0.936	0.789	0.807	NA	0.673	0.662
TibiaRUMomRes	0.902	0.663	0.712	NA	0.735	0.748
TibiaRLFz	0.964	0.839	0.883	NA	0.585	0.663
TibiaRLMomRes	0.879	0.672	0.802	NA	0.807	0.863
TibiaLUFz	0.787	0.572	0.665	NA	0.290	0.361
TibiaLUMomRes	0.792	0.722	0.812	NA	0.890	0.702
TibiaLLFz	0.848	0.729	0.774	NA	QD	QD
TibiaLLMomRes	0.720	0.721	0.816	NA	0.793	0.677
Average	0.866	0.789	0.760	NA	0.723	0.658

QD – Questable data

NA – Not applicable, test was not performed for this vehicle

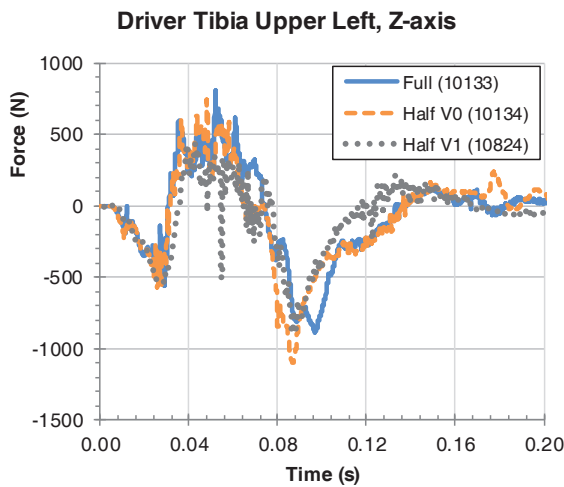


Figure 36 Driver left upper tibia Z-axis force for the Small vehicle in the Full, Half V0, and Half V1 conditions.

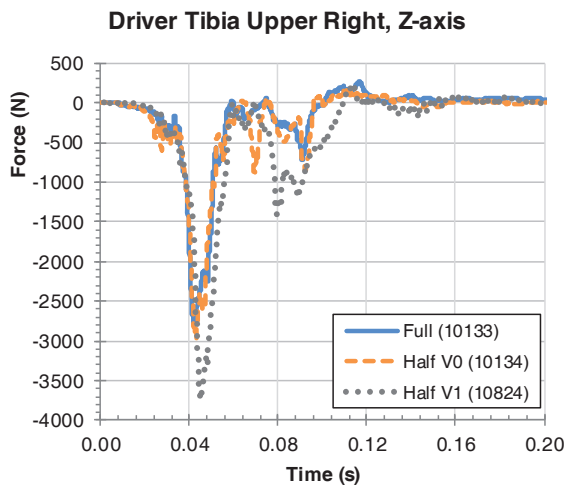


Figure 37 Driver right upper tibia Z-axis force for the Small vehicle in the Full, Half V0, and Half V1 conditions.

For the Mid-size vehicle, where only the Half V0 barrier test was conducted, CORA scores for the driver measurements were evenly split between “Good” and “Acceptable”, with three scores falling in the “Poor” range: ChestLL, ChestRL, and FemurLE. The lower left chest resultant deflection (ChestLL) was higher in the Full condition (Figure 38), while the lower right chest resultant deflection (ChestRL) was higher in the Half V0 condition (Figure 39). However, these differences are unlikely to have implications in injury risk prediction, as the peak resultant deflection occurred in the upper right chest in the Mid-size vehicle in both barrier conditions. That said, the overall peak resultant deflection was about 12 millimeters higher in the Half V0 condition, which is surprising since the shoulder belt force time-histories were nearly identical between the Full and Half V0 conditions, and the vehicle crash pulse in the Full condition was slightly more severe. One possible explanation is the initial position of the driver, which may have been further from the steering wheel airbag in the Full condition compared to the Half V0 condition as evidenced by pre-test position measurements at the chest to dash (Full: 596 mm, Half V0: 570 mm), chest to steering hub (Full: 377 mm, Half V0: 342 mm), and rim to abdomen (Full: 225 mm, Half V0: 197 mm) locations. Similarly, the left knee-to-dash distance was 10 mm greater in the Full condition, which may have reduced the magnitude of interaction of the knee with the knee bolster and subsequently reduced the left femur compressive force (FemurLE) compared to the Half V0 condition (Figure 40).

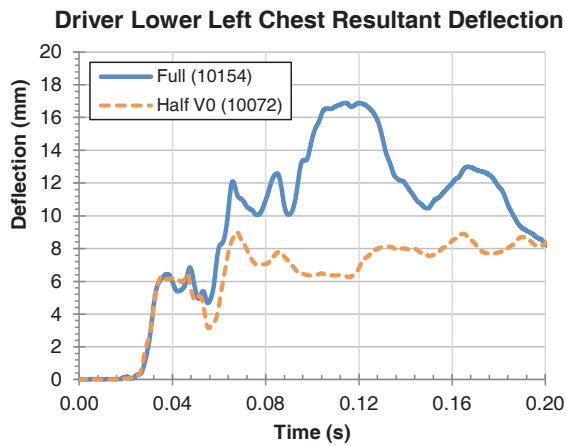


Figure 38 Driver lower left chest resultant deflection for the Mid-size vehicle in the Full and Half V0 conditions.

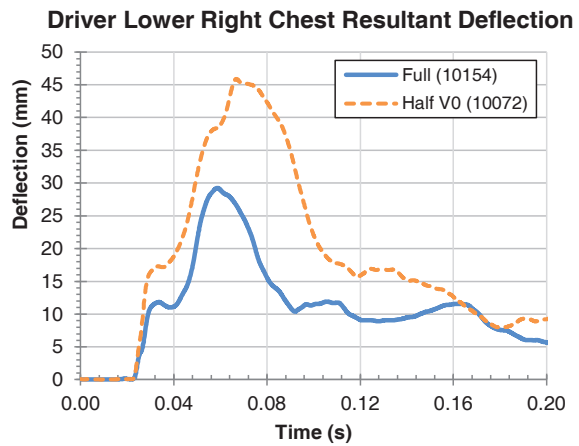


Figure 39 Driver lower right chest resultant deflection for the Mid-size vehicle in the Full and Half V0 conditions.

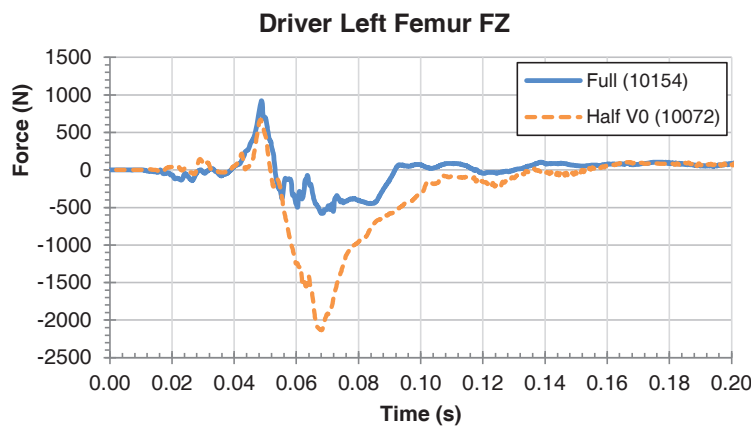


Figure 40 Driver left femur Z-axis force for the Mid-size vehicle in the Full and Half V0 conditions.

The Large PU tests showed more differences in driver response between the Full and the Half barrier tests than the other two production vehicles. In the Half V0 condition, there were 6 “Good” and 2 “Poor” scores, while in the Half V1 condition, there were 3 “Good” and 3 “Poor” scores, with the remainder falling into the “Average” range. The “Poor” scores for the Half V0 condition occurred in the HeadAVz and TibiaLUFz measurements. Differences in the head angular rate about the Z-axis are apparent across all three barrier conditions (Figure 41), as the Half V0 and Half V1 conditions show an early positive peak that does not occur in the Full test. Review of the high-speed video shows that, compared to the Full condition, the head contacts closer to the center of the steering wheel airbag in the Half V0 and Half V1 conditions, resulting in inboard rotation of the head. This difference does result in noticeable differences in the Brain Injury Criterion (BrIC) for the driver in the Large PU tests, as the BrIC in the Full barrier condition (0.66) was lower than in the Half V0 (0.89) and Half V1 (0.86) conditions. Differences in the left upper tibia axial force showed a similar trend, where the Half V0 and Half V1 responses were more similar to each other than to the Full barrier condition (Figure 42). However, the three conditions showed similar peak compressive forces, which were all relatively low both compared to risk of injury (probability of AIS 2+ injury below 1 percent) and compared to the peak tibia compressive forces in other tibia locations throughout the Large PU tests.

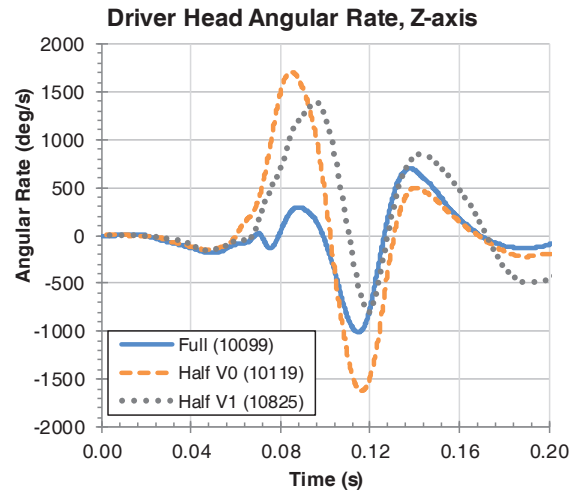


Figure 41 Driver Z-axis head angular rate for the Large PU in the Full, Half V0, and Half V1 conditions.

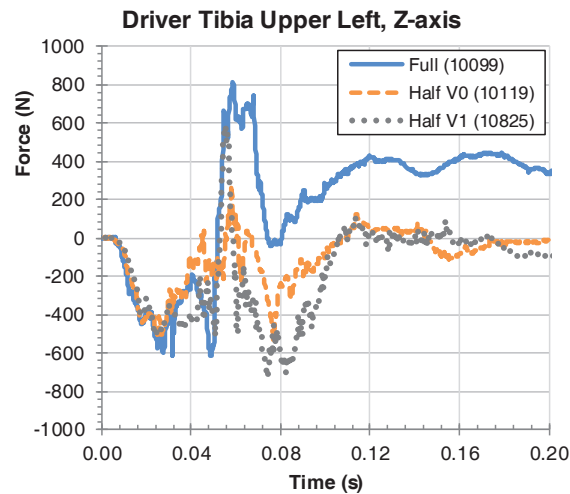


Figure 42 Driver left upper tibia Z-axis force for the Large PU in the Full, Half V0, and Half V1 conditions.

The “Poor” scores for the driver in the Large PU in the Half V1 condition also occurred in the HeadAVz, and TibiaLUFz measurements, as discussed above, but also the NeckFz measurements. The neck axial force time-history (NeckFz) in the Half V1 condition showed similar timing to the Full condition, but the peak tension is about 340 N lower than the Full and Half V0 conditions (Figure 43). Review of the high-speed video from these tests did not identify differences in head and neck kinematics, though the difference in neck tension may have resulted from the difference in vehicle crash pulse (Figure 33).

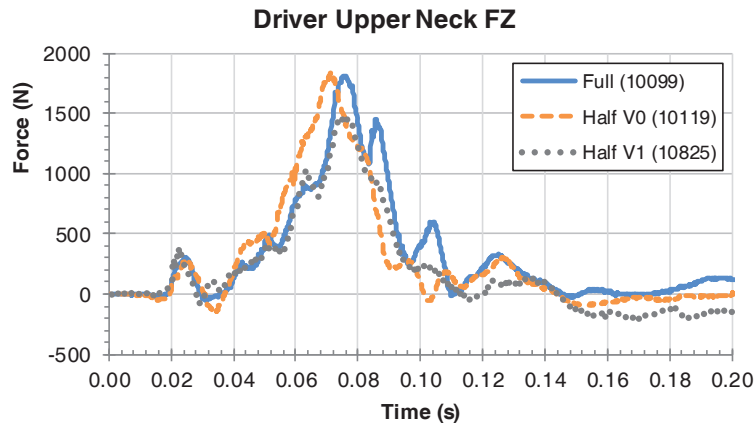


Figure 43 Driver upper neck Z-axis force for the Large PU in the Full, Half V0, and Half V1 conditions.

Occupant Response: Passenger

Within each production vehicle, right front passenger kinematics were similar across all barrier designs. Table 10 shows the CORA scores for the belted THOR-50M passenger. For the Half V0 tests, the average CORA ratings for the right front passenger in the Small, Mid-size, and Large PU vehicles were all in the “Good” range, with scores of 0.867, 0.852, and 0.842, respectively. For the Half V1 tests, the average CORA ratings for the right front passenger in the Small and Large PU were “Acceptable”, with scores of 0.762 and 0.689, respectively.

For the Small vehicle, the Half V0 test showed relatively comparable results for the right front passenger measurements, with all CORA scores in the “Good” or “Acceptable” range, with a lowest CORA score of 0.706. In the Half V1 test, on the other hand, there were more “Acceptable” results and two “Poor” results. One of the “Poor” results was the neck moment (NeckMy), where the Half V1 test showed a similar response to the other two conditions except for between 110 and 160 ms, where the extension moment was lower (Figure 44). While there were differences in the resulting Nij values (Full: 0.38, Half V0: 0.37, Half V1: 0.45), the elevated Nij in the Half V1 condition appears to result from a higher peak in neck axial force (NeckFZ) at roughly 80 ms after impact. The other “Poor” result occurred in the upper right tibia resultant moment measurement (TibiaRUMomRes), where the Half V1 condition showed a different response trend, with lower moments up to 50 ms and higher moments between 50 and 100 ms after impact (Figure 46). The upper left tibia resultant moment (TibiaLUMomRes), which also had a relatively low CORA score at 0.589, showed the opposite trend, with higher moments earlier and lower moments later in the event (Figure 45).

Table 10
CORA scores for belted passenger THOR-50M response when the OMDB impacts production vehicles

	Small		Mid-size		Large PU	
	V0 ¹	V1	V0	V1 ²	V0	V1
HeadACRes	QD	QD	0.892	NA	0.971	0.899
HeadAVx	0.740	0.926	0.824	NA	0.955	0.913
HeadAVy	0.873	0.763	0.880	NA	0.910	0.901
HeadAVz	0.921	0.868	QD	NA	0.919	0.853
NeckFz	0.732	0.830	0.801	NA	0.792	0.739
NeckMy	0.873	0.476	0.783	NA	0.776	0.312
ChestLL	0.956	0.730	0.878	NA	0.862	0.804
ChestRL	0.837	0.758	0.711	NA	0.846	0.565
ChestLU	0.930	0.799	0.915	NA	QD	QD
ChestRU	0.706	0.661	0.830	NA	0.719	0.627
AcetabRIRes	QD	QD	0.885	NA	0.783	QD
AcetabLERes	0.839	0.878	QD	NA	0.718	0.539
FemurLE	0.972	0.843	0.890	NA	0.940	0.830
FemurRI	0.929	0.747	0.890	NA	0.928	0.917
TibiaRUFz	0.952	0.808	0.885	NA	0.842	0.654
TibiaRUMomRes	0.877	0.538	0.708	NA	0.864	0.570
TibiaRLFz	0.964	0.827	0.925	NA	0.849	0.577
TibiaRLMomRes	0.792	0.638	0.916	NA	0.849	0.400
TibiaLUFz	0.928	0.877	0.904	NA	0.725	0.597
TibiaLUMomRes	0.754	0.589	0.708	NA	0.838	0.722
TibiaLLFz	0.928	0.864	0.900	NA	QD	QD
TibiaLLMomRes	0.840	0.812	0.912	NA	0.756	0.678
Average	0.867	0.762	0.852	NA	0.842	0.689

QD – Questable data

NA – Not applicable, test was not performed for this vehicle

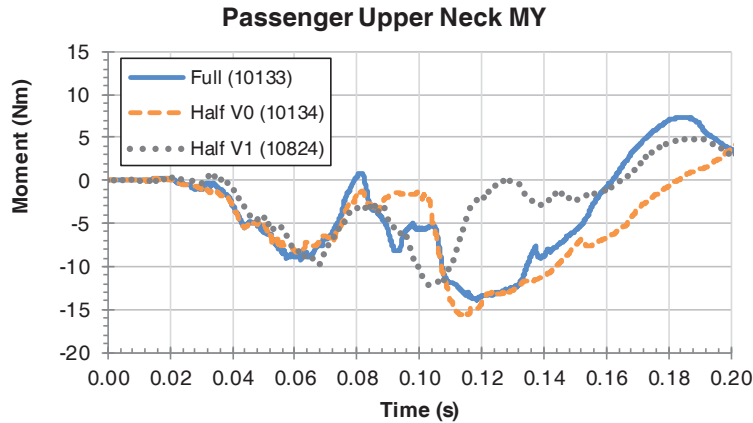


Figure 44 Passenger upper neck Y-axis moment for the Small vehicle in the Full, Half V0, and Half V1 conditions.

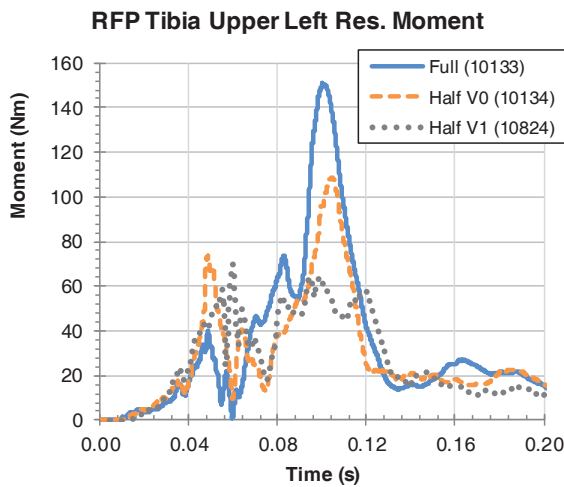


Figure 45 Passenger upper left tibia resultant moment for the Small vehicle in the Full, Half V0, and Half V1 conditions.

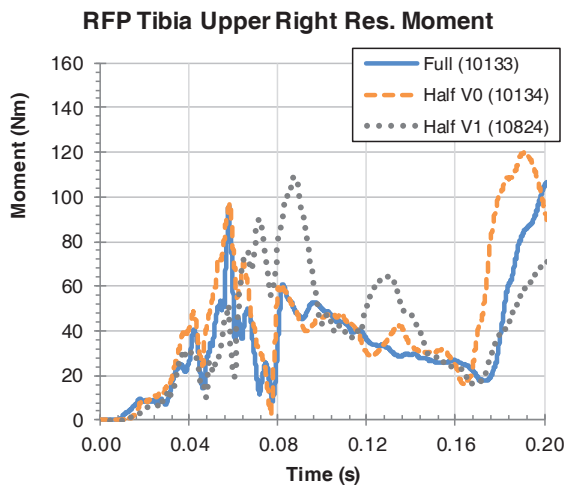


Figure 46 Passenger upper right tibia resultant moment for the Small vehicle in the Full, Half V0, and Half V1 conditions.

The passenger measurements in the Half V0 test of the Mid-size vehicle showed relatively comparable results, with all CORA scores in the “Good” or “Acceptable” range and the minimum CORA score being 0.708. The Half V0 results for the right front passenger in the Large PU were similar, with a few more measurements falling in the “Acceptable” range but with all scores at or above 0.718.

The right front passenger measurements in the Half V1 test of the Large PU, on the other hand, were evenly divided between “Good” (7 measurements), “Acceptable” (7 measurements), and “Poor” (6 measurements). The “Poor” measurements were NeckMy, ChestRL, AcetabLERes, TibiaRUMomRes, TibiaRLFz, and TibiaRLMomRes. As with previous “Poor” assessments of NeckMy, the resulting Nij injury criteria calculation does not appear to be influenced by the variation of the neck Y-axis moment (Full: 0.30; Half V0: 0.27; Half V1: 0.31). Similarly, the variation in the lower right chest resultant deflection (ChestRL) does not influence injury prediction, as the peak resultant deflection occurs in either the upper left or upper right quadrants of the right front passenger in the Large PU tests. The variation in the left acetabulum resultant force (AcetabLERes) occurs primarily after the peak femur force occurs (Figure 47), thus the second peaks that occur after 100 ms in the Half V0 and Half V1 tests (Figure 48) do not contribute to acetabulum injury risk. In both the femur and acetabulum force time-histories, the largest magnitude of force occurs in the Full condition, followed by the Half V0 and then the Half V1 conditions. This is

consistent with the vehicle crash pulses shown in Figure 32 and Figure 33, which suggest that the Half V1 condition presented the least severe pulse to the occupants. Similarly, in the lower leg of the right front passenger of the Large PU, the right upper tibia resultant moment (TibiaRUMomRes), right lower tibia Z-axis force (TibiaRLFz), and right lower tibia resultant moment (TibiaRLMomRes) all demonstrate forces that are generally lower for the Half V1 than the Half V0 and Full conditions (Figure 50 through 52).

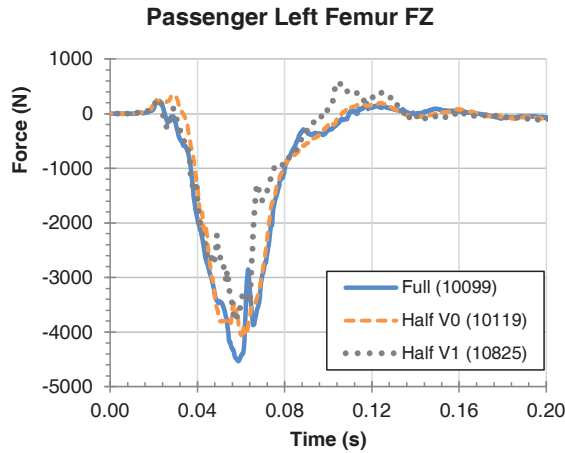


Figure 47 Passenger left femur Z-axis force for the Large PU vehicle in the Full, Half V0, and Half V1 conditions.

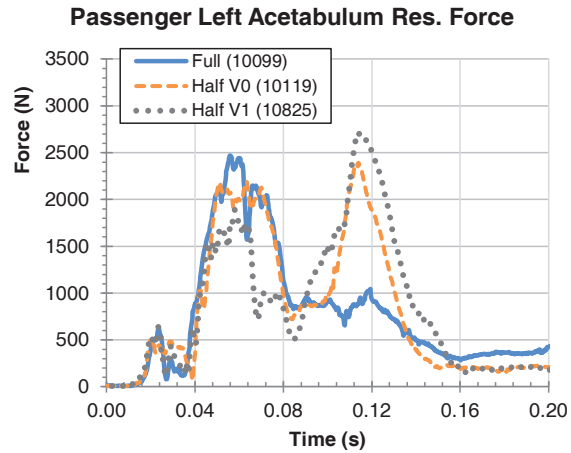


Figure 48 Passenger left acetabulum resultant force for the Large PU vehicle in the Full, Half V0, and Half V1 conditions.

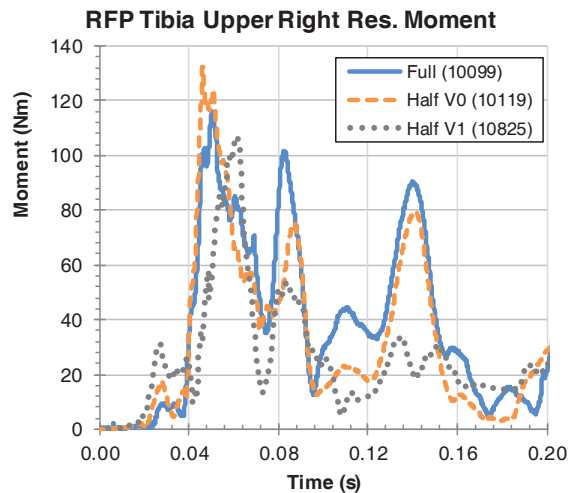


Figure 49 Passenger upper right tibia resultant moment for the Large PU vehicle in the Full, Half V0, and Half V1 conditions.

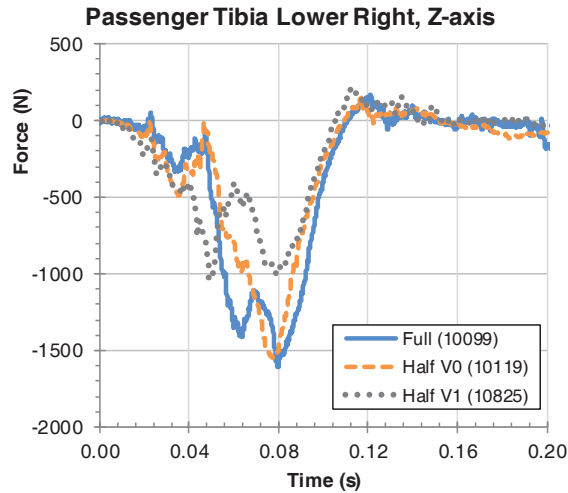


Figure 50 Passenger lower right tibia Z-axis force for the Large PU vehicle in the Full, Half V0, and Half V1 conditions.

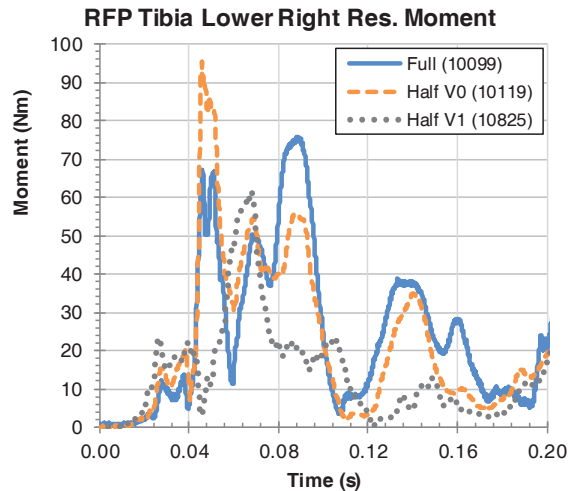


Figure 51 Passenger lower right tibia resultant moment for the Large PU vehicle in the Full, Half V0, and Half V1 conditions

Rigid Moving Barrier Response

Half V0 seems to be a suitable replacement of the Full barrier. Therefore, a set of tests were performed using a rigid moving barrier instead of production vehicles to eliminate variability in response of production vehicles. Using this rigid barrier eliminates the variability of vehicle deformation. The rigid moving barrier used for this testing was an FMVSS No. 301 Moving Contoured Barrier (MCB) (Figure 52).

Six tests were performed with alternating installation of full and half honeycomb barriers (Table 11). The first test was performed at an impact speed of 70 km/h with a full honeycomb barrier installed on the OMDB. The energy of the OMDB impact caused some of the MCB's face plate fasteners to fail and resulted in minor deformations to the MCB supporting structure. The MCB was repaired and strengthened to prevent deformation in further testing. This led to an increase in the MCB weight of approximately 92 kg, resulting in a final weight of 1,898 kg, without a significant change in the fore/aft location (< 8 mm) of the vehicle center of gravity (CG).

For the remaining five tests, the impact speed of the OMDB was reduced to 60 km/h. A total of three half honeycomb barrier and two full honeycomb barrier tests were run at this test speed. Tests using the half honeycomb barrier mounted it on the left side of the OMDB.

Table 11
Test matrix for MDB testing

NHTSA Test Number	Barrier Type	Naming Convention
9796	Full	NA *
9797	Full	Full 1
9799	Full	Full 2
9796	Half V0	Half V0 1
9798	Half V0	Half V0 2
9800	Half V0	Half V0 3

* NA – Not applicable, test caused damage to cart



Figure 52 Picture of the moving contoured barrier (MCB)

Figure 53 shows the energy absorbed by the honeycomb when impacting the MCB. It is seen that the average energy absorbed by the honeycomb Half V0 is decreased by 15 percent when compared to Full.

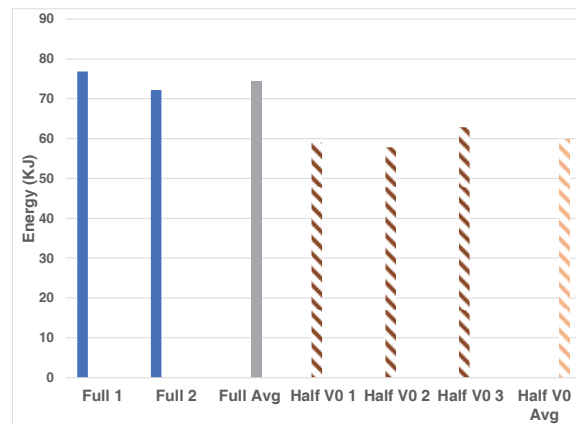


Figure 53 Energy absorbed by the honeycomb when the OMDB impacts the MCB

Figure 54 through Figure 56 show the crush profiles, for different rows, for the Full and Half V0 when impacting the MCB. It is seen that the crush profile of Half V0 is shifted to the right when compared to Full. R3 had more variability in crush compared to R6 and R9.

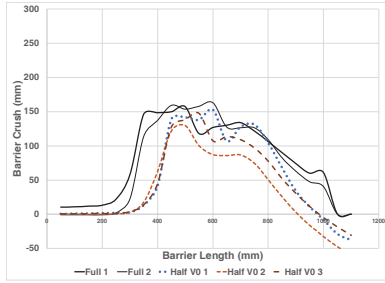


Figure 54 R3 honeycomb crush when impacting MCB

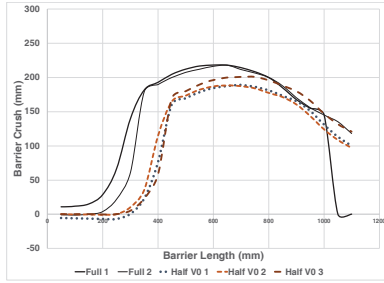


Figure 55 R6 honeycomb crush when impacting MCB

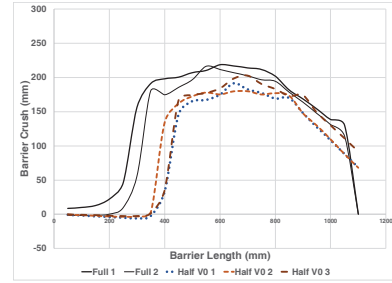


Figure 56 R9 honeycomb crush when impacting MCB

Table 12 shows the naming convention for MCB time-histories when using MCB as a target vehicle. Table 13 shows the naming convention for the OMDB when using the MCB as a target vehicle.

Table 14 shows the CORA scores for the OMDB when impacting the MCB. It is seen that the lowest CORA score is for the OMDBMCBCGav (0.902) and the average CORA score for all OMDB parameters was 0.947. Table 15 shows the CORA scores for the MCB responses. It can be seen from this table that the CORA scores ranged from 0.424 to 0.997 and the average CORA score was 0.807. The MCBCGav and MCBCGang were graded “poor.” To investigate why the CORA scores were “Poor”, film analysis was performed on the MCB. Figure 57 shows the time-histories for the MCB rotation. The figure shows differences between each test, but film analysis showed closer similarity of the rotation (Figure 59). Running CORA on the film analysis increased the CORA score to Acceptable (0.789). It is unknown why the integration of the angular velocity showed different results than the film analysis.

Table 12
Naming convention for MCB time-histories when using MCB as target vehicle

Name	Description
MCBCGaccRes	MCB CG resultant acceleration (x,y)
MCBCGvelRes	MCB CG resultant velocity (x,y)
MCBCGav	MCB CG angular velocity (z)
MCBCGang	MCB CG rotation (z)
MCBRearAccRes	MCB centerline rear resultant acceleration (x,y)
MCBRearVelRes	MCB centerline rear resultant velocity (x,y)
MCBLeftAccRes	MCB left frame resultant acceleration (x,y)
MCBLeftVelRes	MCB left frame resultant velocity (x,y)

Table 13
Naming convention for OMDB time-histories when using MCB as target vehicle

Name	Description
OMDBMCBCGaccRes	OMDB CG resultant acceleration (x,y)
OMDBMCBCGvelRes	OMDB CG resultant velocity (x,y)
OMDBMCBCGav	OMDB CG angular velocity (z)
OMDBMCBCGang	OMDB CG rotation (z)*
OMDBMCBRearAccRes	OMDB centerline rear resultant acceleration (x,y)
OMDBMCBRearVelRes	OMDB centerline rear resultant velocity (x,y)
OMDBMCBLeftAccRes	OMDB left frame resultant acceleration (x,y)
OMDBMCBLeftVelRes	OMDB left frame resultant velocity (x,y)*

Table 14
CORA scores for the OMDB when the OMDB impacts the MCB

Name	CORA	Name	CORA
OMDBMCBCGaccRes	0.869	OMDBMCBRearAccRes	0.943
OMDBMCBCGvelRes	0.965	OMDBMCBRearVelRes	0.989
OMDBMCBCGav	0.902	OMDBMCBLeftAccRes	0.952
OMDBMCBCGang	0.972	OMDBMCBLeftVelRes	0.987
		Average of all scores	0.947

Table 15
CORA scores for the MCB when the OMDB impacts the MCB

Name	CORA	Name	CORA
MCBCGaccRes	0.887	MCBRearAccRes	0.820
MCBCGvelRes	0.954	MCBRearVelRes	0.908
MCBCGav	0.424	MCBLeftAccRes	0.967
MCBCGang	0.497	MCBLeftVelRes	0.997
		Average of all scores	0.807

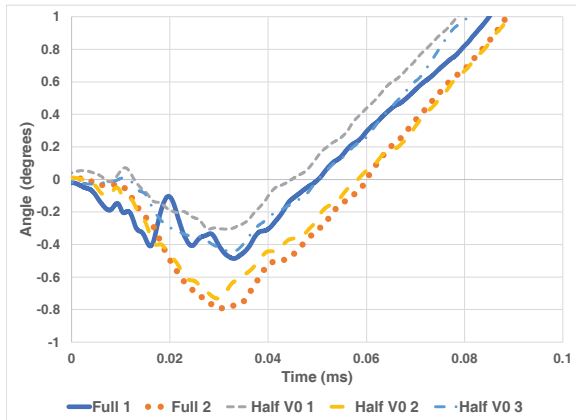


Figure 57 MCB rotation about the z-axis time-histories

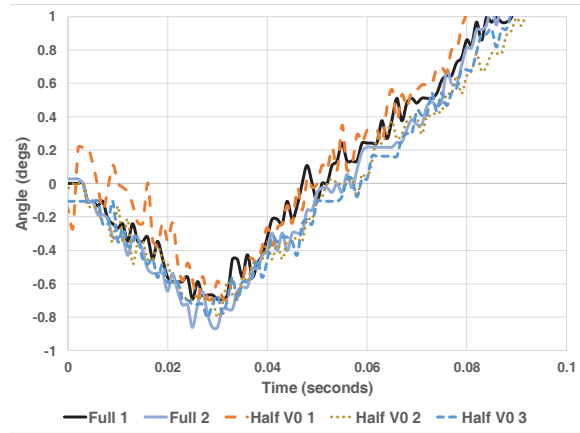


Figure 58 MCB rotation about the z-axis from film analysis

DISCUSSION

OMDB, Vehicle

Attaching the left side of the honeycomb to the OMDB attachment (Half V1) prevented the honeycomb from expanding out from the OMDB (Figure 59), but it did not prevent all barrier separation. Figure 60 shows an example of the honeycomb separation with the small vehicle when impacted with the Half V1. Again, it is unknown what effect this separation has on the performance of this test procedure. A side effect of attaching the medial end of the cladding to the barrier support in the Half V1 design was that it changed the magnitude of energy absorbed by the honeycomb (Figure 8). This was especially true for the Large PU, where the energy absorbed in the Half V1 design was 32 percent lower than in the Full design. Similarly, the interior intrusions differed in the Half V1 design compared to the other barrier faces, especially for the Large PU (Figure 31). The Half V1 also showed a difference in acceleration.



Figure 59 No honeycomb pulling apart from the Half V1

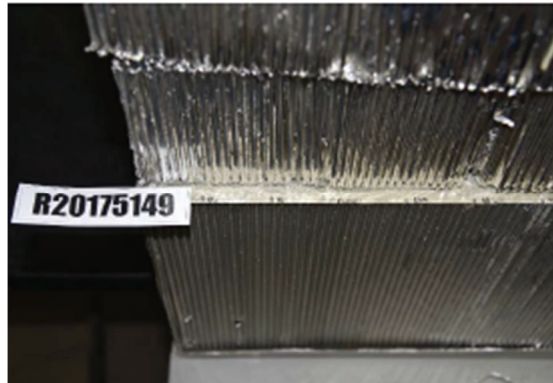


Figure 60 Separation of the two pieces of honeycomb for the Half V1 when impacting the small vehicle

Occupant Response

Overall, the occupant kinematics in tests of different barrier designs using the same production vehicle were similar, as evidenced by review of the high-speed video from cameras mounted within the vehicle looking over the inboard shoulder of the occupant. Contacts with the restraint system occurred at similar times and locations, with the exception of the driver contact with the steering wheel airbag in the Large PU tests, where the head impacted closer to the center of the airbag in the Full test than tests of the Half V0 and Half V1 designs. This visible difference in head kinematics was captured by the head injury criteria, as the HIC and BrIC metrics in the Full condition were 10 percent and 25 percent lower, respectively, than in the Half V0 and Half V1 conditions. Otherwise, many of the differences in occupant kinetics time-histories occurred in the femur and upper tibia, areas which were not readily visible in these camera views due to interference from frontal airbags and the torso of the occupant.

In the Small and Large PU OMDB tests, the Half V0 barrier face showed higher CORA scores for occupant response than the Half V1 barrier, suggesting that the Half V0 performance is more similar to the Full barrier face than the Half V1 design. While there was no data available to compare Half V0 and Half V1 in the Mid-size vehicle, the average CORA scores for the Half V0 were similar to those in the Small and Large PU vehicles. In a previous study of the repeatability and reproducibility of the OMDB test procedure, average CORA scores across three tests using the same Full barrier face in impacts with a production sport-utility vehicle ranged from 0.772 to 0.850 depending on the test lab conducting the tests [3]. Therefore, based on objective evaluation of occupant response time-histories, the difference between the Half V0 barrier face and the Full barrier face is within the range of expected test-to-test repeatability of the Full barrier face itself.

The driver occupant location appeared to be more sensitive to changes in the barrier face, as the average CORA scores for each vehicle/barrier comparison were equal or lower for the driver than for the right front passenger. One possible explanation for this finding is that the driver side of the occupant compartment sees more intrusion, both static and dynamic, than the passenger side due to the configuration of the crash test (Figure 6). Measured static intrusions, as shown in Figure 29 through Figure 31, varied between the different barrier face conditions; dynamic

intrusion is more difficult to quantify, but can be seen in the high-speed video. In contrast, the passenger side of the occupant compartment sees little to no intrusion, presenting more consistent boundary conditions to the right front passenger.

In some of the test conditions, the same THOR-50M ATD was used for all two or three tests in a given seating location, while others used a different THOR-50M ATD in the Half V1 test condition (Table 16). For example, the driver in the Large PU was serial number (S/N) 9798 for all three barrier conditions, while the right front passenger was S/N 9207 in the Full and Half V0 conditions, but EG2595 in the Half V1 condition. In theory, this data could be used to assess the repeatability and reproducibility of the THOR-50M, though in practice the variation in barrier face and vehicle response prevented a clean comparison. As an example, since the same THOR-50M ATD was used in the driver location of the Large PU tests, the variability was expected to be the smallest. However, the average CORA scores for both the Half V0 and Half V1 conditions were actually the lowest out of all vehicles and seating positions in the study. Therefore, it is not possible to separate the variability in the ATD response from the variability in the barrier and/or vehicle response. On the other hand, the fact that the tests using EG2595, which included an onboard data acquisition system (DAS), had average CORA scores equal to or higher than the driver ATD in the same vehicle/barrier condition suggests that the differences in response were not driven by the differences between an onboard DAS system and an umbilical configuration.

Table 16. Occupant response repeatability and reproducibility

TSTNO	Vehicle Class	Barrier Face	Driver S/N	Driver Average CORA Score	RFP S/N	RFP Average CORA Score
10099	Small	Full	9207		9798	
10119		Half V0	9207	0.866	9798	0.867
10825		Half V1	9798	0.789	EG2595	0.762
10154	Mid-size	Full	9798		9207	
10072		Half V0	9798	0.760	9207	0.852
10133	Large PU	Full	9798		9207	
10134		Half V0	9798	0.723	9207	0.842
10824		Half V1	9798	0.658	EG2595	0.689

CONCLUSIONS

This study evaluated the performance of two half-width barrier faces compared to a full-width barrier face in OMDB crash tests of three classes of production vehicles. This analysis compared the responses of the barriers, vehicles, and occupants using an objective evaluation method. Based on this objective evaluation using CORA scores, the Half V0 barrier face design was more similar to the Full barrier face than the Half V1 design. The Half V0 demonstrated average CORA scores in the “Good” category for the OMDB and vehicle measurements in tests of all three production vehicles, and average occupant response measurements in the “Good” category for 4 of the 6 occupant locations, and higher CORA scores than the Half V1 barrier in all cases. The Half V0 barrier design did result in post-test separation of the two layers of honeycomb in the design, but it’s not clear how this differs from the Full barrier design. It is also not clear what the consequences of this separation might be, though one possible challenge would be representing this separation in computational models of this barrier face. It was clear, however, that attempts to prevent this separation in the Half V1 design resulted in differences in the barrier face crush, vehicle intrusion, and occupant response compared to the Full barrier. Given these findings, the Half V0 barrier face design appears to be a reasonable alternative to the Full barrier face design for use in OMDB crash tests.

REFERENCES

- [1] [OMDB | NHTSA](#) NHTSA Frontal Mobile Deformable Half Barrier Face V2015b.
- [2] [OMDB | NHTSA](#) OMDB Frontal Mobile Deformable Barrier Face v2014.
- [3] Saunders, J. and Parent, D., “Repeatability and Reproducibility of Oblique Moving Deformable Barrier Test Procedure,” SAE Technical Paper 2018-01-1055, 2018, doi:10.4271/2018-01-1055.
- [4] <https://www.nhtsa.gov/research-data/research-testing-databases#/vehicle>.
- [5] National Highway Traffic Safety Administration, “Oblique Test Procedure,” Docket ID 2015-0119, 2016.
- [6] “CORApplus 4.0.4 (release date 2017-06-21),” [Online]. Available: <http://www.pdb-org.com/en/information/18-coradownload.html>.

**National Highway Traffic Safety Administration
(NHTSA)**

Oblique Mobile Deformable Half Barrier Face Specification

Version 2 (2019)

Table of Contents

1.0	INTRODUCTION.....	3
2.0	BARRIER COMPONENTS.....	4
3.0	MATERIAL SPECIFICATIONS & OVERALL DIMENSIONS.....	7
3.1	REAR HONEYCOMB BLOCK.....	7
3.2	FRONT HONEYCOMB BLOCK.....	7
3.3	BACKING SHEET.....	7
3.4	INTERMEDIATE SHEET.....	7
3.5	CONTACT SHEET.....	8
3.6	CLADDING SHEET.....	8
3.7	SIDE CLADDING.....	8
3.8	FRONT BRACKET.....	8
3.9	ADHESIVE.....	8
4.0	ADHESIVE BONDING PROCEDURE.....	9
5.0	ASSEMBLY PROCESS.....	10
5.1	BONDING HONEYCOMB TO ALUMINUM SHEETS.....	10
5.2	MOUNTING HOLES AND SLOTS.....	12
6.0	ASSEMBLY AND COMPONENT DRAWINGS.....	13

1.0 INTRODUCTION

The NHTSA Oblique Mobile Deformable Half Barrier Face V2019 is a 1200mm wide assembly of two layers of deformable aluminum honeycomb core. Each deformable core is 300 mm thick in the impact direction and is designed to provide a constant load in depth. The cores are adhesively bonded together with different aluminum sheets forming a ready to use deformable barrier to be fixed on a moving cart.

2.0 BARRIER COMPONENTS

The components of the barrier face are listed below and shown in Figure 1. The bonded surfaces are shown in Figure 2. The dimensions of the individual components of the barrier are listed in Section 3, with drawings found in Section 6.

1. Rear honeycomb block
2. Front honeycomb block
3. Backing sheet
4. Intermediate sheet
5. Contact sheet
6. Cladding sheet
7. Side bracket
8. Side cladding
9. Adhesive (Not Shown)

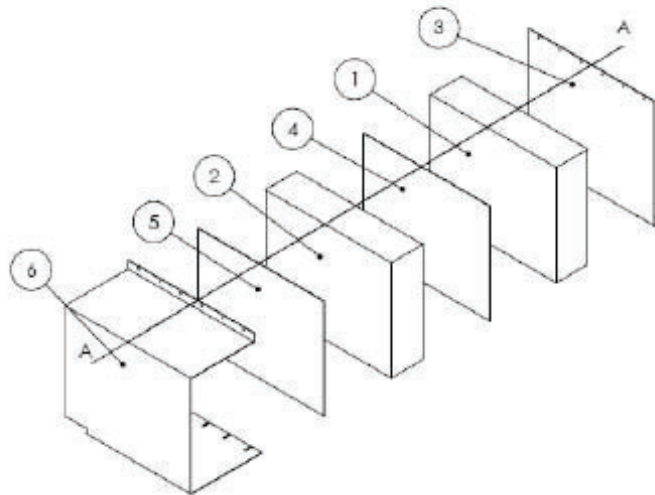


Figure 1 Components of Half Width Oblique Barrier (Core Body)

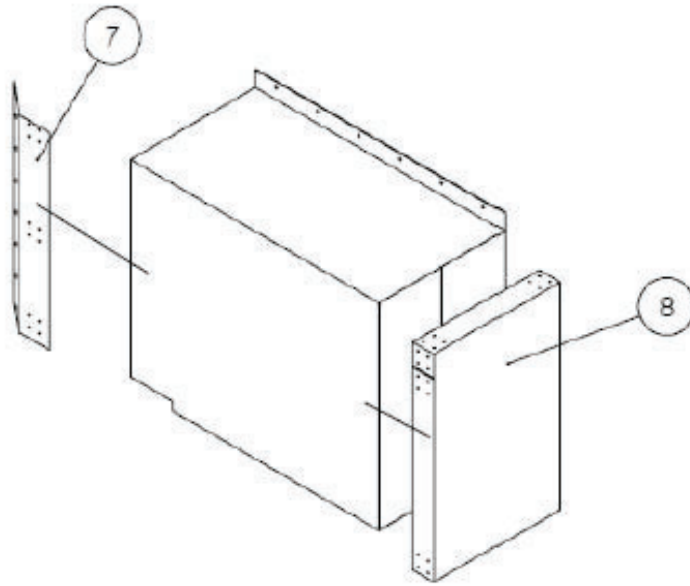
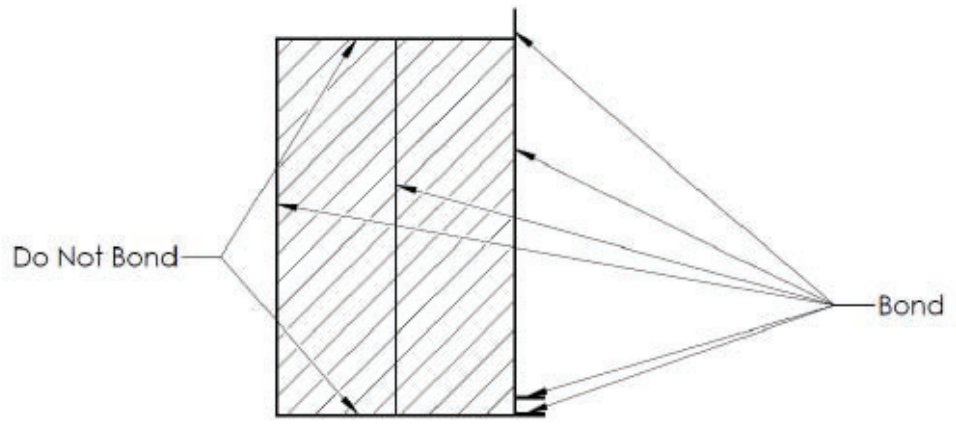


Figure 2 Components of Half Width Oblique Barrier (Core Body with Side Cladding and Side Bracket)



SECTION A-A

Figure 3 Cross-Section A-A – Adhesive Bonding of the Barrier

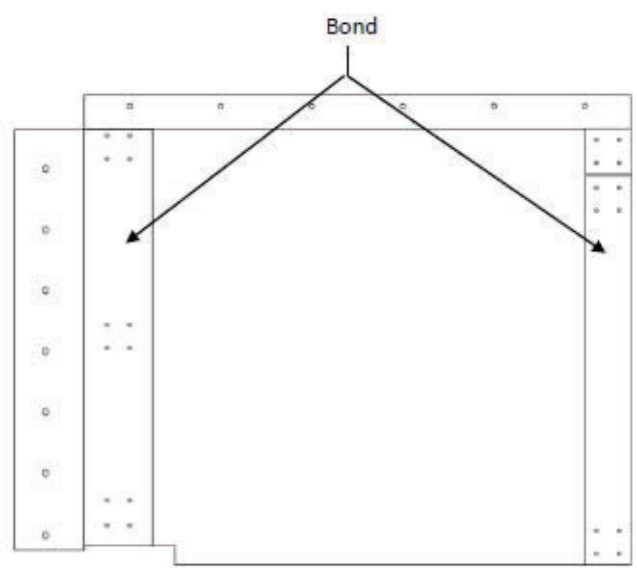


Figure 4 Front view – Adhesive Bonding of the Barrier continued

3.0 MATERIAL SPECIFICATIONS & OVERALL DIMENSIONS

3.1 REAR HONEYCOMB BLOCK

Dimensions:

Height (L): 950 ± 5 mm (in direction of honeycomb ribbon)
Width (W): 1200 ± 5 mm
Depth (T): 300 ± 1 mm (in direction of honeycomb cell)
Material: Aluminum 3003
Cell Size: 6.35 mm ± 20 percent
Crush Strength: 1.711 MPa +0 percent -10 percent¹

3.2 FRONT HONEYCOMB BLOCK

Dimensions:

Height (L): 950 ± 5 mm (in direction of honeycomb ribbon)
Width (W): 1200 ± 5 mm
Depth (T): 300 ± 1 mm (in direction of honeycomb cell)
Material: Aluminum 5052
Cell Size: 6.35 mm ± 20 percent
Crush Strength: 0.724 MPa +0 percent -10 percent¹

3.3 BACKING SHEET

Dimensions:

Height: 1025 mm ± 2.5 mm
Width: 1200 mm ± 2.5 mm
Thickness: 3.0 mm ± 0.25 mm
Material: Aluminum Series AlMg2 to AlMg3 with hardness between 50 and 67 HBS

3.4 INTERMEDIATE SHEET

Dimensions:

Height: 945 mm ± 2.5 mm
Width: 1195 mm ± 2.5 mm
Thickness: 0.5 ± 0.1 mm
Material: Aluminum 5251 H24 or Aluminum 5052 H32

¹In accordance with the certification procedure described in US Department of Transportation, NHTSA Laboratory Test Procedure for FMVSS No. 214 "Dynamic" Side Impact Protection, TP214D Appendix C Latest Revision.

3.5 CONTACT SHEET

Dimensions:

Height:	945 mm ± 2.5 mm
Width:	1195 mm ± 2.5 mm
Thickness:	1.6 mm ± 0.07 mm
Material:	Aluminum 5251 H24 or 5052 H34

3.6 CLADDING SHEET

Dimensions:

Height:	1026 mm ± 2.5 mm
Width:	1200 mm ± 2.5 mm
Thickness:	0.8 mm ± 0.1 mm
Material:	Aluminum 5754 H22 or 5052 H34

3.7 SIDE CLADDING

Dimensions:

Height:	952.5 mm ± 2.5 mm
Width:	601.75 mm ± 2.5 mm
Depth:	101 mm +/-2.5 mm
Thickness:	0.81 mm ± 0.1 mm
Material:	Aluminum 5754 H22 or 5052 H34

3.8 FRONT BRACKET

Dimensions:

Height:	918.5 mm ± 2.5 mm
Thickness:	0.81 mm ± 0.1 mm
Material:	Aluminum 5754 H22 or 5052 H34

3.9 ADHESIVE

The adhesive to be used throughout should be a Polyurethane adhesive or equivalent, with a minimum bonding strength of 0.6 MPa.²

²In accordance with the certification procedure described in ASTM C 297, using a sample of honeycomb representative of that in the impactor, bonded to a back plate material.

4.0 ADHESIVE BONDING PROCEDURE

Prior to bonding, all aluminum sheets shall be cleaned and prepared to provide optimal adhesion performance. The adhesive is only applied to the aluminum sheet surfaces when bonding aluminum sheets to honeycomb surfaces.

When bonding the cladding sheet to the backing sheet and when bonding the contact sheet to the cladding sheet, the adhesive is applied to one surface only.

A maximum of 0.5 kg/m² must be applied evenly over the surface, giving a maximum film thickness of 0.5 mm. Care should be taken to assure adhesive does not run into the honeycomb cells causing an increase in crushing strength of the honeycomb core.

5.0 ASSEMBLY PROCESS

5.1 BONDING HONEYCOMB TO ALUMINUM SHEETS

Verify that all surfaces are clean and prepared for bonding. The main part of the barrier face shall be assembled according to Figure 1. The rear honeycomb block shall be adhesively bonded to the backing sheet such that the cell axes are perpendicular to the backing sheet. The intermediate sheet shall be adhesively bonded to the rear and front honeycomb blocks. The cell axes of the front honeycomb block shall be perpendicular to the intermediate sheet. The contact sheet shall be adhesively bonded to the front honeycomb block. The outer cladding shall be adhesively bonded to the contact sheet. The top and bottom surfaces of the cladding sheet shall not be adhesively bonded to the main honeycomb block but should be positioned closely to it. The cladding sheet shall be adhesively bonded to the backing sheet at the mounting flanges. Side cladding will be adhesively bonded and riveted to the main body of the barrier. Likewise, the Front Bracket will be adhesively bonded, and riveted to the front of the main barrier body. All Rivets (32 in total) shall be ¼" aluminum button head Rivets. Bonding points can be seen in Figure 5 and Figure 6.

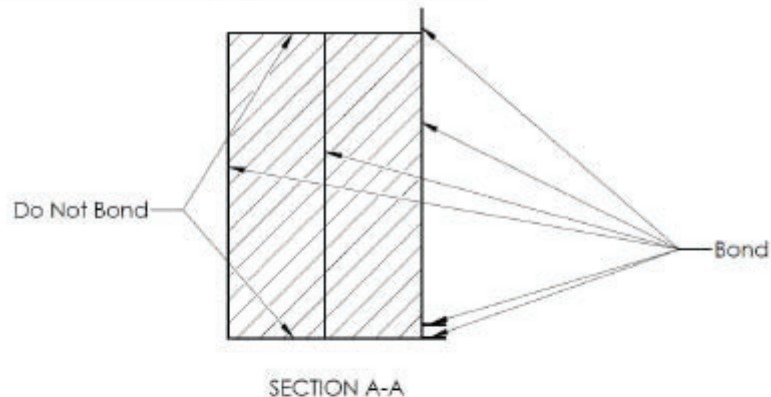


Figure 5 Main Body Assembly of the Barrier

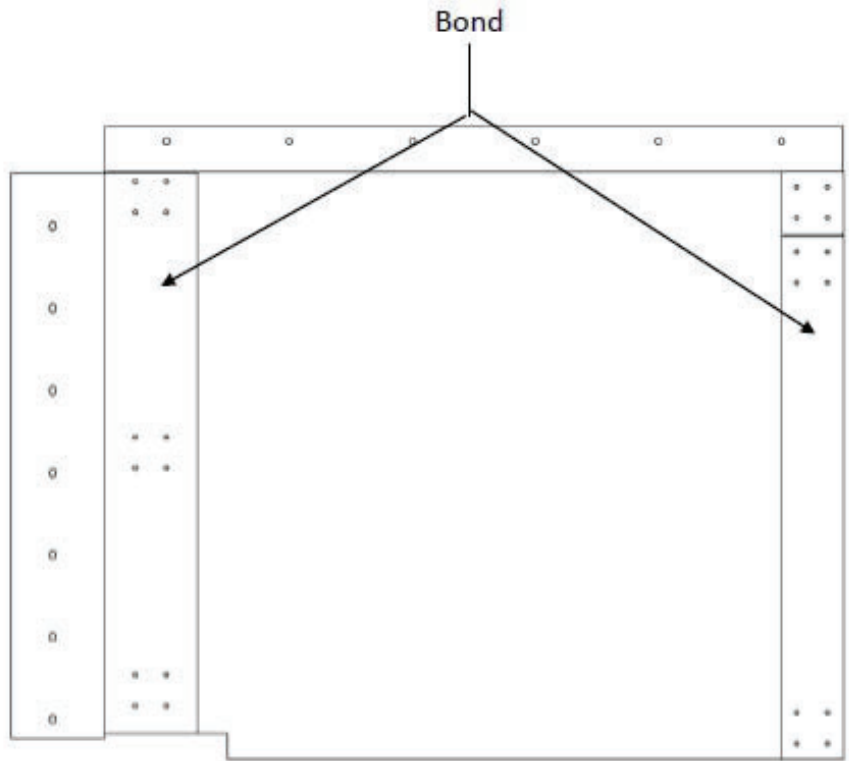


Figure 6 Main Body Assembly of the Barrier

5.2 MOUNTING HOLES AND SLOTS

The NHTSA Oblique Mobile Deformable Half Barrier V2019 has clearance holes and slots for mounting of the barrier. The holes shall have a diameter of 10.5mm. Six holes shall be located in the top flange at a nominal distance of 24.3mm from the top edge of the flange and six open slots in the bottom flange ending at a nominal distance of 60.2mm from the bottom edge of that flange. The holes and slots shall be at the locations shown in Figures 4 and 5. All holes and slots shall be located to ± 1 mm of the nominal distances.

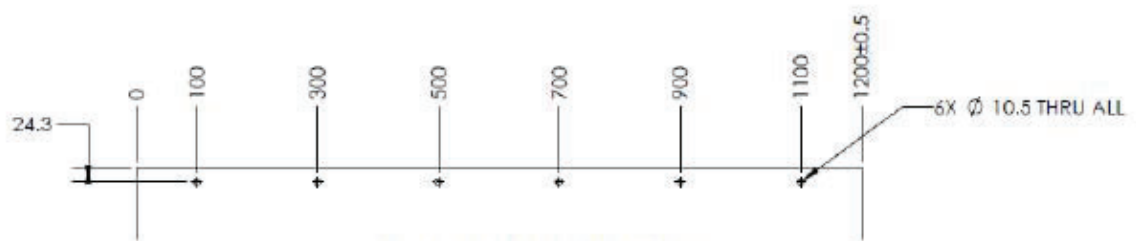


Figure 4 Top Flange Mounting Holes

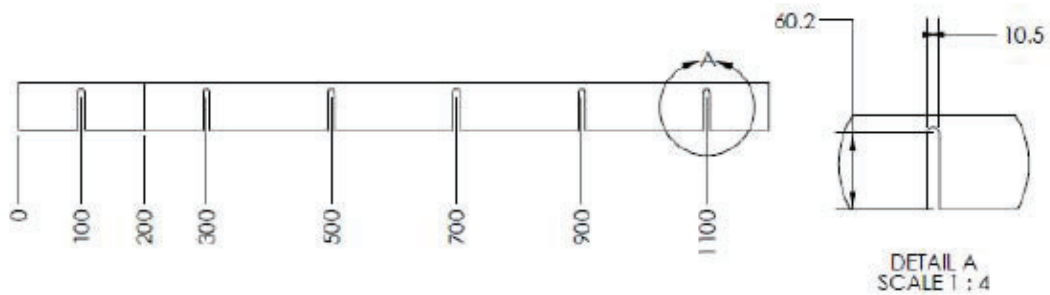
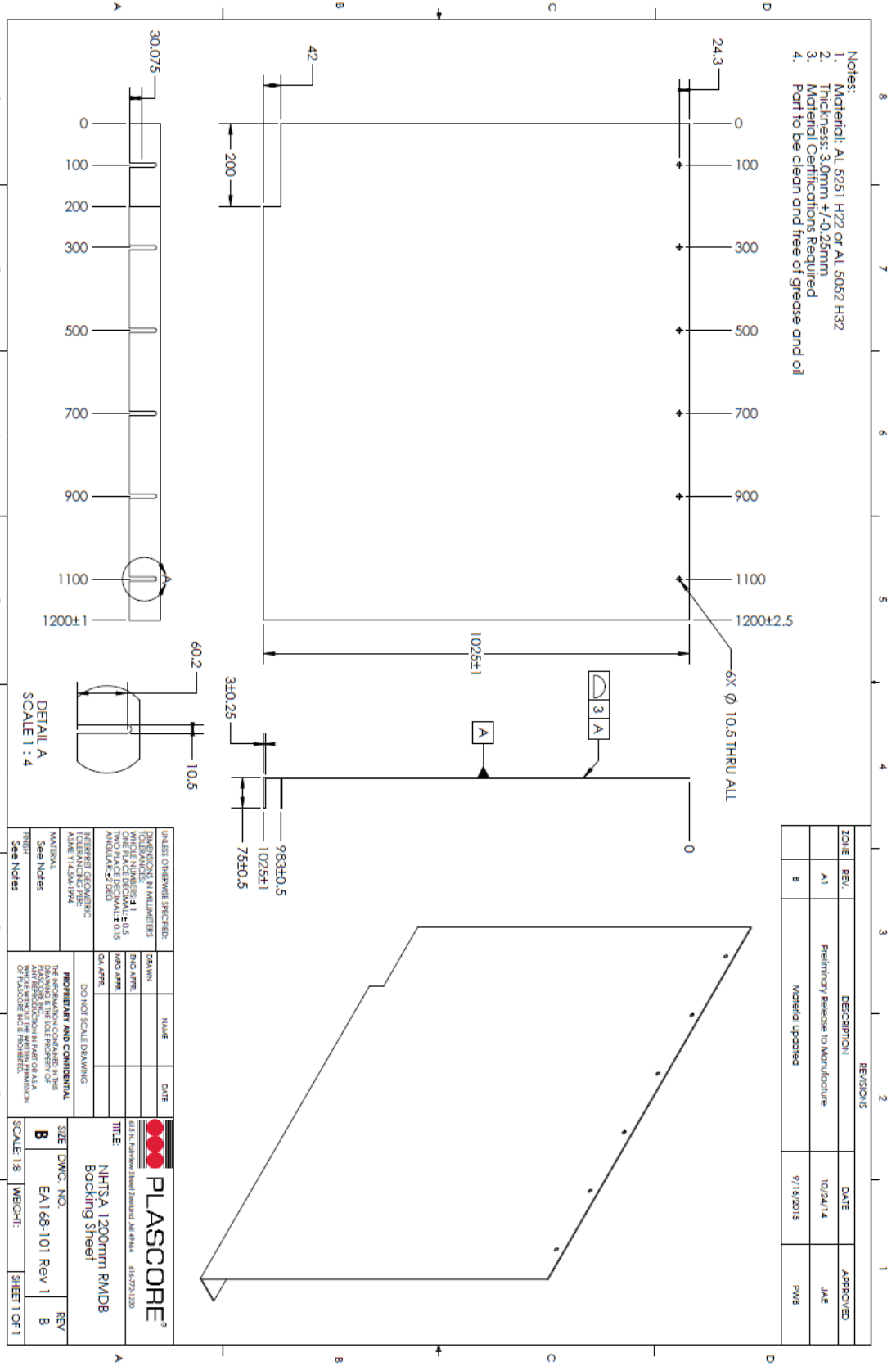


Figure 5 Bottom Flange Mounting Slots

6.0 ASSEMBLY AND COMPONENT DRAWINGS

The following pages show dimensioned drawings for the components and the assembly of the NHTSA Oblique Moving Deformable Half Barrier Face V2019

- Notes:
1. Material: AL 5251 H22 or AL 5052 H32
 2. Thickness: 3.0mm +/-0.25mm
 3. Material Certifications Required
 4. Part to be clean and free of grease and oil



ZONE	REV.	DESCRIPTION	DATE	APPROVED
A1		Preliminary Release to Manufacture	10/24/14	JAE
B		Material updated	9/16/2015	PWB

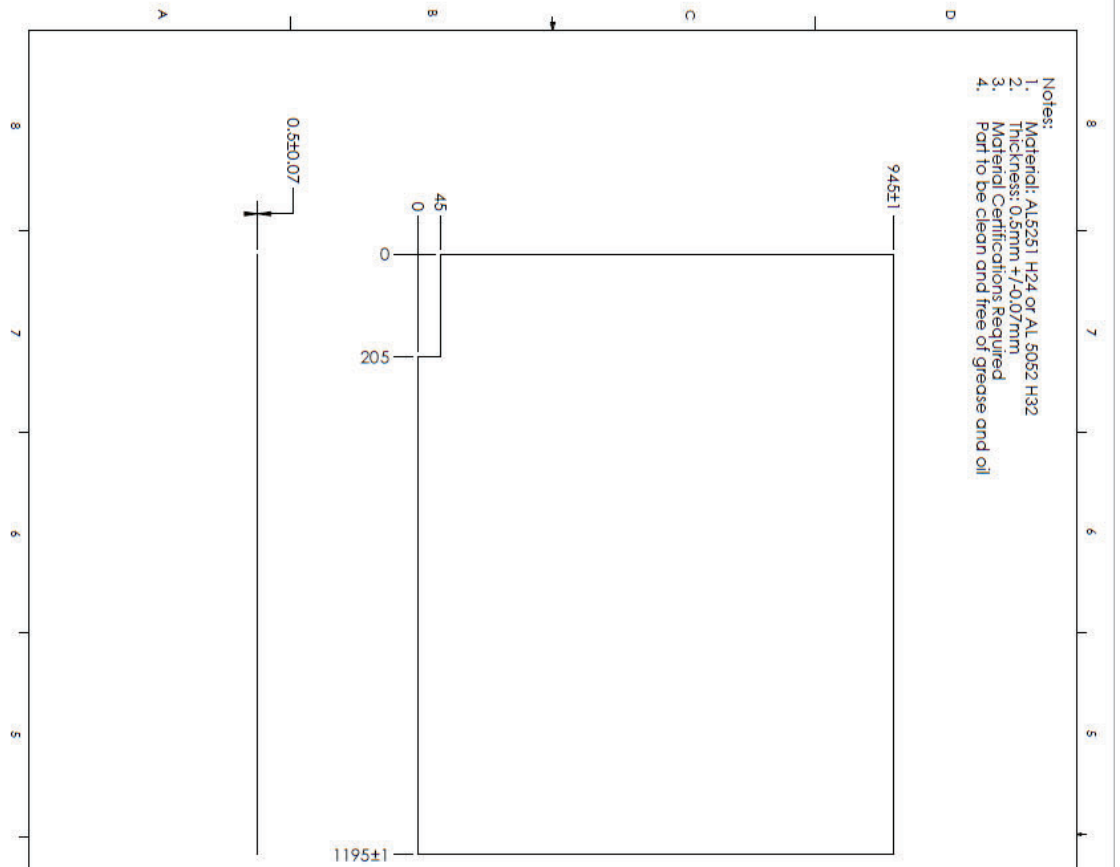
UNLESS OTHERWISE SPECIFIED:	DRAWN	NAME	DATE
DIMENSIONS IN MILLIMETERS	ENG APPR		
TOLERANCES UNLESS NOTED:	CA APPR		
ONE PLACE DECIMAL ±0.15			
TWO PLACE DECIMAL ±0.05			
THREE PLACE DECIMAL ±0.015			
ANGLE ±0.50			
FORMING GEOMETRIC			
AS PER Y14.5M-1:04			
MANUFACTURE			
SEE NUMBER			
FORM			
SEE NUMBER			

PLASCORE[®]
 1111 N. Gateway Street, Portland, ME 04104 414-272-1220

PLASCORE[®]
 NHTSA 1200mm RMD8
 Backing Sheet

SIZE: DWG. NO. EA168-101 Rev 1
 SCALE: 1:8 WEIGHT: SHEET 1 OF 1

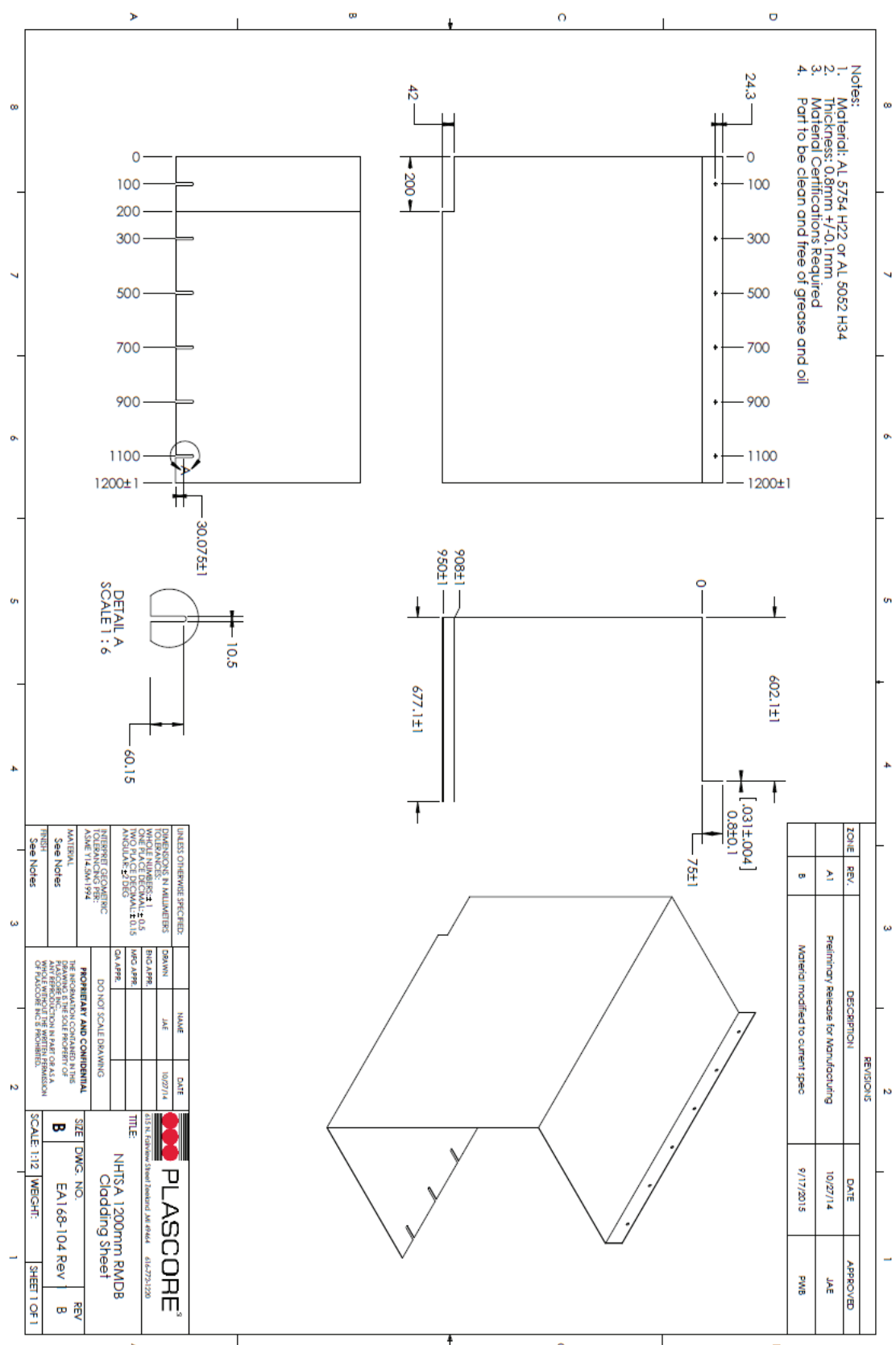
- Notes:
1. Material: AL5251 H24 or AL 5052 H32
 2. Thickness: 0.5mm \pm 0.07mm
 3. Material Certifications Required
 4. Part to be Clean and free of grease and oil



ZONE	REV.	DESCRIPTION	DATE	APPROVED
A1		Preliminary Release for Manufacture	10/24/14	JAE

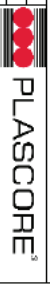
UNLESS OTHERWISE SPECIFIED:		DRAWN	NAME	DATE
DIMENSIONS IN MILLIMETERS		JAE		10/24/14
TOLERANCES:		FINO APPE		
HOLE DIMENSIONS: \pm 0.15		FINO APPE		
TWO PLACE DECIMALS: \pm 0.15		FINO APPE		
ANGULAR: \pm 0.05		FINO APPE		
INTERFERING GEOMETRIC TOLERANCING PER: ASME Y14.5M 2014		FINO APPE		
MATERIAL: See Notes		DO NOT SCALE DRAWING THE INFORMATION CONTAINED HEREIN IS UNCLASSIFIED EXCEPT WHERE SHOWN OTHERWISE. IT IS THE PROPERTY OF THE MANUFACTURER AND IS TO BE USED ONLY FOR THE PURPOSES SPECIFIED IN PART OF AS A CONTRACT. THE MANUFACTURER ASSUMES NO LIABILITY FOR THE INFORMATION CONTAINED HEREIN.		
TITLE: NHISA 1200mm PMDB Intermediate Sheet				
SIZE: B		4125 N. Eldorado Street, Lombard, IL 60148 (630) 275-1220		
DWG. NO.: EA168-102		SCALE: 1:8 WEIGHT: SHEET 1 OF 1		
REV: A1				

- Notes:
1. Material: AL 5754 H22 or AL 5052 H34
 2. Thickness: 0.87mm \pm 0.1mm
 3. Material Certifications Required
 4. Part to be clean and free of grease and oil



ZONE		REVISIONS		DATE	APPROVED
A1	REV.	DESCRIPTION	DATE	JAE	
B		Preliminary Release for Manufacturing	10/27/14		
		Material modified to current spec	9/17/2015		PWB

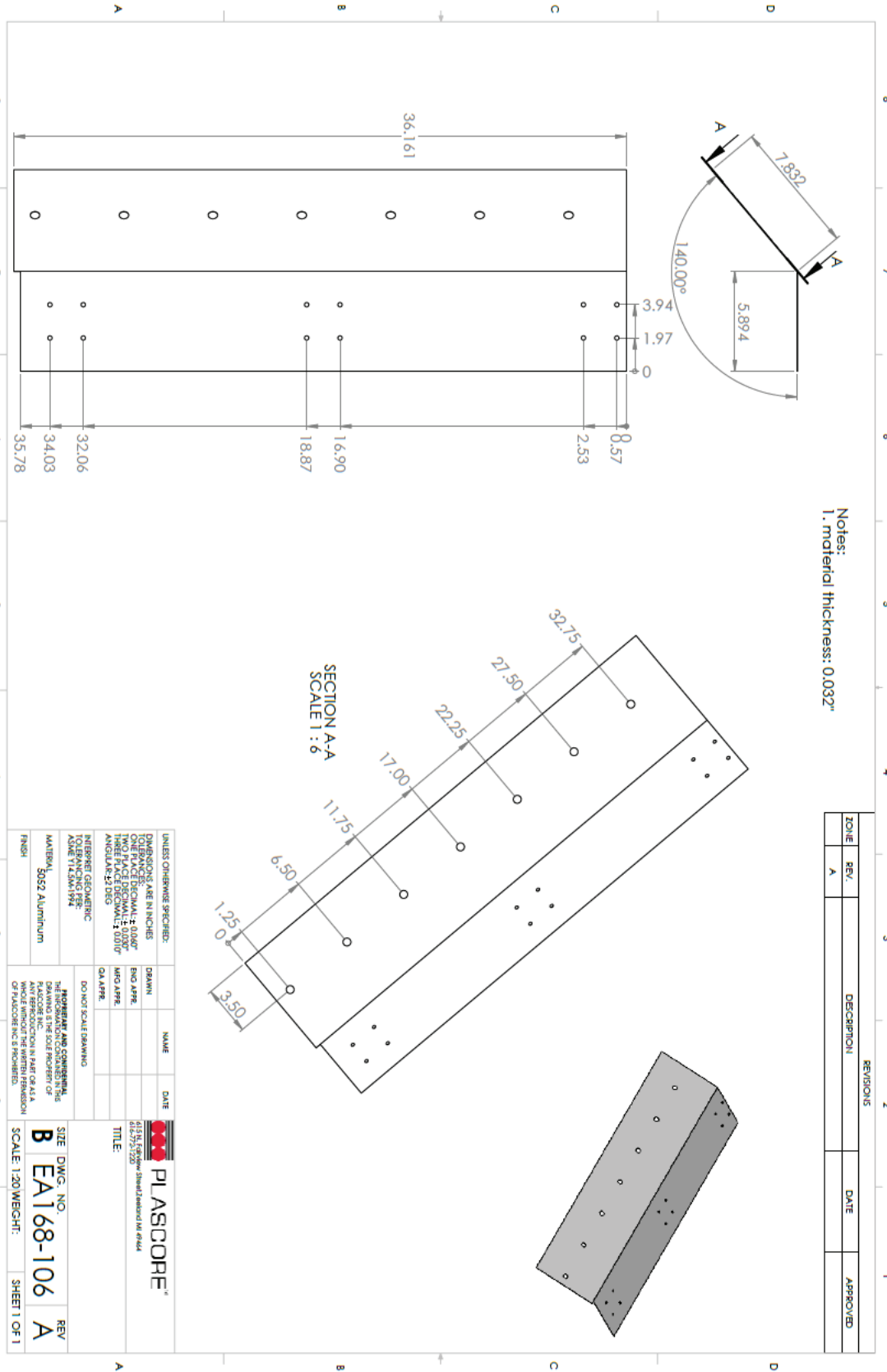
UNLESS OTHERWISE SPECIFIED:		DESIGN	NAME	DATE
DIMENSIONS IN MILLIMETERS		DRAWN	JAE	10/27/14
TOLERANCES:		ENG APPR		
ONE FACE DECIMAL ± 0.1		WFO APPR		
TWO FACES DECIMAL ± 0.15		CA APPR		
ANGULAR ± 0.50		DO NOT SCALE DRAWING		
FINISHING GEOMETRIC TOLERANCING PER: ASME Y14.5M-1994		PROPRIETARY AND CONFIDENTIAL		
MATERIAL: See Notes		DRAWING IS THE SOLE PROPERTY OF PLASCORE		
FRONT: See Notes		ANY REPRODUCTION IN PART OR AS A WHOLE WITHOUT THE WRITTEN PERMISSION OF PLASCORE IS STRICTLY PROHIBITED		
		SIZE	DWG. NO.	REV
		B	EAI 68-104	B
		SCALE: 1:12	MECH:	SHEET 1 OF 1



NHTSA 1200mm RMDB
Cladding Sheet

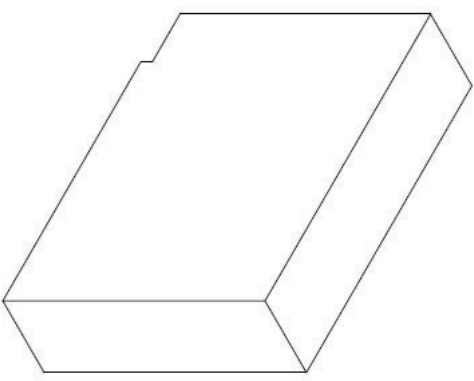
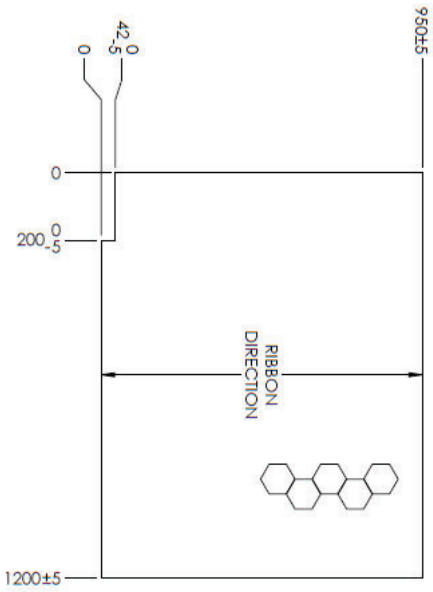
Notes:
1. material thickness: 0.032"

ZONE		REVISIONS		DATE	APPROVED
REV.	DESCRIPTION				
A					



UNLESS OTHERWISE SPECIFIED:		DATE	NAME	DATE
DIMENSIONS ARE IN INCHES		DRAWN		
TOLERANCES UNLESS OTHERWISE SPECIFIED:		ENG APPR.		
FRACTIONS: DECIMALS: ± 0.0007		MFG APPR.		
HOLE PLACES: DECIMALS: ± 0.0107		QA APPR.		
ANGLES: MINUS 0.0107		DO NOT SCALE DRAWING		
INTERFERE GEOMETRIC		PROGRAMMER AND COMMENTS		
NAME: 11/25/1987		DRAWING IS THE SOLE PROPERTY OF		
MATERIAL: 30032 ALUMINUM		ANY REPRODUCTION IN PART OR IN FULL		
FINISH:		WHICH VIOLATES THE WRITTEN PERMISSION		
		OF PLASSCORE INC. IS PROHIBITED.		
SIZE	DWG. NO.	PLASSCORE®		REV
B	EA168-106	411 N. FAYETTE STREET, DUNDALK, MD 21222		A
SCALE	1:20 WEIGHT:	TITLE:		SHEET 1 OF 1

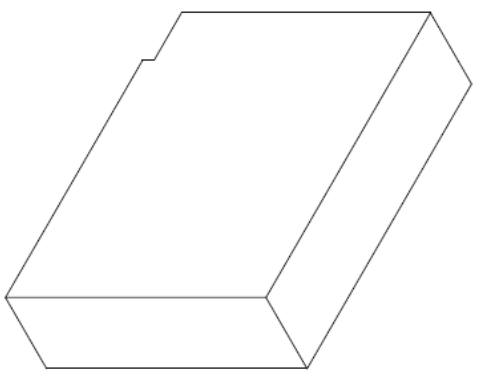
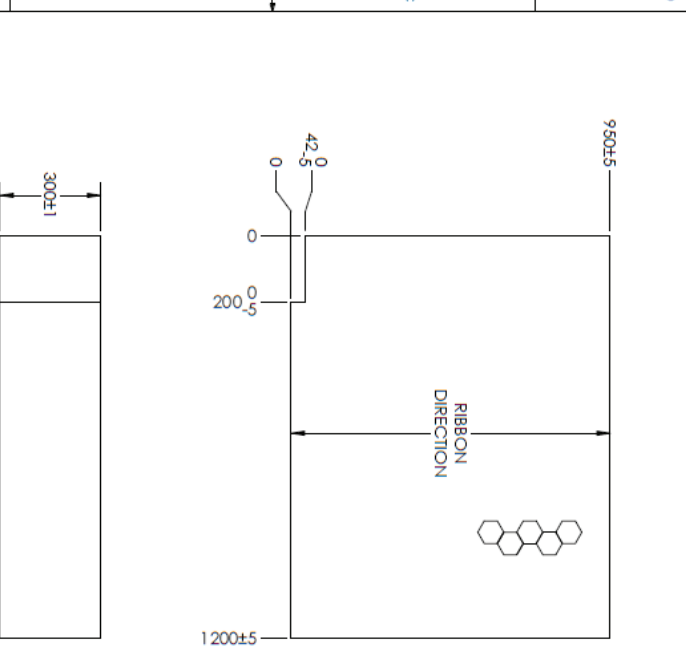
- Notes:
1. Material: 5.2.1/4-003-3003
 2. Cell Size: 6.35mm +/-20%
 3. Crush Strength: 1.71 MPa +/-10% Per NHTSA TP214D Test Procedure



ZONE		REV.		DESCRIPTION		DATE		APPROVED	
A1				Preliminary Release for Manufacture		10/24/14		JAE	

UNLESS OTHERWISE SPECIFIED:		DIMENSIONS IN MILLIMETERS	
TOLERANCES: UNLESS OTHERWISE SPECIFIED:			
ONE PLACE DECIMAL: ±0.15			
TWO PLACE DECIMAL: ±0.15			
THREE PLACE DECIMAL: ±0.15			
FOUR PLACE DECIMAL: ±0.15			
FIFTH PLACE DECIMAL: ±0.15			
SIXTH PLACE DECIMAL: ±0.15			
SEVENTH PLACE DECIMAL: ±0.15			
EIGHTH PLACE DECIMAL: ±0.15			
NINTH PLACE DECIMAL: ±0.15			
TENTH PLACE DECIMAL: ±0.15			
ELEVENTH PLACE DECIMAL: ±0.15			
TWELFTH PLACE DECIMAL: ±0.15			
THIRTEENTH PLACE DECIMAL: ±0.15			
FOURTEENTH PLACE DECIMAL: ±0.15			
FIFTEENTH PLACE DECIMAL: ±0.15			
SIXTEENTH PLACE DECIMAL: ±0.15			
SEVENTEENTH PLACE DECIMAL: ±0.15			
EIGHTEENTH PLACE DECIMAL: ±0.15			
NINETEENTH PLACE DECIMAL: ±0.15			
TWENTIETH PLACE DECIMAL: ±0.15			
PROHIBITARY AND CONFIDENTIAL			
THE INFORMATION CONTAINED IN THIS DRAWING IS THE SOLE PROPERTY OF PLASCORE. ANY REPRODUCTION IN PART OR AS A WHOLE WITHOUT THE WRITTEN PERMISSION OF PLASCORE IS STRICTLY PROHIBITED.			
DRAWN: JAE		DATE: 10/24/14	
CHECKED: JAE		DATE: 10/24/14	
DESIGNED: JAE		DATE: 10/24/14	
APPROVED: JAE		DATE: 10/24/14	
SCALE: 1:1		WEIGHT: 300g	
SIZE: B		DWG. NO.: EA168-301	
SHEET: 1 OF 1		REV: A1	

- Notes:
1. Material: 2.3-1/4-001-5052
 2. Cell Size: 6.35mm +/-20%
 3. Crush Strength: 0.724Mpa +/-10% Per NHTSA TP21 AD Test Procedure



REV		DESCRIPTION	DATE	APPROVED
A1		Preliminary Release for Manufacture	10/27/14	JAE

UNLESS OTHERWISE SPECIFIED:		DIMENSIONS IN MILLIMETERS	
TOLERANCES:		FRACTIONS DECIMALS	
ONE PLACE DECIMALS		±0.5	
TWO PLACE DECIMALS		±0.15	
THREE PLACE DECIMALS		±0.05	
INTERPRET GEOMETRIC		DO NOT SCALE DRAWING	
MATERIAL		PROPERTY AND CONFIDENTIAL	
See Notes		DRAWING IS THE SOLE PROPERTY OF	
See Notes		ANY REPRODUCTION IN PART OR AS A	
See Notes		WHOLE WITHOUT THE WRITTEN PERMISSION	
See Notes		OF PLASCORE INC IS PROHIBITED.	
SIZE	DWG. NO.	REV	
B	EA168-302	A1	
SCALE: 1:12	WEIGHT:	SHEET 1 OF 1	



NHTSA 1200mm RMD8
Front Honeycomb Block

FRONTAL CRASH INCOMPATIBILITY OF HEAVY GOODS VEHICLE IN CRASH TEST WITH PASSENGER CAR

Robert Thomson

Chalmers University of Technology, Sweden

Rikard Fredriksson

Swedish Transport Administration, Sweden; Chalmers University of Technology, Sweden

Krystoffer Mroz

Dion Kruse

Autoliv Research, Sweden

Fredrik Törnvall

Volvo Technology AB, Sweden

Paper Number 23-0321

ABSTRACT

In 1997 the Swedish parliament adopted Vision Zero, which reduced fatalities almost by 2/3 down to 1.9 road fatalities per 100,000 inhabitants for 2020. One guiding principle is to only allow maximum speed limits of 80 km/h without physically separating opposing lanes. Fatal frontal crashes between passenger cars and Heavy Goods Vehicles (HGVs) are a problem for the rural road network with speed limits between 50 and 80 km/h. A road network following the Safe System principles should not lead to fatalities if safe vehicles, safe infrastructure, and safe road users are present. In the scenario described above, a rural road posted at 80 km/h without median separation would need to be operated with safe vehicles, that is, vehicles that are capable of protecting occupants in frontal crashes. While it may be possible for late model cars with good safety performance to protect occupants in crashes with similar cars at relative crash velocities above 120 km/h, the case of a car-to-HGV impact is less obvious.

A study of real-world crash data and current vehicle technology suggested that a frontal crash between an HGV and passenger car with relative velocity of 100 km/h (50 km/h per vehicle) and 50% overlap would be a reference to assess infrastructure and vehicle safety levels. The test was based on both vehicles having active safety systems that reduce the original travel speeds to the proposed test speed before an impact. State-of-the-art vehicles, a Euro NCAP 5 star rated mid-sized sedan and HGV with energy absorbing Front Underride Protection Device (FUPD), were chosen. The test is also comparable with the Moving Progressive Deformable Barrier (MPDB) test currently used in Euro NCAP.

The test results showed that both vehicles need structural protection system improvements to provide consistent protection for road users in these types of high-severity crashes. The car sustained extensive deformations to the outboard area of the vehicle front resulting in significant deformation to the left wheel and A-Pillar area. This focused damage was due to the fracture of the FUPD on the HGV early in the crash event. The FUPD did not engage the energy absorbing structures in the car (longitudinal crash beams), which were essentially undamaged. The 50%ile male Hybrid III (HIII) dummy's head slid off the driver's airbag and struck the left A-Pillar due to a gap that developed between the side curtain and front airbag, this was related to the excessive A-Pillar deformation. High head accelerations exceeded the upper limit for recommended Head Injury Criteria (HIC).

Compatibility between HGVs and cars must be improved for frontal impacts when less than 50% of the car width engages the truck structures. The existing FUPD legal requirements should be reviewed to ensure that geometric and structural requirements for these structures reflect the real-world demands in a crash. Opportunities for improved passenger car restraint systems need vehicle structure interactions that can maintain a stable passenger car compartment and efficiently use energy absorption systems designed into both HGVs and passenger cars. The new EC regulation (2019/1892) for extended fronts is an opportunity that can be exploited to achieve better car-HGV compatibility by providing more design space in the HGV front-end.

INTRODUCTION

The Swedish parliament adopted Vision Zero in 1997 and has since then reduced road fatalities by almost 2/3. Sweden currently has a fatality rate of 1.9 road fatalities per 100,000 inhabitants in 2020 [1]. Together with Norway, this is the lowest traffic fatality rate in the world [1]. Vision Zero anticipates that people make mistakes so the transport system should be designed using biomechanical limits. This facilitates an environment where

crashes involving safe vehicles, safe infrastructure, and safe road users won't produce fatal or severely injured individuals. Using a Safe System approach [2], one would design specific road elements (motorways, intersections, etc.) anticipating the speeds of vehicles and types of crashes that road users could experience. The Safe System approach for the non-motorway, rural road network, would propose lower speed limits when there is no physical separation (median barriers) of opposing travel lanes than if median barriers were present. This is due to the potential occurrence of high speed, head-on crashes when a vehicle crosses the centerline into oncoming traffic. Head-on crashes are severe and have a higher fatality risk. With a median barrier present, the speed limit could be higher if other crash scenarios, such as single vehicle crashes, would not be fatal at the posted speed limit using safe roadside design principles.

While Heavy Goods Vehicles (HGVs) over 3.5 tonnes only make up 6% of vehicle mileage [3] in Sweden, they are involved in 15-20% of road fatalities in the last decade. The high involvement of HGVs in fatality crashes is not restricted to Sweden. The AEROFLEX¹ project investigated newer front designs for trucks for aerodynamic benefits and investigated the potential for increasing safety. They reported that HGVs were responsible for 14.2% of road fatalities in 2015 even though they were only involved in 4.5% of all road accidents [4]. The SAFE-UP Project analyzed crash scenarios in detail and reported that frontal crashes between cars and HGVs represented 5-11% of their target population [5]. The median crash configuration consisted of a 50% vehicle frontal overlap and relative impact speed of 71 km/h (car moving 39 km/h, truck 32 km/h). The remainder of fatalities involving HGVs were mainly associated with Vulnerable Road Users (VRUs), HGV-HGV, and HGV run-off-road [4].

The overrepresentation of traffic fatalities related to frontal HGV crashes with cars can be explained with basic physics. Passenger cars are designed, approved, and assessed for frontal impact protection. All vehicles must pass local legislated tests setting a minimum protection level (UNECE, FMVSS, etc.). Manufacturers also design vehicles to achieve good ratings in consumer testing conducted in regional New Car Assessment Programs (NCAP) programs. European passenger cars are approved for sales by tests defined in UNECE regulations and assessed with Euro NCAP tests. All of these tests involve kinetic energies that are in the order of magnitude of the passenger car's mass and impact velocity. In a crash with an HGV moving in the opposite direction, the passenger car is exposed to its own kinetic energy and the HGV's kinetic energy, which is typically much higher. This higher impact kinetic energy must be managed with the structures in both vehicles. Unfortunately, mainly passenger cars have structures designed to control the crash loads and keep them below biomechanical limits. The HGV is designed with a rigid frame, typically above those in the passenger car as shown in Figure 1 (left) and no biomechanical based crashworthiness requirements. To address the vertical misalignment of structures, European HGVs must now have a front underrun protection device (FUPD) that fulfills the requirements of UNECE Regulation 93 (R93) [6] with the intent of engaging the passenger car's main structures (Figure 1, right).

FUPDs have geometric and loading characteristics defined in R93 [6] (Appendix B). Krusper [7], demonstrated through simulations that these requirements are not sufficient to ensure passenger car occupant safety. The studies showed that both the existing geometric and load resistant definitions in R93 are insufficient, compared to a dynamic event like a crash. Part of the issue with R93 can be attributed to a lack of development crash tests with both the car and HGV in motion to define sufficient structural load requirements. One of the major research projects investigating FUPDs and their evaluation was VC-Compat [8]. In this project, several crash tests were conducted between passenger cars and HGVs, but always with the HGV stationary. Even at higher test speeds (75 km/h) – which is beyond Euro NCAP levels (64 km/h) – the tests never had energy levels comparable to a real-world crash. The most severe crash test in terms of kinetic energy conducted in VC-Compat was 311 kJ (1.43 tonne car, 11.9 tonne HGV, car impact speed 75 km/h) [8], compared to a crash severity of at least 1620 kJ for a closing speed of 112 km/h (56 km/h for each vehicle) the same two vehicles. Even for a lower closing speed of 100 km/h, the kinetic energy is 1290 kJ for 2 moving vehicles, 4 times that investigated in VC-Compat.

¹ Horizon 2020 Project: Aerodynamic and Flexible Trucks for Next Generation of Long Distance Road Transport - Aeroflex (aeroflex-project.eu)

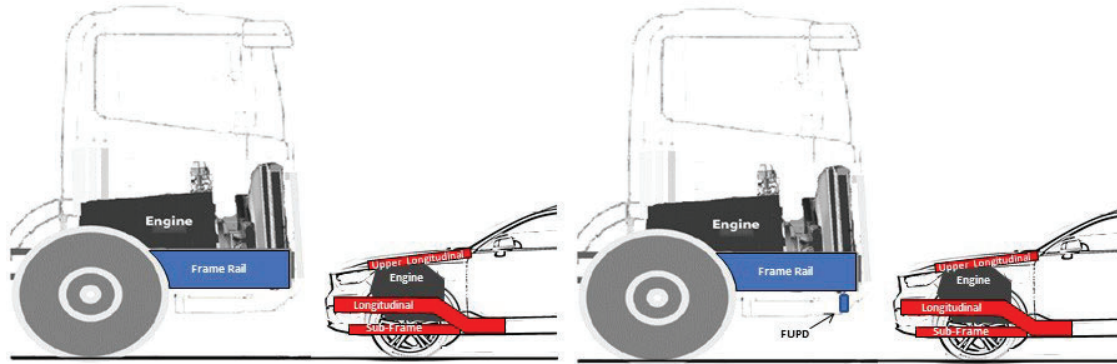


Figure 1. Illustration of HGV and Passenger Car structures without FUPD (left) and with FUPD (right)

A Safe System anticipates that the combined safety of the infrastructure, vehicle, and road user ensures no fatal injuries arise in a crash [2]. Based on the Swedish statistics and Vision Zero strategy, roads with speed limits 90 km/h and higher would have median barriers, essentially eliminating the occurrence of fatal head-on crashes. Installing median barriers on all roads up to 80 km/h is both economically and practically prohibitive (overtaking provisions, intersection opening, emergency service operations, etc.) and the road user and vehicle are primarily responsible for safety. If vehicles are to provide safety systems that protect road users from potential frontal crashes on roads with speed limits between 50 and 80 km/h, both the car and HGV must be able to exhibit controlled deformations that reduce the loading on all vehicle occupants and prevent severe secondary consequences such as post-crash trajectories that interfere with surrounding traffic. This is the philosophy of EN1317 [9] that describes redirection limits for impacts with guardrails and other vehicle restraint systems. Testing of road infrastructure structures requires that the vehicles do not rebound adversely into surrounding traffic lanes.

It is believed that modern passenger cars can, in the near future, experience high speed crashes with another passenger car in this network configuration and still have survivable outcomes. Earlier test and simulation results [10] indicated that these designs were within reach if the vehicle intrusions were not excessive for an 80 km/h full frontal barrier impact. More recent simulations suggest that passenger cars could have adaptive restraint systems capable of protecting occupants in severe crashes with an HGV [11]. The upper limit, in terms of closing crash velocity, for a survivable frontal crash between a car and HGV is still to be determined with a physical test.

Research Question/Objective

Modern vehicles now have active safety systems that can avoid crashes or at least reduce the speed of crash when it cannot be prevented. These systems reduce the burden of the passive safety systems to manage all the kinetic energy of vehicles with closing speeds above 120 km/h. Based on the collision data above from Sweden and Europe [1] [5] [11] and the potential protection for passenger car vehicles [12] [11], a crash test to evaluate reasonable car-HGV impacts needs to be identified. Physical crash test data for the car-HGV impact scenario is needed to confirm simulation results from previous studies. Aside from the crash data, the current test configurations for passenger vehicles (there are none for HGVs) should be reviewed to identify synergies between real-world crashes and available laboratory testing.

A Safe System approach to car-truck impacts should start with the state-of-the-art vehicle and infrastructure designs to identify what is feasible. A well performing (Euro NCAP 5 star) passenger car colliding with a fully loaded HGV fitted with a state-of-the-art FUPD would be the vehicle technology starting point for this type of investigation. An analysis of crash scenarios for road types is also needed to identify road types and speed limits for survivable collisions when the driver makes a mistake.

METHODS

Accident Data

The Swedish Transport Administration (STA) investigates all road fatalities [13] where accident investigation teams investigate every fatal road crash performing a detailed analysis of the crash site and the vehicles. Each crash is also analyzed in detail by two special teams to conclude if suicide or sudden sickness was the cause. If

such evidence can be found these cases are removed from the official road fatalities. These investigations are compiled in an In-Depth Study database used to monitor road safety in Sweden [13].

Crash Test Definition

An investigation of car-HGV collision scenarios based on European and Swedish crash data was conducted to determine the type of crash that could be a reference for further analysis. Data collected from in-depth crash investigations was collected and analyzed to identify the crash configurations representative of the fatal crash conditions for car to HGV frontal impacts. Data from the GIDAS [14] and STA In-Depth databases were analyzed to identify a crash test configuration defined by horizontal overlap and closing speeds (relative velocities) for the vehicles.

Vehicle impact testing configurations from regulatory (UNECE & FMVSS) and consumer testing (Euro NCAP & IIHS) were also reviewed to identify existing protocols that can be exploited.

Car-to-HGV Crash Test

A crash test between an HGV and a passenger car, based on the crash data analysis, was identified and conducted. The HGV was a Volvo FH, model year 2014, with the latest generation of front structure and FUPD. It was loaded to maximum allowable load, resulting in a total mass of 28 tonnes. The passenger car was a Seat Leon model year 2021, with total test weight of 1.57 tonnes, and selected as it is a 5-star rated car in Euro NCAP (tested in 2020 with the latest protocol). The Leon has the highest score in adult protection (92%) and 13.9 out of 16 points in frontal crash protection. The car was equipped with driver airbag, knee airbag, and far-side airbag as well as an inflatable curtain. The passenger airbag was disconnected in the test. A pre-tensioned and 4 kN force-limited seat belt was used for the driver side.

The car was fitted with a HIII 50% male dummy (HIII 50M) in the driver position. The driving robot employed did not interfere with the upper body of the HIII 50M. The throttle actuator did not allow for the right foot to be positioned on the throttle (Figure 3). No dummy was placed in the HGV.

Both vehicles were fitted with accelerometers on key structural members and power trains. Contact switches were placed on left bumper fascia to detect initial contact. Airbag deployment information and seat belt loads (shoulder and lap segments) were collected from the car driver side. Data from the vehicle mounted sensors were sampled at 20 kHz.

External cameras, including those on drones following the vehicles, captured the collision event above and beside the vehicles. Interior cameras were mounted in the car, filming from the front passenger and right rear passenger seat. Key views were filmed at 1kHz. Vehicle mounted (external views) and drone cameras filmed at 120 Hz.

The compatibility of the vehicles was the focus for the test, so geometric data for key energy absorbing structures were documented prior to the test.

RESULTS

Accident Data

A screening of HGV crashes for the years 2012-2021 identified a total of 2556 road fatalities. Of these, 455 fatalities involved a heavy goods vehicle (HGV) with a curb weight over 3.5 tonnes. The deceased individual in these crashes was, in almost all cases (92%), sitting in the collision partner. Almost half (47%) of the HGV involved fatalities were the two accident types defined as “Oncoming” and “Overtaking”. A more detailed study of the Swedish fatal crashes was conducted for the accident years 2017-2021 covering 223 fatalities involving HGVs. There were 101 fatalities in oncoming (frontal) accidents, and 77 of those were between a passenger car and an HGV. Over half (64%) of these accidents occurred at speed limits of 70 and 80 km/h, with 80 being the predominant speed limit (38%). Figure 2 presents the distribution of crashes for different posted speed limits. The majority of the deceased car occupants (78%) were belted (14% unknown) and the most common age group was 51-65 years old (median age 56). Of the 77 oncoming car-to-HGV fatalities, 36 fatalities were in passenger cars with model year 2010 and newer with a median curb weight of 1620 kg. The accidents were distributed equally on roads with speed limits of 70 and 80 km/h (62% together), and 89% of the deceased car occupants were belted (8% unknown) and 86% had a functioning frontal airbag. The deceased were predominantly the driver of the passenger car (86%) and right front passenger (11%). A majority of the accidents happened in daylight (69%) and good weather conditions without precipitation or fog (91%) [1]. Although the crash speeds

were not objectively reconstructed, the speed limit is a fairly good proxy of the crash speed in these cases. The data shows that for newer cars (model year 2010 and onwards), the speed limit distribution is not significantly different than older cars so these crash fatalities are still an issue with modern cars (Figure 2). Also, fatalities do not seem to be due to a lack of restraints system availability or use in the passenger car. The majority of victims were belted and had functioning airbags. It is difficult to draw any more conclusions on the data without information on the exposure of these vehicle types to these accident conditions.

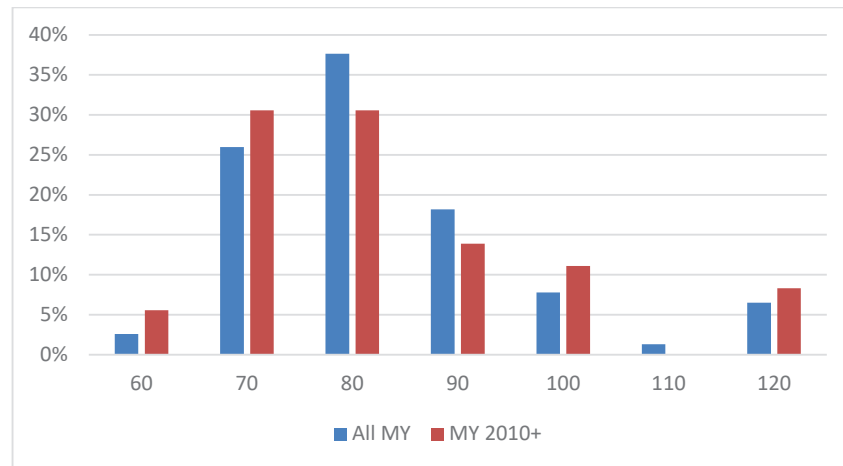


Figure 2. Speed limit in fatal oncoming crashes between passenger car and heavy truck (divided by passenger car model year - MY).

The SAFE-UP project identified different crash scenarios involving HGVs and passenger cars [5]. Crash configurations included 0 and 10 degree frontal crashes, relative impact speeds from 57-92 km/h, and overlaps between 25% and 80%. Further investigations of these crash conditions investigated the potential for adaptive restraints to provide protection for these extreme cases. To identify the potential for restraint systems when vehicle intrusion is not excessive, Mroz et. al. [12] simulated the range of conditions identified in SAFE-UP. Their results indicated that the lower relative speed ranges (below 75 km/h) were within the protection levels controlled by existing frontal impact regulations. Smaller overlaps and higher oblique impact angles were beyond the structural interaction performance of vehicles when relative impact speeds were 100-110 km/h.

Crash Test Definition

The results of the STA fatal analysis and simulation results from [12] indicate that initial travel speeds, speed limits of 70-80 km/h and relative impact velocities of 100 km/h are conditions future vehicle restraint systems and rural networks could protect passenger car occupants when one vehicle crosses the centerline and collides with oncoming traffic. If these vehicles have an impact overlap between 50% and 80% of the car width, there should be structural compatibility potential that produces a high crash pulse (>90 g) but limited vehicle intrusions. These are pre-requisites to develop a future traffic environment using Safe System principles.

The existing crash tests that could be candidates for benchmarking an exploratory crash test between an HGV and car were identified as:

- IIHS Small Overlap test [15]
- Euro NCAP Moving Progressive Deformable test [16]

The IIHS small overlap test (fixed rigid barrier) is a challenging test for existing vehicles for the test speed of 64 km/h and 25% overlap prescribed in the protocol. The simulation results from [12] suggested that increases in the test severity for small overlap conditions can be catastrophic for the structure and difficult to promote for future restraint development. The Euro NCAP MPDB (moving trolley with progressive deformable barrier) was previously proposed for HGV underwrite testing [8] and may provide future potential for comparison with new crash tests of cars and HGVs. The latter test is currently used by Euro NCAP to evaluate compatibility for passenger cars using barrier deformation patterns to assess the structural interaction and comparing accelerations in the trolley and test vehicle.

Car-to-HGV Crash Test

Based on the review of real-world crash data and existing crash test procedures, the test setup was chosen to be similar to the MPDB [16]. The car and the HGV were prescribed to both move at 50 km/h and impact with an overlap of 50% (relative the car). Both vehicles were outfitted with driving robots to accelerate up to the test speed (50 km/h +/- 1 km/h) and maintain their lateral position to achieve a 50% offset on the passenger car (+/-25 mm). The MPDB protocol prescribes the THOR 50% male dummy in the driver seat but was replaced by the HIII dummy due to the anticipated high severity and exploratory nature of the test. The Euro NCAP HIII passenger positioning protocol was used [16].

The crash test was completed successfully with the impact precision essentially within specifications. The vertical deviation was less than 5 mm and the lateral offset was estimated to be 26 mm, slightly increasing the overlap to 51% of the car's width. The car had an impact velocity of 49.9 km/h and the truck was moving 50.0 km/h at the time of impact.

The lateral placement of the main longitudinal and frontal cross beam structures (FUPD on HGV and bumper cross beam for car) are shown in Figure 6. Note that the left longitudinal in the car is outboard of the HGV's left frame rail but both cross beams overlap identifying the potential for structural interaction.



Figure 3. Driver position - note position of right foot.

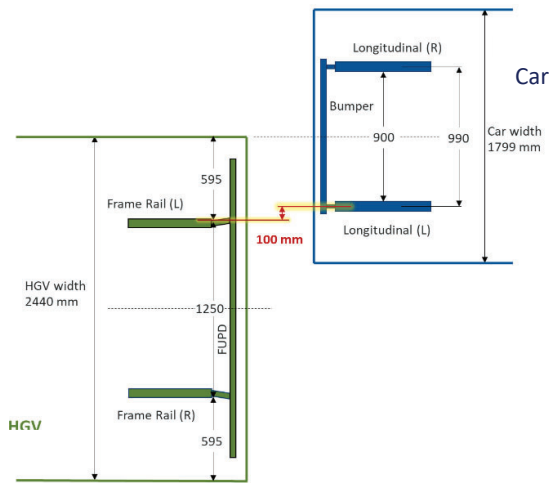


Figure 4. Lateral Alignment of main structures.

The bumper of the car is mounted on the main longitudinal as illustrated in Figure 5. The original ground clearance was 420 mm to the underside of the bumper beam which has a 100 mm section height. The FUPD's lower surface was measured to be 300 mm above the road surface before the test. It has a section height of 167 mm. The HGV has an energy absorbing FUPD design. It is "hung" from the main frame rails and has energy absorbing struts that control the rearward deflection of the FUPD [6]. The tested HGV has type approval for this FUPD in accordance with UNECE R93 [6].

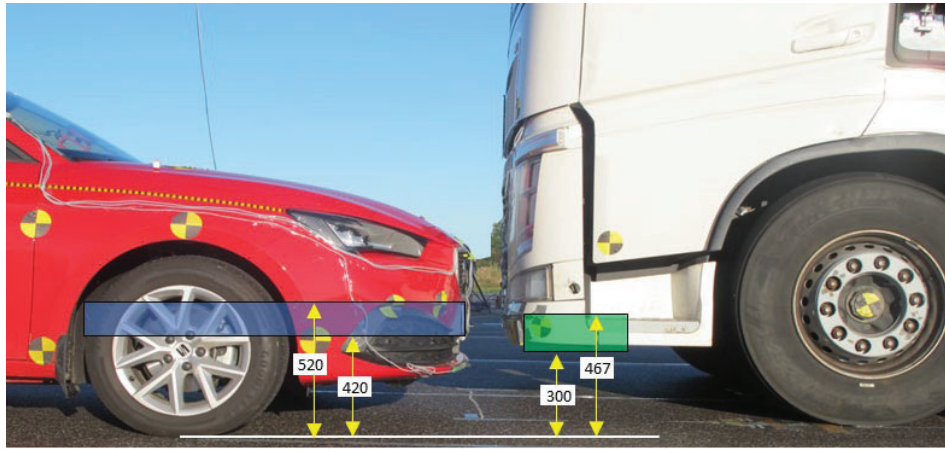


Figure 5. Vertical alignment of main frontal structures.

The car experienced a 100 km/h change in velocity as seen in Figure 7. The car came to rest approximately 30 m from the point of impact and rotated 460 degrees counterclockwise. The HGTV and car brakes were activated after the time of impact as per the test protocol. The truck's velocity change during the impact was less than 6 km/h (Figure 7). The vehicle positions and orientations after the collision are shown in Figure 8.

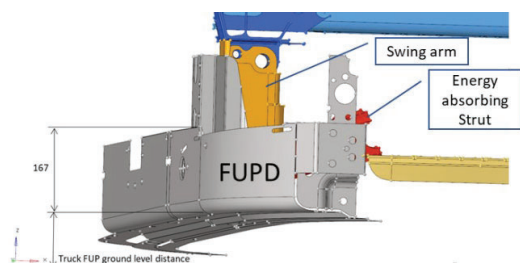


Figure 6. FUPD design.

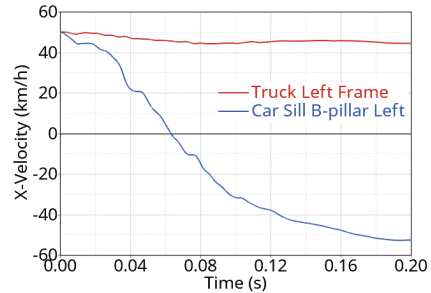


Figure 7: Car and truck velocity time profiles.

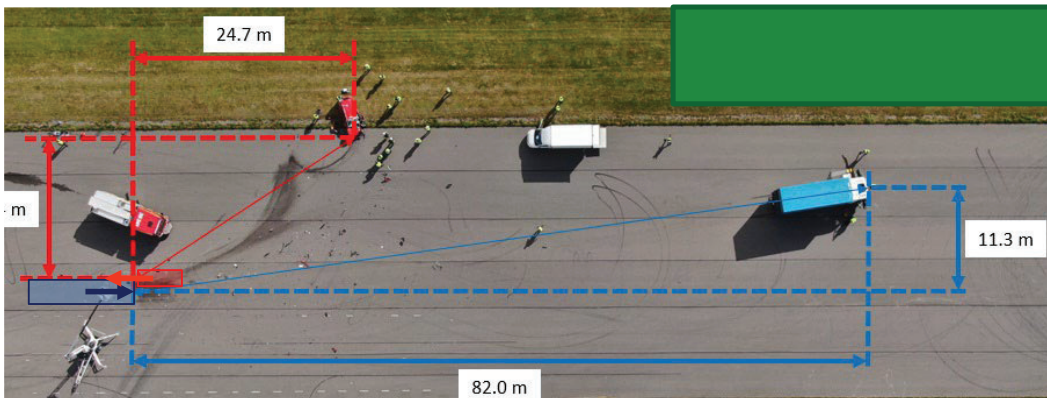


Figure 8. Final rest positions of vehicles.

The passenger car displayed the most deformations of the vehicles involved in the test, as expected. The car's structures outboard of the left longitudinal were peeled off and pushed rearward (Figure 9). The left longitudinal is easily identified and is essentially undamaged. The lower A-Pillar base at the beltline has been pushed laterally outward from the vehicle, compromising the occupant compartment. Figure 9 inserts a & b provide different views of the A-Pillar, driver door region. The dummy was not ejected from the vehicle.

The interior intrusions were most notable in the left A-Pillar regions. Figure 10 shows the measurement reference points. Some footwell measurements were not possible to measure post-test and thus no intrusion values are available. The steering wheel and foot pedals exhibited 20-50 mm rearward deformation. Interestingly the left foot rest (Point 7) was not as affected as much as the left A-Pillar base (Point 9) even though there is only

212 mm lateral difference between them. The instrument panel intrusion to the right of the steering wheel was 38 mm.



Figure 9. Damage to Car.

	Change (mm)		
	X	Y	Z
Steering column DAB (1)	-50	-177	5
Interior IP (right knee) (2)	-38	-50	35
Accelerator pedal (3)	-26	56	-48
Brake pedal (4)	3	51	-33
Brake pedal - Unloaded robot (5)	-10	60	-32
Interior Toepan (6)	-69	-3	63
Interior Left footrest (7)	-67	-72	66
A-pillar left Top (8)	-390	227	-48
A-pillar left Bottom (9)	-323	31	-6
B-pillar left Top (10)	-2	-2	3
B-pillar left Bottom (11)	-1	1	3
A-pillar right Top (12)	2	-3	19
A-pillar right Bottom (13)	5	7	18
Door Opening change	-388	229	-51

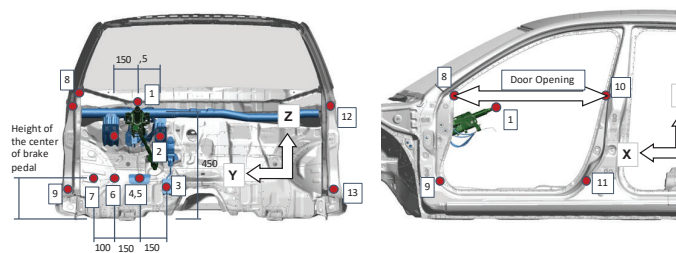


Figure 10. Intrusion measurements (Negative X values indicate intrusion). Right: Intrusion measurement locations shown in a generic interior which does not correspond to the actual tested car.

The left outboard section of the FUPD on the HGV fractured at the connection bracket to the energy absorbing element. This fracture eliminated potential for intended interactions between the HGV FUPD and car's main structural members. The HGV steering arm separated from the steering rack and the steering servo was sheared from the frame rail where it is mounted. The car bumper loaded the left front tire of the truck, puncturing it and driving the rim rearward. Figure 11 shows the damage to the HGV which was confined to the structures below the cab. As seen in Figure 8, the combination of steering system damage and punctured left front tire caused the HGV to move laterally to the left after the impact.



Figure 11. Damage to the HGV.

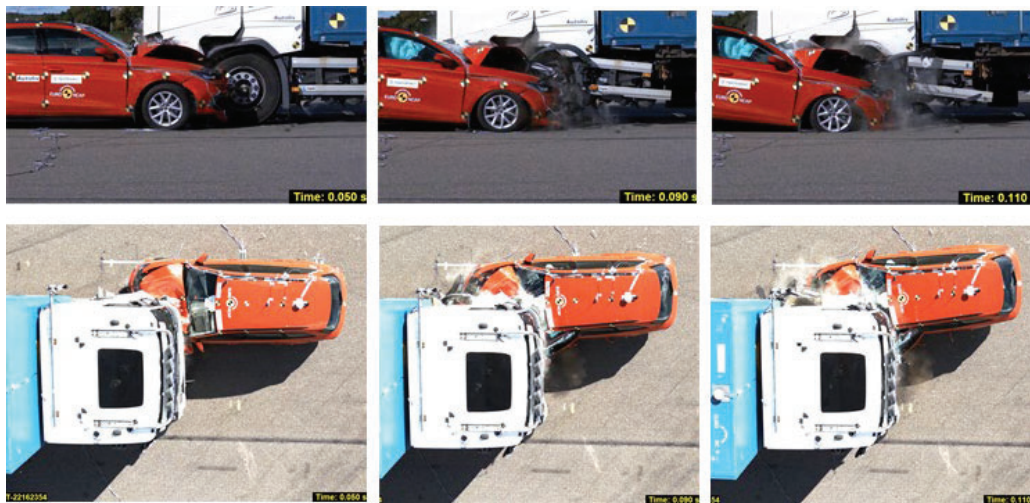


Figure 12. Crash Loading at 50, 90 and 110 ms.

The passenger car accelerations, shown in Figure 13 exhibit three main peaks corresponding to the events observed in the videos. The initial loading of the FUPD and metallic structures with a peak in the first 50 ms, the contact and loading of the tire after 60 ms, and the vehicle-rim bottoming out on the rear wheel-well structures. The concentrated loads on the left side of the car are readily apparent in the high (70 g) accelerations measured in the left B-Pillar compared to the right (40 g). The car rotation was minimal during contact with the truck but the resulting rotation post crash was considerable (over 400 degrees).

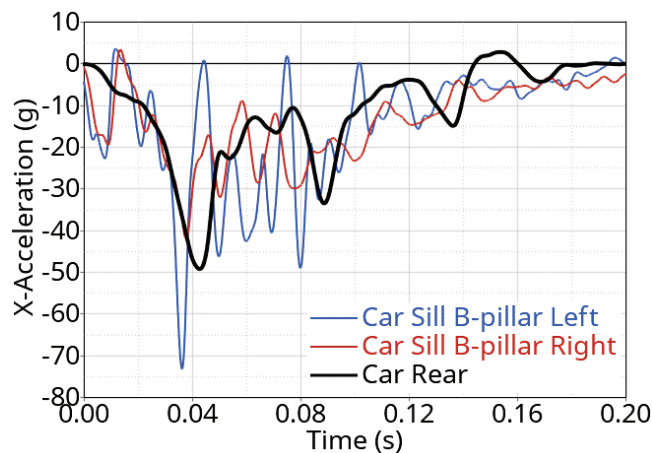


Figure 13. Car x-accelerations.

The HIII 50M dummy in the driver position experienced considerable loading with several injury criteria exceeding the proposed performance limits. The head, chest, and lower extremities all had weak to poor injury ratings, shown in Table 1, compared to the Euro NCAP criteria proposed in [16]. Time-history data of the HIII head and chest accelerations, chest deflections and femur forces together with seat belt forces are shown in the Appendix A: Figure A1.

Table 1. HIII 50th percentile dummy injury results and rating, derived according to the Euro NCAP frontal test protocol for the passenger side [16] - Green=Good, Yellow=Adequate, Orange=Marginal, Brown=Weak, Red=Poor).

Injury Parameter	Test results	Higher Performance Limit	Lower Performance Limit
Head 3ms Clip	90.4 g	72 g	80 g
HIC15	754.4	500	700
Upper Neck Tension	2589.2 N	2700 N	3300 N
Upper Neck Extension	38.9 Nm	42 Nm	57 Nm
Thorax Compr.	32.6 mm	22 mm	42 mm
Thorax V*C	0.37 m/s	0.5 m/s	1 m/s
Left Femur Force	7070.4 N	3800 N	9070 N
Left Tibia-Femur Disp.	13.4 mm	6 mm	15 mm
Left Tibia Compr. Force	3348.4 N	2000 N	8000 N
Left Upper Tibia Index	1.24	0.4	1.3
Left Lower Tibia Index	0.79	0.4	1.3
Right Femur Force	10048.7 N	3800 N	9070 N
Right Tibia-Femur Disp.	13.2 mm	6 mm	15 mm
Right Tibia Compr. Force	4010.2 N	2000 N	8000 N
Right Upper Tibia Index	0.82	0.4	1.3
Right Lower Tibia Index	0.78	0.4	1.3

Due to failure of the onboard high speed video cameras, only the first 80 ms of the impact was recorded and it was not possible to identify all the occupant kinematics during the collision. It was possible to see that the driver's head slid to the left of the driver airbag (Figure 14) and moved towards the left A-Pillar through a gap between the driver airbag and inflatable curtain, Figure 14. The gap developed as the steering wheel (and airbag) displaced rearward and right from its original position (Figure 10) in combination with A-pillar deformations that reduced the tension in the strap between the front and rear attachment points of the inflatable curtain. With reduced head impact mitigation from the inflatable curtain, high lateral head accelerations dominated the head injury criteria calculations which suggest the dummy's head struck the left A-pillar during the impact.



Figure 14. Occupant kinematics at 45, 60 and 75 ms into the crash.

DISCUSSION

Accident Analysis

Accident data shows the large over-representation of HGVs in road crashes. One cause is the incompatibility problem in car-to-HGV crashes, with oncoming (head-on) crashes being the most common accident type highlighting this issue. These crashes happen predominantly on rural roads with limited possibilities of redesign with median barriers or dramatic speed limit reductions, for example. Further, crash data shows that for cars of model year 2010 and later, the speed limit distribution is not changed significantly for older vehicle models so exposure to this crash scenario is still an issue with modern cars. The fatalities are not due to a lack of restraints, since the majority of victims is belted and has functioning airbags. The remaining factor that could be addressed is the HGV front-end design. Road regulations have historically limited the total length of HGVs including the driver cabin, leading to minimization of cabin length to maximize load volume. However, since 2019 there is a new rule change in Europe that allows extended truck cabins, without reducing the load capacity, if safety or environmental benefits can be shown [17]. This opens up for new front-end designs and more space for energy absorption and crash load management concepts.

Car-to-HGV Crash Test

The test demonstrated the severity of frontal crashes when there is a large mass difference between the vehicles. What is most striking from the test is the lack of structural capacity in the HGV FUPD. Figure 9 highlights the lack of structural interaction between the two vehicles where the main energy absorbing structures, the car longitudinals, are completely intact. The contact surface between the vehicles was limited to the softer outboard structures which were pushed rearward (car left fender and A-pillar) or sheared off (HGV). Metal fracture cannot be considered a desirable vehicle response in this type of crash.

The two main reasons for the poor interaction are the lack of structural alignment (originally foreseen in Figure 4, Figure 5) and the contact loads that exceeded the FUPD legislated requirements. R93 requires that the FUPD does not deflect rearward more than 400 mm when horizontal loads are applied separately to loading points “P1” and “P2” (Appendix B) [6]. These loads are based on the HGV mass but are not required to exceed 80 and 160 kN, respectively. In a crash, these points may be loaded simultaneously and simulations indicate crash interface forces easily exceed 400 kN during a frontal crash of this configuration.

The consequences of the loading observed in the crash test was that the FUPD was not able to prevent passenger car underride and resulted in the extreme loading to both vehicles. Had the FUPD been able to engage and activate the longitudinal in the car, the crash loads would not have been limited to the car tire and HGV frame. As seen in Figure 15, the car was loaded primarily through the wheel into the A-pillar. If the FUPD was stronger, the loads would have been distributed across more structures (Figure 15, right) and would not have compromised the passenger compartment as much. While the occupant compartment was not completely breached, the car deformations represent an unstable condition that could be much worse in a similar crash.

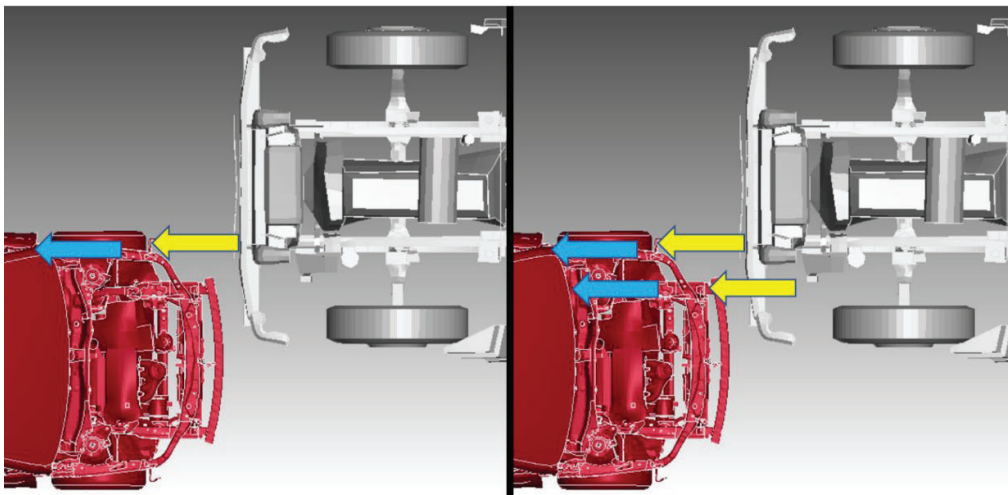


Figure 15. Load paths observed in test (left) and possible (right) with increased FUPD capacity.

Although the test wasn't a small overlap frontal impact like the IIHS test [15], the resulting damage to the car was not unlike that observed in those tests. The essentially undeformed car longitudinals is evidence of the lack of structural interaction. The narrow damage pattern focused on the front wheel and A-Pillar was comparable to

other small overlap cases although the velocity change was considerably higher in this test compared to the IIHS small overlap barrier test.

Notwithstanding the poor horizontal alignment seen in this test, the vertical misalignment also contributed to the poor results and would have contributed to a poor test outcome even if the horizontal alignment was improved. Figure 5 show that the centerlines of the FUPD and car bumper do not line up. Regulation 93 requires that for N3 HGVs (over 12 tonnes), FUPD cross beams must have a minimum 120 mm vertical dimension and with a lower edge no higher than 400 mm in the unladen condition [6]. There are no requirements for FUPD positions when the vehicle is loaded.

The car's left longitudinal appeared to be slightly bent upwards, indicating that its original engagement with upper part of the FUPD caused the car's longitudinal to slide over top of the FUPD, which later contacted the engine structures positioned lower than the longitudinal. The VC-Compat [8] and FIMCAR [18] projects reported that even for passenger car impacts, bumpers that are slightly misaligned vertically lead to diminished structural interaction and reduced compatibility.



Figure 16: Front Longitudinal Deformation and Apparent Upward Rotation

Considering the severe loading in this crash, the car's safety systems performed reasonably well. The right femur loads were the highest and surprising given the severe loading to the vehicle structures in the vicinity of the left femur. It is possible that the driving robot equipment and resulting right leg positioning (Figure 3) influenced the loading to the right leg and could be ignored in further analyses. With restraint systems adapted to the high severity of the car-to-HGV crashes, car occupant protection can be improved in terms of reducing occupant motion to prevent head impact to interior structures. With stiffer seat belts (higher load limiting force), excessive motion of the chest and head can be reduced, without increasing the loading to the chest if the stiffness of interior components such as seat and knee bolster can be adjusted accordingly [11]. Improved head protection also seems feasible using larger frontal airbags [10], or non-symmetric frontal airbags [19] which can have larger airbag volume in the left A-pillar region to prevent head rolling off the airbag and to avoid head strike-through. Finally, inflatable curtains extended to cover the A-pillar is another means of mitigating head impact to the near side structures in oblique crashes [20]. All such countermeasures are feasible if they can be made adaptive, so that protection in moderate-severity crashes is retained.

If the FUPD can be designed to better take up the forces, improve geometric compatibility, and prevent under-ride; the next challenge is to manage the energy in the crash. This possibility has been limited due to the HGV cabin size minimization to maximize load capacity. The maximum HGV length in Europe is the combined load and cabin length. It is now legal to extend the HGV front length, without reducing vehicle length allowed for cargo space, if safety and environmental benefits can be shown. If an improved FUPD could better prevent under-ride and a new extended front (possibly up to 800 mm) could better manage energy, this could increase the compatibility and lead to better survivability for occupants in passenger cars in these types of crashes.

CONCLUSIONS

Although Sweden has spent large resources on reducing speed limits and separating traffic with median barriers, there is a remaining problem with crashes between cars (even modern cars) and heavy goods vehicles (HGVs). Accident data showed that even though the car occupant generally was protected well with restraints, even the modern vehicles and moderate speed limits, crashes often lead to fatal outcomes. The incompatibility between

passenger cars and heavy goods vehicles (HGVs) is not only due to mass incompatibility, but also geometrical and stiffness incompatibility. Recent changes in legislation now allow extended HGV fronts for safety with more space for structures that absorb and manage crash loading.

The test illustrated the compatibility challenge for HGVs and passenger cars. Passenger cars can be designed with improved restraint systems and structural designs, but there must be a crash partner that exhibits geometrical compatibility as well as a structural integrity that will engage the crash structures of the passenger car and promote a better crash interaction. In this test, the FUPD collapsed/fractured early in the test and resulted in significant underride of the passenger car. In addition, the lack of engagement with the car's longitudinal beams created a small overlap condition with all the contact forces being directed through the wheel and A-pillar. The resulting deformations compromised the passenger compartment and reduced the efficiency of the existing occupant restraint systems. The test underlines the need for better FUPD requirements for HGVs. Similarly, passenger car structures should be promoted, through legislated or consumer testing, to interact with truck structures.

A future truck front-end could optimally consist of both a front structure that can better prevent under-ride and through a forward extension with energy absorbing capability to reduce crash loads to the opponent. Improved structural interaction would allow passenger car restraint systems to perform more efficiently.

Current restraint systems in the car need to be further improved take the high crash severity into account. Such systems are expected to be adaptive so that protection in moderate-severity crashes can be retained – which require more research into sensors that can distinguish between different crash severities. Although the performed test wasn't intended to be a small overlap test, the results highlighted the exposure of occupants to the high risk of sustaining head injuries in these cases. The extreme head and torso forward excursion could be limited by the Oblique Inflatable Curtain which is an improved protection system for this type of load case.

The unique test arrangement with two moving vehicles also highlighted the need for post-crash evaluation of HGVs where the vehicle damage may compromise the steering and braking system of the HGV, causing a high mass vehicle to potentially move uncontrolled in surrounding traffic, producing more crashes.

The future for vehicle safety further requires that active safety systems can mitigate the crash through automatic emergency braking systems and potentially steering. These automated systems should be active even after the crash to assist the vehicles come to a controlled stop or at least steer away from traffic. This requires that these mechanical systems must be designed or protected to remain functional in foreseeable crashes.

REFERENCES

- [1] K. Amin, J. Hedlund, Å. Forsman, A. Vadeby, R. Fredriksson, P. Hurtig, P. Larsson, M. Lindholm, S. Sternlund and M. Rizzi, "Analysis of Road Safety Trends 2020 - Management by objectives for road safety work towards the 2020 interim interim targets," Swedish Transport Administration, Publication 2021:173, 2021.
- [2] P. Larsson and C. Tingvall, "The Safe System Approach - A Road Safety Strategy Based on Human Factors Principles," in *Engineering Psychology and Cognitive Ergonomics. Applications and Services. EPCE 2013*, Berlin, 2013.
- [3] Transport Analysis, "Vehicles Mileage on Swedish roads," 2022. [Online]. Available: <https://view.officeapps.live.com/op/view.aspx?src=https://trafa.se/globalassets/statistik/trafikarbete/2022/trafikarbete-pa-svenska-vagar---1990-2021---2022-09-28.xlsx>. [Accessed 12 12 2022].
- [4] R. Schindler, M. Jansch and N. Parera, "D5.1: Safety issues for safety system design," AEROFLEX, 2018.
- [5] A. Balint, V. Labenski, C. Vogl, J. Stoll, L. Schories, L. Annan, G. Baroda Sudhakaran, P. Huertas Leyva, T. Pallacci, M. Östling, D. Schmidt and R. Schindler, "D2.6 Use Case Definitions and Initial Safety-Critical Scenarios," Horizon 2020 Project proactive SAFETy systems and tools for a constantly UPgrading road environment (SAFE-UP), 2021.
- [6] UNECE, "Regulation R93: Front Underrun Protective Devices," 1994.
- [7] A. Krusper and R. Thomson, "Truck frontal underride protection – compatibility factors influencing passenger car safety," *International Journal of Crashworthiness*, 17:2, pp. 217-232, 2012.
- [8] M. Edwards, P. de Coo, C. van der Zweep, R. Thomson, R. Damm, T. Martin, P. Delannoy, H. Davies, A. Wrige, A. Malczyk, C. Jongerius, D. Stubenböck, Knight, I. Knight, Sjöberg, M. Sjöberg, O. Ait-

- Salem Duque and R. Haschemi, "Improvement of Vehicle Crash Compatibility through the Development of Crash Test Procedures (VC-Compat)," EC - Competitive and Sustainable Growth Program GRD2/2001/50083, 2007.
- [9] CEN, "Road Restraint Systems," 2010.
- [10] B. Pipkorn, H. Melander and Y. Håland, "Car Protection at Frontal Impacts up to 80 km/h (50 MPH)," in *Proceedings of the 19th Technical Conference on the Enhanced Safety of Vehicles*, Washington, 2005.
- [11] M. Östling, L. Eriksson, M. Dahlgren and J. Forman, "Frontal Head-On Car-to-Heavy Goods Vehicle Crashes and their Effect on the Restraint System," in *Proceedings of the 27th Technical Conference on the Enhanced Safety of Vehicles*, Yokohama, Japan, 2023.
- [12] K. Mroz, M. Östling and N. Lubbe, "Passenger Cars in Head-On Crashes with Heavy Goods Vehicles: For What Severity Should Future Car Restraint Systems Be Designed," in *Proceedings of the 27th International Technical Conference on the Enhanced Safety of Vehicles*, 2023.
- [13] STA, "Data Collection," 2019. [Online]. Available: <https://bransch.trafikverket.se/en/startpage/operations/Operations-road/vision-zero-academy/Vision-Zero-and-ways-to-work/data-collection/>.
- [14] GIDAS, "German In Depth Accident Study," [Online]. Available: <https://www.gidas.org/start-en.html>.
- [15] IIHS, "Small Overlap Frontal Crashworthiness Evaluation Crash Test Protocol," Insurance Institute for Highway Safety, 2021.
- [16] Euro NCAP, "MPDB Frontal Impact Testing Protocol," Euro New Car Assessment Program, 2022.
- [17] European Commission, "Commission regulation (eu) 2019/1892 of 31 october 2019 amending regulation (eu) no 1230/2012 as regards type-approval requirements for certain motor vehicles fitted with elongated cabs and for aerodynamic devices and equipment for motor vehicles," 2019. [Online]. Available: https://eur-lex.europa.eu/legal-content/EN/TXT/?uri=uriserv:OJ.L_.2019.291.01.0017.01.ENG.
- [18] H. Johannsen, T. Adolph, M. Edwards, I. Lazaro, T. Versmissen and R. Thomson, "Proposal for a Frontal Impact and Compatibility Assessment Approach Based on the European FIMCAR Project," *Traffic Injury Prevention*, vol. 14:sup1, pp. S105-S115, 2013.
- [19] K. Mroz, O. Boström, B. Pipkorn, J. Wismans and K. Brolin, "Comparison of Hybrid III and human body models in evaluating thoracic response for various seatbelt and airbag loading conditions," in *IRCOBI*, Hanover, 2010.
- [20] O. Boström and D. Kruse, "Curtain Airbag for Small Overlap Crashes," in *Society of Automotive Engineers International, Government and Industry Meeting*, Washington, D.C., 2013.

APPENDIX A

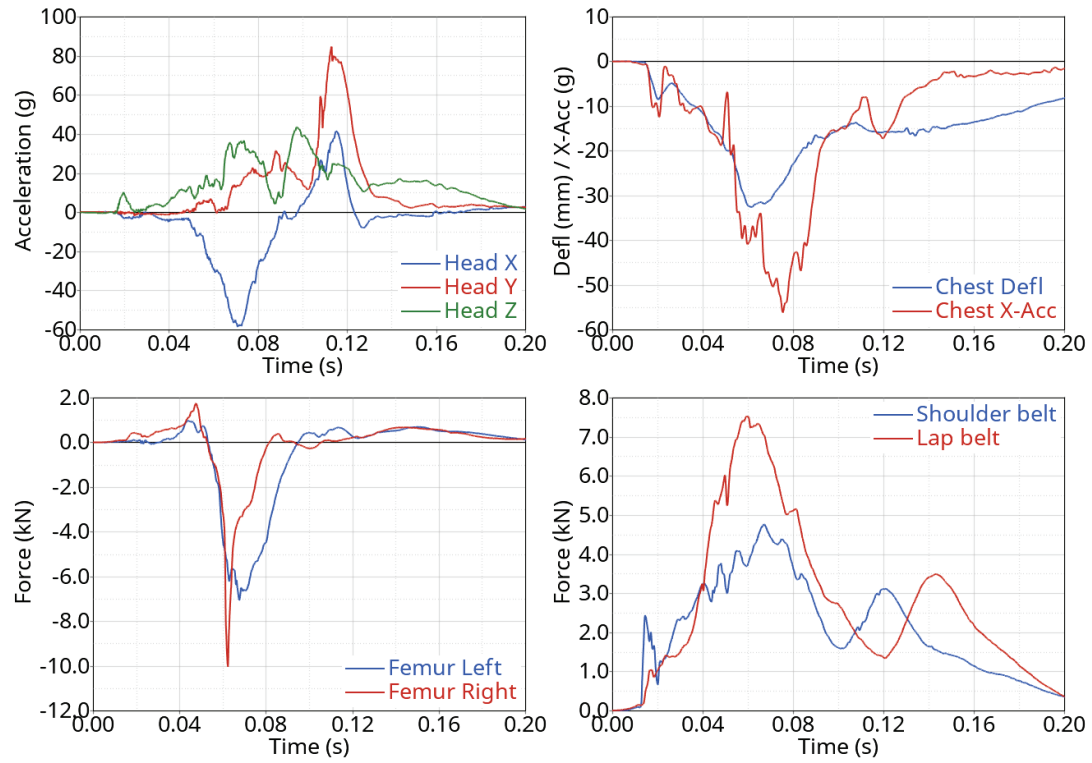


Figure A1. HIII head accelerations (upper left), chest deflections and accelerations (upper right), and femur forces (lower left). Car seat belt forces (lower right).

APPENDIX B. R93 Test Load Locations

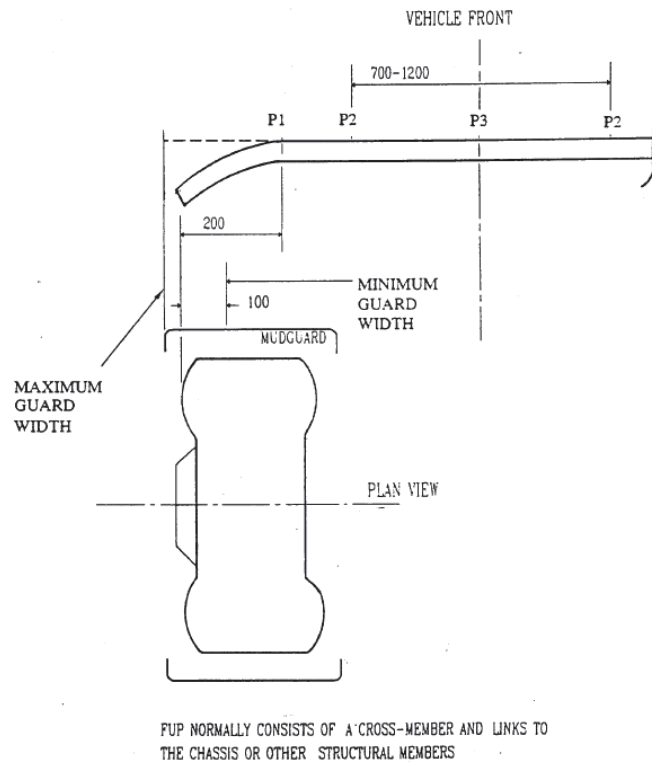


Figure B1: Extract from Regulation 93 showing test load application points on FUPD [6].

FIREWORTHINESS OF CABIN EXHAUSTER VENTS AND THE EFFECT OF AGEING

Christopher Clarke
Brian Herbst
Lauren Bell
SAFE
USA

Jack Bish
SAFE Laboratories
USA
Paper Number 23-0324

ABSTRACT

In many case studies, post-collision fires originating outside the occupant compartment were found to have propagated into the occupant compartment through the cabin exhauster vents. HVAC systems in modern vehicles include exhauster vents to flow air out of the occupant compartment, while preventing air, moisture and dirt from flowing in. Cabin exhauster vents are typically constructed with a matrix of elastomeric flaps mounted to a rigid plastic grate and attached directly to the sheet metal of the vehicle body. This study evaluates the ability of production and improved exhauster vent designs to resist fire propagation.

INTRODUCTION

Modern vehicles rely on cabin exhauster vents to enable the HVAC system to flow air out of the cabin and to mitigate the shock of doors closing. These vents are typically located at the lower rear corners of the vehicle underneath the bumper fascia. In pickups, the vents are typically placed at the lower portion of the rear bulkhead and are concealed by the forward bulkhead of the bed. Figure 1 shows the location of an exhauster vent under the rear bumper fascia in a 2010s vintage domestic sedan. This vent uses a matrix of 9 elastomeric flaps to control airflow. The flaps are attached along their top edges to a plastic housing in a normally closed position and bend outward to allow air to flow out of the interior of the vehicle. When air pressure is applied from outside the vehicle, the flaps seal against the plastic housing to resist airflow into the interior of the vehicle.

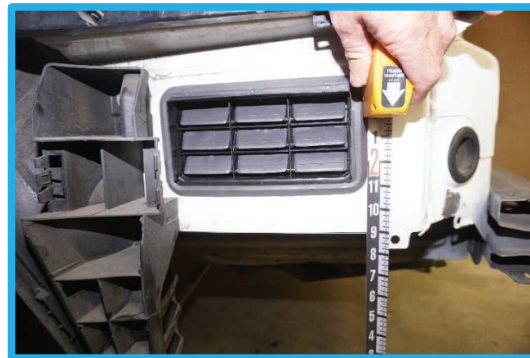
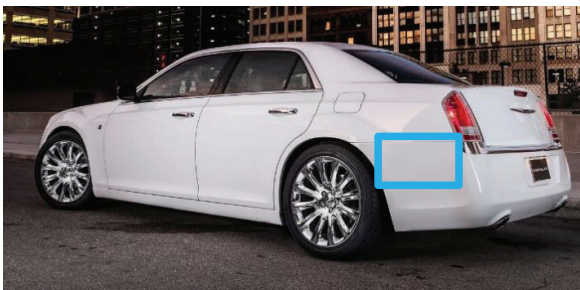


Figure 1: Cabin Exhauster Vent

Numerous real world post-collision fire incidents have been analyzed in which it was determined that fire propagated into the occupant compartment through exhauster vent openings in the body sheet metal. Exhauster vent openings are among the largest openings found in body panels, rivaled only by openings in the cowl for the HVAC air intake. In addition, exhauster vents are typically located low on the vehicle where they are exposed to pool or underbody fire scenarios. Because of their exposed location and construction with combustible materials, exhauster vents are not well suited to protect the large openings they occupy in the body structure.

Nearly 3 out of 4 vehicle fires are caused by mechanical or electrical failures or malfunctions, but these fires only account for 11% of vehicle fire deaths. Collisions and overturns contribute to ignition in only 3% of vehicle fires, however, these fires result in 3 out of 5 vehicle fire deaths.[1] Occupant extrication often requires 15-20 minutes from the time of a crash. However, death can occur in as little as 1-3 minutes once fire enters the occupant compartment.[2],[3] Vehicles must therefore be designed to resist the ingress of fire for a sufficient time to facilitate extrication to protect entrapped or incapacitated occupants. There is no federally mandated testing standard to evaluate how long it takes for fire to penetrate the occupant compartment of a motor vehicle.

EXEMPLAR VENT SURVEY

Exhauster vents are typically positioned behind the vehicle's rear bumper but that does not preclude them from damage and degradation. Throughout their lifetime, exhauster vents are subject to environmental factors, road debris and temperature changes that cause material degradation. Figure 2 below shows an aged exhauster vent obtained from an exemplar 2013 model year sedan compared to a new OEM replacement vent for the same vehicle. The elastomeric flaps in the aged vent have degraded significantly, two of the flaps have become displaced and one of the flaps is missing.

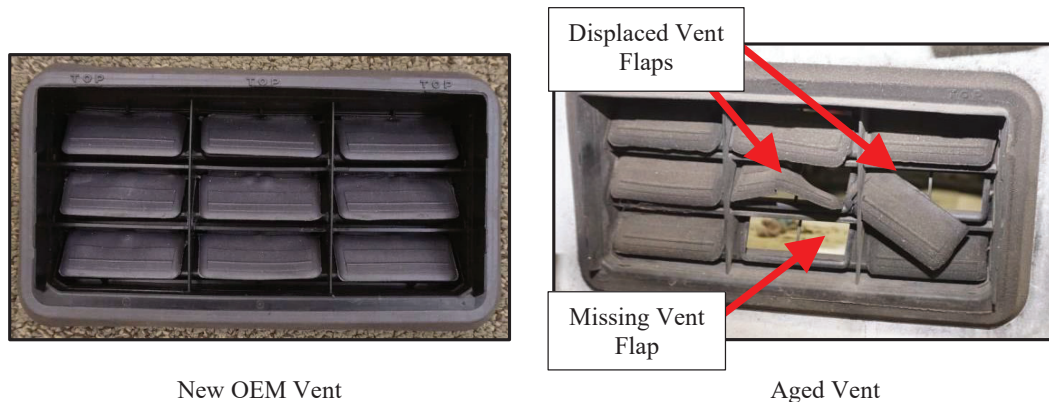


Figure 2: New OEM vs Aged Vent Comparison

Motor vehicles have the potential to last for many decades. According to data from the National Household Travel Survey, or NHTS, nearly half of the vehicles on the road are 10 years old or older. In addition, nearly 1 in 4 vehicles on the road are 15 years old or older, and nearly 1 in 10 vehicles is 20 years old or older.

A survey was conducted on the condition of exhauster vents on 33 vehicles ranging from 8 to 25 years old. Each examined vent was checked for three categories of ageing and deterioration. Degraded material classifies vents that have weak or brittle flaps, or other changes in material properties that impair the functionality or integrity of the vent. Displaced flaps categorizes vents that have flaps that are distorted, partially detached, or otherwise out of position. Finally, missing flaps classify vents that are missing at least one of their flaps. It was observed that 7 of the 33 vehicles exhibited the above signs of ageing, summarized in Table 1 below. Examples of the vents listed in Table 1 are presented in Figure 3 through Figure 6.

Table 1: Summary of Vehicles with Degraded Vents

Vehicle Number	Model Year	Degraded Material	Displaced Flaps	Missing Flaps
4a	2004 BMW X3*	Yes	No	No
4b	2004 BMW X3*	Yes	Yes	No
7a	2003 Chevrolet K1500	Yes	No	No
7b	2003 Chevrolet K1500	Yes	No	No
12	2004 Hyundai Elantra	No	No	Yes
15a	1996 Jeep Grand Cherokee	Yes	No	No
15b	1996 Jeep Grand Cherokee	Yes	No	No
22	1998 Nissan Altima	Yes	Yes	No
25	2000 Toyota 4Runner	-	-	Yes
28	2000 Toyota Celica	Yes	No	No

*Flaps inoperable, material disintegrated when touched



Figure 3: Exhauster vent 4a driver's side (Left) and 4b passenger's side (Right)



Figure 4: Exhauster vent 7a driver's side (Left) and 7b passenger's side (Right)



Figure 5: Exhauster vent 12



Figure 6: Exhauster vent 15a driver's side (Left) and 15b passenger's side (Right)

It was determined 7 of 33 vents examined in the survey, 21% of the sample size, showed signs of ageing. However, many vents did not have any visible evidence of ageing or degradation despite being found in vehicles that were of similar or older vintage compared to the vehicles with degraded vents. Factors such as design and material selection determine whether a vent deteriorates with age. In addition, the survey found that vehicle 15 had degraded vents while another vehicle of the same make and model and only one model year newer did not have degraded vents. This suggests that environmental factors and differences in usage also influence the degradation of vents. More exposure to the elements and temperature extremes, and more hours of usage of the HVAC system would be expected to hasten the ageing process.

PRODUCTION DESIGN BURN TESTING

Burn testing has been conducted on new OEM replacement and aged vents utilizing fuel sources representative of the fuels identified in real world vehicle fire incidents. This testing has been run utilizing partial vehicle clips obtained from exemplar vehicles to represent the area of fire propagation identified in the case studies, as well as sheet metal bench testing fixtures representing the pass-through openings in the subject vehicles. New OEM replacement exhauster vents and pass-through seals were tested, as well as aged exhauster vents obtained from exemplar vehicles and improved vent and pass-through designs.

Test Series 1

Burn testing was conducted to evaluate the fire resistance of the vent design used on a domestic pickup cab using gasoline in a burn pan positioned underneath the exhauster vent. An exemplar cab was obtained from a vehicle that was approximately 18 years old at the time of the test. The aged vent in this cab was subjected to testing. In addition, a new OEM vent was subjected to burn testing in a sheet metal bench testing fixture configured in a manner consistent with the portion of the cab where the vent is installed. The setup for each test is shown in Figure 7. It was noted that the design of the new OEM replacement vent had changed compared to the vent from the 18 year old exemplar cab. While both vents were designed to fit the same opening, the new OEM vent had fewer flaps.



Aged Vent from 18 Year Old Exemplar Cab

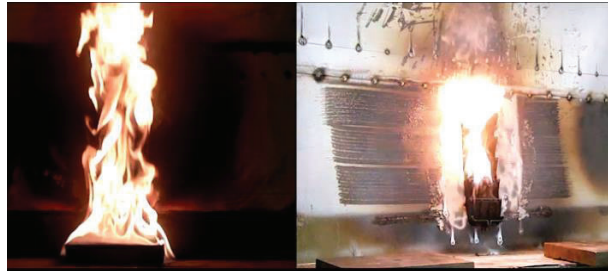


New OEM Vent

Figure 7: Test Setup

In the new OEM vent test, fire broke through and ignited the inside of the vent at approximately 78 seconds after ignition and the vent had fallen completely out of the opening by approximately 99 seconds. In the aged vent test, flames were first visible on the interior side of the exhauster vent at approximately 42 seconds after ignition and the vent had fallen completely out of the opening by approximately 53 seconds after the fire was ignited. Figure 8 shows the point when the fire ignited the inside portion of the vent in each test.

New OEM Vent
~78 seconds



Aged Vent from 18 Year Old
Exemplar Cab
~42 seconds

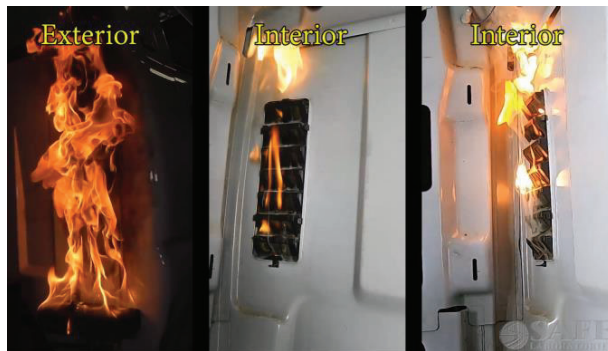


Figure 8: Test Results

Test Series 2

Burn testing was conducted to evaluate the fire resistance of the vent design used on a 2014 import sedan. A rear clip obtained from an approximately 7 year old exemplar vehicle was tested with the aged vent that arrived with it. The test was run using gasoline in a burn pan positioned underneath the exhauster vent and igniting it with an external source. Flames were first visible on the interior side of the exhauster vent at approximately 24 seconds after ignition, shown in Figure 9. The vent was completely engulfed and was melted out of the cut-out by approximately 40 seconds after ignition.

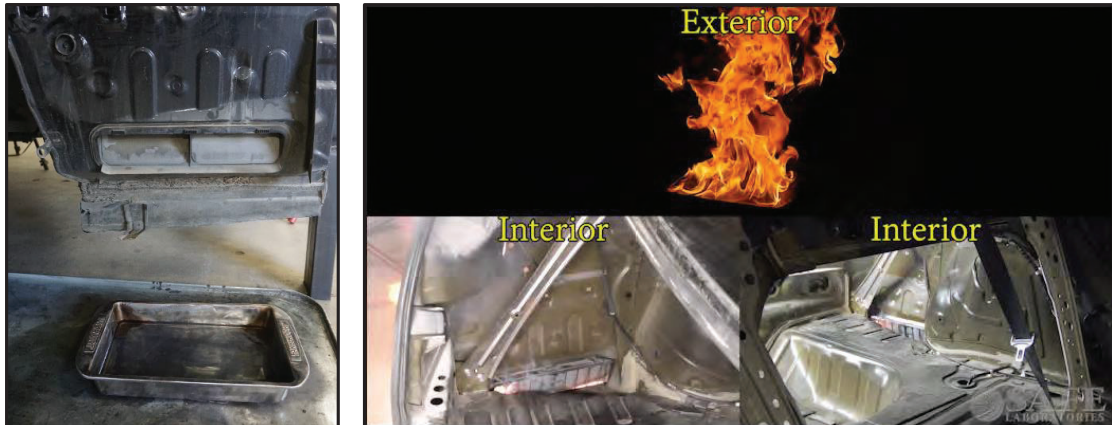


Figure 9: Test Setup and Results

Test Series 3

A pair of burn tests was conducted to evaluate the fire resistance of the vent design used in a 2013 model domestic sedan. The vents were fitted in a steel panel benchtop fixture and straw was positioned underneath each vent and ignited with an external source. The first test evaluated a new OEM replacement vent and the second evaluated an aged vent obtained from an exemplar vehicle that was approximately 8 years old at the time of testing. Flames began coming through the new OEM vent approximately 68 seconds after ignition, and flames were observed coming through the aged vent 15 seconds after ignition. The benchtop testing is shown in Figure 10.

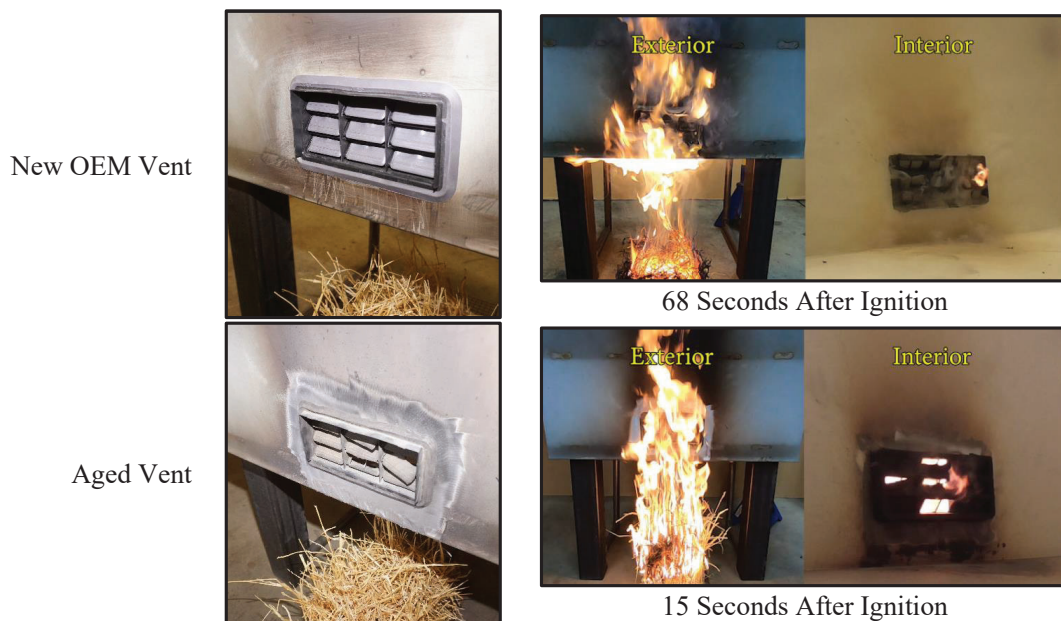


Figure 10: Test Setup and Results

An additional burn test was conducted on a new replacement OEM vent installed in the rear clip of an equivalent vehicle using straw similarly positioned underneath the exhauster vent and ignited with an external source. Flames were first visible on the interior side of the exhauster vent was at approximately 71 seconds after ignition, shown in Figure 11.



Figure 11: Test Setup and Results

IMPROVED DESIGN BURN TESTING

Test Series 1 Flame Arrestor Shield

An improved design flame arrestor type vent was evaluated under burn conditions identical to those of the production test. A steel housing was fitted around the interior of the OEM exhauster vent. A commercially available flame arrestor type fire resistant vent assembly consisting of an aluminum honeycomb core with an intumescent coating encased with perforated sheet metal on one side and a fine stainless-steel mesh on the other was installed in the housing. The improved design exhauster vent was subject to the same test procedure used to evaluate the OEM pass-throughs. The fire burned for approximately 564 seconds and no flames were able to pass through the exhauster vent, shown in Figure 12.

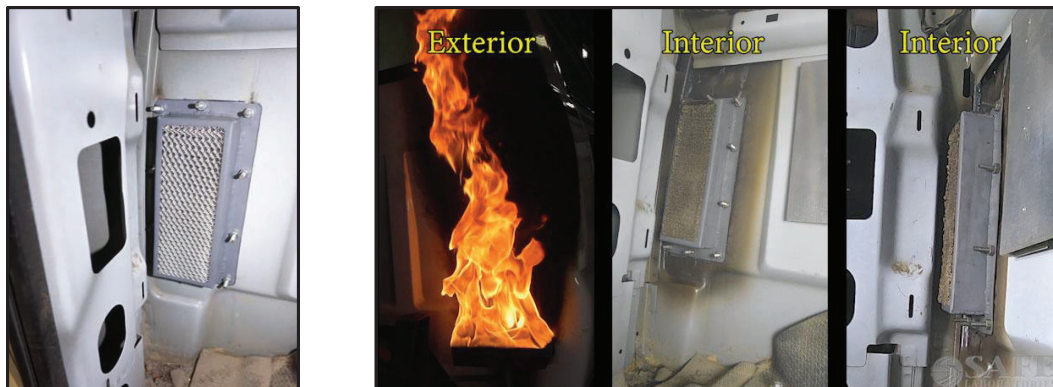


Figure 12. Test Results

In the production vent test, flames were visible in the occupant compartment approximately 42 seconds after the gasoline in the burn pan was ignited. Therefore, the improved vent design resisted the fire for a significantly longer time period than the production design and could likely have continued to resist fire for a longer period of time. The results of test series 1 are summarized in Table 2.

Table 2. Summary of Test Series 1 Results

Test	Time at Ignition of Interior of Vent	Time when Vent Falls out of Opening
New OEM Bench Test	78 seconds	99 seconds
Aged Vent Exemplar Cab Test	42 seconds	53 seconds
Flame Arrestor Exemplar Cab Test	N/A*	N/A*

*The interior of the vent did not ignite and the vent remained intact until the fuel source was exhausted approximately 564 seconds after ignition.

Test Series 3 Flame Arrestor Shield

An improved design flame arrestor type vent was evaluated under burn conditions identical to those of the production test. The vent design was improved by constructing a housing around the interior of the OEM exhauster vent opening capable of fitting on top of an OEM vent assembly. The housing was fitted with a commercially available flame arrestor type fire resistant vent assembly. The assembly consists of an aluminum honeycomb core with an intumescent coating encased with perforated sheet metal on one side and a fine stainless-steel mesh on the other. The OEM elastomeric vent assembly was not installed for the test in order to evaluate the performance of the flame arrestor alone. The improved design vent was subject to the same test procedure used to evaluate the OEM vent. The fire burned for approximately 221 seconds at which time the fuel source was consumed and no flames were able to pass through the exhauster vent, shown in Figure 13.



Figure 13: Test Results

In the production vent test flames were visible in the occupant compartment approximately 71 seconds after the straw was ignited. Therefore, the improved vent design resisted the fire for a significantly longer time period than the production design and could likely have continued to resist fire for a longer period of time. The results of test series 3 are summarized in Table 3.

Table 3. Summary of Test Series 3 Results

Test	Time at Ignition of Interior of Vent
New OEM Bench Test	68 seconds
New OEM Exemplar Clip Test	71 seconds
Aged Vent Bench Test	15 seconds
Flame Arrestor Exemplar Clip Test	N/A*

*The interior of the vent did not ignite and the vent remained intact until the fuel source was exhausted approximately 221 seconds after ignition.

Benchtop Testing Series

Improved vent designs were fabricated and subjected to burn testing in a benchtop fixture similar to the one used in Test Series 3. A new OEM replacement vent of the same design evaluated in Test Series 3 was also tested in order to establish a baseline level of fire resistance. For each test, a tray containing a quantity of gasoline sufficient to burn for approximately 20 minutes was ignited underneath the vent.



Figure 14: Test Setup

Baseline Test

A new OEM replacement vent of the same design evaluated in Test Series 3 was subjected to burn testing. Fire was observed to have started on the inside of the vent approximately 57 seconds into the test. This time was approximately 10 seconds shorter than observed in Test Series 3, but the gasoline fuel source ignited more quickly and was located slightly closer to the vent. After approximately 82 seconds the vent was observed to be falling out of the opening. At approximately 95 seconds the vent was observed to be burning on the inside of test fixture. Figure 15 shows the progression of the test.

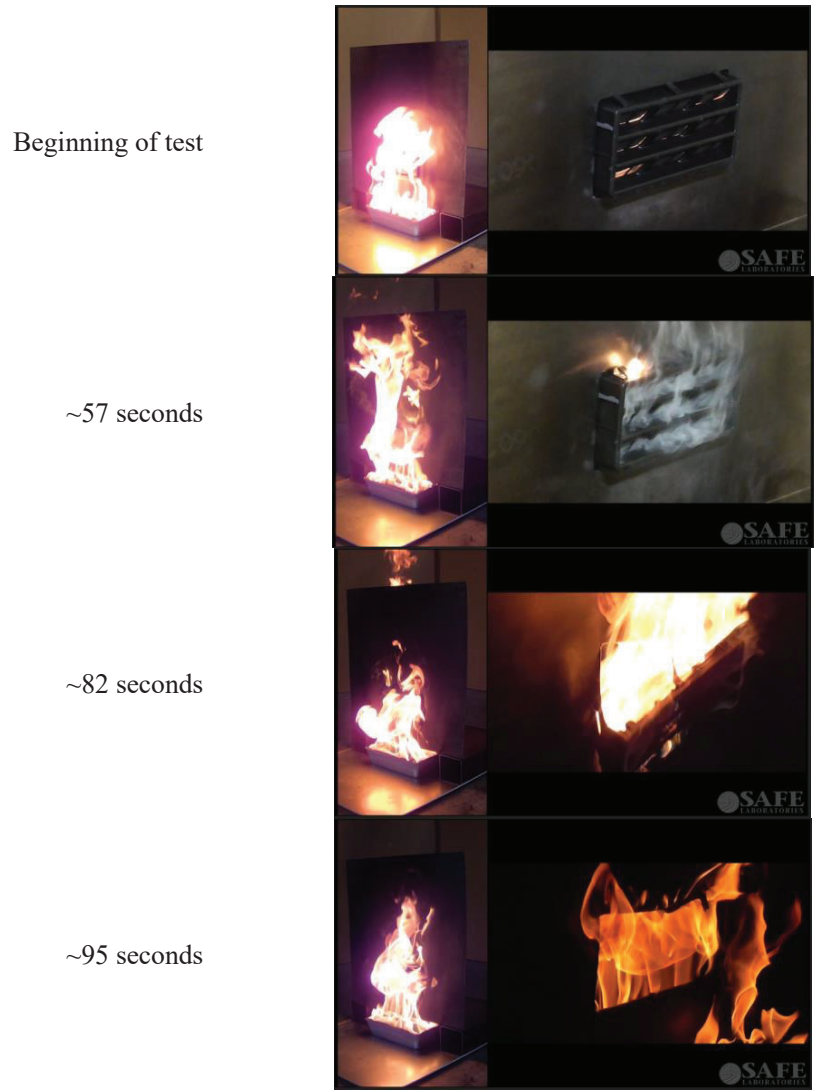


Figure 15: Baseline Test Results

Diverter Shield

A diverter shield was constructed and fitted to the test fixture, shown in Figure 16. The shield was approximately 3 inches wider and 2 inches taller than the OEM vent assembly, and extended from the surface of the test fixture at its base to approximately 3 ½ inches away from the test fixture at its top.



Figure 16: Improved Design – Diverter Shield

A new OEM vent was fitted in the test fixture behind the diverter shield and subjected to burn testing. As the test progressed, some smoke was observed to emanate from the interior side of the vent but it did not ignite. At approximately 285 seconds, the plastic vent assembly had melted to the extent that it fell into the interior side of the test fixture. However, it did not ignite. An elastomeric flange from the exterior side of the vent remained in place, stuck to its original position on the exterior side of the opening in the fixture. This flange eventually caught fire and fell away from the opening, propagating the fire to the inside of the vent opening. At approximately 522 seconds, the body of the vent on the inside of the test fixture was observed to have ignited. Figure 15 shows the progression of the test.

Beginning of test



~ 285 seconds



~ 522 seconds



Figure 17: Test Results

Metal Vent Assembly

An all metal vent assembly was fabricated and subjected to burn testing. The vent was designed to fit the same opening as the production OEM vents tested previously. The vent assembly was constructed with a machined aluminum housing, and a single flap made of thin steel was attached to the top of the housing at two pivot points as shown in Figure 18.

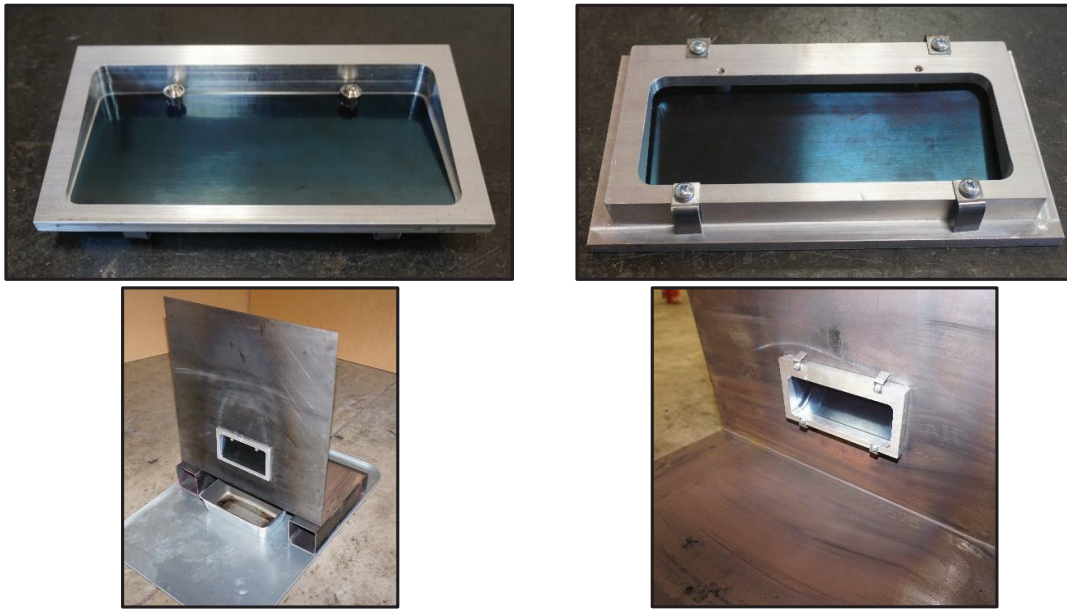


Figure 18: Improved Design – Metal Vent Assembly

The all metal vent assembly was installed in the test fixture and subjected to burn testing. The vent assembly remained intact during the test and did not ignite. Some slight warping of the flap was observed during the test. The gasoline burned out after approximately 20 minutes. Figure 19 shows the beginning of the test and shortly before the gasoline burned out.

Beginning of test

Just before 20 minutes



Figure 19: Test Results

The results of this test series are summarized in Table 4.

Table 4. Summary of Benchtop Testing Results

Test	Time at Ignition of Interior of Vent	Time when Vent Falls out of Opening
Baseline	57 seconds	82 seconds
Diverter Shield	522 seconds	285 seconds
Metal Vent	N/A*	N/A*

*The interior of the vent did not ignite and the vent remained intact until fuel source was exhausted approximately 20 minutes after ignition.

DISCUSSION AND CONCLUSIONS

The new OEM replacement vents evaluated were found to resist fire propagation for only 1 to 2 minutes. Aged vents were observed to allow fire to enter the occupant compartment in as little as 15 seconds when subjected to burn testing under the same conditions. When exhauster vents ignite, become a fuel source that facilitates propagation of fire. The aged vents tested ignited very quickly and would be expected to expedite the propagation of fire into the occupant compartment.

No service or replacement intervals are specified by the manufacturers for the vent designs that were evaluated. However, the elastomeric flaps on aged vents obtained from used vehicles were observed to have deteriorated to varying degrees, and in some cases portions of the flaps had become distorted or fallen away. Exhauster vents are typically located in parts of the vehicle that are extremely difficult to access, making replacement burdensome. Many vehicles on the road have been in service for 20 years or more, and the age of the vehicle fleet has been trending higher in recent years. Therefore, vehicle manufacturers should endeavor to design exhauster vents to last the life of the vehicle.

The testing presented in this paper also shows that exhauster vents could serve an important safety function in addition to their role as a part of the HVAC system. In order to ensure occupant protection in crashes, designers must also ensure that vehicles can protect occupants from post-collision fires. Care should be taken in the design of exhauster vents to ensure they provide a suitable level of resistance to fire propagation and to select materials that maintain that level of protection for the life of the vehicle.

Finally, the improved vent design tests demonstrate the potential to substantially increase the fire resistance of exhauster vents. This improvement in fire resistance can be achieved by adding shielding to protect typical production elastomeric vents, and by replacing the elastomeric materials used in typical vent designs with more resilient materials. These improvements not only increase fire resistance, but also increase the service life of the vent. Vehicle manufacturers could apply similar design concepts to improve fire resistance and to ensure that exhauster vent openings maintain a suitable level of fire resistance for the life of the vehicle.

REFERENCES

- [1] Ahrens, Marty, July 2008, 'U.S. Vehicle Fire Trends and Patterns,' NFPA.
- [2] Digges, K.H., Sep. 3-5, 2007, 'Improving Survivability in Motor Vehicle Fires,' in *Interflam 2007 Conference*, Royal Holloway College, University of London, UK, Interscience Communications, London.
- [3] Hirschler, M., 2002, "Rate of Heat Release of Plastic Materials from Car Interiors", Business Communications Company Eleventh Ann. Conference on Recent Advances in Flame Retardancy of Polymeric Materials, Norwalk, CT.

A FORENSIC ANALYSIS OF RECLINER RELEASE VIA CONNECTING ROD IN REAR IMPACT AUTOMOTIVE COLLISIONS

Steven Meyer

Jeremy McMillin

Safety Analysis and Forensic Engineering (SAFE)

USA

Paper Number 23-0327

ABSTRACT

Occupant safety in rear impact automotive collisions relies heavily on freestanding seats to restrain front seated occupants without intruding into the survival space of occupants in the rear seat [1] [2]. The seatback must absorb crash energy while remaining sufficiently upright to prevent occupant ramping and injurious contact with rear seated occupants and / or rear vehicle structures. Additionally, the front seats must be designed to accommodate all different occupant statures comfortably [3]. Adjustability is typically achieved by equipping the seats with a number of features including fore / aft adjustment, recline adjustment, and often seat height adjustments. These adjustment features are either manually, or electrically adjustable.

A failure mode in manually adjustable dual recliner seats has been identified wherein the recliner connecting rod can disengage one, or both, recliners during a rear impact event, undermining the seat back's ability to restrain the relative rearward movement of the front occupant. This catastrophic failure mode presents both front and rear seated occupants with higher risks of severe injury.

Three real world cases are presented wherein manually adjustable recliners were found to release in a rear impact due to the recliner connecting rod. Testing and / or demonstration of the failure mode is shown in each case which shows matching evidence between the accident and test seats.

INTRODUCTION

In rear impact collisions, the force to the impacted vehicle accelerates it forward. As the vehicle accelerates forward, the occupant's seatback applies force to the occupant in order to also accelerate the occupant forward. Failure of the seatback to accelerate the front occupants forward can result in the occupants moving rearward relative to the vehicle, allowing them to make forceful contact with rear vehicle structures, and / or occupants seated in the rear seat, increasing potential for serious injury.

Early vintage automotive seats were generally designed with a single recliner mechanism on the outboard side of the seat, and a simple pivot on the inboard side of the seat. Under rearward impact loading, the asymmetry of the single recliner design can allow the seatback to twist, providing uneven, and suboptimal support to the occupant's upper torso. Automotive manufacturers and seat suppliers have recognized this issue and have migrated to mostly dual recliner seat systems. The dual recliner system replaces the inboard seat back pivot with a second recliner, allowing the inboard side of the seatback to evenly provide support for the occupant in a rear impact event.

In order for a manually adjustable seatback recline angle to be adjusted to accommodate different size users and recline positions, the two recliners must disengage simultaneously when the user pulls on the recliner adjustment handle, and re-engaged simultaneously when the user releases the recliner adjustment handle. This is commonly achieved by the use of a recliner connecting torsion rod.

MANUAL DUAL RECLINER MECHANISM WORKINGS

A typical design for dual manual recliner seats contains two pawl and sector recliners controlled by a cam in each recliner. The two cams are connected via a recliner connecting rod, and the recliner adjustment handle is connected to the recliner connecting rod itself, or controls one of the cams (see Figure 1). As the recliner handle is pulled up by the user, the outboard cam rotates while the recliner connecting rod rotates the cam in the second recliner at the same time. The rotation of the cams allow the pawls to disengage from the sectors, releasing the recliners, and the

seat back is then able to be adjusted in recline (see Figure 2). As the user releases the spring loaded handle, the cams are both rotated back, pushing the pawl teeth back towards the sector teeth to re-engage both recliners and prevent further movement of the seatback at the recliners.

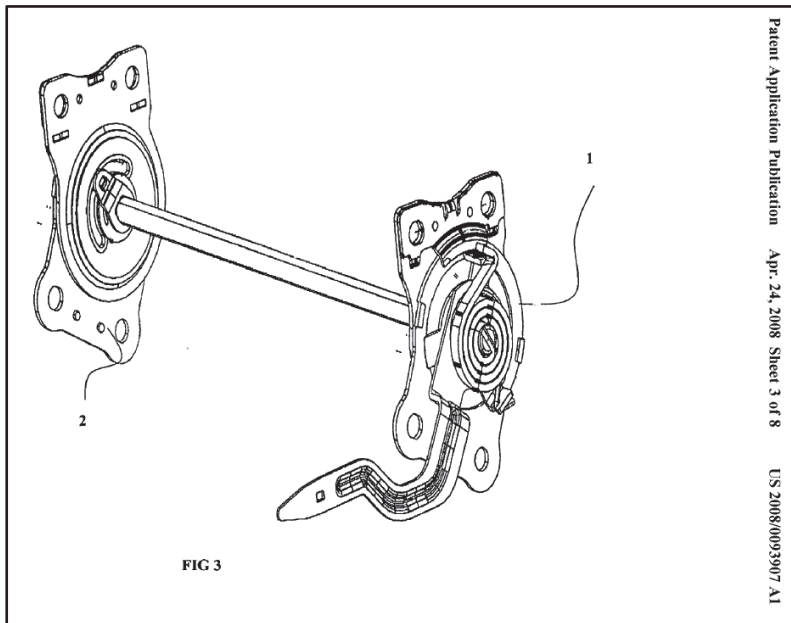


Figure 1: Drawing of dual recliner system with pawl and sector gears and connecting rod [4].

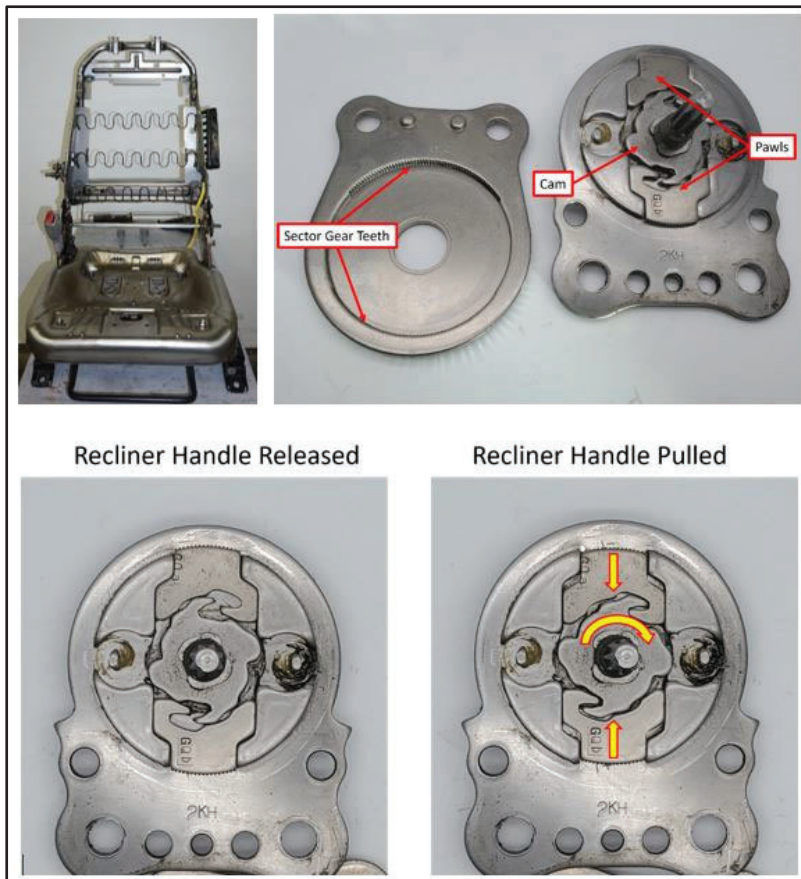


Figure 2: Typical dual manual recliner seat with pawl and sector recliners.

During the analysis of real-world cases with seats of this design, it has been found that inadvertent and / or unintended rotation of the recliner connecting rod during occupant seat back loading, can release one, or both, of the recliners. Such a release allows the seat back to freely rotate rearward in recline thereby undermining the seat structure's ability to deform / yield, absorb crash energy, and provide effective occupant ride down and restraint.

CASE 1 – RECLINER RELEASE VIA ASSYMETRIC DEFORMATION BELOW RECLINER ASSEMBLY

The first case involves a 2011 passenger vehicle which was slowing for stopped traffic when it was rear impacted by a minivan. As a result of the collision, the driver sustained serious head injuries.

During inspection of the subject rear ended vehicle, the driver's seat was found with the seat back angle at a recline angle further rearward than would be expected. The seat was removed from the vehicle, and the cloth upholstery was removed for further inspection and analysis. During the analysis, the following was identified:

- The inboard lower recliner attachment to the seat base was torn (see Figure 3).
- The inboard lower recliner attachment and outboard lower recliner attachment were asymmetrically designed, with the inboard side having a hole in the middle (see Figure 4).
- The tear across the inboard lower recliner attachment allowed the inboard recliner to rotate rearward.
- The inboard and outboard recliners were found post-crash in different adjustment positions.
- Additionally, the recliners were disassembled to inspect the teeth of the pawls and sectors. The outboard sector gear teeth and pawls were found to be damaged.

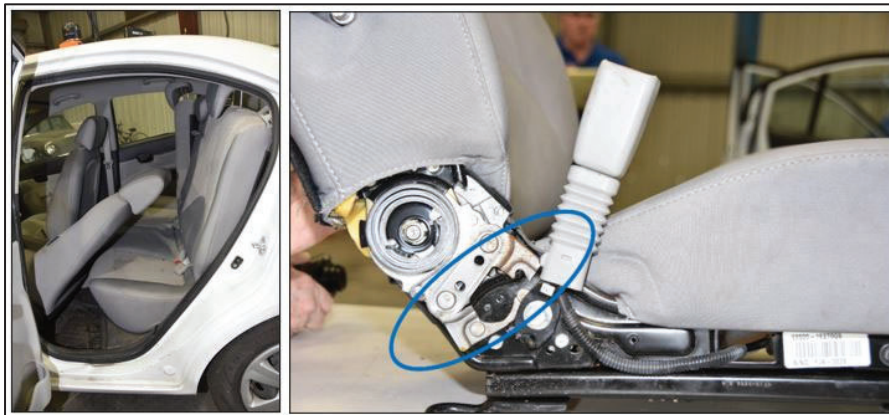


Figure 3: Subject rear-ended vehicle seat with torn inboard lower recliner plate.

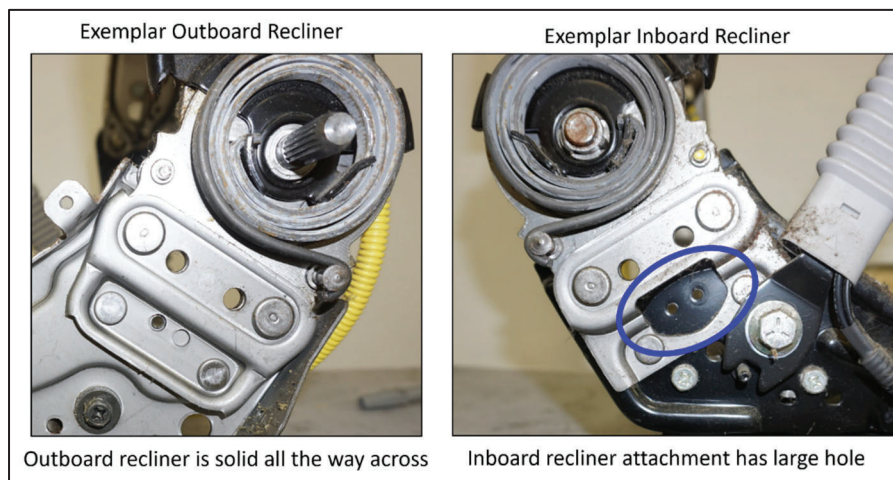


Figure 4: Exemplar seat with asymmetric lower recliner plate designs.

A sled test was performed by SAFE Laboratories of an exemplar seat in an exemplar test buck, with a modified 50th percentile Hybrid III Anthropomorphic Test Device (ATD) to match the seated height and weight of the driver of the rear impacted vehicle [5] [6]. The sled was subjected to an approximately 11.2 m/s (25 mph) rear delta-V, consistent with the accident reconstruction of the subject rear collision. The seatback was seen to rotate rearward in recline such that it failed to restrain the ATD, and the ATD made forceful head contact with the rear seat back (see Figure 5).



Figure 5: Sled test with ATD head contact at rear seat.

Further analysis of high-speed test video and inspection of the tested seat revealed the inboard lower recliner attachment plate tore similar to the accident seat (see Figure 6). The tearing occurred early in the seat loading phase of the test and caused the inboard recliner mechanism to rotate rearward. This rearward rotation of the inboard recliner also rotated the recliner connecting rod which in turn released the outboard recliner. This chain of events resulted in the failure of the seatback to provide any additional support to the ATD in the rear impact collision, and occupant containment was lost. The evidence identified on the test seat was found to be remarkably similar to the evidence identified on the subject accident seat. The posttest recliner inspection further revealed that the seat recliners became adjusted to different positions as a result of the release of the outboard recliner during the occupant loading event.

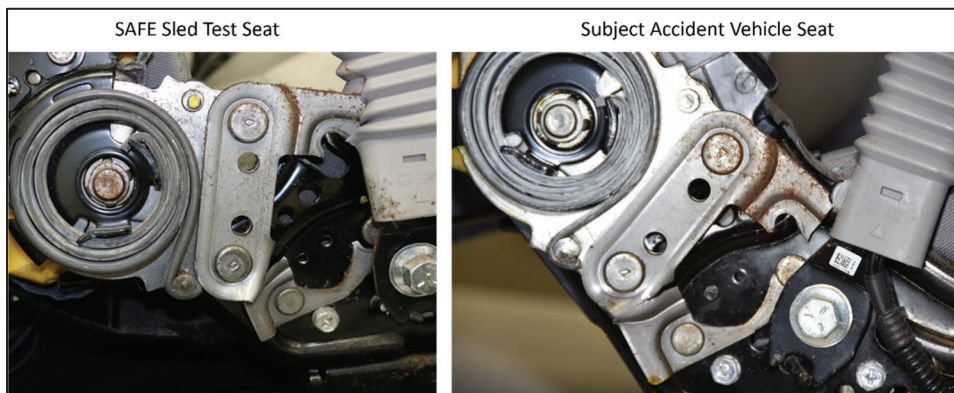


Figure 6: Sled test and accident vehicle seat comparison of inboard lower recliner attachment plates.

CASE 2 – RECLINER RELEASE VIA ASYMMETRIC DEFORMATION BELOW RECLINER ASSEMBLY DEMONSTRATION

The second case occurred when a 2013 light pickup truck was stopped behind a pickup truck at a controlled intersection. The subject pickup truck was rear ended by an SUV and pushed into the pickup truck stopped in front of it.

An inspection of the subject rear-ended vehicle post-crash revealed the occupied right front passenger's seat was reclined to a point such that it was in contact with the second row bench seat. The seat was removed and detrimmed for further analysis and comparison to an exemplar seat. The following was identified during the analysis:

- The seat base and lower recliner attachment plate were deformed on the outboard side (see Figure 7), whereas the inboard side was relatively undeformed.
- The inboard recliner was found in a further rearward recliner adjustment than the outboard recliner (see Figure 8).

- The forward portion of the “banana slot” for the recliner release rod pin was visible on the inboard side, but not the outboard side (see Figure 9).

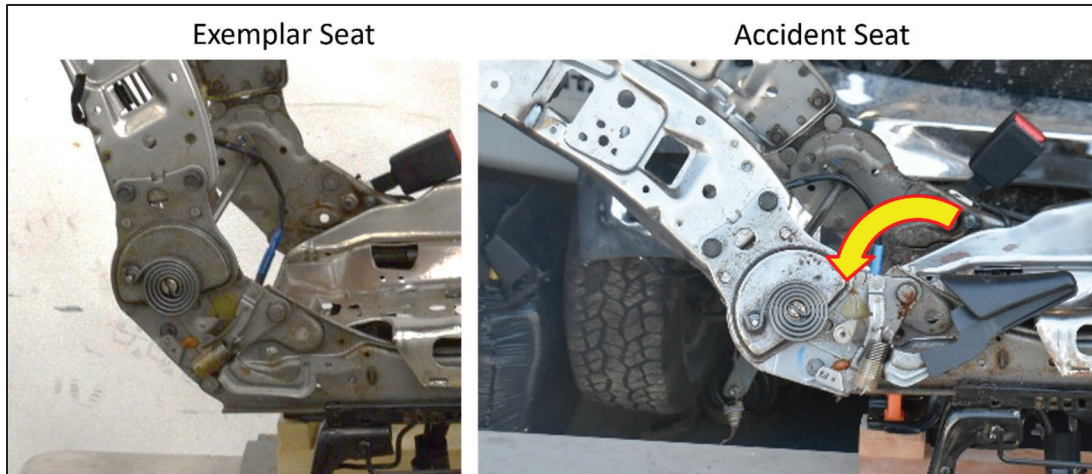


Figure 7: Deformation below outboard recliner.

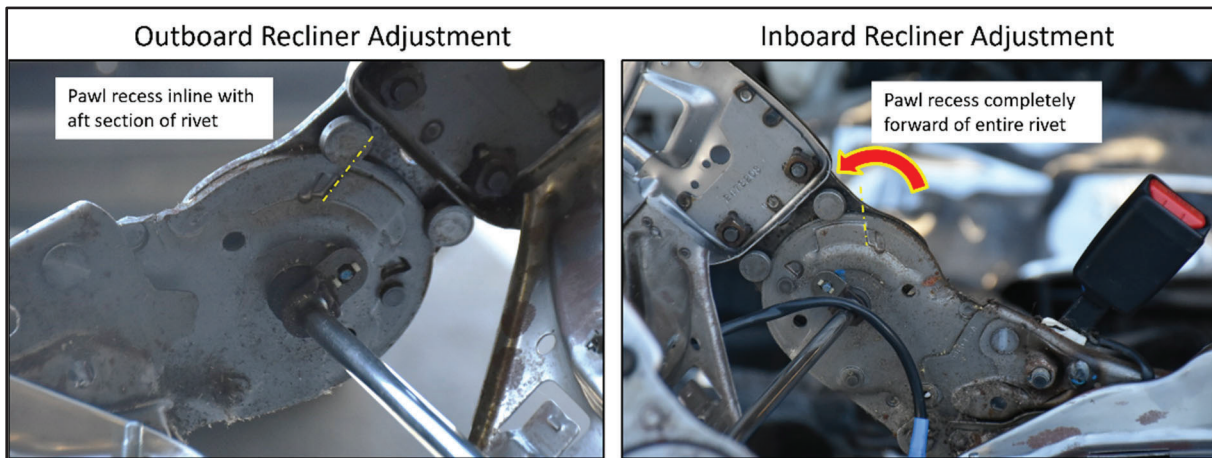


Figure 8: Inboard recliner adjusted further rearward than outboard recliner.

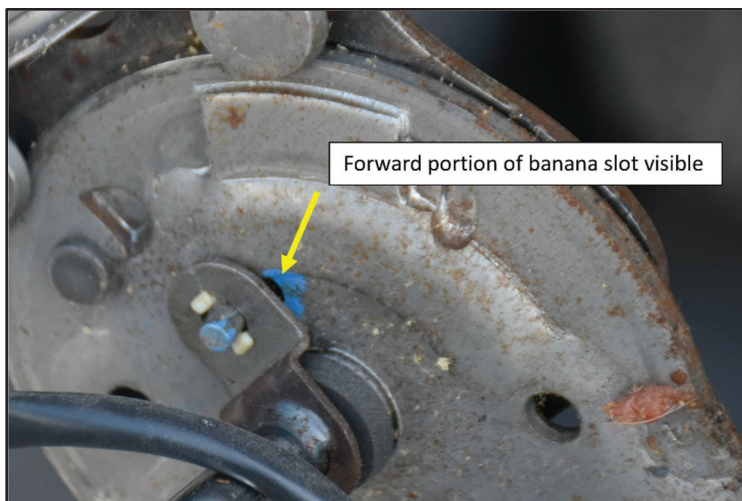


Figure 9: Forward portion of “banana slot” visible.

Inspection and analysis of an exemplar seat showed that during normal operation, pulling up on the recliner adjustment lever (located on the outboard side of the seat) moves the outboard recliner release pin rearward, while rotating the recliner release tube which also moves the inboard recliner release pin rearward, allowing both recliners to then be in the released position and the seatback recline angle to be adjusted. Comparing this to the condition of the accident seat reveals the accident seat inboard recliner was found in the released position while the outboard recliner was engaged. This condition is the result of the outboard seat base and recliner plate deforming below the recliner, causing recliner rod rotation, while the inboard side stayed relatively undeformed.

A demonstrative video was filmed to demonstrate this release mechanism. An exemplar seat was obtained and detrimmed. The recliners were disassembled and modified in order to view the internal pawls in relationship to the sector gears during the demonstration. The recliners were reattached to the seat, however, the lower front attachment was omitted, allowing the seat to experience a “deforming condition” for the demonstration. The “deforming condition” allowed for the outboard recliner to rotate rearward in relation to the inboard recliner, similar to the condition allowed by the outboard lower recliner support structure deformation seen in the accident seat. The top of the seatback was then loaded rearward and the inboard side recliner was seen to release by the rotating connecting rod (see Figure 10).

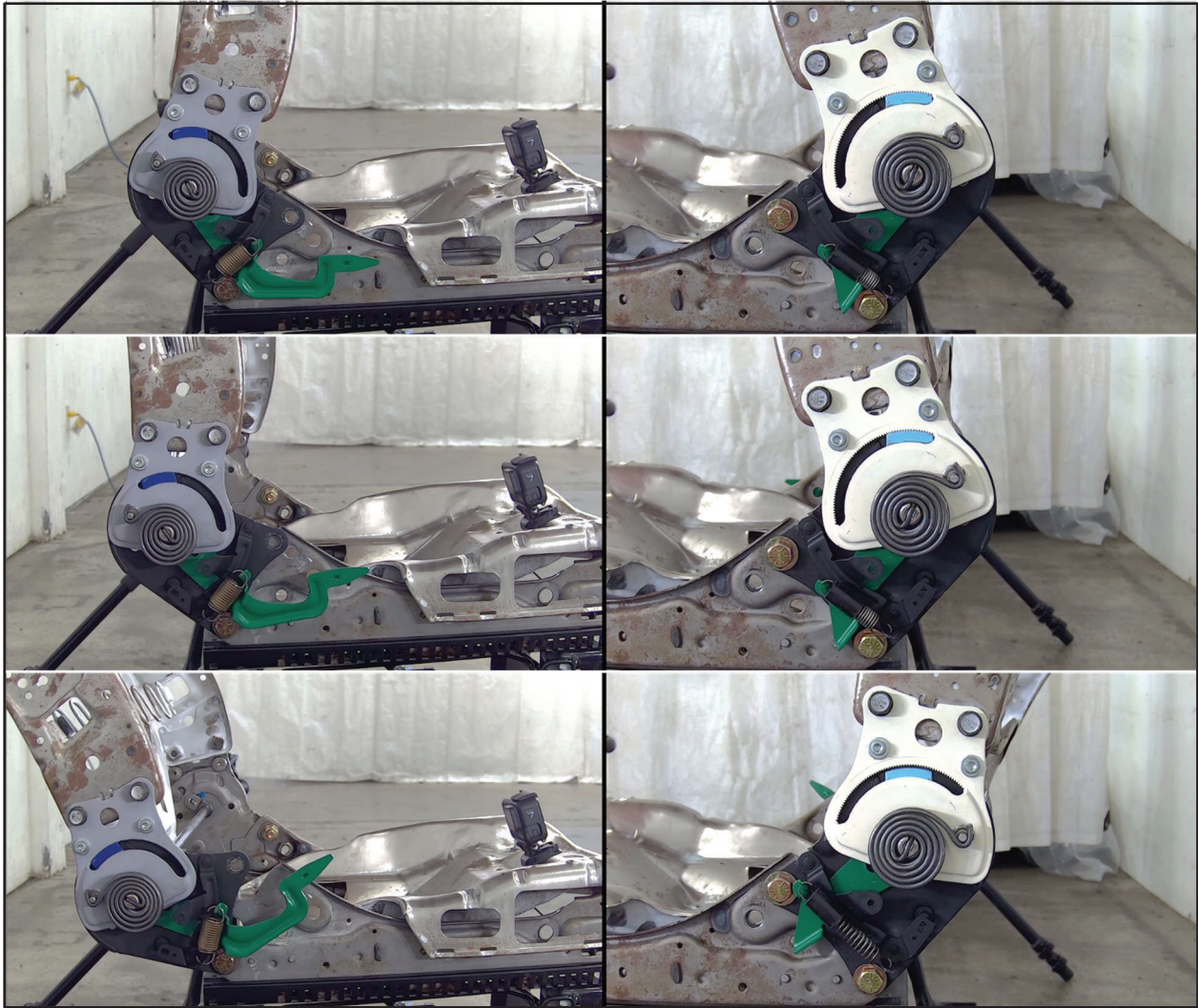


Figure 10: Video demonstration of recliner release via connecting rod.

Analysis of the video demonstration shows that as the outboard side recliner itself rotates rearward, the recliner rotates the recliner connecting rod rearward along with it. As the recliner connecting rod rotates rearward, the inboard cam begins to rotate, and the inboard recliner releases (see Figure 11). At the end of the demonstration, the inboard recliner is found in a further rearward recline adjustment position than the outboard recliner, the front of the “banana slot” on the inboard side is visible, and the inboard recliner remains disengaged, even after load is removed, all consistent with the evidence found on the subject rear impacted vehicle.

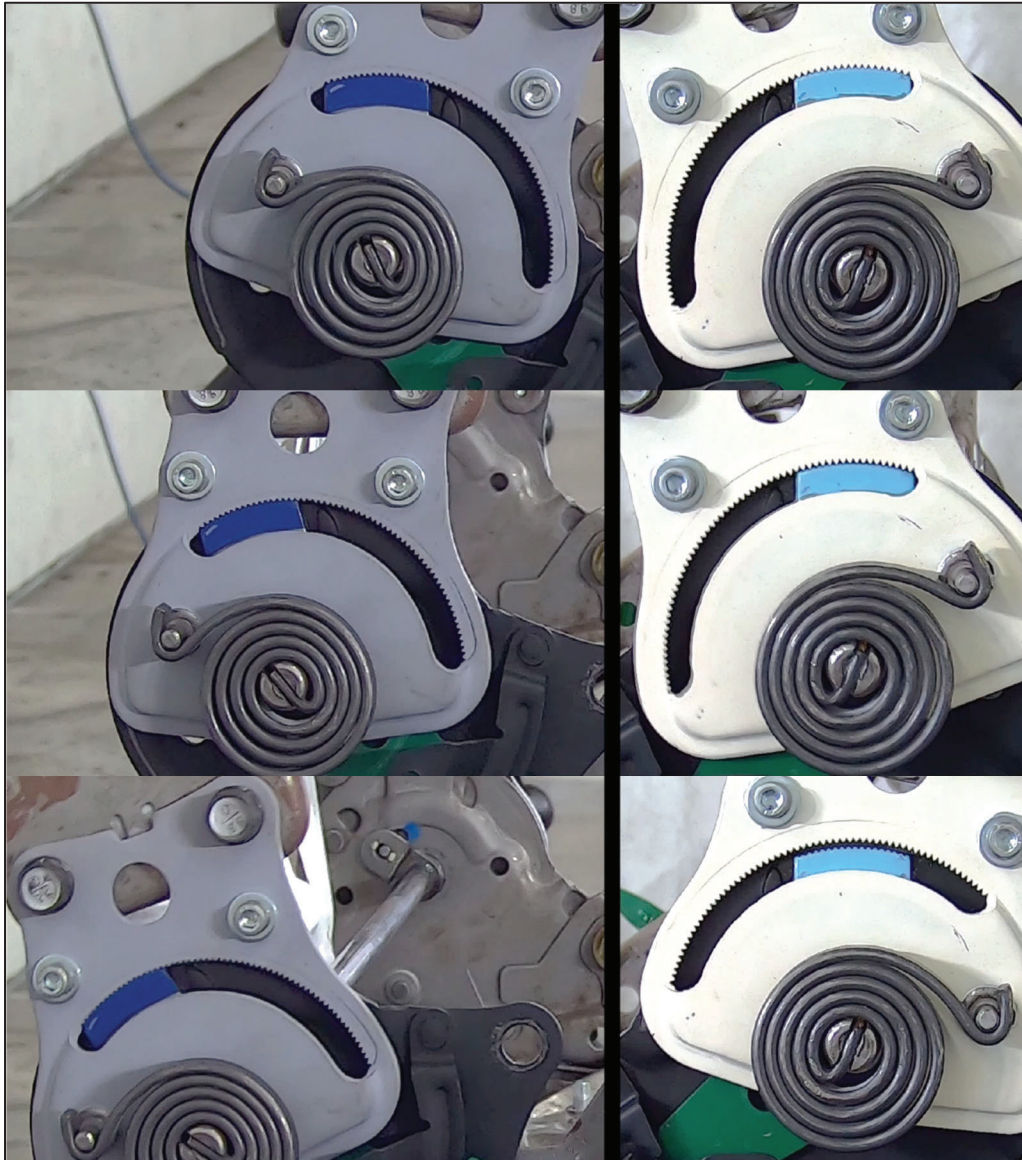


Figure 11: Video demonstration zoomed in.

CASE 3 – RECLINER RELEASE VIA OCCUPANT INTERACTION WITH CONNECTING ROD

The third case occurred when a 2012 passenger vehicle was slowing for stopped traffic when it was rear ended by a sedan. The impact pushed the subject passenger vehicle into another sedan slowed / stopped in front of it and came to rest against a guard rail. As a result of the accident, the child sitting in the left rear seat sustained serious anterior head injury.

A post-crash analysis of the plastic deformation of the driver’s seat revealed very little static deformation when compared to an exemplar seat (see Figure 12). There was no gross asymmetrical tearing or deformation below the

recliners as seen above in case 1 and case 2 however the recliner connecting rod was noted to be bent rearward (see Figure 13). This minimal deformation was inconsistent with the relatively high energy rear end collision as determined by the rear delta-V and occupant weight.

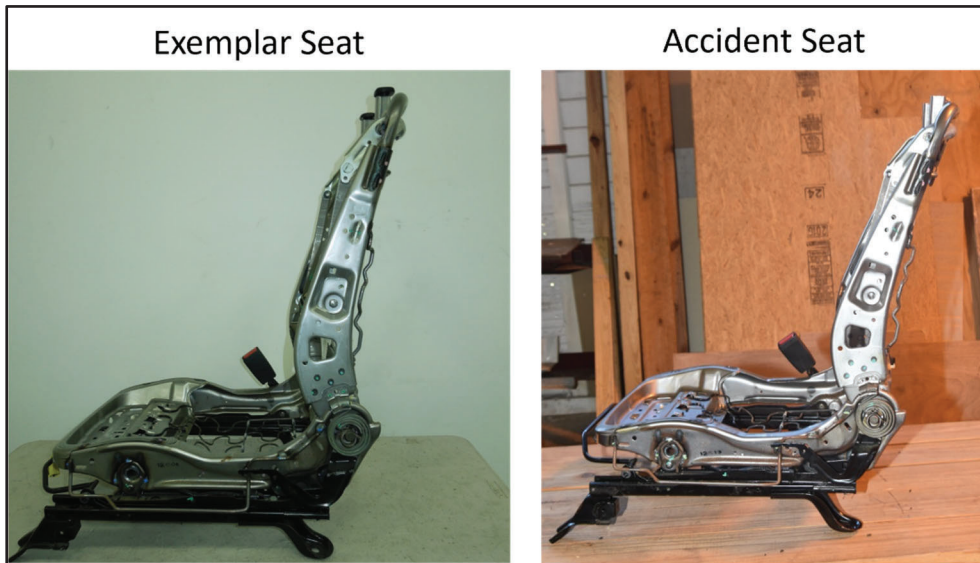


Figure 12: Comparison of exemplar seat and accident seat – minimal deformation.

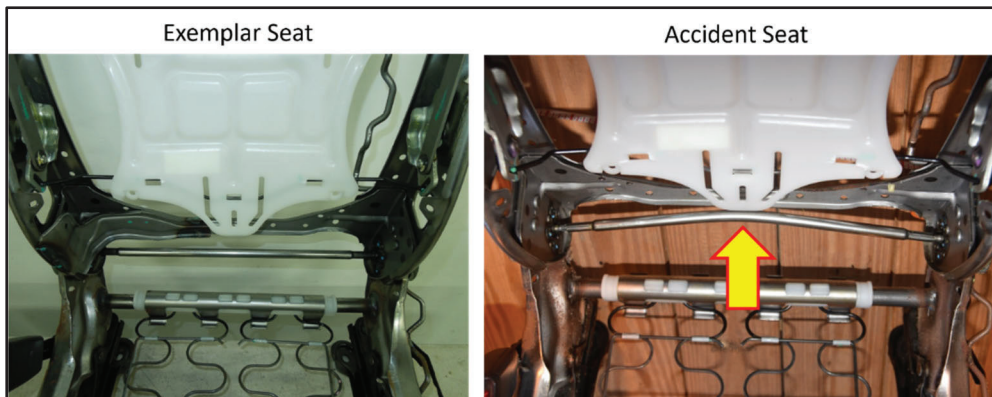


Figure 13: Comparison of exemplar seat and accident seat – recliner connecting rod deformation.

A Failure Mode and Effect Analysis (FMEA) concluded that the occupant's buttocks / lower torso had loaded the recliner connecting rod rearward and then downward, such that it could create a moment on the connecting rod and rotate it sufficiently far to release the recliners during the early phase of the rearward occupant loading the seat (see Figure 14).

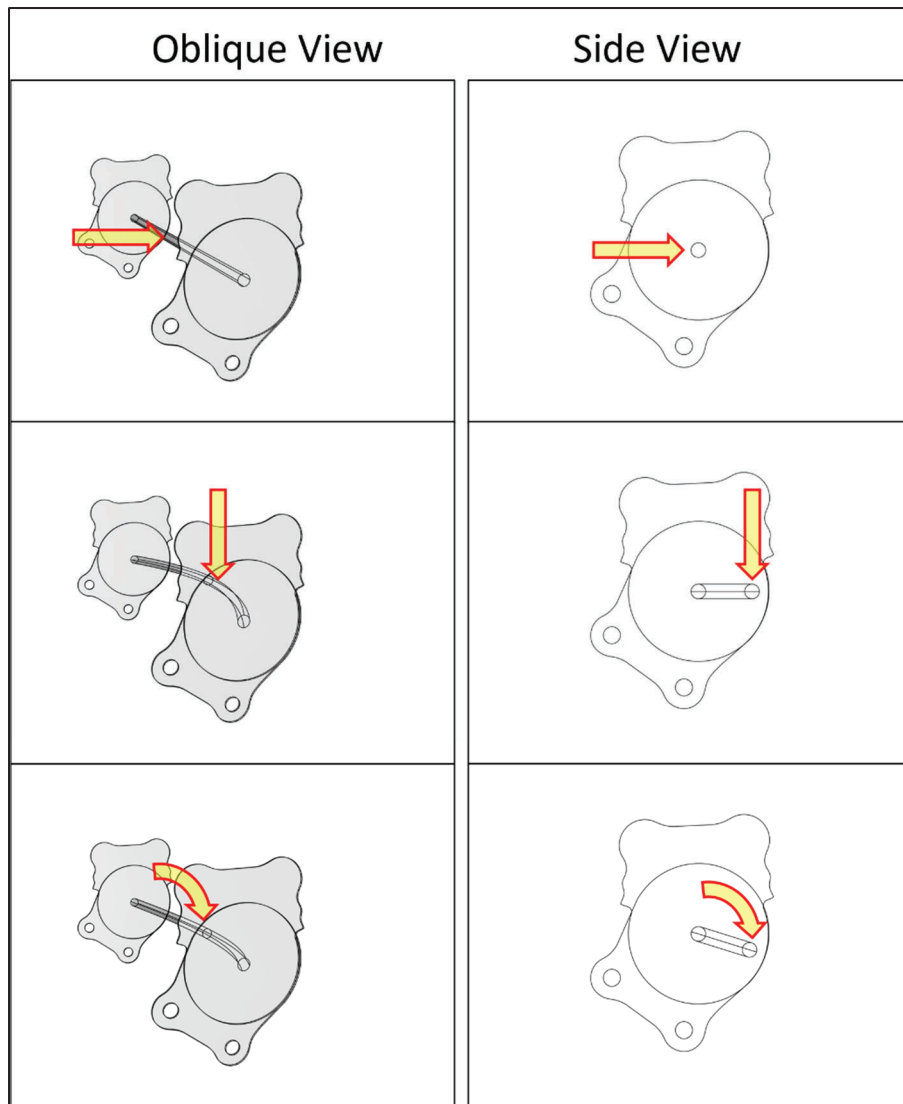


Figure 14: Recliner release mechanism from occupant loading of recliner connecting rod.

Two sled tests were conducted in order to evaluate seat deformation under occupant loading in two different scenarios. An exemplar test buck substantially similar to the subject rear-ended vehicle was obtained and mounted to a sled fixture. A forward-facing child seat was placed in the left rear seat with spacers between the child seat and left rear seat to model the intrusion resulting from the rear end collision. A 3-year-old Hybrid III ATD was placed in the child seat and belted. Sled test #1 was conducted with an OEM seat and a modified 50th percentile Hybrid III ATD to match the seated height and weight of the driver of the subject rear-ended vehicle. The test buck was subjected to a delta-V consistent with the accident reconstruction. Sled test #2 was conducted with the same Hybrid III ATD configuration, however the seat was modified to model the recliner connecting rod releasing the recliners during the rear impact.

In sled test #1, the driver's seat recliners both remained engaged and transferred load into the seat structure such that the seat structure yielded rearward as the occupant loaded the seatback and moved towards the 3-year-old ATD. The seat contained the driver ATD and injurious head contact to the 3-year-old was avoided (see Figure 15). The seat statically deformed rearward in recline approximately 19 to 20 degrees (approximately 15 degrees more than the subject seat) (see Figure 16).



Figure 15: Sled test #1 occupant kinematics – no head-to-head contact.

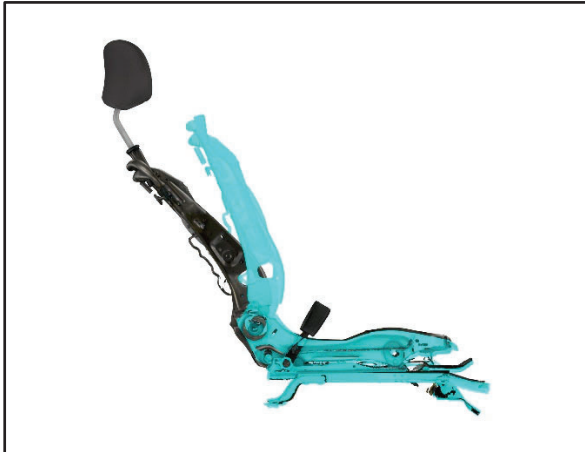


Figure 16: Sled test #1 seat deformation.

In sled test #2, the seatback was seen to rotate rearward in recline without transferring occupant load into the seat structure to provide crash energy absorption, occupant ride down, and occupant restraint. The driver ATD was seen to move rearward relative to the occupant compartment and made heavy head to head contact with the anterior of the 3-year-old ATD head seated in the child seat (see Figure 17). Posttest analysis showed the seat in test #2 was minimally deformed (similar to and consistent with the evidence seen in the subject seat) due to the recliners being disengaged throughout the entire occupant loading phase (see Figure 18).



Figure 17: Sled test #2 occupant kinematics – heavy head to head contact.



Figure 18: Sled test #2 seat deformation – minimal deformation.

CONCLUSIONS

One design challenge of creating modern manually adjustable dual recliner automotive seats is to actuate both recliners in unison in order to be able to adjust the seatback angle for a variety of users. The use of pawl and sector type recliners with an intermediate recliner connecting rod has been seen to result in unintended recliner release during rear impacts. Causes of this unintended release include asymmetric structural deformation below the recliners and occupant interaction with the recliner connecting rod. During the course of post-crash investigation, signs of a single recliner release include asymmetric deformation or structural failure below the recliners and differing recliner adjustment positions between the inboard and outboard recliners. Indicators of dual recliner release include a bent recliner connecting rod and less than expected static seat deformation. Incorporation of rotary continually engaged recliner designs, rather than the sector pawl designs, or use of boden type cables for recliner pairing rather than the torsion recliner connector rods are effective countermeasures to eliminate these risks of unintended or inadvertent recliner release in rear impact collisions.

REFERENCES

- [1] Saczalski, K., Syson, S., Hille, R., and Pozzi, M., "Field Accident Evaluations and Experimental Study of Seat Back Performance Relative to Rear-Impact Occupant Protection," SAE Technical Paper 930346, 1993, <https://doi.org/10.4271/930346>.
- [2] TES Limited. "Accidents Involving Seat Back Failures." Report No. C1322/2. Prepared for Transport Canada. December 1989.
- [3] Kale, HN, Dhamejani, CL. "Design Parameters of Driver Seat in an Automobile." *International Journal of Research in Engineering and Technology*.
- [4] Nag et al. (2008), *Twin Recliner for Automotive Seats*, US 2008/0093907 A1, U.S. Patent and Trademark Office.
- [5] Saczalski, KJ, Burton, JL, Lewis, PR, Jr., Saczalski, TK, & Baray, PE. "Evaluation of Rear Impact Seat System Performance Using a Combined Load Neck Injury Criteria and Hybrid III Surrogates." *Proceedings of the ASME 2001 International Mechanical Engineering Congress and Exposition. Crashworthiness, Occupant Protection and Biomechanics in Transportation Systems*. New York, New York, USA. November 11–16, 2001. pp. 65-102. ASME. <https://doi.org/10.1115/IMECE2001/AMD-25444>
- [6] Herbst, Brian & Meyer, Steven & Oliver, Arin & Forrest, Stephen. (2009). REAR IMPACT TEST METHODOLOGIES: QUASISTATIC AND DYNAMIC.

POTENTIAL INJURY CRITERIA FOR COLLISIONS WITH HEAVY GOODS VEHICLES

Jason Forman¹, Martin Östling², Krystoffer Mroz², Nils Lubbe²

1 University of Virginia Center for Applied Biomechanics

2 Autoliv Research Sweden

Paper Number 23-0334

ABSTRACT

Background:

Collisions with heavy goods vehicles (HGVs, large trucks) comprise approximately 21% of fatalities in two-vehicle collisions in the United States, and 14-15% of car occupant fatalities in Europe. While the immediate need in these collisions lies in compatibility and the structural integrity of the smaller vehicle, once these are addressed it will be up to the restraint system to manage protection of the occupants at collision severities that are greater than are commonly evaluated now. For restraint evaluation in high-severity collisions where survivability is the focus, different injury criteria targets may be warranted, focused on balancing injury risk across the body regions to fully utilize the load-bearing capability across the body. In this study we seek to identify potential injury criteria target values (and knowledge gaps) for predicting injury risk across the body in evaluations of high-severity collisions.

Methods and Data Sources:

This study consisted of a literature review, combined with a field data analysis to contextualize the types and distributions of injuries that occur among collisions of various severity. Data from NASS-CDS (years 2010-2015) and CISS (years 2017-2019) were examined to observe the relative distribution of injury severities by injury type, focusing on belted occupants in frontal collisions. Contemporary injury risk functions were then reviewed (using exemplar high-severity collision simulations) to observe the relative injury risks predicted across the body in collision severities representative of car-to-HGV collisions. Injury risks were further evaluated in high-severity collision simulations with an improved restraint system designed to manage occupant energy in such scenarios, demonstrating that injury risk can be reduced by adapting the restraint system to the severity of the crash.

Results and Discussion:

Across collision severities, injury risks were relatively balanced among the body regions. Most AIS2+ and AIS3+ injury cases occurred in relatively low-severity collisions, due to the very high exposure to low-severity collisions. AIS4+ injury cases occurred with similar total counts in low-severity and high-severity collisions, affected by the balance of exposure and per-crash risk. In high-severity collisions, the most common injury types were to the ankle, tibia & fibula, brain, thorax, and lumbar spine, all occurring with similar frequency. In simulations with the THOR-50M finite element model in high-severity impact scenarios, the injury risk predicted across the body regions exhibits similar balance to that observed in the field data, except for the risks predicted in the chest and the hip. Upon examination of the risks observed in the field data, as well as those observed in high-severity impact simulations with different restraint systems, injury assessment reference values were developed targeting a risk of 40%, representing a target that is feasible to achieve and which has a high likelihood of providing a tangible benefit to the field.

Conclusions:

Injuries occur as a result of both exposure and per-incident risk. Injury reduction likely requires safety systems that can adapt to the crash severity, providing more compliant restraint in low-severity collisions (where the exposure is very high), and stiffer restraint designed to eliminate strike-through in higher severity collisions (where the per-crash risk is high). Such adaptive-restraint design requires injury risk targets designed for the specific collision severities targeted for evaluation – including more conservative targets for low-severity evaluations, and higher practical targets for high-severity evaluations (focusing on survivability). This study has identified potential means for defining injury criteria values specifically for evaluations in high-severity collision scenarios, targeting a balance among the body regions informed by recent field data.

INTRODUCTION

Car-to-heavy goods vehicle (C2HGV) collisions comprise approximately 14-15% of the car occupant fatalities in Europe [1-3], and 21% of the car occupant fatalities in the U.S. in two-vehicle crashes [4]. Until now, most efforts to address crashworthiness considerations for C2HGV collisions have focused on geometric compatibility and the structural integrity of the passenger vehicle. Prior to the push for improved compatibility, many of the C2HGV collisions in the U.S. were prone to underride of the passenger vehicle, resulting in loading of the occupant compartment with limited engagement of the elements designed for structural crashworthiness [5-9]. Even once geometric compatibility concerns are addressed, however, there remain challenges in mass compatibility and the structural integrity of the passenger vehicle. Heavy goods vehicles (e.g., loaded tractor trailers) tend to be roughly 10 times the mass of typical passenger vehicles. As a result of the difference in momentum of the collision partner, collisions with heavy goods vehicles can result in very high ΔV s in smaller vehicle, meeting or exceeding the smaller vehicle's initial over-the-ground speed (often at highway speeds, and often with limited overlap [10]). Collisions of such severity can exceed those typically assessed in standardized regulatory or consumer information crash test modes, and can challenge the structural integrity of the smaller vehicle. The first countermeasure for such collisions will lie in improving geometric compatibility and the passenger vehicle structure to preserve occupant compartment integrity in such collisions. Once occupant compartment integrity is ensured, however, the next challenge will lie in providing adequate occupant restraint in the face of very high severity ΔV pulses [10-11]. This may be aided by energy-absorbing countermeasures integrated into the heavy-goods vehicle, designed to stretch out the collision pulse and decrease the acceleration magnitude imparted to the smaller vehicle [12]. The final step in the protection chain will rely on restraint systems tuned to manage the occupant's energy and momentum when faced with a large change in velocity.

This study contemplates future needs for addressing occupant restraint in high severity collisions associated with either C2HGV crashes or high speed C2C crashes, after compatibility and structural integrity are addressed. In particular, future efforts to evaluate restraint performance in high severity collisions will require targets for Injury Assessment Reference Values for injury criteria tailored to feasible target values that represent an improvement relative to the current state of the field, while still presenting a target that is feasible to achieve with conceivable restraint systems. To develop such safety systems, we need target injury criteria that capture measures pertinent to injuries that occur in the field, while also presenting targets that may feasibly be addressed through refinement of restraint-based occupant protection systems.

The goal of this study was to identify potential field-relevant injury criteria (and associated target thresholds) that may aid in reducing injury risk in high-severity collisions. To identify the injury types to target, we examine field data for frontal impact collisions with belted occupants across multiple collision severity ranges. These data also will serve to identify relative rates of injury among the various body regions, providing insight into whether the risk for certain body regions is higher than others. Similarly, by comparing across multiple collision severity ranges we can observe the progression of risk, elucidating whether certain injury types become disproportionately more common in higher severity collisions compared to the relative distribution of injuries in low-to-moderate severity collisions. Such an analysis also provides context for the relative frequency of injury across ΔV ranges, including the combined effects of exposure and per-crash injury risk. Finally, results from an exemplar set of simulations with the THOR-M50 model were examined to observe injury risks calculated from injury criteria that have been proposed for that anthropomorphic test device (ATD) compared to the risks indicated by the field data. By combining the field data observations with the injury risks calculated from the exemplar simulations, we discuss potential options for injury criteria and target threshold values that capture the balance of injury risks observed across the various body regions in the field, while providing targets that would represent improvements to the current state of risk in the field.

METHODS & RESULTS

The National Automotive Sampling System Crashworthiness Data System (NASS-CDSS) and the U.S. Crash Investigation Sampling System (CISS) were both queried to observe the relative distributions of injuries for belted occupants of passenger vehicles (sedan, MPV, SUV, light truck, etc.) in frontal collisions across three categories of collision severity: 0-34 km/h ΔV , 35-59 km/h ΔV , and 60+ km/h ΔV . Data were queried from NASS-CDS collection years 2010-2015 and CISS collection years 2017-2019, each with vehicles ≤ 10 years old at the time of the collision. Frontal impact collisions were examined, defined based on a PDOF from 300°-60° with a General Area of Damage (GAD) code of F (Front) or L/R if the horizontal location was coded as Front. Belted occupants age 13+ were

examined. Rollovers, fires, and ejections were excluded. Injuries were examined by body region and by AIS level, using the most recent version of AIS available for each case collection year. The body region categories are for the most part self explanatory. To clarify for those injury types there may be some ambiguity – hip injuries included injuries to the proximal femur (femoral neck and above) as well as the acetabulum; femur injuries included fractures to the middle and distal femur not counted in the hip injury category (to avoid double-counting); pelvis injuries included all pelvis injuries except for acetabulum injuries; and ankle injuries included injuries to the distal tibia and fibula (which were excluded from the tibia/fibula category to avoid double-counting), injuries to the talus, injuries to the calcaneus, and ankle ligament injuries of the target severity category.

The distributions of injury types for the three ΔV categories are shown in Figure 1 (unweighted results) and Figure 2 (weighted results) below. Note that in the weighted analysis one case from the middle ΔV category (35-59 km/h) was removed because it had a very high weight (over 4,000) and had fractures in each of the spine regions, which caused spine fractures to appear to comprise a larger portion of the injury distribution in that ΔV range than they likely do. All other observations were relatively consistent between the unweighted and weighted distributions.

In the lowest ΔV range (0-34 km/h), the vast majority (over 85%, weighted) of injury cases only had a maximum AIS severity (MAIS) of 2. Approximately 10% of injury cases (weighted) were MAIS 3. Less than 3% of injury cases in that category were MAIS 4+. For the MAIS 2 cases in that ΔV range, brain injuries were the most common injury type among the injury types studied. This was followed by thoracic organ injury, lumbar spine injury, tibia/fibula and ankle injury, and abdomen injury. The most common MAIS 3 injuries were rib fractures. For the mid ΔV range (35-59 km/h), the most common AIS2 injuries were to the tibia/fibula and ankle, lumbar spine, brain, and thoracic organs. The most common AIS 3 injuries were rib fractures and femur fractures. For the higher ΔV range (60+ km/h), the most common AIS2 injuries were similar to those of the 35-59 km/h range (i.e., tibia/fibula and ankle, lumbar spine, brain, and thoracic organs). The most common AIS 3 injuries were thoracic organ injuries, rib fractures, and femur fractures. The most common AIS4+ injuries were brain and abdomen injuries. Considering relative frequencies - across all ΔV ranges - femur fractures occurred with greater frequency than hip or pelvis injuries. In the 60+ km/h ΔV range, there is a relatively even balance in injury frequency between rib fractures, femur fractures, and brain injury.

Figures 1 and 2 also show the total number of collision exposures in the dataset for each ΔV range. When survey weights are applied (Figure 2), approximately 3.7 million people were exposed to collisions in the 0-34 km/h ΔV range, 274 thousand people were exposed to collisions in the 35-59 km/h ΔV range, and 23 thousand people were exposed to collisions in the 60+ km/h ΔV range. Table 1 shows the per-crash injury risk for each AIS level for each ΔV range. For crashes in the 0-34 km/h ΔV range, there is a 3.7% chance that any individual crash will result in AIS2+ injury. For crashes in the 60+ km/h ΔV range, there is a 46% chance that any individual crash will result in AIS2+ injury. The risks decrease for each elevated AIS level. The per-crash risk for AIS3+ injury is 0.46% for the 0-34 km/h ΔV range, and 27% for the 60+ km/h ΔV range. The risk is decreased to 0.09% and 13.7%, respectively, for AIS4+ injury.

Table 1: Injury risk calculated from the field data (count of injury cases divided by count of exposures) for each ΔV range, by AIS severity level (weighted)

Per-Crash Risk (weighted)			
	0-34 km/h	35-59 km/h	60+ km/h
AIS2+	3.72%	16.0%	46.3%
AIS3+	0.46%	5.07%	26.9%
AIS4+	0.09%	0.41%	13.7%

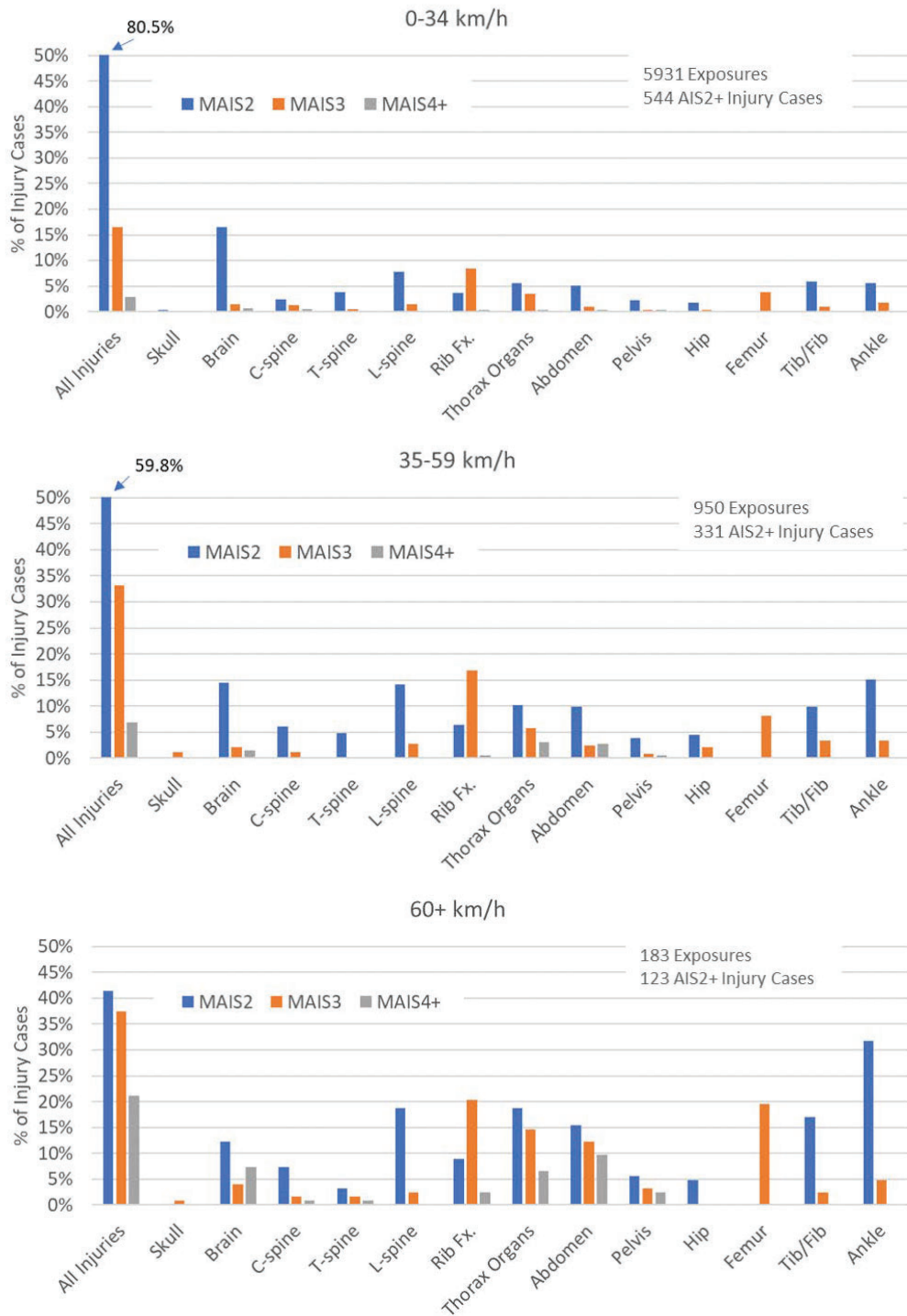


Figure 1: Unweighted distribution of injured body regions by ΔV range and AIS severity level (belted occupants in frontal collisions, in vehicles less than 10 years old at the time of the collision; NASS-CDS 2010-2015 and CISS 2017-2019). [Note: The injury types shown here were selected based on injury types that may conceivably be predicted using ATD-based measures. There are some other injury types that occurred with considerable frequency but are not shown here (e.g., sternum fractures). Those contribute to the “All Injuries” count, but are not shown in the individual body regions.]

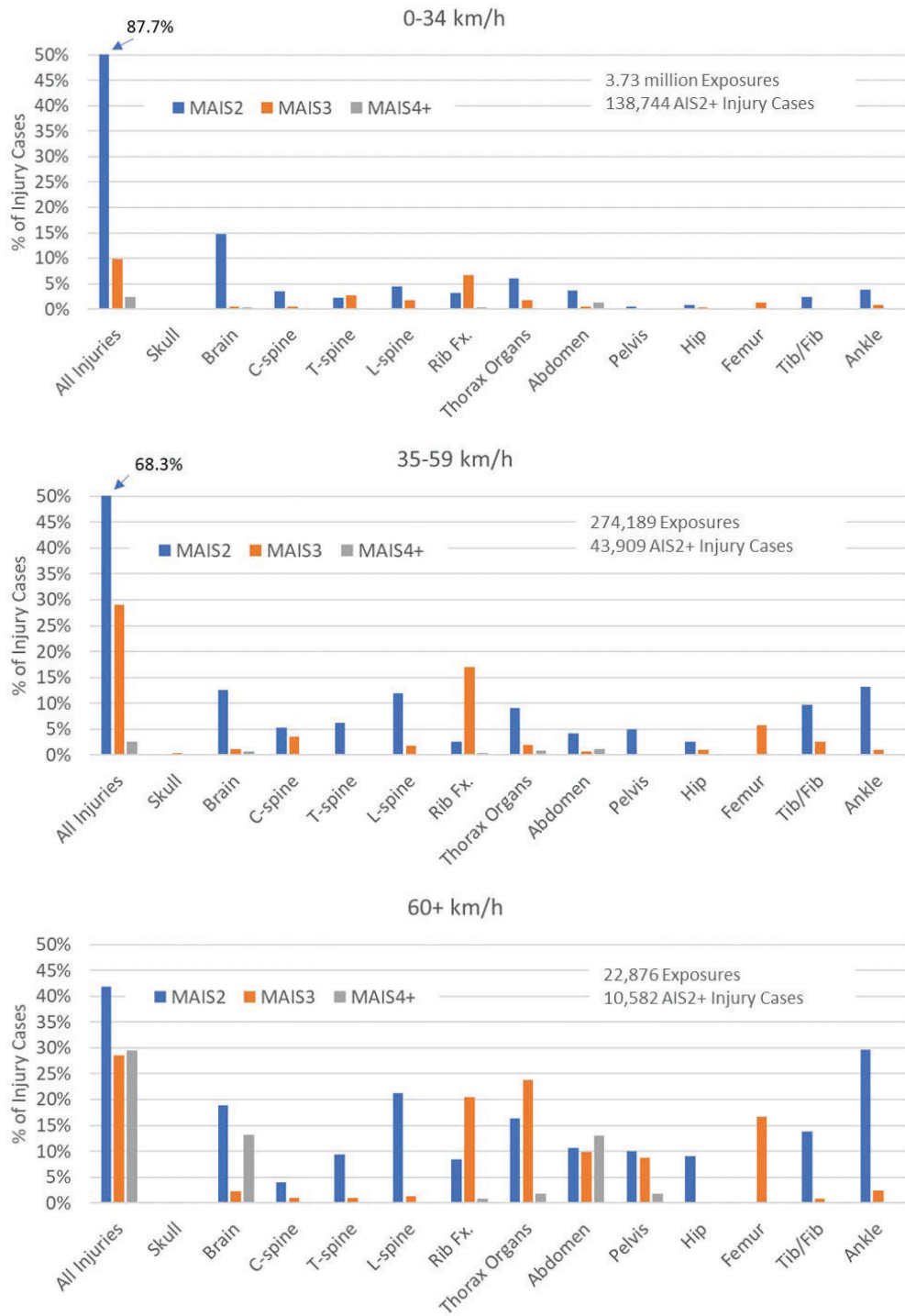


Figure 2: Weighted distribution of injured body regions by ΔV range and AIS severity level (belted occupants in frontal collisions, in vehicles less than 10 years old at the time of the collision; NASS-CDS 2010-2015 and CISS 2017-2019). [Note: The injury types shown here were selected based on injury types that may conceivably be predicted using ATD-based measures. There are some other injury types that occurred with considerable frequency but are not shown here (e.g., sternum fractures). Those contribute to the “All Injuries” count, but are not shown in the individual body regions.]

Table 2 shows the distribution of injuries by ΔV , capturing the combined effects of exposure and per-crash risk. Applying the survey weights, 72% of cases of AIS2+ injury occur with ΔV 's in the 0-34 km/h range, presumably due to the very high exposure of crashes in that range. The proportion of injury cases in the 60+ km/h ΔV range increases to 17% and 41% for AIS3+ and AIS4+ injury, respectively. Unweighted distributions are also presented for context, naturally showing a decrease in the proportion comprised by low-severity crashes (due to the intentional under-sampling of low-severity crashes in NASS-CDS and CISS, which is then corrected for by applying the survey weights).

Table 2: Distribution of injury cases by ΔV range.

Weighted				
% of injury cases that each ΔV category comprises				
	0-34 km/h	35-59 km/h	60+ km/h	N†
AIS2+	72%	23%	5%	197,609
AIS3+	46%	37%	17%	37,161
AIS4+	44%	15%	41%	7,600
N*	138,755	48,281	10,582	--
Age**	48.9	52.3	41.2	
Unweighted				
% of injury cases that each ΔV category comprises				
	0-34 km/h	35-59 km/h	60+ km/h	N†
AIS2+	55%	33%	12%	998
AIS3+	34%	43%	23%	311
AIS4+	25%	35%	40%	65
N*	544	331	123	--
Age**	49.6	45.3	39.8	

* Number of AIS2+ injury cases within each ΔV range.

** Average age (in years) of AIS2+ injured occupants within each ΔV range.

† Total number of injury cases of each AIS level, summing across the ΔV ranges.

To compare to the injury frequency distributions noted above, injury risks were calculated for a series of exemplar simulations described in a parallel study by Östling et al. [11]. That study simulated collisions representing car-to-heavy goods vehicle crashes (C2HGV) with two different pulses (a long-duration pulse of approximately 40 g plateau, and a short-duration pulse of approximately 85 g plateau [10-11]) with a contemporary restraint system, and with a restraint system improved to reduce injury criteria values in such a collision (details described in [11]). That study also simulated a 56 km/h full frontal rigid barrier crash (FFRB) for comparison. Those simulations were performed with the THOR-50M v1.9 Euro NCAP occupant model distributed by Humanetics Inc., and injury risks were calculated using the injury risk functions (IRFs) described by Craig et al. [13] (Table 3). For the chest, injury risk was calculated using the IRFs developed for prediction of 3+ rib fractures and 6+ rib fractures described by Craig et al. [13] (2020). For the hip injury risk predicted from the force measured by the acetabulum load cells, the risk was calculated for both a 15° hip flexion angle and a 0° hip flexion angle using the functions described by Craig et al. [13]. For all other body regions, injury risk was calculated using the final IRFs ultimately recommended by Craig et al. [13].

As can be seen in Table 3, from these simulations the THOR measurements and the IRFs of Craig et al. [13] resulted in relatively balanced injury risks predicted for the brain, femur, abdomen, and tibia. The chest injury risk predicted with the IRF designed for 3+ rib fractures tended to result in a predicted risk that was disproportionately higher than the other body regions. The chest injury risk predicted with the IRF designed for 6+ rib fractures tended to result in a predicted risk that was more balanced with the other body regions.

Table 3: ATD measures and associated risk predictions from exemplar simulations with the THOR-50M*

Crash pulse	Unit	56 km/h FFRB		Car-to-HGV High Acc. Pulse – Contemporary Restraint System		Car-to-HGV High Acc. Pulse – Improved Restraint System	
		Value	Risk	Value	Risk	Value	Value
HIC15 (AIS3+)		365	2%	2162	62%	1382	38%
BrIC (AIS3+)		0.55	1%	1.15	74%	0.85	33%
Nij (AIS3+)		0.32	1%	1.42	84%	0.98	33%
Chest deflection (3+ fracture 40 years)	mm	40.4	29%	56.8	61%	56.4	60%
Chest deflection (6+ fractures 40 years)	mm	40.4	17%	56.8	41%	56.4	40%
Acetabulum resultant force (AIS2+), 15°	N	3851	71%	20813	100%	5667	99%
Acetabulum resultant force (AIS2+), 0°	N	3851	37%	20813	100%	5667	91%
Femur compression (AIS2+)	N	2683	0%	34697	100%	9742	39%
Upper Tibia axial force (AIS2+)	kN	1.6	1%	11.0	96%	3.3	5%
Lower Tibia axial force (AIS2+)	kN	1.8	5%	6.9	38%	3.4	10%
Tibia bending moment (AIS2+)	Nm	104	2%	1145	100%	234	22%
Revised Tibia index (AIS2+)		0.53	5%	5.68	100%	1.23	49%

* Risks calculated using the injury risk functions described by Craig et al. [13], from the simulation results described by [11].

Each of the predicted injury risks decreased in the C2HGV simulations with the improved restraint system (decreasing from roughly 60-100% risk with the contemporary restraint system to 40% or less across most body regions with the improved system). The one apparent outlier was the injury risk predicted using the force measured in the acetabulum load cell, which was substantially higher than the risk predicted for the other body regions (including the femur) for both the C2HGV simulations with the improved restraint system, and the reference simulations representing a lower-severity 56 km/h FFRB condition.

DISCUSSION

Balance of Risk and Implications in Injury Prediction

Optimal restraint design relies on a balance of injury risk throughout the body. To decelerate a person during a collision, we need to apply force to the body. Wherever we apply force to the body, there is a risk that force may result in injury. The key is to apply restraining force to the body in a distributed fashion designed to utilize the load-bearing capacity of every body region, while mitigating the risk that any particular body region will be over-loaded and injured. In an ideal case, the restraint system will be designed to load every body region up to the very threshold of its load bearing capability, but not over. To maximize the potential efficiency of a restraint system in this manner, we need to understand the balance of injury tolerance and injury risk throughout the body, and replicate that balance in our injury prediction tools.

The results above suggest that in most collisions, injury frequency is relatively balanced between brain injury, rib fracture injury, tibia/fibula fractures, and femur fractures. Ankle fractures also occur with considerable frequency in collisions above 35 km/h, though those injuries are challenging to monitor by dummy measures in standardized crash

tests [14]. Aside from ankle fractures, the balance of injury frequency across body regions is relatively consistent with the balance of risks observed in the injury predictions of Table 3. The chest injury risks predicted with the 3+ rib fracture function tended to predict risks somewhat higher than the other body regions, contrary to the relative rates observed in the field data. This was improved with the chest injury risks predicted with the 6+ rib fracture function, which resulted in risks more consistent with those observed in the other body regions [11].

The balance of injury risks predicted by the injury criteria of Table 3 also carry through across the other conditions studied, with each body region exhibiting a decrease in risk with the improved restraint system applied to the C2HGV collision, and in the lower severity 56 km/h reference simulations. In each of these cases (the improved restraint system, and the 56 km/h reference case) the injury risk decreases by similar amounts for the head, neck, chest, and femur injury measures. For the C2HGV simulations with the improved restraints, the risks across most of those body regions decrease from approximately 60-100% risk with the contemporary restraints, to approximately 40% risk with the improved restraints. The risk for chest injury remained elevated using the 3+ fracture definition, but as noted above was more consistently balanced with the other body regions using the 6+ fracture definition. For most body regions the risks are further reduced below approximately 20-30% in the reference 56 km/h reference simulations.

The one notable exception in terms of both balance and reduction in risk lies in the acetabulum injury measures. Using the acetabulum force IRF of Craig et al. [13], the predicted risk of hip & acetabulum injury is consistently higher than the other body regions in a manner that is not consistent with the relative frequency of injuries that occur in the field. For example, the predicted risk of hip & acetabulum injury from the THOR simulations is consistently higher than the risk predicted for femur injury (even with the improved restraints and lower collision ΔV). This is contrary to the field data, which show that femur fractures occur at a much higher frequency than hip & acetabulum injuries (Figure 1 and 2). While the risk of most injury types is substantially reduced with the improved restraints in the C2HGV condition, and in the reference 56 km/h condition, the risk predicted from the acetabulum load cells remain high even for the improved-restraint and lower speed conditions. These observations are contrary to the field data, which suggest that the injury risks for the various body regions should be relatively balanced, and the risk predicted for the hips should be less than the risk predicted for the femurs.

Injury Assessment Reference Values Based on Target Risk Thresholds

In the development of restraint systems to improve protection in high severity crashes, we need injury criteria targets to design towards. These targets need to strike a balance between being feasible to achieve, while still challenging enough to drive improvement. There are many different ways that such target thresholds can be identified, and the thresholds can be changed over time to continue to drive improvement as safety systems are refined. For example, target injury criteria may be identified by examining current risks exhibited in the field data, combined with risks predicted with contemporary restraint systems. As noted in Table 1, for the 60+ km/h ΔV range the risk of AIS2+ injury is approximately 46%. As noted in Table 3, the risk predicted in the C2HGV simulations with a contemporary restraint system ranged from approximately 60-100%. Aside from the acetabulum, these risks decreased with the improved restraint system, falling under 40% risk for most body regions (once the chest injury risk is predicted with the 6+ rib fracture function). Considering this, a target predicted risk of 40% may represent an achievable goal – if the risks predicted from the injury criteria are indicative of risk in the field, a goal of 40% would also present a target that would improve risk compared to the current state of the field. Note also that the improved restraint system described here would not immediately achieve the goal of <40% predicted risk – further refinement would be needed to drop the risk predicted for some body regions below that target. Once a target risk threshold is identified, this may be translated into target injury criteria values using the associated injury risk functions. An example of target injury criteria values based on a threshold of 40% risk is shown in Table 4. [Note that these targets would apply to a goal of <40% risk in any individual body region. Calculating aggregated risk across the whole body would require a combined probability approach similar to that used by U.S. NCAP, however these individual targets may serve as a reasonable first step for initial improvements.]

Table 4: Example THOR-50M Injury Assessment Reference Values for high severity crash evaluation, targeting a 40% risk threshold.*

Criteria	Unit	Risk	Value
HIC15 (AIS3+)		40%	1430
BrIC (AIS3+)		40%	0.89
Nij (AIS3+)	mm	40%	1.04
Chest deflection (3+ fracture 40 years)	mm	40%	46.5
Chest deflection (6+ fracture 40 years)	mm	40%	56.5
Acetabulum resultant force (AIS2+), 15° Femur flexion	N	40%	3180
Acetabulum resultant force (AIS2+), 0° Femur flexion	N	40%	3910
Femur compression force (AIS2+)	N	40%	9800
Upper Tibia axial force (AIS2+)	kN	40%	6.5
Lower Tibia axial force (AIS2+)	kN	40%	7.15
Tibia bending moment (AIS2+)	Nm	40%	290
Revised Tibia index (AIS2+)		40%	1.13

* Note: These simply represent the values that result from direct calculation via the IRFs of Craig et al. (2020) at the shown risk level. Additional investigation is needed to determine if these are actually achievable with the THOR-50M.

Low-to-Moderate Speed Collisions with High Exposure

While the highest individual per-crash risks were observed in the 60+ ΔV range, most injury cases actually occurred in the 0-34 km/h ΔV range due to the very high collision exposure in that range. As shown in Figure 2, there are an order of magnitude more collision exposures in the 0-34 km/h ΔV range compared to the 35-59 km/h ΔV range. There is a further order of magnitude decrease moving to the 60+ km/h ΔV range. As a result, even though the per-crash risk in the 0-34 km/h range is quite low, the very high exposure causes there to be more injury cases in that range compared to the other ranges. As a result, it may be pertinent to consider continuing improvements to drive down risk in that range even further, in addition to refinements implemented targeting cases with high per-crash risk. This may require safety systems with increased adaptation and sensing capabilities, including refined classification of the collision severity (potentially with classification of the closing speed between the two vehicles, and the size/class of the collision partner).

Risk threshold targets for the 0-34 km/h ΔV range may be developed using a process similar to that described above, for example targeting a very low risk (e.g., 3.5% or below) to drive improvements relative to the current state of risk in the field. This presents an additional challenge, however, in the precision of current IRFs in the low-risk range – due to the limited test data sample size available to fit traditional IRFs, the current IRFs likely exhibit limited precision when discerning the very fine gradations of risk at low risk levels. This may be at least partially addressed by adjusting the age range that we are targeting for risk prediction to older ages, who tend to exhibit greater risk for a given exposure (and for whom we have greater amounts of injury tolerance data from reference tests with post mortem human surrogates). Ultimately, however, increasing the precision of IRFs may require revisiting our approach to IRF development, potentially leveraging advanced means to augment the limited test data with simulations or with field data to increase the amount of information available to develop the IRFs (potentially combining data sources with advanced statistical techniques such as Bayesian analyses).

Further, evaluation in high-exposure, lower-speed collisions requires an occupant modelling tool that will be sensitive to changes in restraint design in a biofidelic manner in the target speed range. This sensitivity to restraint system changes can be affected by factors such as the body region coupling, dictated by the stiffness of the interconnecting components (e.g., the spine). For example, it is possible that an occupant model with an artificially stiff spine may appear reasonably biofidelic in high-severity loading, yet may over-state the coupling stiffness between the body regions when exercised in lower-severity impacts. This may in turn obscure the true effects of changes to the restraints - for example, misstating the effects of load sharing between the lap belt, shoulder belt, and airbag. Thus, any effort to develop an evaluation method in low-to-moderate speed collisions should include a critical evaluation of the target

occupant model (be it an ATD or human body model) to ensure that it will interact with the restraint systems in a biofidelic manner in that ΔV range.

CONCLUSIONS

Improving occupant restraint during high-severity frontal crashes may require injury criteria targets tailored for high severity collisions (striking a balance between feasibility and targets that are challenging enough to prompt an improvement relative to the current state of risk). In this study, we examined field data for belted occupants in frontal impacts to observe how injury patterns, severities, and risks change with collision severity. With these data we also examined the relative rates of injury across various body regions to provide a comparison for the relative rates of risk predicted in occupant simulations. In collisions with a ΔV at or above 60 km/h, the most common injuries were injuries to the ankle, tibia & fibula, femur, ribs, thoracic organs, brain, and lumbar spine, all of which occurred at relatively similar rates. This suggests that the injury risk for these injury types is relatively balanced in the field, with no individual injury type exhibiting a risk that was substantially greater than the others. This balance of injury risk was also observed in exemplar simulations of high severity crashes for all injury types except for hip injury (which tended to exhibit a much higher risk than the other injury types when predicted using the acetabulum injury risk function that has been proposed for the THOR-50M). The exemplar simulations and field data may also be used to identify a potential injury risk threshold that may serve as a target for high severity crash evaluations – for example, the simulations suggest that a target injury risk threshold of 40% may be feasible to achieve in the crash conditions studied using an improved restraint system, and would represent a substantial reduction in risk relative to that predicted with a contemporary restraint system. A target risk threshold of 40% would also likely represent an improvement relative to the contemporary risks observed in the field data for high severity crashes. Considering this, potential injury criteria values are presented targeting a risk threshold of 40% for each individual body region. Future work may include developing similar injury criteria targets tailored for use in low-speed crash evaluations (where collision exposure is very high), and translating to combined-probability criteria aggregating risk across body regions.

ACKNOWLEDGEMENTS

This study was supported by Autoliv Research. The opinions expressed here are solely those of the authors.

REFERENCES

- [1] European Commission. 2020. European Road Safety Observatory Facts and Figures Buses / coaches / heavy goods vehicles - 2020. Brussels, European Commission, Directorate General for Transport. https://road-safety.transport.ec.europa.eu/system/files/2021-07/facts_figures_buses_and_hgv_final_20210323.pdf. Accessed 24.10.2022.
- [2] Schindler R, Jansch M, Bálint A, Johannsen H. 2022. Exploring European Heavy Goods Vehicle Crashes Using a Three-Level Analysis of Crash Data. *Int J Environ Res Public Health*. 2022 Jan 7;19(2):663. doi: 10.3390/ijerph19020663. PMID: 35055484; PMCID: PMC8775486.
- [3] European Commission, Mobility and Transport. 2021. Road traffic Fatalities in the EU in 2019. https://road-safety.transport.ec.europa.eu/system/files/2021-11/DG%20MOVE%20ROAD%20SAFETY_INFOGRAPHICS_twitter.pdf. Accessed 24.10.2022.
- [4] National Center for Statistics and Analysis. 2022. Traffic safety facts 2020: A compilation of motor vehicle crash data (Report No. DOT HS 813 375). National Highway Traffic Safety Administration.
- [5] Adalian C, Russo JL, Cesari D and Desfontaines H. 1998. October. Improvement of car-to-truck compatibility in head-on collisions. In the Proceedings of the 16th International Technical Conference on the Enhanced safety of Vehicles (pp. 883-891).

- [6] Goudswaard AP, Nieboer JJ. and Janssen EG. 1991. Truck front underrun protection. TNO Road-Vehicles Research Institute, Netherlands. IRCOBI.
- [7] Krusper A, and Thomson R. 2008. Crash compatibility between heavy goods vehicles and passenger cars: structural interaction analysis and in-depth accident analysis. In International Conference on Heavy Vehicles.
- [8] Thomson R, Edwards M, Martin T, Van der Zweep C, Damm R and Valle GD. 2007. Car-car crash compatibility: development of crash test procedures in the VC-Compat project. International journal of crashworthiness, 12(2), pp.137-151.
- [9] Gabler HC and Hollowell WT. 2000. The crash compatibility of cars and light trucks. Journal of Crush Prevention and Injury Control, 2(1), pp.19-31.
- [10] Mroz K, Östling M, Lubbe N. 2023. Passenger cars in head-on crashes with heavy goods vehicles: for what severity should future car restraint systems be designed? The 27th International Technical Conference on the Enhanced Safety of Vehicles Conference (ESV), Yokohama, Japan 2023. Paper Number 23-0060.
- [11] Ostling M, Eriksson L, Dahlgren M, Forman J. 2022. Frontal head-on car-to-heavy goods vehicle crashes and their effect on the restraint system. The 27th International Technical Conference on the Enhanced Safety of Vehicles Conference (ESV), Yokohama, Japan 2023. Paper Number 23-0198.
- [12] de Coo PJA, Blaauw GJ and Huijbers JJW. 1997. EEVC Working Group 14 Activities in Energy-Absorbing Front Underrun Protection. SAE heavy vehicle underride protection TOPTEC, 15-16 April, 1997, Palm Springs, CA, USA.
- [13] Craig M, Parent D, Lee E, Rudd R, Takhounts E, Hasija V. 2020. Injury criteria for the THOR 50th male ATD. National Highway Traffic Safety Administration.
- [14] Gepner B, Bollapragada V, Acosta SM, Park G and Forman J. 2017. Comparison of THOR LX Xversion and Dorsiflexion Response in Component Tests, Sled Tests and Full Vehicle Crash Tests. In 25th International Technical Conference on the Enhanced Safety of Vehicles (ESV) National Highway Traffic Safety Administration.